



Response of 2D materials due to mechanical stimuli: exploring the fracture regime

A Dissertation Submitted to

The Department of Chemical Engineering of

The University of Patras by

Elli Bellou

In Partial Fulfilment of the Requirements of the Degree

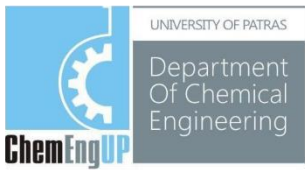
of Doctor of Philosophy in Chemical Engineering

Patras, December 2024

Πανεπιστήμιο Πατρών, Τμήμα Χημικών Μηχανικών

Έλλη Μπέλλου

© 2024- Με επιφύλαξη παντός δικαιώματος



Response of 2D materials due to mechanical stimuli: exploring the fracture regime

By

Elli Bellou

Laboratory of Nanotechnology and Advanced Materials Nanotechnology Area

Department of Chemical Engineering of University of Patras

Supervisor: Professor Costas Galiotis, University of Patras

SEVEN MEMBER COMMITEE:

Costas Galiotis, Professor, Department of Chemical Engineering, University of Patras, Greece

Spyros N. Yannopoulos, Professor, Department of Chemistry, University of Patras, Greece

Konstantinos Dassios, Associate Professor, Department of Chemical Engineering, University of Patras, Greece

George Voyiatzis, Research Director, FORTH/ICE-HT

Dimitris Kouzoudis, Professor, Department of Chemical Engineering, University of Patras, Greece

Nektaria Marianthi Barkoula, Professor, Department of Materials Engineering, University of Ioannina, Greece

Dimitris A. Saravanos, Professor, Department of Mechanical Engineering & Aeronautics, University of Patras, Greece

ΠΡΑΚΤΙΚΟ ΣΥΝΕΔΡΙΑΣΗΣ ΤΗΣ ΕΠΤΑΜΕΛΟΥΣ ΕΞΕΤΑΣΤΙΚΗΣ ΕΠΙΤΡΟΠΗΣ ΓΙΑ ΤΗΝ ΤΕΛΙΚΗ ΑΞΙΟΛΟΓΗΣΗ ΚΑΙ ΚΡΙΣΗ ΤΗΣ ΔΙΔΑΚΤΟΡΙΚΗΣ ΔΙΑΤΡΙΒΗΣ[1]

της Έλλης Μπέλλου

Η Επταμελής Εξεταστική Επιτροπή, η οποία ορίσθηκε κατά την αρ. 672/5.11.2024 Συνεδρίαση της Γενικής Συνέλευσης, συνεδρίασε την Τρίτη 10/11/2024 και ώρα 9:00 στην αίθουσα της βιβλιοθήκης του Τμήματος Χημικών Μηχανικών Α. Χ. Παγιατάκης και ήταν παρόντα τα εξής μέλη:

1) Κων/νος Γαλιώτης (επιβλέπων)

2) Σπύρος Γιαννόπουλος

3) Κων/νος Δάσιος

4) Γεώργιος Βογιατζής

5) Δημήτρης Κουζούδης

6) Νεκταρία Μπάρκουλα

7) Δημήτρης Σαραβάνος

Καλείται και εισέρχεται στην αίθουσα η υποψήφια Έλλη Μπέλλου και αναπτύσσει για 50 λεπτά, όπως όρισε η Επταμελής Εξεταστική Επιτροπή, το περιεχόμενο της διατριβής, με θέμα: «Response of 2D materials due to mechanical stimuli: exploring the fracture regime»

Στη συνέχεια γίνονται επιστημονικές ερωτήσεις στην Υποψήφια Διδάκτορα από την Επταμελή Εξεταστική Επιτροπή, σχετικές με το περιεχόμενο της Διατριβής, οι οποίες

[1] ΦΕΚ_τΒ_2988_25.07.2018

σκοπό έχουν τον έλεγχο της επιστημονικής συγκρότησης του Υποψηφίου, της γνώσης του θέματος της Διατριβής και των σχετιζομένων θεμάτων του οικείου επιστημονικού κλάδου.

Μετά το τέλος της ανάπτυξης της εργασίας, εξέρχεται από την αίθουσα η Υποψήφια Διδάκτορας και το λόγο παίρνει ο επιβλέπων Καθηγητής κ. Κων/νος Γαλιώτης, ο οποίος προτείνει να κριθεί η υποψήφια ως επιτυχούσα, καθώς η Διατριβή αποτελεί ουσιαστική συμβολή στην επιστήμη. Με την άποψη αυτή συμφωνούν και τα άλλα παρόντα μέλη της Επταμελούς Εξεταστικής Επιτροπής.

Μετά από τα παραπάνω, ο επιβλέπων κ. Κων/νος Γαλιώτης θέτει σε ψηφοφορία το ερώτημα «αν η Υποψήφια Διδάκτορας, κα Έλλη Μπέλλου, πέτυχε στη δοκιμασία».

Τα μέλη της Επταμελούς Εξεταστικής Επιτροπής ψηφίζουν μετά από κλήρωση, αρχίζοντας από το γράμμα Β:

1) Βογιατζής Γεώργιος	ΝΑΙ
2) Γαλιώτης Κων/νος	ΝΑΙ
3) Γιαννόπουλος Σπύρος	ΝΑΙ
4) Δάσιος Κων/νος	ΝΑΙ
5) Κουζούδης Δημήτρης	ΝΑΙ
6) Μπάρκουλα Νεκταρία	ΝΑΙ
7) Σαραβάνος Δημήτρης	ΝΑΙ

Ο επιβλέπων, κ.Κων/νος Γαλιώτης ανακοινώνει ότι η Υποψήφια Διδάκτορας, κα Έλλη Μπέλλου, πέτυχε στη δοκιμασία, δεδομένου ότι και τα επτά παρόντα μέλη της επταμελούς εξεταστικής επιτροπής, που είχαν και δικαίωμα ψήφου, ψήφισαν καταφατικά.

Μετά το παραπάνω αποτέλεσμα της ψηφοφορίας, η Επταμελής Εξεταστική Επιτροπή αποφασίζει ότι η κα. Έλλη Μπέλλου πέτυχε στη δοκιμασία.

Μετά το παραπάνω αποτέλεσμα της ψηφοφορίας, η επταμελής εξεταστική επιτροπή αποφασίζει να απονεμηθεί στην κα Έλλη Μπέλλου ο τίτλος του Διδάκτορα και προτείνει στη Συνέλευση την αυτοδίκαιη ανακήρυξή της σε Διδάκτορα του προγράμματος.

Με τιμή,

Η ΕΠΤΑΜΕΛΗΣ ΕΞΕΤΑΣΤΙΚΗ ΕΠΙΤΡΟΠΗ

1) Κων/νος Γαλιώτης (ΕΠΙΒΛΕΠΩΝ)	CONSTANTINE GALIOTIS Digitally signed by CONSTANTINE GALIOTIS Date: 2024.12.11 11:41:26 +02'00'
2) Σπύρος Γιαννόπουλος	SPYRIDON YANNOPOULOS 10/12/2024 14:15
3) Κων/νος Δάσιος	KONSTANTINOS DASIOS 12/12/2024 13:35
4) Γεώργιος Βογιατζής	GEORGIOS VOGIATZIS Digitally signed by GEORGIOS VOGIATZIS Date: 2024.12.11 10:01:06 +02'00'
5) Δημήτρης Κουζούδης	DIMITRIOS KOUZOUDIS 10/12/2024 15:09
6) Νεκταρία Μπάρκουλα	Nektaria Manoudis Barkoula Nektaria Manoudis Barkoula 10.12.2024 14:31
7) Δημήτρης Σαραβάνος	DIMITRIOS SARAVANOS 10/12/2024 23:43

To my parents Vasileios and Kleoniki, to my brother Marios and my companion in life Nikolaos

Acknowledgements

The research presented in this Ph.D. dissertation was conducted both in Foundation of Research and Technology Hellas – Institute of Chemical Engineering Sciences (FORTH/ICE-HT) and in the Department of Chemical Engineering of University of Patras (UoP), under the supervision of Dr. Costas Galiotis, Professor at the Chemical Engineering Department of UoP.

Words are not enough to express my gratitude and respect to Prof. Costas Galiotis, Professor at the Chemical Engineering Department of UoP, not only for the assignment of this innovative project, but also for his trust and kindness, for his guidance and support, for his encouragement in the pursuit of new ideas. There is no doubt that his mentorship and work ethics have inspired me not only as a researcher, but also as a personality. I would also like to thank Dr. Spyros Yannopoulos, Professor at the Chemistry Department of UoP, for kindly agreeing to be member of my advisory committee, and for providing access to the laser equipment that was used for the fabrication of defects in graphene-based nanolaminates. I would also like to thank Dr. Konstantinos Dassios, Associate Professor at the Chemical Engineering Department of UoP, for eagerly accepting to be member of my advisory committee. In addition, I am thankful to Dr. George Vogiatzis, Research Director at FORTH/ICE-HT, Dr. Dimitris Kouzoudis, Professor at the Chemical Engineering Department of UoP, Dr. Nektaria Barkoula, Professor at the Materials Science & Engineering Department of University of Ioannina, and Dr. Dimitris Saravanos, Professor at the Mechanical Engineering & Aeronautics Department of UoP, for accepting to become members of the examination committee.

In addition, I am grateful to Dr. Maria Giovanna Pastore Carbone, who had great contribution in the realization of this work, and also in the strengthening of my scientific capabilities, for her valuable guidance and assistance throughout my Ph.D. studies, which made as well as for our everyday discussions, which were not only limited to science, but also involved other daily life aspects. I am also deeply thankful to Dr. Anastasios Manikas for his support, valuable advice, and training in Raman spectroscopy technique, as well as for our fruitful discussions during my studies. Another person that I would like to thank is Dr. Nikos Koutroumanis, a great friend and colleague, not only for teaching me how to perform microtensile testing experiments,

but also for his valuable guidance in the field of mechanics. I am also thankful to Dr. Christos Pavlou for sharing knowledge on the fabrication of graphene/polymer nanolaminates, Dr. Christos Tsakonas for the provision of CVD graphene sheets, and Stella Peloni for the conduction of FEA. I am deeply thankful to Dr. Nikolaos Samartzis for the fabrication of defects in graphene-based nanolaminates.

In addition, I would like to sincerely thank all my lab mates including Dr. George Paterakis, Dr. George Gorgolis, Stefanos Matsalis, and Asemina Toliza, for the great time that we had together, inside and outside of the lab. I would also like to thank Costas Tragoulias, working in the machine shop of FORTH/ICE-HT, for helping me in the microdrilling of samples.

From the depths of my heart, I would like to thank my family for their unconditional love and support, and especially my parents Vasilis and Kleio, my brother Marios and Anna Gatzoudi. Lastly, I want to thank my companion in life Dr. Nikolaos Samartzis for being always there for me, especially in times when I needed it the most.

I acknowledge the financial support of the research project “Graphene Core 3, GA: 881603, which is implemented under the EU-Horizon 2020 Research & Innovation Actions (RIA) and is financially supported by EC financed parts of the Graphene Flagship.





Abstract

Graphene-based materials exhibit exceptional mechanical properties and therefore they are suitable candidates for high performance real-world applications. However, these properties degrade in the presence of defects, which act as stress concentration points, leading to the premature failure of materials. Hence, it is essential to gain insight into the parameters affecting fracture and the crack impeding mechanisms developed due to the presence of graphene. This dissertation delves into the fracture mechanics of graphene, both supported and embedded in polymers, utilizing either *in-situ* Raman spectroscopy or Atomic Force Microscopy (AFM), combined with micromechanical tensile testing. A thorough investigation over the influence of a defect on the fracture behavior and the morphology of graphene is conducted, as the introduction of an induced defect can serve as a model to simulate real-world conditions, where imperfections are inevitable. The presented findings reveal that its existence significantly affects the mechanical behavior and the fracture toughness of both graphene and graphene-based nanocomposites. Therefore, it is essential to monitor the strain/stress distribution close to defects, when external deformation is applied, as an increased stress field could potentially result to crack initiation and propagation. Herein, the fracture behaviour of a novel class of nanocomposites, CVD graphene-based nanolaminates, and the fracture behaviour of mechanically exfoliated graphene is examined. The use of monolayer CVD graphene both as a sensor in polymers and as an enhancing filler impeding the fracture of graphene-based nanolaminates is studied. The analysis emphasizes on the determination of the stress distribution profiles at the vicinity of an induced defect. In the case of graphene-based nanolaminates, valuable information is provided over the fracture procedure, such as the fracture toughness, the energy dissipation and the mechanisms that impede the crack propagation. The insights of this investigation offer a comprehensive understanding of fracture mechanics in graphene-based materials offering pathways over the harnessing of their exceptional properties. In the case of mechanically exfoliated graphene, a comprehensive analysis over the fracture behaviour of mono- and few- layered graphene, in which a defect has been induced, is conducted, unravelling unique crack and wrinkle patterns, due to strain imposition.

The content of this dissertation can be conceptually divided into 6 Chapters. An introduction to graphene and its exceptional properties, which renders its incorporation into nanocomposites as an enticing alternative towards the reinforcement of materials is provided in **Chapter 1**. **Chapter 2** delves into fracture mechanics and its important parameters, focusing on the fracture toughness of graphene-based materials, as well as the role of factors affecting the mechanical properties of graphene-based nanocomposites (i.e. filler content, size, dispersion etc.). In **Chapter 3**, a detailed description of all experimental techniques used in this dissertation is provided. In **Chapter 4**, the use of CVD graphene (produced via Chemical Vapor Deposition) as a strain sensor for the quantification of strain close to defects, and for the extraction of valuable parameters related to fracture, such as Stress Concentration Factor (SCF) is proposed. The results were validated both analytically and numerically via Finite Element Analysis, with the SCF values being remarkably similar, suggesting that CVD graphene can be successfully used as a strain sensor for the assessment of strain/stress distribution close to defects in polymers, and therefore to polymer-based composites. **Chapter 5** deals with the study of fracture mechanisms in a novel class of graphene nanocomposites, the CVD graphene/polymer nanolaminates, when subjected to tension. A thorough investigation over their fracture behaviour reveals that a low graphene content leads to the enhancement of the nanolaminate's fracture toughness, whereas a higher graphene content leads to its embrittlement, despite the enhancement providing to the nanocomposite. In **Chapter 6**, fracture mechanics and strain-induced morphological alterations of notched mechanically exfoliated graphene flakes are investigated, unveiling novel insights and contribute to the advancement of nanotechnology field, through the design and optimization of nanomaterials with tailored properties and functionalities for future applications. Lastly, in **Chapter 7**, the results obtained in this thesis are summarized and potential topics for future work in the study of fracture of 2D materials and graphene-based nanocomposites are proposed.

Περίληψη

Τα γραφενικά υλικά παρουσιάζουν εξαιρετικές μηχανικές ιδιότητες, οι οποίες τα καθιστούν κατάλληλα για χρήση σε διάφορες προηγμένες εφαρμογές. Ωστόσο, η παρουσία ατελειών μπορεί να υποβαθμίσει τις ιδιότητες αυτές, καθώς λειτουργούν ως σημεία συγκέντρωσης τάσης, οδηγώντας σε πρόωρη αστοχία των υλικών. Επομένως, η γνώση των παραμέτρων που επηρεάζουν τη θραύση, καθώς και των μηχανισμών που καθυστερούν την τελική θραύση του υλικού είναι μείζονος σημασίας. Στην παρούσα διατριβή μελετάται η θραυστομηχανική συμπεριφορά του γραφενίου, το οποίο έχει εναποτεθεί σε πολυμερικό υπόστρωμα, καθώς και η συμπεριφορά νανοσύνθετων πολυστρωματικών μεμβρανών με βάση το γραφένιο. Επιπλέον, το γραφένιο εισάγεται ως έγκλεισμα σε πολυμερική μήτρα, για τη μελέτη της συμπεριφοράς του poly(methyl methacrylate) (PMMA), το οποίο είναι ένα πολυμερές που χρησιμοποιείται ευρέως σε τεχνολογικές εφαρμογές. Για την υλοποίηση της παρούσας διατριβής επιστρατεύεται η φασματοσκοπία Raman και η Μικροσκοπία Ατομικής Δύναμης (AFM), σε συνδυασμό με μηχανικές δοκιμές μικρο-εφελκυσμού. Συγκεκριμένα, ενδελεχής έρευνα διεξάγεται σχετικά με την επίδραση μιας ατέλειας στη θραυστομηχανική συμπεριφορά και στη μορφολογία του γραφενίου, κατά την άσκηση εξωτερικού φορτίου. Η δημιουργία μιας τεχνητής ατέλειας μπορεί να προσομοιώσει συστήματα σε πραγματικές συνθήκες, στα οποία η ύπαρξη ατελειών είναι αναπόφευκτη. Τα αποτελέσματα που παρουσιάζονται δείχνουν ότι η ύπαρξή της επηρεάζει σημαντικά τη μηχανική συμπεριφορά και την αντοχή στη θραύση του γραφενίου και των γραφενικών νανοσυνθέτων. Επομένως, η μελέτη της κατανομής της τάσης κοντά σε ατέλειες, όταν ασκείται εξωτερική παραμόρφωση, είναι υψηλής σημασίας, καθώς δυνητικά η αύξηση της συγκέντρωσης τάσης μπορεί να οδηγήσει στην έναρξη και διάδοση ρωγμών. Στην παρούσα διατριβή, εξετάζεται η θραυστομηχανική συμπεριφορά νανοσύνθετων πολυστρωματικών μεμβρανών γραφενίου παραγόμενου μέσω της χημικής εναπόθεσης ατμών (CVD), καθώς και μηχανικά αποφλοιωμένων γραφενικών φύλλων. Συγκεκριμένα, μελετάται η χρήση μονοστρωματικών CVD γραφενικών φύλλων τόσο ως αισθητήρας τάσης σε πολυμερή, όσο και ως ενισχυτική φάση ενός νανοσυνθέτου, δίνοντας έμφαση στην ανάλυση της κατανομής της τάσης κοντά στην ατέλεια. Κατά τη μελέτη των νανοσυνθέτων, παρατηρείται η ανάπτυξη μηχανισμών που εμποδίζουν τη θραύση του υλικού, λόγω της διάχυσης της ενέργειας κατά την έναρξη ρωγμών. Τα ευρήματα αυτής της έρευνας προσφέρουν μια ολοκληρωμένη κατανόηση της μηχανικής θραύσης

υλικών με βάση το γραφένιο, διευκολύνοντας την αξιοποίηση των εξαιρετικών ιδιοτήτων τους. Στην περίπτωση του μηχανικά αποφλοιωμένου γραφενίου, εκτεταμένη ανάλυση πραγματοποιείται σχετικά με την θραύση μονοστρωματικών και πολυστρωματικών φύλλων γραφενίου, στα οποία έχει δημιουργηθεί μια ατέλεια, αποκαλύπτοντας μοναδικά μοτίβα πτυχώσεων, λόγω της εξωτερικά εφαρμοζόμενης παραμόρφωσης.

Η διατριβή χωρίζεται εννοιολογικά σε 6 Κεφάλαια. Στο πρώτο κεφάλαιο παρατίθονται πληροφορίες σχετικά με το γραφένιο και τις εξαιρετικές του ιδιότητες, οι οποίες το καθιστούν ελκυστική επιλογή για την ενίσχυση άλλων υλικών. Το Κεφάλαιο 2 πραγματεύεται βασικές έννοιες της θραυστομηχανικής, εστιάζοντας στους παράγοντες που επηρεάζουν τη μηχανική συμπεριφορά του γραφενίου, καθώς και γραφενικών νανοσυνθέτων. Στο Κεφάλαιο 3 παρουσιάζονται οι πειραματικές τεχνικές που χρησιμοποιήθηκαν στην παρούσα διατριβή. Στο Κεφάλαιο 4 προτείνεται η χρήση CVD γραφενίου ως αισθητήρας για την ποσοτικοποίηση της τάσης κοντά σε κυκλική ατέλεια, καθώς και για την εξαγωγή παραμέτρων που σχετίζονται με την αντοχή του υλικού στη θραύση, όπως ο Συντελεστής Συγκέντρωσης Τάσεων (SCF). Τα αποτελέσματα επαληθεύτηκαν μέσω της Ανάλυσης Πεπερασμένων Στοιχείων, με τις τιμές του SCF να είναι εξαιρετικά παρόμοιες, υποδεικνύοντας ότι το CVD γραφένιο μπορεί να χρησιμοποιηθεί επιτυχώς ως αισθητήρας για την εκτίμηση της κατανομής τάσης κοντά σε ατέλειες σε πολυμερή και πολυμερικά σύνθετα υλικά. Το Κεφάλαιο 5 πραγματεύεται τη μελέτη των μηχανισμών θραύσης νανοσύνθετων πολυστρωματικών μεμβρανών CVD γραφενίου, όταν αυτές υποβάλλονται σε εφελκυσμό. Διεξοδική έρευνα για τη συμπεριφορά θραύσης τους αποκαλύπτει ότι η ενσωμάτωση χαμηλών ποσοστών γραφενίου οδηγεί σε βελτίωση της αντοχής των γραφενικών μεμβρανών στη θραύση. Αντιθέτως, η ενσωμάτωση υψηλότερου γραφενικού ποσοστού καθιστά το νανοσύνθετο πιο ψαθυρό, παρά τη βελτίωση των μηχανικών του ιδιοτήτων. Στο Κεφάλαιο 6 μελετώνται οι μηχανισμοί θραύσης και οι μορφολογικές μεταβολές σε μηχανικά αποφλοιωμένα γραφενικά φύλλα, στα οποία έχει δημιουργηθεί μια νανο-εγκοπή. Η μελέτη αυτών των συστημάτων αποκαλύπτει νέα πεδία εφαρμογών και συμβάλλει στην ανάπτυξη του πεδίου της νανοτεχνολογίας, μέσω του σχεδιασμού και της βελτιστοποίησης νανουλικών με προσαρμοσμένες ιδιότητες και λειτουργικότητες για μελλοντικές εφαρμογές. Τέλος, στο Κεφάλαιο 7 παρουσιάζονται τα συμπεράσματα της διατριβής και προτείνονται εναλλακτικές προσεγγίσεις για την περαιτέρω

διερεύνηση της θραυστομηχανικής συμπεριφοράς 2D υλικών και άλλων νανοσύνθετων. Συνοψίζοντας, η μελέτη της συμπεριφοράς θραύσης διαφόρων συστημάτων μπορεί να προσφέρει πολύτιμες γνώσεις για τους μηχανισμούς θραύσης που δρουν συνεργατικά, βελτιώνοντας την αντοχή στη θραύση των υλικών.

Table of contents

Abstract....13
Περίληψη....15
1. Graphene: fundamentals and nanocomposites....20
1.1 Introduction to carbon....20
1.2 Graphene: fundamentals and properties....22
1.3 Production methods of graphene....26
1.3.1 Top-down approach....26
1.3.2 Bottom-up approach....28
1.4 Transfer of graphene onto desirable substrates....29
1.4.1 Wet Transfer procedure....31
1.5 Graphene-based nanocomposites....32
1.5.1 Production of graphene-based nanocomposites....36
1.5.2 Graphene-based nanolaminates....37
2. Fracture mechanics....40
2.1 Types of fracture....40
2.1.1 Linear Elastic Fracture Mechanics....41
2.2 Griffith's brittle fracture....44
2.3 Fracture Parameters....45
2.3.1 Stress Intensity Factor and Stress Concentration Factor....46
2.3.2 Energy Release Rate....47
2.4 Nonlinear Fracture Mechanics....47
2.5 Defects....48
2.6 Fracture toughness....49
2.7 Fracture toughness of graphene and other 2D materials....50
2.8 Fracture toughness of graphene-based nanocomposites....53
2.9 Factors that affect the toughness of graphene-polymer nanocomposites....55
2.10 Graphene-PMMA nanocomposites: Nanofillers impact in mechanical reinforcement58
3. Characterization techniques....62
3.1 Optical Microscopy....62
3.2 Raman Spectroscopy....64
3.3 Atomic Force Microscopy....70
3.4 In-situ mechanical testing....75
3.5 Scanning Electron Microscopy (SEM)....77
4. Using large-size graphene sensor for the assessment of stress concentration in the vicinity of a notch....78
4.1 Experimental methods for measuring the stress concentration factor....78

4.2 Specimen fabrication 81
4.2 Quality control of the CVD graphene membrane 83
4.4 *In-situ* Raman spectroscopy combined with micro-tensile testing 85
4.5 Conclusion 100
5. Fracture toughness of graphene-PMMA nanolaminates 101
5.1 Fabrication of PMMA/CVD graphene nanolaminates 101
5.2 Fracture processes in defected graphene-PMMA nanolaminates 106
5.3 Monitoring the stress distribution across the area of a defect using Raman spectroscopy 116
5.4 Conclusions 132
6. Crack propagation and related morphological changes of exfoliated graphene monitored via Atomic Force Microscopy 135
6.1 Production and selection of exfoliated graphene samples 135
6.2 Quality control of the specimens via Raman spectroscopy and Atomic Force Microscopy 136
6.3 Optimization of AFM tip-induced defect 138
6.4 Cracking of exfoliated graphene: formation and propagation 141
6.4.1 The case of monolayer graphene 142
6.4.2 The case of few-layered graphene 148
6.4.3 Other strain-induced morphological features observed in monolayer and few-layered graphene 151
6.5 Fatigue of exfoliated graphene 154
6.6 Conclusions 161
7. Conclusions and Future work 163
References 167

1. Graphene: fundamentals and nanocomposites

1.1 Introduction to carbon

Carbon lies in the "heart" of organic chemistry, being the fourth most common element in the universe (after hydrogen, helium, and oxygen). While its quantity is practically constant in our planet, carbon is continuously formed inside the stars as a result of the collision of three α particles (He_2^4), a nuclear fusion event that is rather common at such extreme temperature and pressure conditions.

The electronic configuration of carbon, at its ground state, is $1s^2 2s^2 2p^2$. Out of the six total electrons, the ones occupying the inner 1s atomic orbital do not participate in the formation of bonds, unlike the remaining four outer electrons, which combined with the ability of carbon to catenate are responsible for the formation of endless different molecules. The electron density distribution in a molecule is represented by molecular orbitals, which form by the combination/mixing of the atomic orbitals of the individual atoms comprising the molecule. In the case of carbon, its orbitals can be either sp, sp^2, or sp^3 hybridized, depending on how many of the $2p_{x,y,z}$ orbitals mix with the 2s orbital (**Figure 1.1(a)**).

Figure 1.1(b) depicts the geometries of carbon's hybridized orbitals. The four sp^3 hybridized orbitals adopt a tetrahedral arrangement with bond angles of 109.5° to minimize electron repulsion. The three sp^2 hybridized orbitals lie in-plane with a bond angle of 120°, while the remaining 2p orbital is perpendicular to the plane. The two sp hybridized orbitals align linearly at a 180° angle, with the two unhybridized 2p components perpendicular to each other and to the line defined by the sp orbitals.

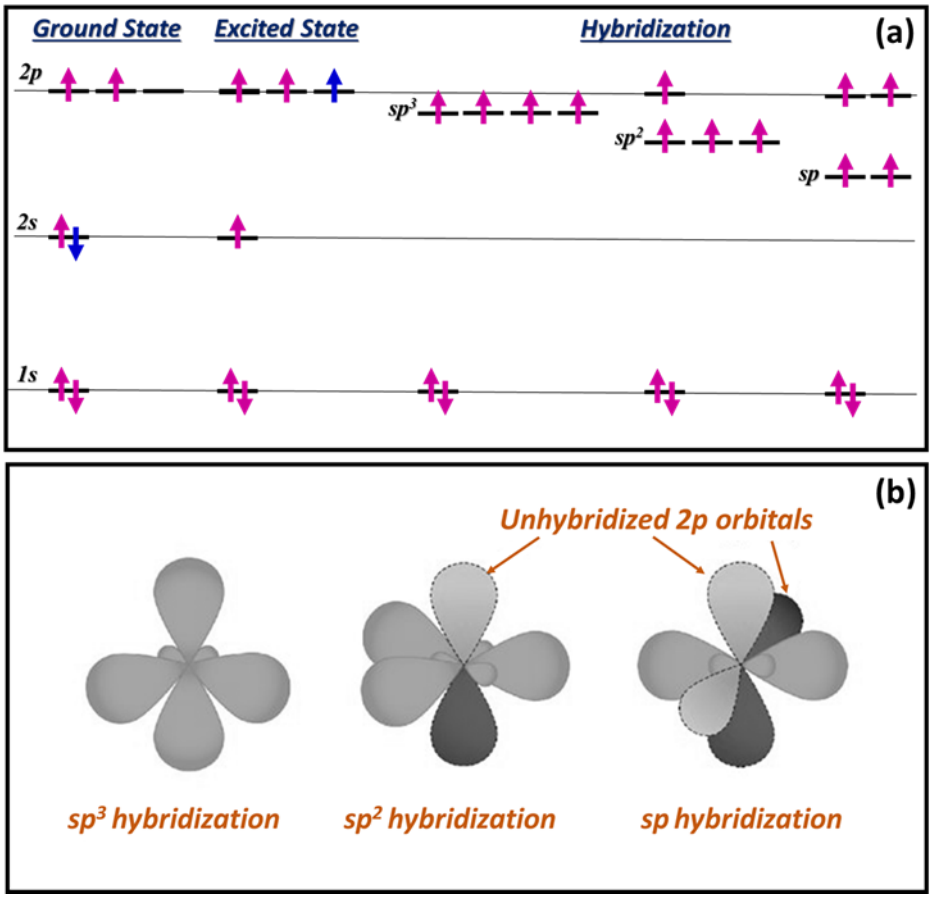


Figure 1.1: (a) Electronic configuration, and (b) atomic orbitals of carbon.

Due to its electronic configuration, carbon exhibits a unique propensity for catenation, wherein atoms of the same element bond to form chains, leading to an extensive array of carbon-based compounds (**Figure 1.2(a)**). Being the smallest tetravalent atom, is beneficial for forming strong carbon-carbon bonds, ultimately leading to stable long chains. Apart from its various compounds, carbon is known to form numerous allotropes.

Allotropes of carbon can be found both in nature and be composed in the lab. Naturally occurring allotropes are graphite, diamond and lonsdaleite (hexagonal diamond). Graphite is composed of atomically thin layers (connected via weak Van der Waals interactions) of sp^2 hybridized carbon atoms arranged in a hexagonal lattice, whereas diamond is composed of sp^3 hybridized carbon atoms arranged in a cubic crystalline structure. Lonsdaleite can be obtained after suitable treatment (temperature and pressure) of graphite or cubic diamond [1]. Despite that both graphite and diamond are pure carbon, their different structure leads to entirely different material properties, such as hardness, color, electric conductivity, etc. In the past decades, low-dimensional

allotropes have been successfully synthesized in the laboratory, including 0-D buckminsterfullerene (C60) [2], 1-D carbon nanotubes (CNTs) [3], and 2-D graphene sheets [4], as well as hybrid forms like carbon nanobuds [5]. Carbon allotropes composed of six-membered aromatic rings are referred to as graphitic allotropes. As shown in **Figure 1.2(b)**, the two-dimensional allotrope, graphene, can be considered as the "parent" of all graphitic allotropes, as it can yield them by changing its topology. For instance, wrapping graphene around an axis or a point can yield one-dimensional carbon nanotubes or zero-dimensional fullerenes, whereas its stacking through Van der Waals forces can result to three-dimensional graphite [6].

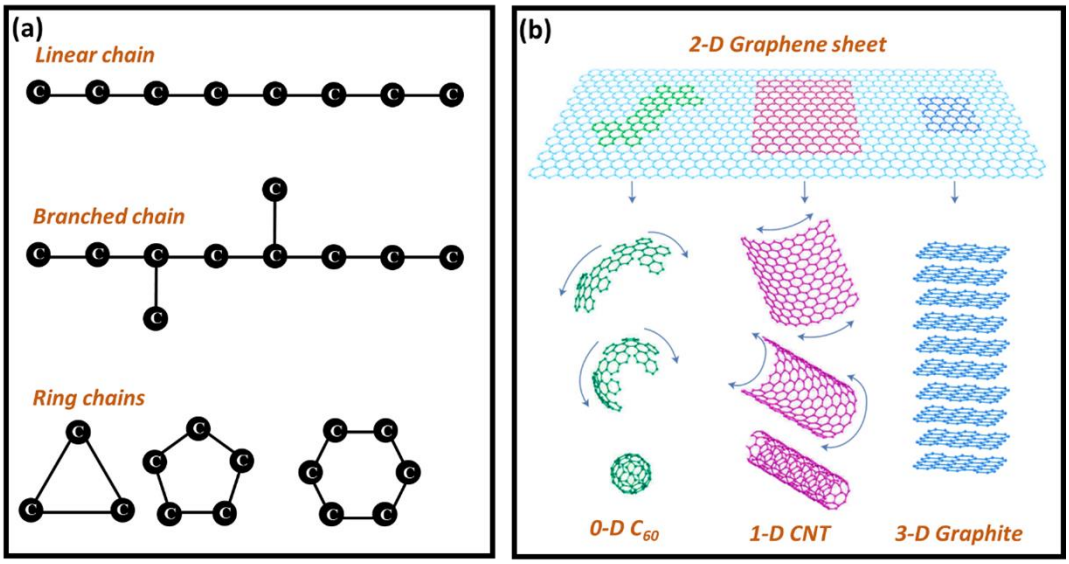


Figure 1.2:(a) Catenation in carbon, and (b) derivation of 0-D, 1-D and 3-D allotropes from 2-D graphene [6].

1.2 Graphene: fundamentals and properties

Graphene is known as the first two-dimensional atomically thin material, and its booming popularity in research and industrial applications is owed to the first isolation of mechanically exfoliated graphene by Novoselov et al., two decades ago [4]. Throughout these years, it has been in the center of academic and industrial interest, as it exhibits extraordinary physicochemical properties, due to its unique structure. Specifically, each carbon atom is connected through strong σ covalent bonds to its three nearest-neighbors, forming a hexagonal lattice. These three σ bonds are responsible for the high mechanical strength of all graphitic allotropes [7] and originate from the head-

to-head overlap of the sp^2 hybridized orbitals (indicated in **Figure 1.1(b)**), which arrange in the basal plane of graphene at an angle of 120°. The unbound $2p_z$ electron of each carbon atom, which is perpendicular to the lattice, contributes to graphene's electronic conductivity and optical properties. The side-by-side overlapping of these 2p orbitals, leads to the formation of π bonds, which due to graphene's symmetry correspond to an electron cloud of delocalized π electrons (**Figure 1.3(a)**).

Graphene's honeycomb lattice can be viewed as a combination of two triangular sublattices A, B (**Figure 1.3(b)**), each with a lattice constant $\alpha = d\sqrt{3}$, where d is the C-C bond length, equal to 0.142 nm.

The three nearest neighbor vectors (**Figure 1.3(b)**) are:

$$\boldsymbol{d_1} = d\left(\frac{1}{2}, \frac{\sqrt{3}}{2}\right), \quad \boldsymbol{d_2} = d\left(\frac{1}{2}, -\frac{\sqrt{3}}{2}\right), \quad \boldsymbol{d_3} = -d(1,0) \tag{1.1}$$

The unit vectors (gray-colored arrows of **Figure 1.3(b)**) of sublattice A are:

$$\boldsymbol{a_1} = a\left(\frac{\sqrt{3}}{2}, \frac{1}{2}\right), \quad \boldsymbol{a_2} = a\left(\frac{\sqrt{3}}{2}, -\frac{1}{2}\right) \tag{1.2}$$

where $a = |\boldsymbol{a_1}| = |\boldsymbol{a_2}|$, and the formed angle equals to π/3. Therefore, the unit cell of graphene has the shape of a rhombus and includes 2 atoms (1 atom from sublattice A and 1 atom of sublattice B). The wavevectors of the reciprocal space are:

$$\boldsymbol{b_1} = \frac{2\pi}{3\alpha}\left(1, \sqrt{3}\right), \quad \boldsymbol{b_2} = \frac{2\pi}{3\alpha}\left(1, -\sqrt{3}\right) \tag{1.3}$$

where $|\boldsymbol{b_1}| = |\boldsymbol{b_2}| = \frac{4\pi}{3\alpha}$, and the formed angle equals to 2π/3. The hexagonal Brillouin Zone (BZ) of graphene has the following high-symmetry points: the center Γ, the doubly degenerated corner K, and the edge's center M (**Figure 1.3(c)**).

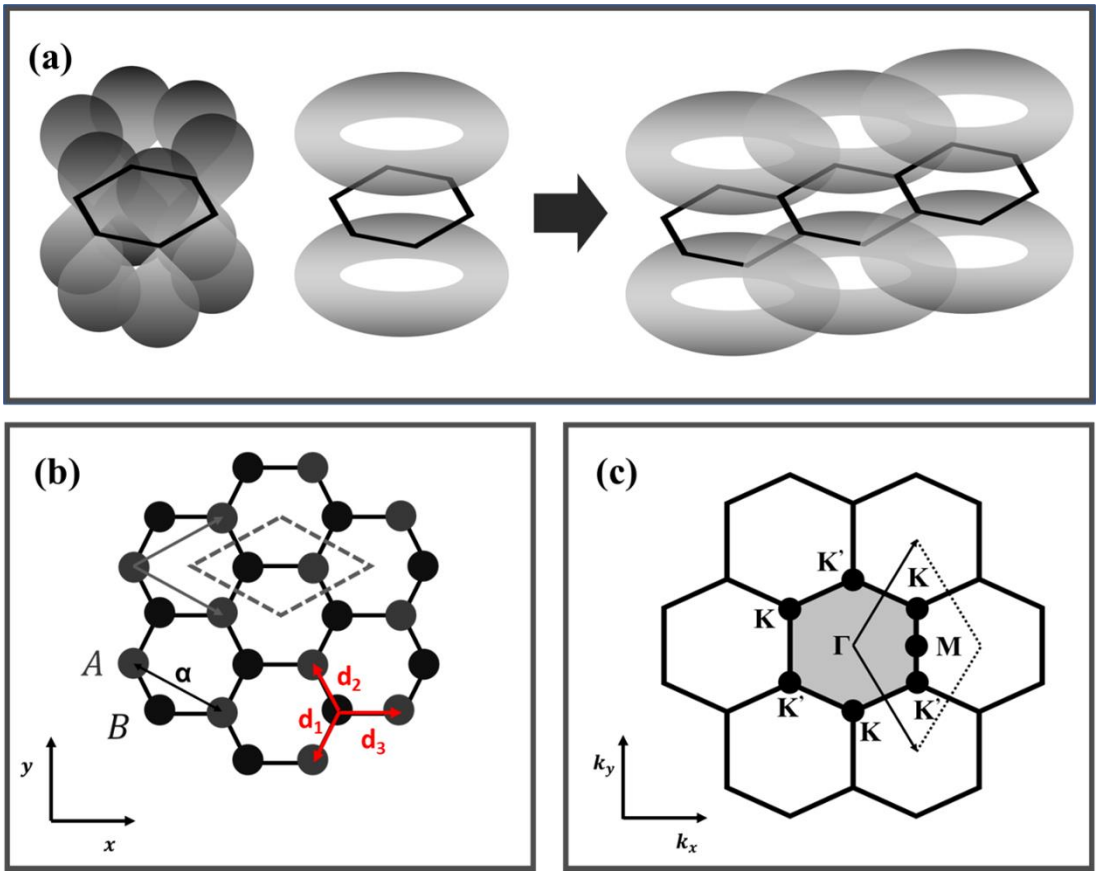


Figure 1.3:(a) Delocalization of 2pz electrons in graphene, (b) formation of the honeycomb lattice by the superimposition of two triangular sublattices, (c) Brillouin zone of graphene and its high-symmetry points.

The study of Wallace, almost 80 years ago, set the foundation on understanding the peak structure of a graphene [8]. In the simplest approximation where electrons transfer only between nearest neighbors, the dispersion relation is [12]:

$$E(k) = \pm\beta\sqrt{e^{i\vec{k}\cdot\vec{d}_1} + e^{i\vec{k}\cdot\vec{d}_2} + e^{i\vec{k}\cdot\vec{d}_3}} \tag{1.4}$$

where the hopping parameter β is related to the probability amplitude for electron transfer between nearest neighbors, whereas $\pm$ corresponds to the conduction and valence peaks respectively. These peaks meet at the six corners of the Brillouin zone (see **Figure 1.4**), where both the density of states and the energy gap is zero. Therefore, graphene is a zero peak-gap semiconductor. At low electron energies, the electron's dispersion relation is linear, and equal to:

$$E(k) = \hbar k v_F \tag{1.5}$$

where v_F is the Fermi velocity, which in the case of graphene is approximately 300 times smaller than the speed of light (the electrons behave as massless Dirac fermions) [8].

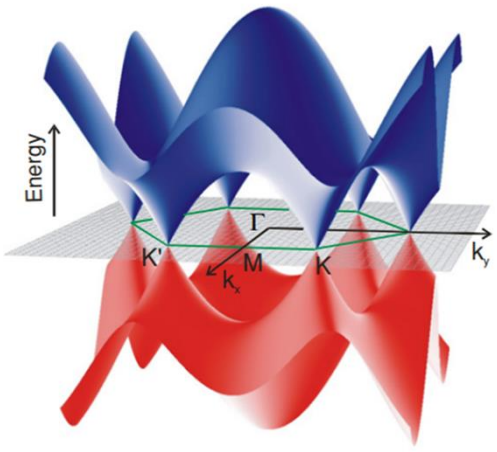


Figure 1.4:Electronic peak structure of monolayer graphene [9].

As a material's conductivity is proportional to the product of carrier mobility and carrier density, the electronic quality of materials is often characterized by the charge carrier mobility. For a suspended graphene at ~5K, an electron mobility of $\sim 200{,}000\ cm^2V^{-1}s^{-1}$ at an electron density of $\sim 2 \times 10^{11}\ cm^{-2}$ has been reported [10]. While the electron mobility is limited by scattering at defects (e.g., wrinkles, grain boundaries, atomic vacancies, adsorbates and so on), there is also the influence of intrinsic scatterers such as phonons (vibrational modes) that cannot be eliminated, setting a fundamental limit on the electron mean free path and hence graphene's electronic quality [10]. On the other hand, the presence of out-of-plane vibrational modes in graphene has been associated with its excellent bending properties [11]. The stacking of graphene layers leads to multilayered graphene and Bernal stacked (AB) graphite, which involves a relative translation between adjacent graphene layers, with interlayer distance of approximately 0.335 nm [12]. The electronic coupling of the adjacent graphene sheets affects the dispersion relation and separates the valence and conduction peaks at the corners of the Brillouin zone, opening a tunable peak gap [13].

1.3 Production methods of graphene

Graphene, at its pristine state, can only be produced via mechanical exfoliation of graphite, using the scotch tape method, a labor-intensive and time-consuming process, providing small sized (<100 μm) graphene flakes [4]. In order to overcome these limitations, various techniques for large scale production of graphene and other 2D materials synthesis, have been developed. Nevertheless, large quantities are achieved at the expense of quality, as the physical properties are significantly downgraded. As depicted in **Figure 1.5,** the routes followed for the synthesis of graphene (as of any other 2D material) can be categorized in two sub-categories, the top-down approach, and the bottom-up approach [14]. Top-down methods encompass the production of atom-thick layered materials via exfoliation of 3D crystals. Bottom-up techniques involve the production of larger 2D materials by utilizing small molecular precursors. Although there are numerous synthesis techniques, there is still need for a low-cost, environmentally benign, safe, and scalable method that does not compromise the quality of graphene [15].

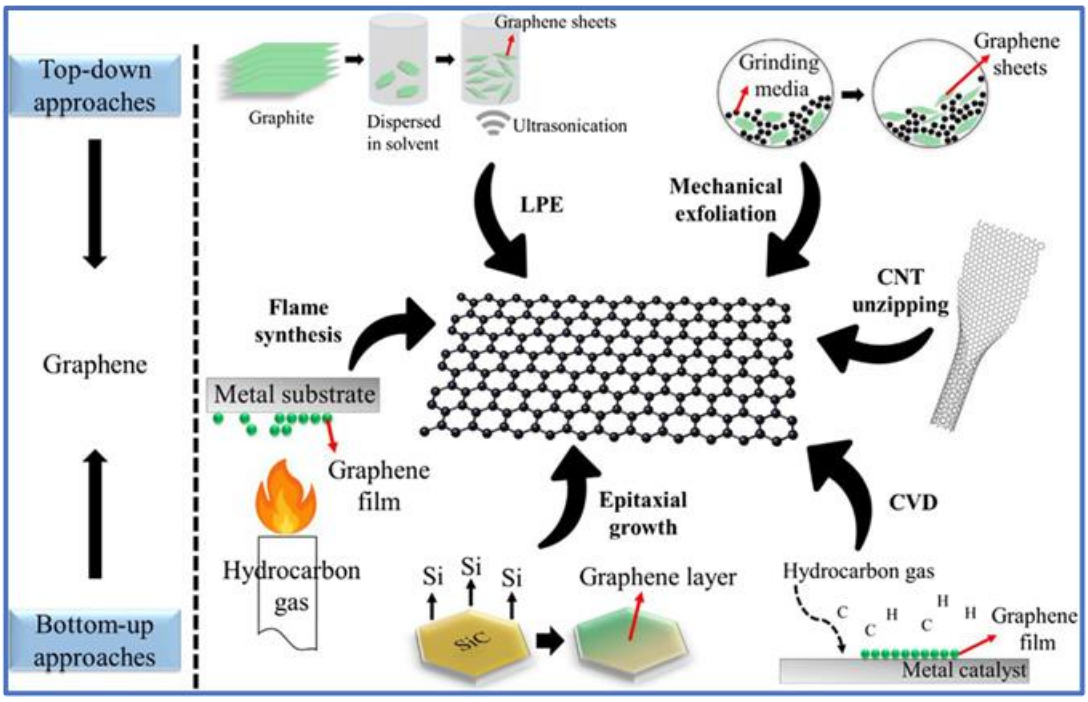


Figure 1.5:Some methods for the production of graphene [14].

1.3.1 Top-down approach

The top-down approach pertains to breaking down graphitic layers in order to isolate atom-thick layers. To achieve this, an external mechanical or chemical stimuli has to

be applied to a 3D crystal in order to segregate the layers that are connected to each other through weak Van der Waals forces.

The mechanical exfoliation method expanded a brand-new field into exploring and exploiting the properties of 2D materials, which are obtained from the breaking of 3D materials. Prof. A. Geim and K. S. Novoselov won the 2010 Nobel Prize in Physics, as they successfully isolated monolayer graphene through the mechanical exfoliation of hexagonally oriented pyrolytic graphite (HOPG) and initiated the "graphene fever era" [4]. The fundamental idea involves the mechanical cleavage of a single graphene layer from a bulk graphite. Scotch tape was used for the transfer and isolation of one/few graphene layers, as the adhesion of graphite to the tape surpasses the week Van der Waals forces, which hold the graphitic sheets together. These one/few layer sheets can be transferred onto a chosen substrate, without compromising their high quality. This method is primarily employed for laboratory research, as it is immensely time-consuming and the produced graphene flakes are characterized by a stochastic nature regarding their shape, dimension and location. Therefore, this technique is the least industrially scalable, which renders it most of the times impractical for commercial graphene-based devices [16].

Liquid phase exfoliation (LPE) is another top-down synthesis method, where lighter exfoliated flakes are disintegrated from bulk crystals. The 3D structures are dispersed into suitable solvents, whose choice is critical for a stable dispersion (to avoid restacking or precipitation), and then ultrasounds [17] or high shear mixing [18] is used for the breakdown of 3D crystals. Generally, LPE is more scalable than mechanical exfoliation, as the human factor which reinforces the randomness in production is eliminated. However, the production of monolayer flakes is not feasible, and the produced flakes follow a thickness and size distribution [19]. Hummer's method is another top-down technique, where graphite undergoes oxidation using strong reagents ($NaNO_3$, $KMnO_4$, and H_2SO_4) [20]. Two-dimensional graphene oxide is derived from the ultrasound-assisted breakdown of three-dimensional graphite oxide, which due to the presence of oxygen groups (epoxy, hydroxyl, carbonyl, and carboxyl) [21], possesses a semi-aromatic carbon structure with both sp^2 and sp^3 hybridization. The elimination of oxygen-containing groups in graphene oxide, through thermal or chemical methods, can lead to reduced graphene oxide (rGO) [21]. While sp^2 hybridization is partially restored, the structural defects in the graphene lattice persist,

and therefore the quality of rGO is inferior to that of graphene synthesized via other approaches [22]. Although Hummer's method allows the large-scale production, there is a great interest for the development of improved methods, due to safety concerns arising from the highly exothermic reaction and the use of hazardous reagents [23].

Graphene sheets can also be obtained electrochemically, through the submerging of graphite in a suitable electrolyte and the application of current [24]. As a result, ions can intercalate between the graphene sheets, weakening their Van der Waals interactions, and the decomposition of the solvent molecules (electrolysis) results to the exfoliation of graphene [25]. This method is called electrochemical exfoliation, and yields a high quantity of product, maintaining its quality, while it is also environmentally friendly. Nevertheless, the thickness of the exfoliated flakes is not uniform [25].

1.3.2 Bottom-up approach

The bottom-up approach is associated with the self-organization of carbon radicals, which form after the decomposition of carbonaceous precursors. These methods include epitaxial growth via the chemical vapor deposition (CVD) technique, or graphene growth on a substrate through laser-based methods.

Chemical vapor deposition (CVD) is a technique employed for relatively high-quality synthesis of graphene. The method necessitates the use of a gaseous carbon precursor, such as methane (CH_4) or ethylene (C_2H_4), whose molecules will be decomposed and adsorbed at sufficient high temperatures, on a catalytic substrate (copper or nickel) [26]. The substrate plays a very important role, as monolayer graphene is usually formed on copper, while few-layered graphene is formed on nickel. The carbon produced from this chemical reaction process diffuses onto the catalyst, forming nucleation points that grow epitaxially. The CVD method is very effective on the large-scale graphene production. However, its polycrystalline nature affects its quality, as the individual graphene crystals are not optimally oriented in respect to each other, forming a "graphene quilt" [27]. Larger graphene single crystals can be produced through the use of liquid metal catalysts [26], however, this procedure requires special equipment.

The growth of graphene using lasers relies on the matching of the laser's wavelength to the absorption spectrum of a carbon-based precursor (most commonly polyimide [28] or graphene oxide [29], which contain aromatic rings in their structure). If these match, then the absorption of the laser's photons leads to an extreme temperature rise (which may exceed 3000 K), which results to its decomposition, and the recombination of carbon radicals [28]. This method is suitable for the preparation of porous graphene structures but cannot be used for the growth of 2D graphene of high quality.

1.4 Transfer of graphene onto desirable substrates

The most common transfer methods of graphene onto different substrates include chemical vapor deposition (CVD) growth on solid catalytic substrates, like copper (Cu) and nickel (Ni), followed by transfer processes, as usually these substrates are not compatible with certain target applications. For example, in the field of electronics, they cannot be integrated into the devices, but instead they have to be transferred onto flexible polymer substrates (required for flexible electronics) or onto silicon wafers or glass substrates, in order to conform with the standard semiconductor processing techniques [30], and simultaneously allow better control over graphene's properties [31]. Moreover, the SiO_2 substrates can be used in electronic devices due to their insulating properties and compatibility with lithography techniques. Therefore, the development of large-scale transferring techniques of graphene onto suitable substrates is crucial. In **Figure 1.6** some typical transfer routes are depicted, including wet and dry transfer, electrochemical and non-electrochemical bubble transfer, roll-to-roll and support-free transfer. In the wet transfer process, a graphene-coated substrate is immersed into a solution, which is used to etch the metal. After the complete removal of the metal, graphene is rinsed with distilled water, and is ultimately transferred onto the desired substrate via fishing procedure [32]. Due to the atom-thick nature of graphene, a polymer layer is often employed in order to avoid graphene's disintegration during the process, as polymers are flexible and can be easily removed after the termination of transfer, without introducing contamination from residues. In a dry transfer procedure, graphene can be transferred to the desired substrate by utilizing a stamping method, in which a polymer such as PDMS acts as a temporary supportive layer. For this approach to be successful, specific adhesion requirements for the system graphene – PDMS – final substrate shall be meet [33]. Electrochemical and non-electrochemical bubble transfer are scalable procedures, where bubbles are generated

through electrolysis and non-electrochemical approaches respectively, that can separate graphene from its metal substrate and deposit it onto the target substrate, with the appropriate maneuvering [34]. In those cases, the control over the experimental conditions and substrate selection is crucial. Roll-to-roll procedure involves the graphene transfer onto a flexible polymeric substrate in a continuous process, through a series of sequential steps, which result in a large-scale production of thin graphene films that can be integrated onto desirable devices [35]. Support-free transfer involves the application of controlled external mechanical pressure or shear forces for the detachment of graphene and its transfer to another substrate [36]. The advantages and disadvantages of each of these methods are taken into consideration before utilizing them for the intended application [34]. The most challenging part remains the transfer of large-size CVD graphene from the metal (catalytic) substrate that it was growth on to the intended one, without compromising its high quality during the sequential procedures of each transfer process, as defects like cracks or wrinkles may be introduced [37].

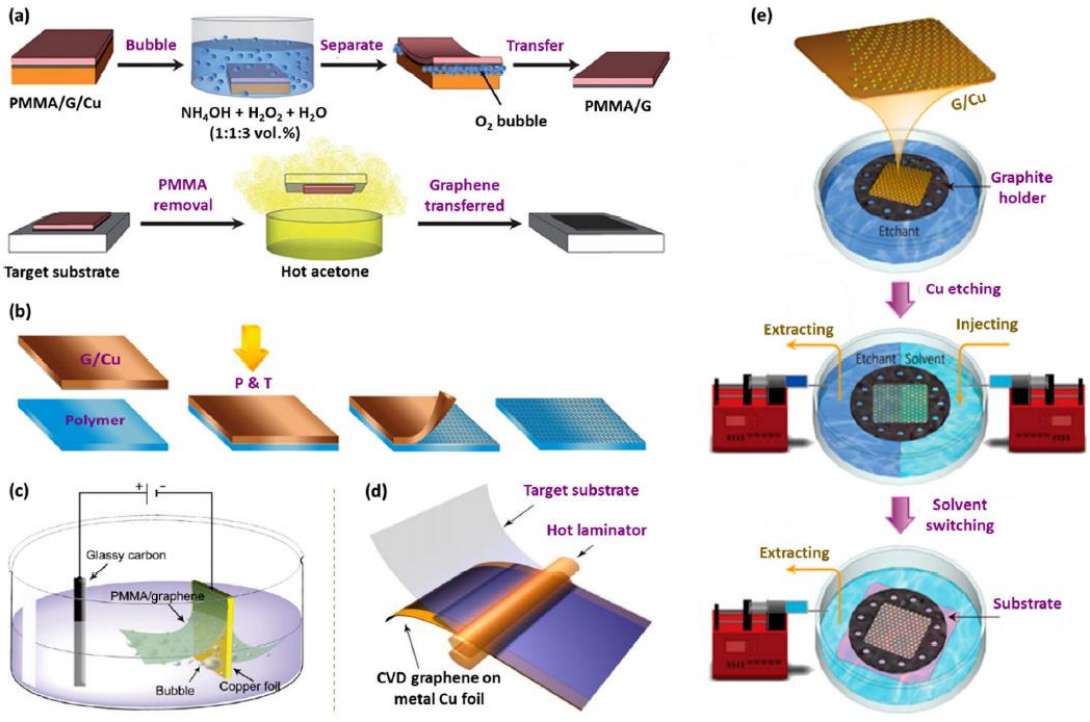


Figure 1.6: Schematic diagrams of typical transfer routes [34].

1.4.1 Wet Transfer procedure

Wet transfer procedure is still the most common technique for the deposition of CVD graphene and was employed in the work described in this dissertation,. The general overview of this procedure is given into the following steps:

- Removal of graphene from the backside of the Cu foil by implementing O_2 plasma.
- Polymer support transfer: A thin polymer layer (PMMA) is applied on top of the graphene-coated Cu foil in order to facilitate its transfer procedure, when the catalyst is removed.
- Etching procedure: The sandwich structure consisting of PMMA/graphene/Cu film is positioned into a suitable etchant, with Cu facing the etchant in order to be removed. After its removal, the PMMA/graphene structure is rinsed off several times with distilled water, in order to ensure the removal of any metallic residues that can act as contaminants.
- Transfer onto the desirable substrate: The PMMA/graphene structure can be deposited to any intended substrate, like PMMA slabs, or SiO_2, via fishing procedure.
- Removal of the supportive layer: The removal of the supportive layer is not always necessary, but it depends on the specific application requirements and the desired properties of the final device or material. The PMMA supportive layer can either be dissolved by immersing the substrate in an organic solvent, such as acetone, followed by thorough rinsing to ensure no residue remains on the graphene surface [38], or by annealing it to high temperatures (300-400 ^oC) in an inert atmosphere (e.g., argon or nitrogen) or vacuum [39]. For instance, in optoelectronic devices, like photodetectors, the polymeric layer may interfere with light absorption or emission and therefore is better to be removed, for the optimization of the device's performance. However, in applications like in flexible electronics, it may serve as a flexible substrate, which provides mechanical support.

1.5 Graphene-based nanocomposites

Composite materials are comprised of two or more distinguishable materials or phases (being in chemical and mechanical equilibrium) functioning in tandem to achieve an enhanced combination of material properties, in comparison to those of its individual components [40]. These distinguishable materials constitute the matrix and the filler(s). The matrix is responsible for the stress transfer to the enhancing or dispersed phase, whereas the filler serves as the reinforcing component, which is responsible for the enhanced properties of the composite, such as electrical, mechanical, and thermal properties. Ideally, the fillers should be efficiently dispersed and stabilized into the matrix. The classification of the composite materials is based on the type and size of the reinforcement and the type of the matrix. As fillers, particles, short fibers, continuous fibers and plates can be used. Regarding the matrix, composites can be classified into Metal Matrix Composites (MMCs), Organic Matrix Composites (OMCs) (further divided into Polymer Matrix Composites and Carbon Matrix Composites), and Ceramic Matrix Composites (CMCs). Composites can be also categorized in accordance to their structure, into three main categories [41], [42],[43]: particulate, fiber-reinforced, and laminar composites. Fillers in particulate composites are small matrix-encapsulated particles of any shape, size and configuration. Particulate composites present high versatility in composition, isotropic structure and low development costs. In fiber-based composites, there are both continuous and discontinuous embedded fibers, with the former exhibiting specific and well-defined orientation and the latter random orientation. The mechanical response of these composites depends on the diameter, orientation, and stiffness of the fibers [41]. It should be noted that in the case of short fibers, the achievement of uniform fiber orientation and distribution density can be a quite challenging task. Laminar composites consist of different layers stacked together, resulting in anisotropic materials in both design and properties.

The filler's dimension plays an important role to the composite's overall properties. When the filler dimension is below 100 nm, the composite is referred to as nanocomposite [44]. The smaller the dimensions of the filler, the higher its surface area will be, and therefore incorporation of nano-fillers results to a very high filler-matrix interface area, affecting the physicochemical properties of the structure. The nanoparticles used as fillers can be both organic and inorganic, such as single-walled,

double-walled, and multi-walled carbon nanotubes, carbon nanofibers, montmorillonite, nanoclay, polyhedral oligomeric silsesquioxanes, nanosilicates, SiO_2, Al_2O_3, and TiO_2, [45][46][47].

As nanocomposites effectively merge the family of composites with nanotechnology, it is of no surprise that these materials are in the center of interest for a wide range of applications where the enhancement of mechanical, electrical and thermal properties is of paramount significance [43]. To leverage from the remarkable physicochemical properties of carbon-based and especially graphene-based nanostructures, these materials have been widely explored as nanofillers in multifunctional nanocomposites [48][49][50][51]. Graphene nanocomposites harness the exceptional physicochemical properties of graphene, enhancing the performance of composites. As graphene is the sp^2 carbon allotrope with the highest specific surface area, graphene-based nanocomposites present groundbreaking mechanical, optoelectronic, chemical, and thermal properties, even at small volume fractions, making them ideal candidates for high-performance applications [52][53][54][55][56][57]. Due to its inherent characteristics, graphene presents remarkable electronic conductivity, as due to its structure, electrons can move through the lattice with minimal resistance, resulting in high electron mobility. Therefore, graphene acts as a highly efficient conductor, reinforcing the overall electrical properties of the material. So, graphene-based nanocomposites respond to a wide range of demanding applications requiring superior electrical conductivity, such as in electronic devices and conductive coatings, and therefore graphene's inclusion into nanocomposites is promising for developing advanced materials with enhanced electronic performance. Furthermore, according to experimental studies, graphene presents a very high thermal conductivity in room temperature, up to $5.30 \times 10^3\ Wm^{-1}K^{-1}$ [58] compared to any type of CNTs $3.00 - 3.50 \times 10^3\ Wm^{-1}K^{-1}$ [59][60], while theoretically, via MD studies this value can reach up to $6.00 \times 10^3\ Wm^{-1}K^{-1}$, indicating that graphene is an ideal choice for applications requiring effective heat management. Consequently, the incorporation of graphene into composites graphene enhances the thermal stability and conductivity of the nanocomposite, addressing challenges related to heat dissipation and thermal resistance. Optically, graphene exhibits remarkable properties, as it presents exceptional transparency (absorbing only 2.3% of light) due to its unique two-dimensional structure. It presents strong light-matter interactions, with its absorption

being wavelength-dependent. Also, quite remarkable are its capabilities to absorb and transmit light across a broad spectrum, from ultraviolet to infrared. Therefore, graphene is an ideal candidate for optoelectronic devices, photodetectors and transparent conductive films. Therefore, its integration into nanocomposites renders them suitable for high-performance applications in optoelectronics, sensors, and transparent conductive films.

Mechanical performance of graphene-based nanocomposites has been beyond doubt in the center of academic research. Previous studies have shown that the addition of graphene into composites presents significant advancements in the mechanical properties of graphene-based nanocomposites [61][62][63]. Nevertheless, conflicting reports state that this procedure effectuates no impact or even a degradation [64][65][66][67]. It should be stressed that a requirement for nanocomposites with high strength and stiffness, is the existence of strong interfacial bonds in regions with high interface area between the filler and the matrix, in order to achieve efficient stress transfer, and effectively utilize the superior mechanical properties of graphene. According to literature, the mechanical response of graphene-based nanocomposites has displayed an augmentation reaching up to 150% for the modulus of elasticity at graphene volumetric fractions around 0.5 vol% [68].

The assessment of the fortification of the mechanical performance is carried out via resorting to fundamental mechanical parameters, i.e. Young's modulus, deformation and tensile strength. Increment of the Young's modulus and strength at low deformation rates, indicate an enhancement of the structure. This is quite common when graphene is used as a filler. Nevertheless, at higher deformation rates, Young's modulus and strength present lower values, due to the slippage mechanism between the filler and the matrix. Increase in the ultimate strain can be achieved by improving the interface between the components of the material, which can be achieved through functionalization or doping, or by following the proper synthetic approach [69]. Moreover, comparing the mechanical properties of carbon fiber-reinforced plastic (CFRP), which deploy the strength of carbon fibers, glass fiber-reinforced plastic (GFRP), which leverages the high strength and cost-effectiveness of glass fibers, composites that include low dimensional sp^2 carbon nanostructures, such as CNTs or graphene [70], with conventional polymer composites, it is evident that there is an enormous difference in their Young's modulus and their tensile strength. According to

literature, CNTs and graphene present the higher Young's modulus and tensile strength. CNT fibers and CFRPs (continuously reinforced composites) are following, while GFRPs display similar tensile strength to CFRPs, but with lower Young's modulus. The Young's modulus of CNT polymer composites and graphene polymer nanocomposites is overlapping with the one of GFRPs, exhibiting lower tensile strength. Generally, continuously reinforced CNT or graphene fiber composites in the future might be employed to create ultralight yet super-strong structures, replacing carbon fibres [70].

In **Figure 1.7,** an Ashby plot depicting Young's modulus against tensile strength compares the mechanical properties of polymers, conventional polymer composites (including glass fiber-reinforced plastic (GFRP) and carbon fiber-reinforced plastic (CFRP)), with CNT or graphene-based polymer composites [70]. The mechanical properties of CNT or graphene polymer composites, considered particulate composites, are scattered between those of GFRPs and polymers. While these properties are shown to be below those of CFRPs, which are conventionally used for load-carrying structures, the mechanical properties of CNT spun fibers suggest that CNT or graphene fibers could potentially replace carbon fiber. If properly designed and manufactured, continuously reinforced CNT or graphene spun fiber composites might be employed to create ultralight yet super-strong structures in the near future [70].

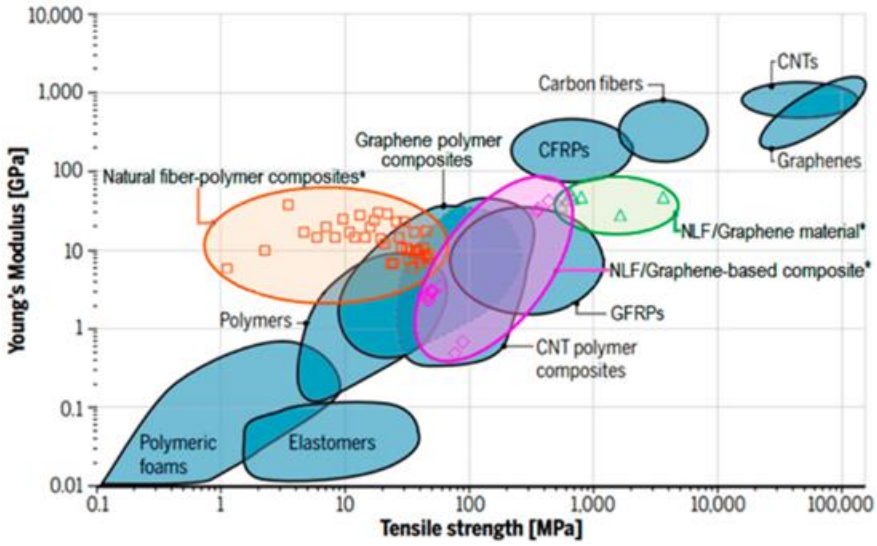


Figure 1.7:Ashby plot of Young's modulus vs. tensile strength comparing the mechanical properties of natural fiber-based polymer composites with glass fiber–reinforced plastic (GFRP) and carbon fiber–reinforced plastic (CFRP), with carbon nanotube (CNT), and graphene-based polymer composites [71].

1.5.1 Production of graphene-based nanocomposites

The production methods of graphene-based nanocomposites have been extensively researched, aiming to obtain the most efficient interface between the graphene filler and the matrix. Solution-based techniques constitute the most common methods for the preparation of polymer nanocomposites with graphene nanofillers, as they present flexibility, speed, simplicity, and effective control over the behavior of the components [72]. Solution mixing technique is an approach where graphene is dispersed in polymer solution or solvent, in order to form a uniform mixture, which usually is utilized for sheet or film production [73]. Melt mixing technique is another beneficial method for producing nanocomposites with a thermoplastic polymer matrix, where insoluble and thermally stable graphene nanofillers are added to the polymeric matrix when it is in its molten state followed by cooling and solidification [74]. *In-situ* polymerization ensures the strong interfacial bonding between the nanofiller and the matrix, as the polymer is synthesized directly, in the presence of graphene [75]. Moreover, electrostatic assembly is utilized for the formation of layered graphene-polymeric structures, using electrostatic forces to deposit graphene onto the substrate [76]. The layer-by-layer (LbL) assembly is a versatile technique for the fabrication of thin and ultrathin films, resembling nanoscale sandwich structures. This approach offers precise control over the distribution and orientation of graphene fillers within the polymer matrix [77], as graphene and polymeric layers are deposited successively, allowing the engineering of the interface between the layers, ensuring a tailored and controlled morphology and adhesion in the final nanocomposite product [52][78][79][80][81]. The most widely used LbL method are dip-coating, spin-coating and spray-coating. Generally, all these LbL techniques display high scalability potential, however, they are time-consuming [52]. All the above mentioned approaches for synthesizing nanocomposites are widely used as they facilitate the controlled integration of graphene nanofillers into polymeric matrices, enabling the exploitation of the exceptional graphene's properties for the enhancement of the overall performance of nanocomposites. Nevertheless, further optimization of these methods, concerning the accomplishment of strong interfacial interactions, uniform dispersion and scalable manufacturing is critical for various industrial, electronical and other applications.

1.5.2 Graphene-based nanolaminates

Another form of graphene-based nanocomposites is the graphene-based nanolaminates. Nanolaminates are composed of well-oriented continuous or discontinuous nano-thin laminae composed of large-size monolayer graphene (produced via CVD) and polymeric layers. This novel approach is used for producing structures that can showcase exceptional physical properties, rarely found in conventional materials, as a result of their variability in the layer thickness and the stacking sequence. The presence of highly aligned interfaces, the 2D character of all phases, and the existence of dominant interfacial phenomena, transfuse extraordinary properties to nanolaminates that are not found neither to conventional composites nor to bulk materials.

Large-sized CVD monolayer graphene is a promising nanofiller for nanolaminate structures. Contrary to graphene derived from other methods, continuous CVD graphene allows the controlled and homogenous filler distribution, while rendering the efficient stress transfer feasible, due to its large aspect ratio. Therefore, their electrical, thermal and mechanic behavior has to be explored. Generally, the literature on CVD graphene nanolaminates is limited [82][83][84], nevertheless, there are some pioneering works exploring the fabrication of polymer/CVD graphene sandwich-like nanostructures, while evaluating their mechanical properties through innovative methods, like the nano-bubble inflation method [84].

The first groundbreaking research in the field of nanolaminate's production was conducted by Vlassiouk et al. [85]. Nanolaminates were produced via sequential wet transfer deposition of Gr/PMMA plies, accomplishing a CVD graphene volume fraction of only 0.13 vol% and displaying an effective modulus of 1.2 TPa and an in-plane electrical conductivity of 800 S/m, indicating that these structures exhibit high stiffness and high conductivity [85]. Polycarbonate (PC) can also be used as a polymeric matrix, as reported by Liu et al. [82], employing the stacking and folding method for the creation of Gr/PC nanolaminate systems, with the graphene content ranging from 0.082 vol% to 0.185 vol%. The effective modulus of this system was reported to be 115 GPa, attributed to in-plane slippage between the graphene and PC layers when the structure is subjected to tension, however the electrical conductivity is 417 S/m [82]. The notably high values of electrical conductivity in both cases are

unparallel to any other discontinuous graphene-related material, even at cases where the graphene loadings are two orders of magnitude higher. In another study, PC/graphene nanolaminates, with the graphene content being at ~0.085 vol%, displayed significant enhancement at their mechanical properties, as there is an improvement up to 73.5% in Young's modulus, and electrical properties (up to 10 S/m) [83]. Generally, with the stacking and folding method, the production of mechanically and electrically enhanced nanolaminates is feasible. Nevertheless, the dimensions of the final structure are significantly smaller than expected, due to the repetitive procedure that is followed. As reported in [32], graphene's volume fraction is critical to the mechanical fortification of nanolaminates. The volume fraction of graphene in CVD graphene-based nanolaminates is defined by the thickness ratio of the filler and the polymer matrix as:

$$V_{Gr} = \frac{t_{Gr}}{t_{Gr} + t_{polymer}} \tag{1.6}$$

Where t_{Gr} is the thickness of graphene 0.334 nm, and $t_{polymer}$ is the thickness of the polymer. It is apparent that attaining a high graphene content in nanolaminates is challenging since this would necessitate very thin polymer layers, which, from both thermodynamic and structural perspectives (e.g., polymer radius of gyration), may be unfeasible. Efforts to produce ultra-thin films through methods like spin coating with thicknesses of 10-30 nm have already been documented in the literature [86], and other techniques such as Langmuir-Blodgett [87] have shown the potential to create even thinner films (5-7 nm) [88]. However, the latter are challenging to handle, and damage can be induced. Several studies have demonstrated that centimeter-sized, ultrathin polymeric membranes can be lifted off without damage for thicknesses no smaller than 15-20 nm [89][90]. Thus, based on the available literature, it is inferred that the current upper limit for graphene content in graphene-polymer nanolaminates is fundamentally around 2 vol%, corresponding to a thickness of the polymeric layer of approximately 15 nm. It is crucial to develop a suitable technique that enables the production of CVD graphene nanolaminates with a relatively larger volumetric fraction of graphene while achieving a greater number of stratifications with larger dimensions than those already reported in the literature.

A novel method able to yield graphene-based nanolaminates with high volumetric fraction and large-sized CVD graphene have been proposed by Pavlou et al. [32] (see **Figure 1.8**). A semi-automatic, scalable process was developed, allowing the iterative deposition of ultra-thin films of maximum dimensions of 7 cm × 7 cm. Part of this procedure is the spin coating of the polymeric solution onto CVD graphene, the wet transfer and the float depositions ("lift-off/float-on"), constructing step by step the final structure. The number of layers of the structures produced were ranging from 10 to 100 and volume fractions of 0.044 to 0.5% and a systematic investigation of mechanical, electrical, and multi-functional properties was conducted [32].

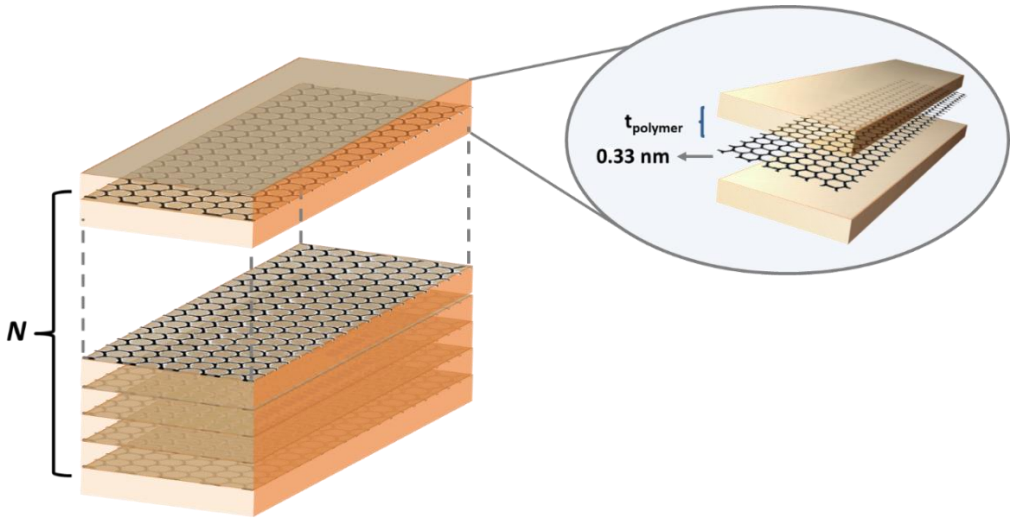


Figure 1.8:Assembly of graphene-Polymer nanolaminates.

2. Fracture mechanics

2.1 Types of fracture

Fracture of materials can be broadly categorized into several types based on different criteria, such as the nature of the material, the mode of loading, the resulting fracture surfaces and the external factors, such as thermal or chemical effects [91]. Based on the nature of the material, fracture can be classified into ductile and brittle. Ductile fracture occurs in materials that exhibit significant plastic deformation before fracture, like metals and some polymers, presenting extensive necking, dimples on the fracture surface, and gradual failure [92] (**Figure 2.1b**). Brittle fracture occurs in materials, such as ceramics and some polymers, that exhibit minimal or no plastic deformation before cleavage. The fracture procedure is abrupt and catastrophic, with small energy absorption, leaving a rather flat surface, without any prior detectable alterations like necking of the material [93] (**Figure 2.1a**). Temperature and strain rate, are also factors that play an important role in fracture behaviour [94]. Higher temperatures enhance ductility, enabling more extensive plastic deformation before fracture, whilst lower temperatures enhance the brittle behaviour. Moreover, increased strain rates may trigger the transition from ductile to brittle behaviour, due to the limited plastic deformation that a material can undergo, whereas at lower strain rates ductility is more favoured [94]. In general, fracture will occur when the applied stress surpasses the fracture strength of the material, which is the maximum stress or loading that it can withstand before failure occurs. **Figure 2.1a** compares the stress-strain curves of a ductile and a brittle material, providing information over the material's mechanical behavior under loading conditions. **Figure 2.1b** presents the points of interest of a stress-strain curve. From the linear region at low strain, the Young's modulus can be derived. Young's modulus defines the material's stiffness and its ability to deform elastically under applied stress. The Yield Strength is defined as the point where the material transcends from the elastic to the plastic region, giving information about the material's resistance to permanent deformation; if the material surpasses its yield strength, then it will not return to its initial state upon removal of the applied load. Fracture Strength or Ultimate Tensile Strength corresponds to the maximum stress that a material can withstand before its failure. Some materials exhibit Strain Hardening, after the yield point, where

the material becomes stronger (increase in stress) and more resistant to deformation with increasing strain.

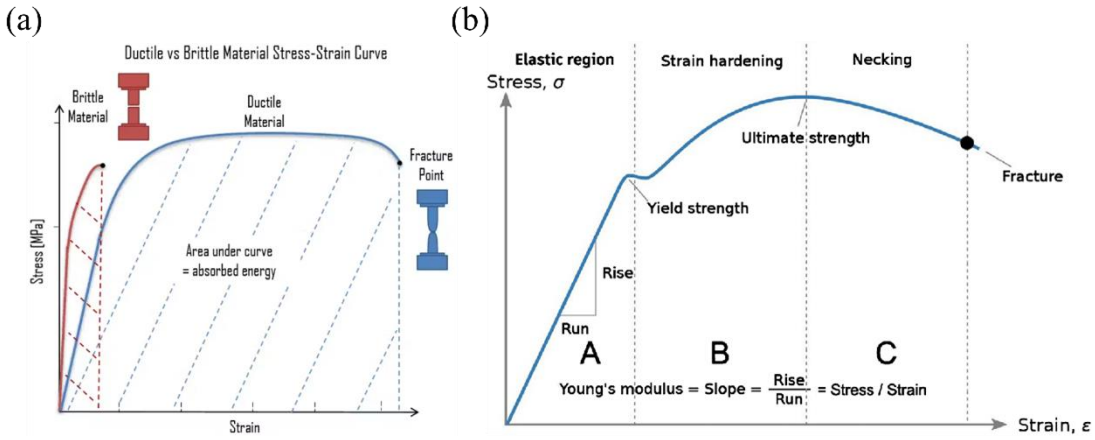


Figure 2.1:(a) Stress-Strain curves of a brittle and a ductile material [95]*, (b) Stress-Strain curve of a ductile material and some points of interest* [96].

The mode of loading is essentially important, as it is related to the fracture surface. Specifically, tensile fracture, which occurs when a material is under tensile stress, leads to fracture surfaces that are often perpendicular to the load direction, while in the case of shear fracture, where the material is under shear stress, angled fracture surfaces are observed. Fatigue fracture occurs in both ductile and brittle materials due to repeated cyclic loading, which leads to the formation of micro-cracks which grow over time until failure [97]. Cracks also propagate through the grains of the material, either it is ductile or brittle (Transgranular fracture)[98], or along the grain boundaries (Integranular fracture) in the case of materials that are susceptible to environmental degradation, such as corrosion [99].

2.1.1 Linear Elastic Fracture Mechanics

Fracture mechanics is a solid-state field, which deals with the study of crack propagation into a material, having as a prerequisite the existence of a crack. There are two approaches utilized for the understanding of fracture, Linear Elastic Fracture Mechanics (LEFM) and Elastic Plastic Fracture Mechanics (EPFM). In the case of LEFM, materials behave in a linear elastic way when subjected to deformation, exhibiting a small-scaled yielding, and rely on Griffith's theory of brittle fracture for

the analysis of crack propagation, whilst in the case of EPFM, the material exhibits large-scale yielding, signifying that the plastic deformation of the material is not negligible compared to the crack size (See **Figure 2.4**) [100]. Similarly to LEFM, fundamental is Irwin's theory of brittle fracture, which employs the Stress Intensity Factor (SIF) approach to examine crack propagation [101]. There are three fracture modes in LEFM, mode I, II, and III (See **Figure 2.2**). In real structures, a combination of mode II and mode III can occur simultaneously. In mode I, the load is applied perpendicularly to the crack surface, requiring the least amount of load and energy for crack propagation. Therefore, regardless of the orientation of the initial crack, it will tend to reorient until it becomes perpendicular to the applied load.

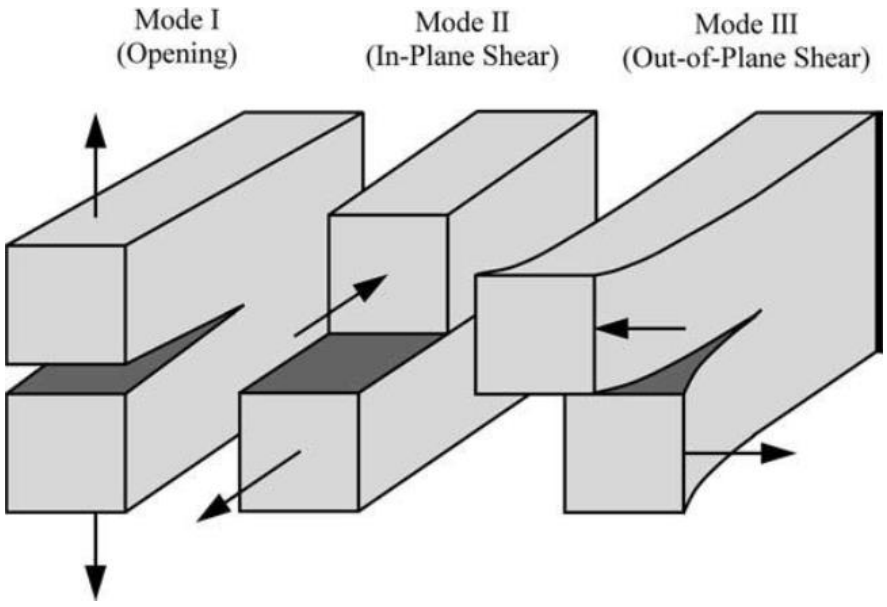


Figure 2.2:Modes of fracture Mode I is referred as the opening or tensile mode, Mode II is the sliding mode and Mode III is the tearing mode [102].

Cracks induced due to the applied load consist of several distinct parts (see **Figure 2.3**). Crack tip is the region at the forefront of the crack where stress is maximized. Therefore, it constitutes area of crack initiation and propagation. Crack opening represents the deformation zone ahead of the crack tip and can vary in width as the crack propagates. This is known as the process zone or plastic zone. Crack body is the area that extends from the crack tip into the material. When higher stress is applied, crack propagates into the material, and crack surfaces are created as the material separates into two parts. Depending on the material and the loading conditions, the

surfaces may display various features (roughness, striation, markings). As the load is increased, crack propagates in a stable way, until it reaches a threshold value; beyond this point, crack propagates unstably, with no need of an increment of the external loading [103].

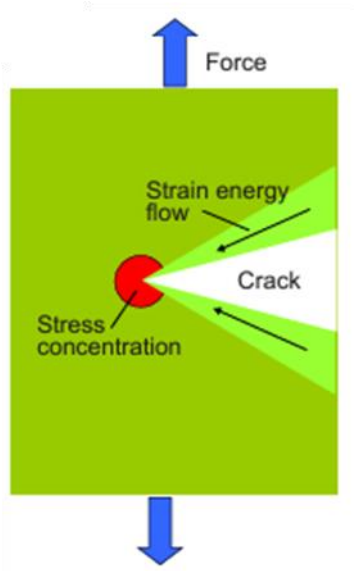


Figure 2.3: Parts of a crack [104].

Figure 2.4 bellow provides a load-displacement curve, along with cracked samples corresponding to a different segment of this curve. In the first region, where the applied strain is low, the stresses are lower than the yield strength of the material; hence, failure of the specimen at this region testifies for brittle fracture. In this case, the plastic zone (marked red in **Figure 2.4**) is minimal, and the LEFM approach can be used, as the linear elastic assumption is valid. If the applied strain increases, the plastic zone will enlarge. Unlike the case of brittle fracture, failure of the sample upon reaching the higher region of the curve is indicative of ductile fracture, and in this case the size of the plastic zone is the largest. In this case, fracture mechanics methods cannot be used, and a strength-of-materials approach is necessary. An intermediate state to the above extreme cases is termed Mixed-Mode Fracture. If the progressively increasing size of the plastic zone (as strain increases) renders LEFM invalid, then elastic-plastic methods such as Failure Assessment Diagram (FAD) can be used to study the fracture of the sample [105].

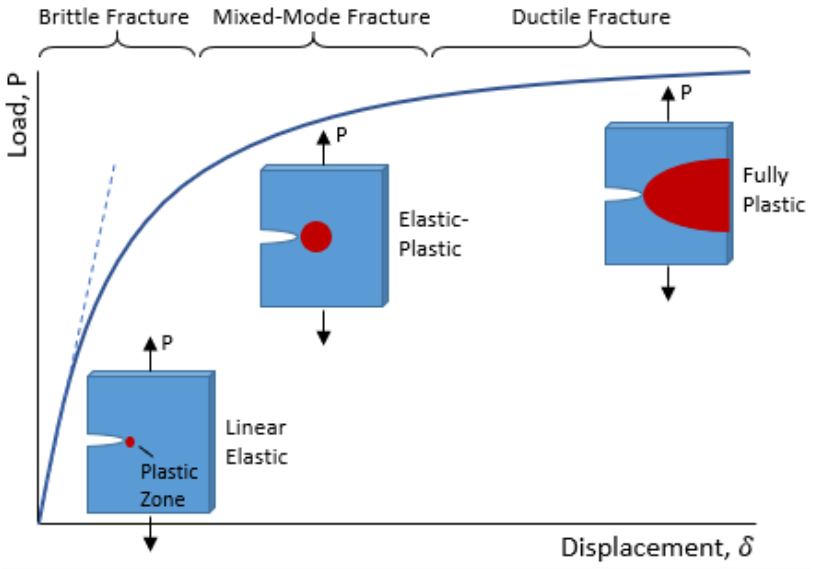


Figure 2.4: Load-displacement curve for various fracture modes [106].

2.2 Griffith's brittle fracture

Griffith's theory of brittle fracture, proposed in 1920 [100], is a fundamental notion in fracture mechanics. This theory, based on the first law of thermodynamics and on a simple energy balance, enlightens the mechanisms of the brittle fracture of materials delving into the role of the pre-existing defects, like cracks or voids [102]. Their role is important, as they act as points of stress concentration resulting to failure, which occurs when stress exceeds the maximum stress that a material can withstand (critical stress σ_c), and the size of the defect attains a critical size. Griffith demonstrated that the critical flaw size is inversely proportional to the material's surface energy and directly proportional to its modulus of elasticity [100]. So, according to Griffith's criterion [100], the critical stress σ_c for onset of unstable crack propagation for a central crack of length $2\alpha_0$ (**Figure 2.5**), is given by the equation:

$$\sigma_c = \sqrt{\frac{2\gamma E}{\pi \alpha_0}} \tag{2.1}$$

where E is the Young's modulus, and γ is the surface energy.

An alternative form of equation (2.1) is:

$$\sigma_c\sqrt{\alpha_0} = \sqrt{\frac{2\gamma E}{\pi}} \tag{2.2}$$

It is evident that the parameters of the left-hand side of the equation, i.e. σ_c, which is the critical stress before fracture and α_0, which is the crack size, can be experimentally measured, whilst the right-hand side of the equation contains only numerical parameters and parameters that depend on the material.

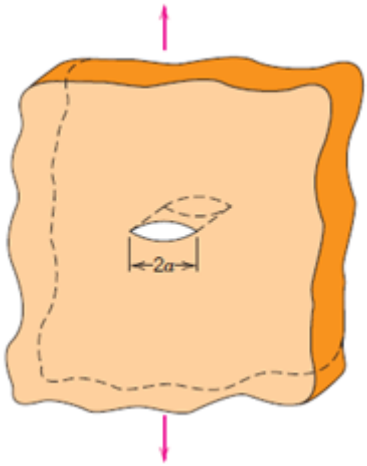


Figure 2.5: Infinite plate with an interior crack [107].

2.3 Fracture Parameters

Fracture parameters describe the properties and the behavior of a material under loading conditions, until its failure [102]. The Stress Intensity Factor, K, expresses the magnitude of the stress field near the tip of a crack in a material, providing information over the stress concentration at the vicinity of a crack tip and therefore predicting crack propagation under external loading. The energy release rate, G, represents the rate at which energy is released as a crack propagates in a material, and can be used to quantify its resistance to crack growth. Fracture toughness, K_{IC}, is an intrinsic property of a material, describing its ability to resist fracture, as it corresponds to the critical stress intensity factor at which a pre-existing crack will propagate unstably in the material. The total energy per unit fracture surface area required for crack propagation in a material is expressed via J-integral, which is a fundamental parameter in nonlinear fracture mechanics.

2.3.1 Stress Intensity Factor and Stress Concentration Factor

The distribution of stress in the vicinity of the edge of a crack in an infinite plate, where mode I (see **Figure 2.2**) predominates is given by the equations [108]:

$$\sigma_{xx} = \frac{K_I}{\sqrt{2\pi r}} \cos\frac{\theta}{2}\left(1 - \sin\frac{\theta}{2}\sin\frac{3\theta}{2}\right) \quad (2.3.a)$$

$$\sigma_{yy} = \frac{K_I}{\sqrt{2\pi r}} \cos\frac{\theta}{2}\left(1 + \sin\frac{\theta}{2}\sin\frac{3\theta}{2}\right) \quad (2.3.b)$$

$$\sigma_{xy} = \frac{K_I}{\sqrt{2\pi r}} \cos\frac{\theta}{2}\sin\frac{\theta}{2}\sin\frac{3\theta}{2} \quad (2.3.c)$$

where θ, r are the polar coordinates and the crack tip is the point of origin. The parameter K_I is the Stress Intensity Factor (SIF) which determines the intensity of the field of stress close to the crack tip. The SIF is defined as:

$$K_I = Y\sigma\sqrt{\pi a} \quad (2.4)$$

Where σ is the applied strain, Y is a geometrical modification factor and a is the crack length, and the subscript I denotes the Mode I fracture condition.

Another important parameter is the Stress Concentration Factor (SCF) which is defined as:

$$K_t = \frac{\sigma_{at\ the\ vicinity\ of\ the\ defect}}{\sigma_{far\ filed}} \quad (2.5)$$

The SIF provides efficient information for the crack propagation analysis, as it quantifies the stress magnitude near the tip of a crack and predicts the critical conditions under which the crack will propagate, giving information over the overall crack behavior of the material. The SCF is the ratio of the maximum stress close to a defect to the normal stress of the material and quantifies the local stress amplification compared to the normal stress, due to the existence of a discontinuity. Therefore, quantitative information over the stress at the vicinity of a defect, prevents a future unexpected material failure.

2.3.2 Energy Release Rate

Another perspective for describing fracture behavior of a material in LEFM is the energy-based approach, where the work, W, that is applied, is sufficient for breaking the atomic bonds, creating new crack surfaces and eventually resulting to fracture [102]. This relationship is given by the equation:

$$W = U + \gamma \tag{2.6}$$

Where U is the internal energy and γ is the bond-breaking energy.

The Energy Release Rate G is defined as the reduction of the total potential energy per increase in fracture surface area A, expressing energy per unit area. Therefore, crack propagation initiates when G reaches a critical value G_{IC}, which is given by the equation:

$$G_{IC} = \frac{dU}{dA} \tag{2.7}$$

The Energy release rate and Stress Intensity Factor approaches are equivalent, therefore they can be expressed as follows:

$G_I = \frac{{K_I}^2}{E}$, for plane stress (2.8)

$G_I = \frac{{K_I}^2(1-v^2)}{E}$, for plane strain (2.9)

where v is the Poisson ratio.

2.4 Nonlinear Fracture Mechanics

Nonlinearities, such as plastic or viscoelastic effects, can be present due to the energy distribution into the material, not only for the atomic bond breakage, but also to the plastic deformation or viscoelastic dissipation [109]. In such cases, EPFM can describe more accurately the non-linear and time-dependent fracture behavior of the material. The crack tip opening displacement (CTOD - δ) and the J-integral (J) are critical parameters for the characterization of the crack behavior and the assessment of material's resistance in the case of elastic-plastic fracture [110]. Specifically, CTOD

provides information over the opening of the crack as it propagates, and the magnitude of plastic deformation occurring ahead of the crack tip in ductile materials. J-integral is defined similarly to the energy release rate and has the unique property of being path-independent line integral of the stress and displacement fields around the crack tip (see **Figure 2.6**). Moreover, it corresponds to the energy dissipated when crack is growing, considering both elastic and plastic deformation. Therefore, it is widely utilized for the determination of the critical crack growth conditions and the prediction of fracture toughness, especially in materials exhibiting nonlinear behavior.

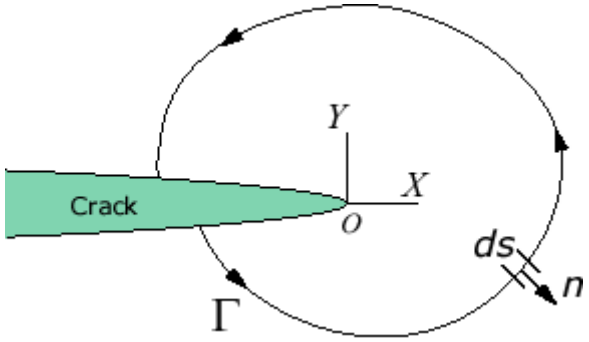


Figure 2.6: Arbitrary contour around the tip of a crack [111].

The J-integral is given by the equation:

$$J = \oint \left(w\, dy - T_i \frac{\partial u_i}{\partial x} ds \right) \tag{2.10}$$

where w is the strain energy density, dy is taken in the direction of the y axis, T_i is the i component of the traction vector, u_i is the i displacement component and ds is the displacement increment along the integral.

2.5 Defects

Defects can be classified into three main categories: The inherent defects that occur during the manufacturing process, including impurities, voids, dislocations and inclusions [112][113], the defects that emerge during processes like forging, welding, machining or casting and are the casting voids, heat-affected zone microstructures, and residual stresses [114], and the defects like corrosion pits, oxide layers, or surface

cracks that occur due to environmental degradation, such as corrosion, oxidation, or fatigue [115][116].

The presence of defects significantly affects the mechanical properties of a material and plays an important role on its fracture behavior. In specific, areas at the vicinity of defects display higher stress concentration leading to initiation of cracks, which will propagate when the value of stress exceeds a critical value, as an external loading is applied [117][118].

2.6 Fracture toughness

Fracture toughness describes the resistance of an already cracked material to fracture and is an intrinsic property that is affected by several factors. The microstructure including grain size, dislocations, etc., as well as the chemical composition of a material, i.e. the different types of atoms and their arrangement can affect crack propagation [119][120][121]. The propagation can be also affected by treatments like heating, or the environment itself, as moisture or corrosive agents may accelerate crack initiation and propagation i.e. in the case of stress corrosion cracking [122]. Loading conditions e.g. tensile, bending, the strain rate and the stress state that a material may be into (i.e. the existence of residual stress) also play an equally important role, affecting fracture toughness by reducing or enhancing its value [123][124][125].

Fracture toughness, denoted as K_{Ic}, where the subscript I denotes the Mode I fracture condition and C the critical stress, is an intrinsic property of a material and represents the maximum stress that it can withstand (given temperature and thickness), before a pre-existing crack moves from the stable phase to the unstable, causing the fracture of the material. Fracture toughness is given by the equation:

$$K_{IC} = Y\sigma_C\sqrt{\pi a_C} \tag{2.11}$$

Where σ_C is the critical stress before fracture, Y is a dimensionless geometric factor and a_C is the critical crack length.

The increment of material's thickness instigates diminishment in the value of fracture toughness, as it ultimately stabilizes at an asymptotic value termed as the plain strain

fracture toughness (**Figure 2.7a**) [102]. This value of the fracture toughness remains unaffected by variations of thickness (**Figure 2.7b**).

Irwin et al. [101] in order to describe the behavior of fracture toughness as a function of the specimen's thickness developed an empirical relationship given by the equation:

$$K_{Crit} = K_{IC}\sqrt{1 + 1.4{B_{IC}}^2} \tag{2.12}$$

Where K_{Crit} is the measured fracture toughness for thinner sections, K_{IC} is the presumed asymptotic fracture toughness for large section thicknesses and B_{IC} is the minimum thickness. Therefore, the requirement that has to be fulfilled in order to assure the plain strain fracture criterion is given by the equation:

$$B \geq 2.5\left(\frac{K_{IC}}{\sigma_y}\right)^2 \tag{2.13}$$

Where σ_y is the plane strain.

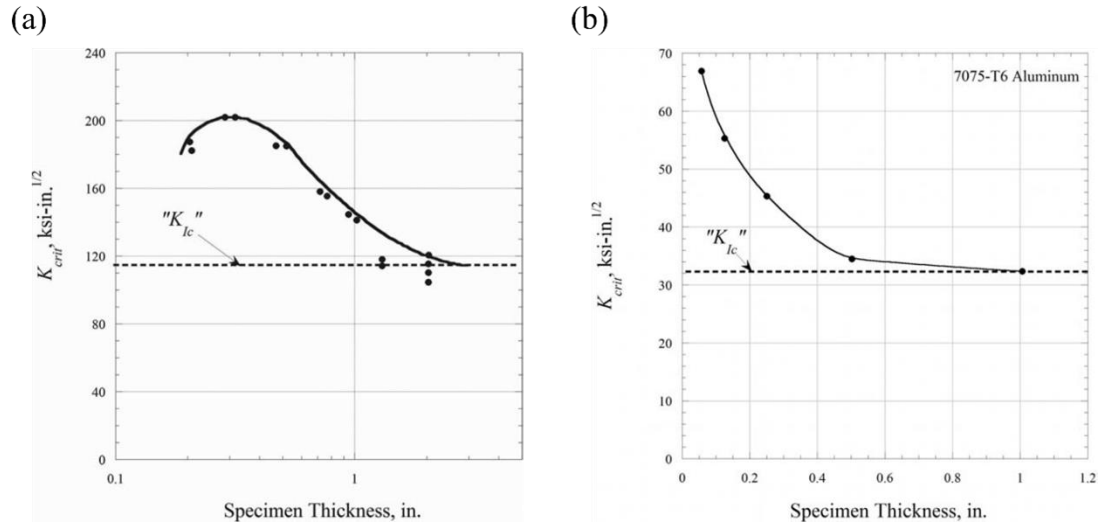


Figure 2.7: (a) Variation of measured fracture toughness with specimen thickness for an unspecified alloy. (b) Variation of measured fracture toughness with specimen thickness for 7075-T6 Aluminum [102].

2.7 Fracture toughness of graphene and other 2D materials

The fracture toughness of graphene has been in the center of interest through the past years. Due to its unique atomic structure, especially in its pristine form, graphene displays extraordinary properties. However, its brittle nature when unavoidable

imperfections, like cracks, impurities, or dislocations exist, may have a serious impact on the manufacturing and the utilization of graphene-based nanodevices. Fracture toughness and crack propagation have been investigated mainly through theoretical studies, numerical or atomistic simulations, and less experimental, as the procedure is quite challenging, due to the difficulty of load applications in nanoscale materials and the fast crack propagation when the crack becomes unstable [126].

The first experimental evidence on the exceptional strength of ~100 GPa and high Young's modulus of 1 TPa of pristine graphene was given through nanoindentation experiments with AFM [127]. Specifically, either exfoliated or CVD graphene can be transferred on a wafer with holes, in order for the graphene membrane to be freestanding, at the top of the wafer holes. Then, controlled force is applied at various locations of the graphene membrane with an AFM probe, consisting of a sharp tip at the end of a cantilever, leading to indentation. The force applied by the cantilever, as well as its displacement are measured, extracting information over the mechanical response of graphene, including its elastic modulus and strength. In general, nanoindentation using AFM has proven to be a powerful method for characterizing the mechanical properties of graphene, as well as other 2D materials with high spatial resolution and precision [128].

The first experimental determination of fracture toughness of CVD graphene was conducted by Zhang et al. [129], combining scanning electron microscopy (SEM) with in-situ tensile tests, resulting in the Stress Intensity Factor of $K_{IC} = 4.0 \pm 0.6\ MPa\sqrt{m}$ and the equivalent critical strain energy release rate of $G = 15.9\ J\ m^{-2}$. In specific, in this groundbreaking study, in situ tensile tests were conducted on suspended CVD graphene, with a pre-existing crack of various initial lengths induced by Focused Ion Beam (FIB) inside a SEM, in order to extract also qualitative information over the cracking process. An external deformation was applied to the CVD graphene, until brittle fracture occurred at a stress significantly lower than the intrinsic strength of graphene, indicating that due to graphene's inherent brittleness, its fracture toughness is lower than its intrinsic strength. The Griffith's theory over the brittle fracture is also affirmed, through the linear stress-strain curve of graphene samples which end by an abrupt load drop, a result of the dynamic crack propagation. The experimental results are also validated through Molecular Dynamic Simulations (MDs) and confirm the applicability of Griffith's theory over the brittle fracture of graphene, while

simultaneously evaluating the influence of crack orientation on fracture load and manifesting that fracture stress is the lowest for the zigzag crack edge, and the largest along the armchair one[129]. By using a similar, method, Jang et al. reported a higher fracture toughness, $K_{IC} = 21.25 MPa\sqrt{m}$ [130], which is attributed to the nonlinearity of graphene during deformation [131]. Stacked bilayer graphene sheets (SBLG) also present high fracture toughness $K_C \approx 28.06 \pm 7.5\ MPa\sqrt{m}$, ascribing it to the complementarity that individual monolayer graphene sheets exhibit, as in the case that they possess flaws, they are not coordinated to each other, and therefore one of the layer each time assist with the retain of the load bearing [132]. Raman spectroscopy combined with tensile testing was utilized by Wang et al. [133], reporting fracture toughness of $K_C = 6.1 \pm 0.6\ MPa\sqrt{m}$ and a critical strain energy release rate of $G_C = 37.4 \pm 6.7\ J\ m^{-2}$, while Young et al. quantified the strain distribution close to a preexisting defect in monolayer pristine graphene, reporting fracture toughness $K_C = 4.0\ MPa\sqrt{m}$ [134]**.** Concluding, even though graphene exhibits remarkable strength [127], when a pre-crack exists, it exhibits a relatively low fracture toughness, indicating that a defect can significantly weaken it.

Apart from graphene, the mechanical properties of other 2D materials have been studied. For instance, Transition Metal Dichalcogenides (TMDs), such as MoS_2, $MoSe_2$, $MoTe_2$, WS_2, present varying fracture properties and their response to stress has been studied both experimentally [135] and via atomistic modelling [136][137]. Monolayer TMDs, like MoS_2 present high intrinsic strength, 15 N m^{-1}, and Young's modulus, 211 GPa, but relatively low fracture toughness, indicating that their resistance to crack propagation is limited [138]. There are some cases where fracture toughness has been improved using vacancies [139], nevertheless this field is yet to be explored. On the other hand, hexagonal Boron Nitride (h-BN) presents extremely high fracture toughness ($K_{eff} \approx 8.7\ MPa\sqrt{m}$) [140], even compared to graphene, as despite their atomic structural similarities, the presence of the slightly asymmetric bonding arrangements within h-BN can result to crack deflection and brunching during fracture, leading to the final increment of fracture toughness,

2.8 Fracture toughness of graphene-based nanocomposites

The understating of fracture toughness in graphene-based nanocomposites is essential for the design and optimization of reliable and robust materials, the prediction of their mechanical behavior in real world conditions, as well as their utilization in cutting-edge technologies. As mentioned before, the incorporation of graphene into polymeric matrices can enhance their mechanical performance, ascribing them high strength and stiffness. The presence of graphene can lead to increased energy dissipation mechanisms, crack deflection, and bridging effects, all of which contribute to enhanced toughness (**Figure 2.8**). There are several factors that affect fracture toughness, such as the quality of graphene used as nanofiller (GO, rGO), the dispersion and alignment of graphene flakes within the matrix, and the properties of the matrix. For instance, fracture toughness is improved with the addition of uniformly dispersed graphene nanoplatelets (GNPs) into an epoxy matrix, as the average energy release rate G_I, for Mode I fracture toughness tests is increased, leading to higher ultimate strength of the composite [141].

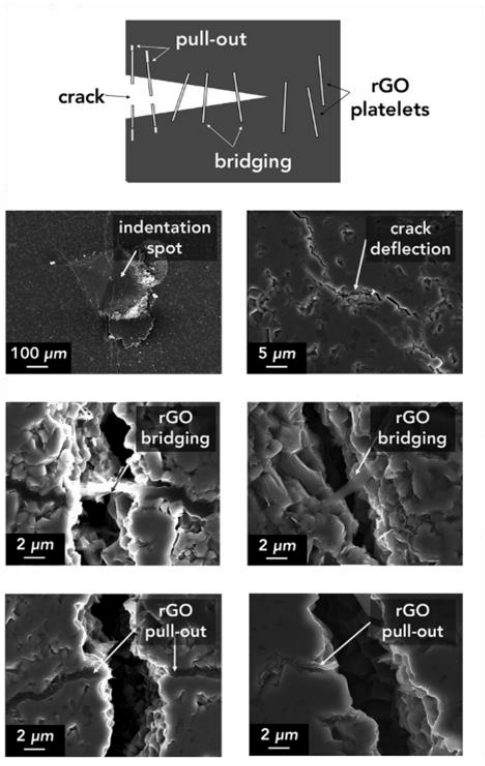


Figure 2.8: Fracture toughness reinforcement mechanisms [142].

The incorporation of graphene into polymeric, ceramic or metal matrices can enhance their mechanical performance, ascribing them high strength and stiffness. For instance,

in the case of graphene/ceramic nanocomposites, which are of interest for high-temperature applications and structural ceramics[143], graphene has been incorporated into ceramic matrices such as alumina (Al_2O_3) [144], silicon carbide (SiC), and titanium dioxide (TiO_2) [145], improving their fracture toughness and mechanical strength [146][147]. Fracture toughness of graphene/metal nanocomposites has been also investigated [148], as the inclusion of graphene into metal matrices such as aluminum[149], copper [150], and nickel [151] is widely utilized in lightweight structural applications [152] and thermal management [153]. Graphene/Carbon nanotube (CNTs) and Graphene/Carbon Fiber Reinforced Polymer (CFRP) can also be added to various matrices, acting synergistically, for the creation of nanocomposites with superior mechanical performance and high fracture toughness [154][155]. Graphene/epoxy nanocomposites, in which either graphene sheets or its derivatives such as graphene oxide (GO) or reduced graphene oxide (rGO) are encompassed into epoxy matrices, overall exhibit a promising potential in enhancing fracture toughness [156], as for instance, polyaniline (PANI) coated graphene nanoplatelets (GNP) added in carbon fiber reinforced polymer (CFRP) composites present an improvement of approximately 79% in mode-I fracture toughness with the addition of 5 wt% GNP [157]. Nevertheless, in some cases, fracture toughness slightly decreased when the graphene loading was increased [158]. Graphene/Polymer nanocomposites, where graphene is added into matrices such as polyethylene (PE), polypropylene (PP), polycarbonate (PC), and polyurethane (PU), present an enhancement in fracture toughness [159], rendering them adequate for industrial applications, from automotive to aerospace.

Overall, the enhancement of the fracture toughness of graphene-based nanocomposites is attributed to several factors. Namely, graphene's intrinsic extraordinary properties, including high strength and stiffness render it an excellent candidate as a reinforcing filler into a nanocomposite matrix. Furthermore, the ability to act in a synergistic way with other nanomaterials or additives included in the matrix, further enhances the fracture toughness of the composite, as the reinforcement mechanisms of the counterparts act synergistically. The strong interfacial bonding between graphene/CNT/CFRP and the matrix, reinforces the effective load transfer and stress distribution, contributing to the improvement of the mechanical characteristics of graphene-based nanocomposites [91][160]. Crack deflection, crack pinning and crack

bridging are also active toughening mechanisms [161]. Crack deflection occurs when a crack extends through the nanocomposite, changing direction and increasing its overall length, while generating micro-cracks, resulting in an increase of the total fracture surface area [162]. Crack pinning involves the interruption of the crack propagation due to the presence of obstacles like defects and impurities, leading to an increased resistance towards catastrophic failure [163]. Crack bridging includes mechanisms impeding crack propagation, as reinforcing elements (i.e. particles, fibers, platelets, fibrils) within a material span across the crack or fracture surface [161]. For instance, particles in particulate-reinforced composites, such as metal matrix composites (MMCs) [149], platelets in graphene-based nanocomposites [141], fibrils in nanofiber-reinforced polymers [164], and fibers in fiber-reinforced composites, such as carbon fiber reinforced polymers (CFRP) [91] act like bridges, transferring stress from the matrix to them, behaving as local stress concentrators, preventing crack extension and therefore increasing the material's toughness.

Concluding, graphene-based nanocomposites often exhibit improved fracture toughness compared to their pure matrix counterparts due to the presence of increased energy dissipation mechanisms, crack deflection, and bridging effects, all of which contribute to increased toughness. Nevertheless, achieving optimal fracture toughness in graphene-based nanocomposites requires careful control over factors such as graphene dispersion, interfacial bonding between graphene and the matrix, and processing conditions. Improvements in these areas can lead to further enhancements in fracture toughness and the development of advanced materials with superior mechanical properties.

2.9 Factors that affect the toughness of graphene-polymer nanocomposites

Toughness of graphene-polymer nanocomposites is affected by the morphology of graphene flakes, their thickness and their size. For instance, wrinkles may act as an enhancing toughening mechanism due to the increased interfacial adhesion between graphene and the matrix [165], however the existence of wrinkles may cause a reduction in the aspect ratio of graphene, impeding the effective interfacial load transfer [166][167]. The thickness of the graphene-based nanofillers significantly influences the

toughening performance of graphene/polymer nanocomposites. Previous studies have shown that optimum toughening of a polymeric matrix (PDMS) is achieved through the utilization of nanofiller of lower thickness [168]. Precisely, the use of monolayer graphene as a nanofiller compared to multilayer graphene nanoplatelets (GNPs) using the same filler loading, is more beneficial for the improvement of the nanocomposite's toughness [168]. Another crucial parameter for the refinement of the nanocomposite's toughness is the size of the nanofiller. The optimal graphene size depends on the type of the graphene nanofiller used, as previous studies have shown that in some cases the larger the graphene flake, the higher the toughening efficiency of the composite, as better stress transfer is accomplished [169], however, there are some cases where smaller flake size lead to more efficient toughening of the nanocomposite [170]. For instance, larger flake size GNPs (25 μm) have shown better toughening efficiency of the epoxy matrix compared to the smaller ones (5 μm) when added at the same weight percentage to the epoxy matrix, showcasing a clear augmentation of K_{IC}, as a percentage of 82% is demonstrated in the case of larger flakes, compared to 60% displayed in the case of smaller flakes [171]. However, in the case of GO as nanofillers, smaller flakes exhibited better toughening efficacy of the epoxy matrix [170]. Moreover, the selection of the adequate polymer as a matrix plays significant role, as the same graphene content in a different polymeric host, leads to a different toughness enhancement of the material (**Figure 2.9**).

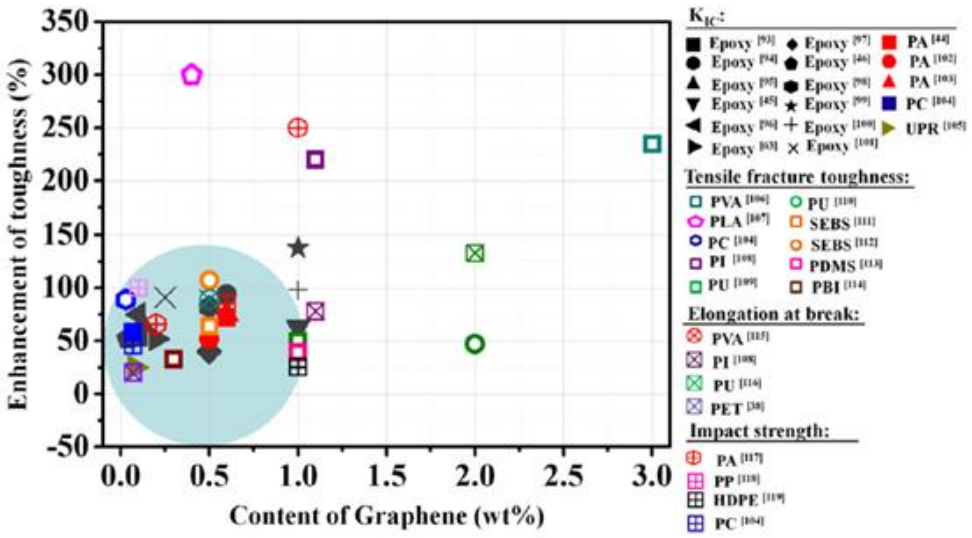


Figure 2.9: Enhancement of various polymer matrices as a function of graphene content [172].

The optimal filler loading along with the dispersion and the distribution of graphene are critical factors over the enhancement of the nanocomposite's toughness. The

amount of graphene nanofiller added to the polymeric matrix ranges from 0.1 wt% up to approximately 5.0 wt%, depending on the desired properties [173]. Precisely, a small amount of graphene in some cases may lead to insufficient reinforcement of the nanocomposite [174], whereas in other cases it significantly affects the mechanical properties of the composite due to its exceptional strength and stiffness [175][176]. Moreover, uniform distribution and high dispersion of graphene nanofillers throughout the matrix improves the toughness efficiency of the nanocomposite [177], and facilitates the strong interfacial interaction (increased graphene-matrix interface area) resulting to the increase of Young's modulus and higher fracture toughness (see **Figure 2.10**) [172][178]. A non-homogenous dispersion of graphene nanoparticles may be caused by the addition of a large amount of graphene, which may lead to negative effects and downgrading of the polymer's mechanical properties [177][159]. For instance, the presence of microcracks acts as a toughening mechanism in graphene/epoxy nanocomposites, impeding the fast fracture of the material when low graphene content is utilized [179]. When the graphene content is increasing, the fracture toughness of the material is increased, as more toughening mechanisms, like crack deflection and pinning act synergistically for the fracture procrastination [165][180]. However, if the graphene content is significantly increased, the fracture toughness will eventually decrease, as the microcracks will merge with each other, due to their close distance, resulting to a central crack in a faster way [179]. Therefore, the optimization of graphene loading, as well as of its appropriate dispersion and distribution inside the matrix play an important role to the improvement of fracture toughness.

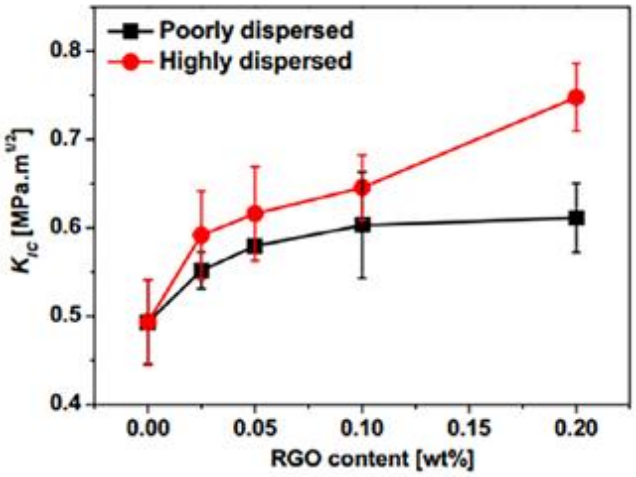


Figure 2.10: Fracture toughness of highly and poorly dispersed GO as a function of graphene content [181].

2.10 Graphene-PMMA nanocomposites: Nanofillers impact in mechanical reinforcement

The incorporation of graphene or graphene derivatives into PMMA-nanocomposites results to the enhancement of their mechanical properties, among which their modulus, strength and fracture toughness [182][183]. For instance, the incorporation of nano-sized graphene nanoplatelets (GNPs) and hydroxyapatite (HA) with combined loadings ranging from 0.5 to 2.5 wt% in PMMA bone cement have shown an increase over the flexural modulus by 30.80%, the flexural strength by 49.28%, the compression strength by 31.7%, and the compression modulus by 57.41%, corresponding to the addition of 1.5 wt% GnP and HA nanoparticles [184]. Generally, depending on the processing conditions and the desired level of toughness improvement, low concentration, up to few wt% graphene content is added in PMMA-nanocomposites [185][186]. As demonstrated by Sun Guanhong, in **Figure 2.11**, the nanocomposites with the higher graphene content (3.0%) break at lower applied strain compared to the other samples, whereas the ones with lower graphene content (0.5%, 1.5%) tend to break at higher strains, reaching approximately the same stress level at break.

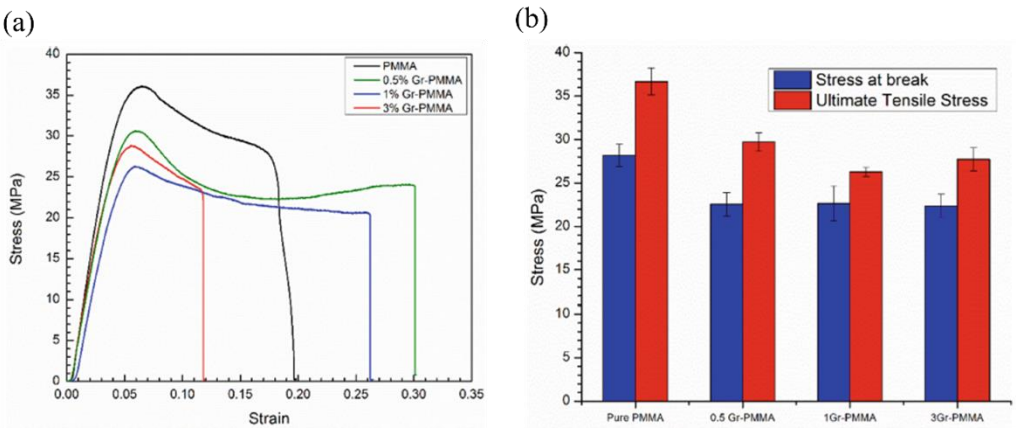


Figure 2.11: (a) Stress-strain curves, and (b) Tensile strength of neat and graphene-PMMA nanocomposites with various graphene loadings [185].

The addition of a low graphene-silver nanoparticles loading (1.0 wt%) in a PMMA matrix can significantly increase its flexural strength by 174%, and present endurance to higher applied loads, compared to the unmodified PMMA [187]. Moreover, PMMA nanocomposites with 1.0 wt% graphene and 0.25 wt% TiO2 nanoparticles recorded the best wear resistance performance compared to the pure specimen [188].

Nanofiller concentrations even lower than 0.5 wt%, are able to provide enhanced mechanical properties to the nanocomposites. For instance, the mechanical performance of graphene-PMMA and GO-PMMA bone cements is significantly reinforced at low loadings (≤0.25 wt%), where their fatigue performance is enhanced by 30% compared to the control group and their fracture toughness was improved by 23% and 32%, for the graphene and GO nanocomposites, respectively [189]. The introduction of 0.09, 0.18 and 0.27 wt% graphene oxide nanosheets in PMMA-PVA nanocomposites, significantly enhances properties like the bulk modulus, up to 225%, compared to the blended polymers, rendering them promising materials for a wide range of applications, including ultraviolet filters applications and their use as a car glass [190]. It is interesting to note that graphene concentrations even lower than 0.1 wt% lead to enhancement of the graphene-PMMA nanocomposites. For instance, by tuning the migration and selective location of mere 0.05 wt% graphene nanosheets (GNs) during melt blending in a PC/PMMA/GNs composite, the strength and toughness are significantly enhanced, as the tensile strength and the elongation of the composite is increased by approximately 62.96% and 94.54%, respectively as compared to the PC/PMMA blends [191]. Additionally, the production of CVD graphene-PMMA nanolaminates of 0.06% volume fraction, significantly enhances the stiffness, the toughness and the strength of the traditional composites with similar filler content [192]. Furthermore, the addition of Chopped Carbon Fiber (CCF) in PMMA composites, which are discontinuous carbon reinforcements, leads to the production of composites with superior mechanical properties compared to those made from polymers, as they present improvement on tensile strength, impact resistance, and thermal stability, due to their high strength-to-weight ratio [193][194][195]. Fracture toughness of CCF-PMMA nanocomposites may vary due to factors like fiber orientation, aspect ratio, dispersion, and interfacial bonding between the fibers and the polymer matrix. Nevertheless, in general they reinforce the fracture toughness of nanocomposites, as the short carbon fibers span across crack surfaces, creating bridging effects, and therefore impeding the crack propagation [196]. Moreover, Multiwall Carbon Nanotubes (MWCNTs), which are cylindrical nanostructures composed of multiple layers of graphene sheets rolled into concentric tubes, enhance the fracture toughness of polymer matrices like PMMA, as they deflect and bridge cracks, and therefore toughening the graphene-based nanocomposite [197][198]. Carbon nanofibers (CNFs) are nanoscale carbon structures with a fibrous morphology and high

aspect ratio, which act as crack bridges and energy dissipators reinforcing the fracture toughness of PMMA-nanocomposites. In general, all these nanofillers enhance the fracture toughness of graphene-PMMA nanocomposites, however factors such as the aspect-ratio, the dispersion and interfacial bonding characteristics, play an important role over the degree of fracture toughness enhancement [196]. For example, CNFs are more easily dispersed into the PMMA nanocomposite than MWCNTs. The latter maintain their high aspect ratio; however, they are prone to forming agglomerates, in which can be attributed the diminishment of flexural modulus compared to neat PMMA (**Figure 2.12(a)**). On the contrary, CNFs and CCFs, characterized by higher quality dispersion, present increased flexural modulus. In terms of fracture toughness, it is significantly increased in the case of CCFs-PMMA nanocomposites (in comparison with the MWCNTs and CNFs -PMMA nanocomposites), as due to their larger dimension compared to the pre-crack length, mechanisms such as crack deflection, crack bridging, and pull-out inhibit the crack propagation (**Figure 2.12(b)**). Lastly, the poor dispersion of graphene derivatives, especially MWCNTs into the PMMA matrix, further reduces the ability of the nanocomposite to resist crack propagation.

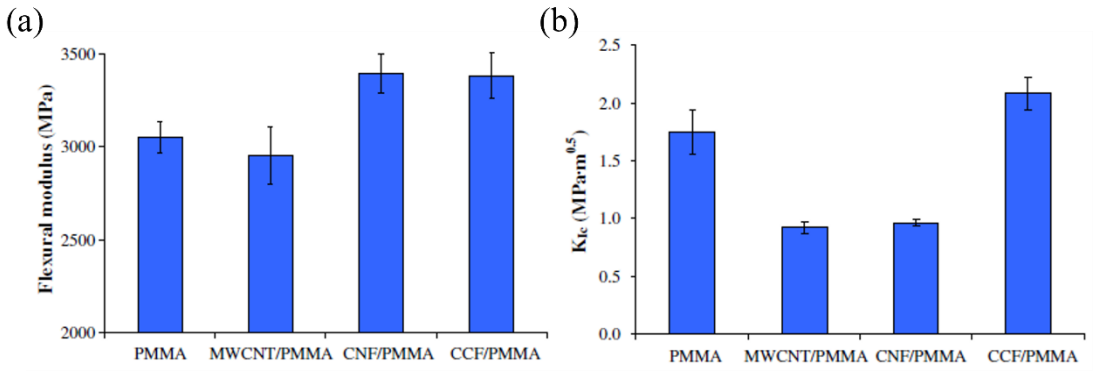


Figure 2.12: (a) Flexural modulus, and (b) Fracture toughness of neat and graphene derivatives-PMMA nanocomposites (a) Flexural modulus, and (b) Fracture toughness of neat and graphene derivatives-PMMA nanocomposites [196].

The incorporation of CVD graphene into PMMA nanolaminates, even in low volume fraction, significantly enhances the stiffness, the toughness and the strength compared to the traditional composites with similar filler content [192]. From the stress-strain curves of graphene-PMMA nanolaminates, corresponding to various graphene loadings (see **Figure 2.13**), the nanolaminates with a higher graphene content tend to break at lower applied strain, whereas the nanolaminates with lower graphene content tend to break at higher strains, reaching approximately the same stress level at break.

Moreover, large-scaled CVD graphene sheets, apart from ensuring the appropriate conditions for adequate load transfer, they are also promising candidates for the procrastination of the crack growth, due to their large dimensionality, allowing fracture toughness mechanisms to inhibit the crack propagation via the formation of microcracks and crack deflection. Consequently, in this dissertation, the fracture toughness of low volume fraction CVD graphene-PMMA nanolaminates along with the fracture mechanisms improving it are studied.

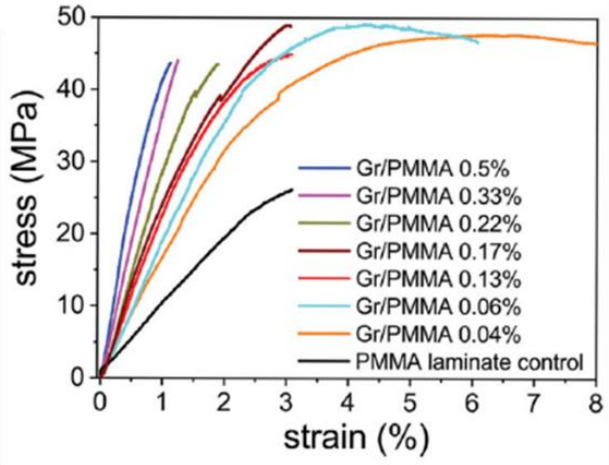


Figure 2.13: Stress-strain curves obtained by uniaxial tensile testing of CVD graphene-PMMA nanolaminates of various graphene content [32].

3. Characterization techniques

This chapter presents the experimental techniques utilized in this dissertation for the study of the samples. Specifically, both imaging techniques such as Optical Microscopy and advanced imaging techniques, such as Atomic Force Microscopy (AFM) and Scanning Electron Microscopy (SEM) were used for the visualization of the samples' surface and the strain-induced morphological changes. Raman spectroscopy was used for monitoring the quality of all samples, and for obtaining the stress distribution near a defect, under the application of external strain. The graphene samples used, were synthesized using both mechanical cleavage and CVD process.

3.1 Optical Microscopy

Optical microscopy is a simple and inexpensive technique, widely used for the observation and the microscopic study of materials [199] and other biological samples [200], providing valuable insight into the characteristics, i.e. its microstructure, its morphology and its composition [201]. In general, optical microscopes use visible light as an illumination source and a system of lenses in order to magnify the surface studied. The optical microscope used in this thesis (Olympus, model here, **Figure 3.1**) was located in a clean room, in order to prevent the contamination of the samples.

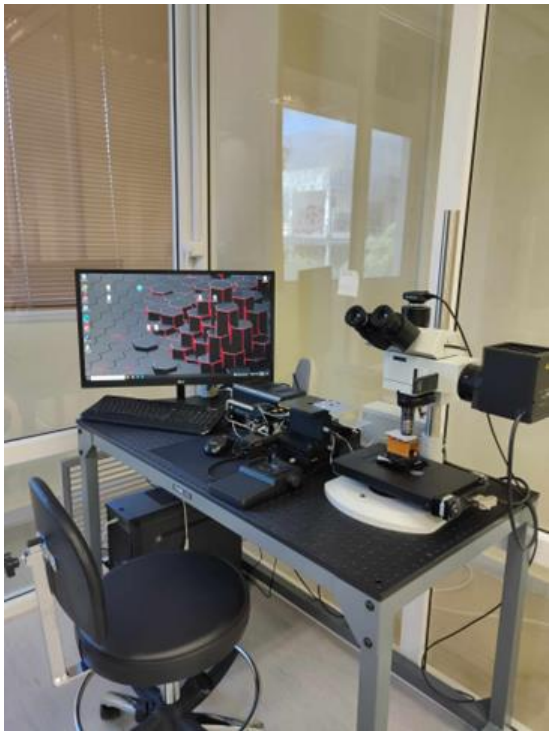


Figure 3.1: Olympus optical microscope.

Optical microscopy is widely used also as an initial step at the study of mechanically cleaved graphene flakes. Its simplicity combined with its ability to provide important preliminary information over samples' location and characteristics (size, shape number of layers), renders this technique a useful tool for a researcher.

In this dissertation, the optical microscope was utilized extensively for the detection of mechanically exfoliated graphene flakes produced via the mechanical cleavage method from HOPG (High Order Pyrolitic Graphite), using a commercially available scotch tape (see **Figure 3.2**). The mechanical exfoliation procedure is presented in detail in Chapter 1 (1.3.1 Top-bottom approach).

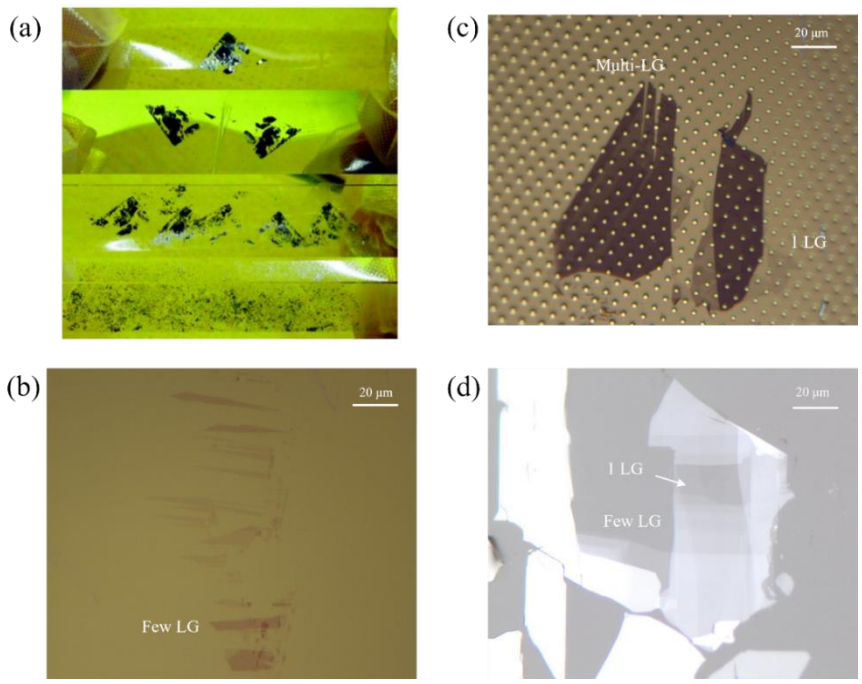


Figure 3.2: (a) Mechanical exfoliation of a graphitic flake on an adhesive tape, cleaved two to several times (top to bottom) [202]*, Mechanical exfoliated graphene flakes deposited onto (b) $Si0_2$ wafer, (c) $Si0_2$ wafer with holes, and (d) SU-8/PMMA substrate.*

In general, graphene flakes are more easily observable when they are deposited onto SiO_2 wafer with 300 nm thickness, with or without holes (**Figure 3.2(b,c)**). The slightest change in the color of the flake, indicates empirically the number of the layers that it consists of [203]. Graphene flakes that are deposited onto PMMA films are not detectable via optical microscope, and thus SU-8 (SU-8 2000.5 Micro-Chem), which is

a photoresist polymer, is spin coated on the top surface of a PMMA film, utilizing incremental rpm until ∼3000 rpm and creating a layer of ∼100 nm thickness, in order to enhance the visibility of the cleaved flakes, whose observation remains a challenging procedure (**Figure 3.2(d)**).

3.2 Raman Spectroscopy

Raman spectroscopy is a powerful diagnostic, versatile, non-destructive technique, used in a wide range of research and industrial applications, as it is utilized for the identification, the characterization, the quality assessment, and the quantification of the chemical components of materials. The operation of this technique is based on inelastic Raman scattering. Following the incidence of light on a molecule, elastic scattering is dominant (Rayleigh scattering). Nevertheless, inelastic scattering (Stokes and anti-Stokes scattering) is also present. Specifically, when a photon interacts with matter, if the energy is sufficient, a molecule is excited from its initial state to a temporary virtual one, and then returns to the ground electronic state, emitting a photon. In the case of Rayleigh scattering, the molecule returns to the same vibrational state from which it was excited, therefore the emitted photon has the same kinetic energy as the incident. However, in inelastic scattering the photon's kinetic energy is not preserved, as the molecule returns to a different vibrational level of the ground state. As shown in **Figure 3.3**, depending on whether the molecule returns to a higher/lower vibrational state than its initial one, the emitted photon will have a lower/higher energy, corresponding to a redshift (Stokes Raman scattering) or a blueshift (anti-Stokes Raman scattering), respectively. According to Boltzmann's distribution, for molecules at thermodynamic equilibrium, the lower the vibrational state the higher the occupation. Therefore, the Stokes Raman scattering events are more probable than the anti-Stokes, and their corresponding intensity in the Raman spectra is higher.

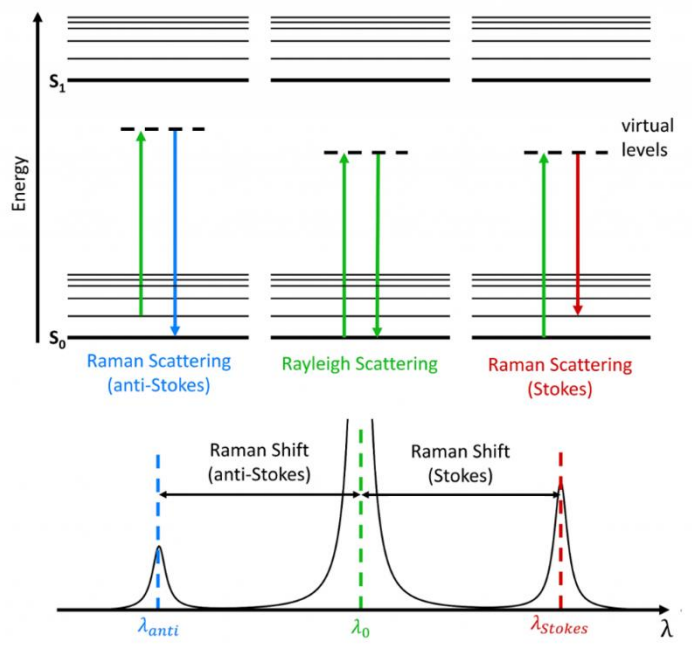


Figure 3.3: Energy diagram and related peaks for Rayleigh and Raman scattering [204].

Raman spectroscopy is a powerful diagnostic technique for the assessment of the structural characteristics of carbon-based materials. Each carbon allotrope presents peaks/peaks with diverse spectral characteristics, according to their unique atomic structure and bonding configurations. Explicitly, in the Raman spectrum of graphite, the G peak at ~1580 cm^{-1} prevails, while there is a low intensity D-peak indicating the structural defects of the material, and the 2D peak is a doublet. Additionally, diamond, which is characterized by sp^3 bonding, presents a sharp peak at 1332 cm^{-1}. Fullerenes, such as C60, showcase notable peaks like the one at ~1470 cm^{-1}, which is related to their spherical geometry, while amorphous carbon, present broader peaks, with the G and D peaks being present at ~1580 cm^{-1} and ~1350 cm^{-1}, respectively, with their I(D)/I(G) ratio providing information over the degree of disorder. The Raman spectrum of Carbon Nanotubes (CNTs) is also characteristic, as the radial breathing mode (RBM), which gives information over the nanotube diameter, and the G-peak (~1580 cm^{-1}), which reflects the electronic structure, are dominant. Finally, Graphene's Raman spectrum is characterized by two peaks, the G peak (~1580 cm^{-1}) and the single-Lorentzian 2D peak (~2700 cm^{-1}), with the latter's intensity and full-width at half-maximum (FWHM) and the ratio I(2D)/I(G) indicative of the number of graphene layers. In the case where defects are present, D peak is also present at ~1350 cm^{-1}. In **Figure 3.4**, the Raman spectra of both carbon allotropes and graphene-based materials

are illustrated, displaying all the differences mentioned above [205][206]. It is obvious that Raman spectroscopy can provide an "arrow in the quiver" for examining the quality of carbonaceous materials.

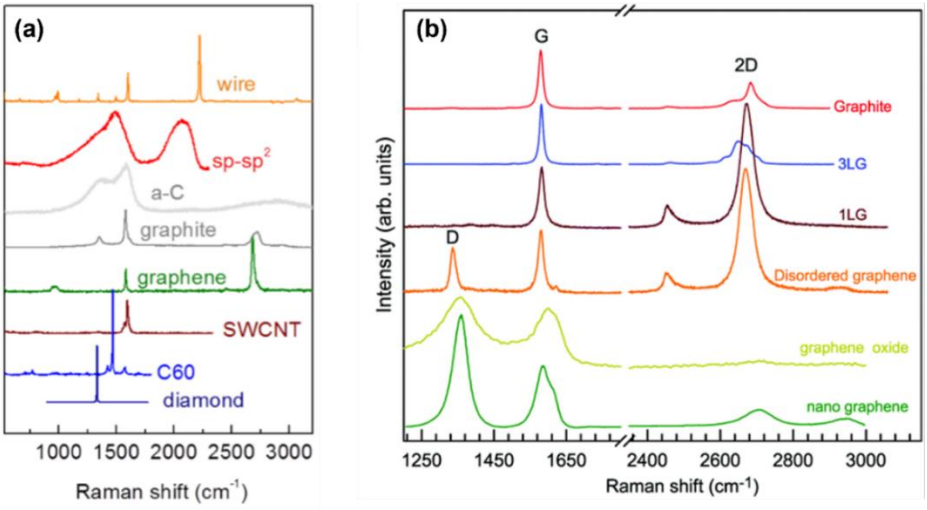


Figure 3.4: (a) "Signature" Raman spectra of some carbon allotropes, (b) Raman spectra of graphene-related materials.

As can be seen in **Figure 3.4**, there are three characteristic peaks dominating graphene-based material's spectra, namely the D, G, and 2D peaks. Their provenance lies on the phonon dispersion relation. Graphene's unit cell includes two atoms and therefore for vibrations in three-dimensional space, six phonon dispersion peaks (branches) are needed to describe these possible vibrations. Depending on whether the nearest neighboring atoms oscillate in- or out-of-phase, the branches are acoustic or optical respectively. Out of the six branches, four branches correspond to in-plane vibrational motion, and two branches (one acoustic and one optical) correspond to out of plane vibrational motion. Out of the four in-plane branches, two are **transverse** and two are **longitudinal**, depending on whether the vibrational motion is perpendicular or parallel to the bond of the two atoms (in the case of out-of-plane vibrations both are transverse). Summarizing the above considerations, the six branches are iLO, iTO, oTO, iLA, iTA, oTA (see **Figure 3.5**).

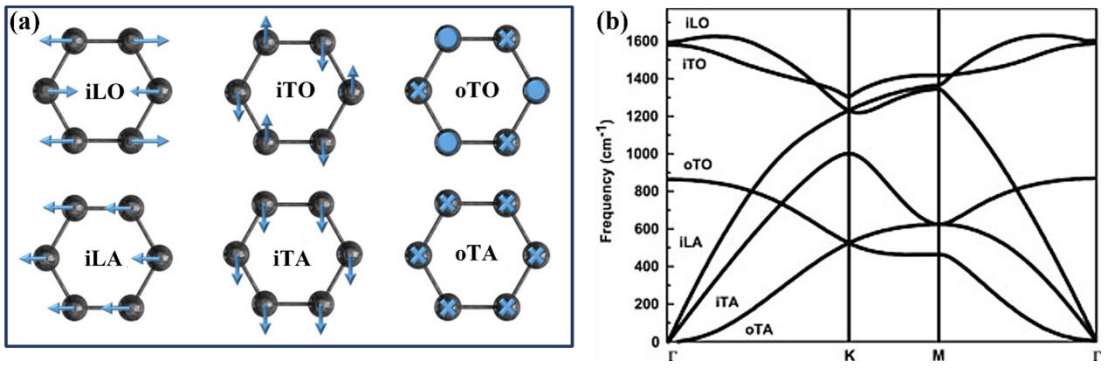


Figure 3.5: (a) Normal vibrational modes of graphene [207]*, (b) phonon dispersion relation of graphene showing the iLO, iTO, oTO, iLA, iTA, oTA branches* [206].

In the Raman spectra of carbon structures comprised of sp^2 configurations, like graphene, the G peak is present due to the first-order Raman scattering process. Its provenance is related to the doubly degenerate iLO and iTO phonon modes at the Brillouin zone center Γ [208]. The degeneracy can be lifted under certain scenarios, such as in carbon nanotubes [209] or under tensile strain [210], resulting in the appearance of a doublet peak (G- and G+). As shown in **Figure 3.6**, the D peak is associated with an intervalley second-order process, where a photon excites an electron, forming an electron-hole pair at the K point of Brillouin zone, where the excited electron undergoes elastic scattering by a defect around the K' point. Followingly, this electron is inelastically scattered by an iTO phonon and returns to the K point, recombining with the hole and emitting a photon. In the case of the 2D peak the excited electron undergoes two inelastic scattering events (instead of one elastic and one inelastic) [208]. The D and 2D peaks, in contrast with the G peak, display dispersion and their peak positions vary depending on the energy of the incident laser photons.

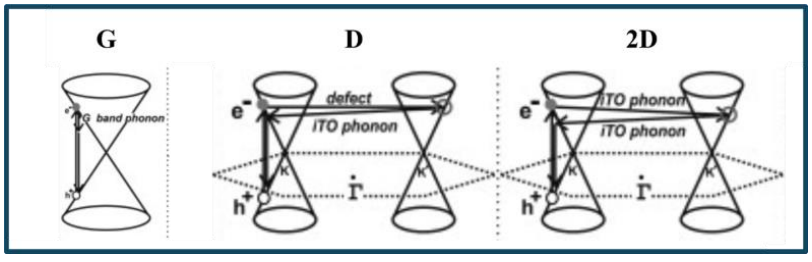


Figure 3.6: Processes that give rise to the G, D, and 2D peaks in graphene-based materials [208].

The nature of the carbon allotrope studied, affects Raman peaks characteristics, such as their shape, their intensity, their position, and their width. A characteristic feature in Raman spectra of carbonaceous materials that have a disorder, or defects, imperfections

in the carbon lattice, such as vacancies, edge effects or grain boundaries, is the D peak. The intensity of this peak is related to the degree of disorder or the increase on the structural defects present in the material, as a higher level of disorder leads to a higher intensity of the D peak. The intensity of G peak is used as a measure of the graphitic content or the crystallinity of the material, as it is related to the number of sp^2 bonds in the material. In general, in most of the graphitic materials, G peak is narrower and has higher intensity than D peak. Ferrari and Robertson have studied extensively the factors that influence both D and G peaks of an amorphous carbon material [211]. Particularly, they studied the effect that bonding configurations and structural features have on the Raman spectrum of amorphous carbon, as the bond disorder, the presence of sp^2 rings or chains, the clustering of sp^2 phase, and the sp^2/sp^3 ratio affects the overlap of the two peaks and their relative peak intensities, as depicted in **Figure 3.7**. The ratio of the intensity of the D peak to that of the G peak (I(D)/I(G)) reflects the degree of disorder in the material. A ratio I(D)/I(G) close to 0, indicates that graphene is flawless, whilst higher values indicate an increased defect density.

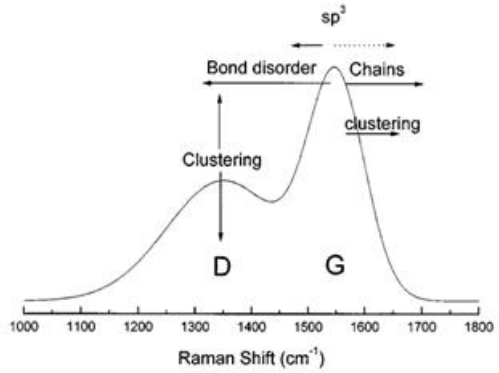


Figure 3.7: Factors influencing the D and G Raman peaks of carbon [212].

External perturbations, such as strain and doping affect the characteristics of the D and G peaks [213]. The application of strain may increase the disorder and the defects of graphene's lattice, resulting to a relative increase of the intensity of D to G peak, while their linewidths become broader. Also, depending on the strain applied, compressive or tensile, G peak's position splits and shifts towards higher or lower wavenumbers, respectively [210][214]. Doping can significantly affect peaks characteristics, depending on the type and the concentration of the charges, influencing intensity, position through shifting and the width of the peaks, due to the insertion of defects [215].

The 2D peak is another important prominent feature in carbonaceous Raman spectra, like graphene and other honeycomb lattice structures, providing information over their electronic and structural properties. At the same time, it displays a high sensitivity in the number of graphene layers and their stacking order. In monolayer graphene, the 2D peak appears as a single-Lorentzian curve, typically observed at ~2700 cm^{-1} (when the excitation laser is 514 nm) or at ~2600 cm^{-1} (when the excitation laser is 785 nm), with a Full-Width at Half-Maximum (FWHM) of approximately 24 cm^{-1} [216]. When individual graphene layers follow Bernal stacking, the layers are arranged in a specific pattern, and the electronic and phonon peaks undergo further splitting. This splitting results to multiple possible second-order processes, which involve two intervalley processes, leading finally to the superposition of several 2D Raman peaks, as the number of layers increases (as shown in **Figure 3.8**) [208]. In bilayer graphene, the 2D peak can be deconvoluted into four peaks [217], while in trilayer graphene, six to fifteen peaks are needed for the fitting of the 2D peak [218]. In the case of bulk Bernal-stacked graphite, such as highly oriented pyrolytic graphite (HOPG), the 2D peak is a doublet, which can be fitted using two Lorentzian curves [208].

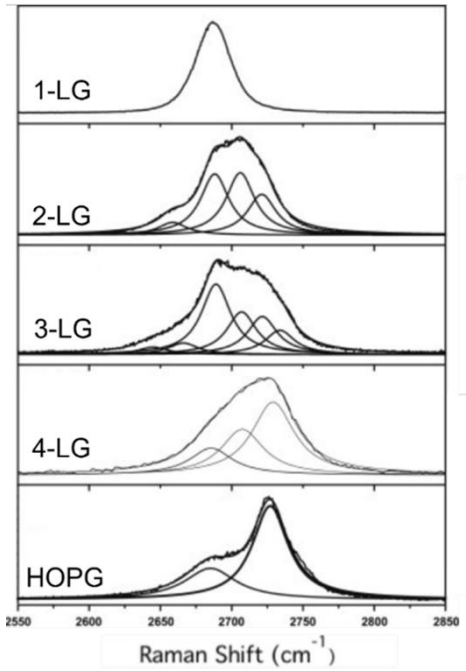


Figure 3.8: Change in the 2D Raman peak as the number of layers increases [208].

In general, the 2D peak is utilized as a diagnostic tool for the quality study and the conditions that carbonaceous materials undergo. Noticeable alterations in both its shape (broadening) and intensity are observed, as the number of graphene layers increase,

from monolayer graphene to bulk graphite, while information over the stacking order of the sheets can be given [219]. Moreover, the 2D peak can be utilized for the assessment of the degree of disorder, the identification of defects presence, as it is an overtone of the D peak, the doping and other structural modifications. Precisely, the ratio of the intensity of the 2D peak to that of the G peak (I(2D)/I(G)) is indicative of graphene's quality, as values greater than 2.5 signify that the graphene is monolayer, whilst lower values suggest a higher number of layers.

The 2D peak is strongly affected by external factors, such as the excitation wavelength, the application of strain, and doping [220]. Concretely, the 2D peak presents high sensitivity (almost double than the G peak) over the external application of strain or compression, as electronic and phonon dispersion near the K and K' points of graphene is affected, resulting to the final splitting of the 2D peak into two distinct components, referred to as 2D1 and 2D2 and their shifting towards lower (tensile strain) or higher (compressive strain) wavenumbers. Both their relative peak intensities and peak width, are modified due to the strain-induced alterations of lattice, resulting to broader or narrower peaks. The peak splitting can also be utilized as a measure of charge doping, detecting charge doping at levels two orders of magnitude lower than what can be measured using the G peak response to doping [220]. Dopant atoms or molecules into graphene have strong effects on 2D peak's shape and position. High concentration of dopants leads to broader linewidths and more significant shifts, due to the higher induced disorder. Precisely, the existence of dopants can cause modifications on graphene's electronic properties, such as in the Fermi level or the carrier concentration, leading to the presence of additional electronic states, which contribute to the broadening of the 2D peak and the shifting of its position toward higher (p-type dopants) or lower (n-type dopants) wavenumbers [221][222].

3.3 Atomic Force Microscopy

Atomic Force Microscopy (AFM) is a versatile nanoscale imaging technique utilized for the high-resolution visualization of surfaces in various fields, such as biology, chemistry and engineering [223]. The basic principle of AFM's operation lies in the interaction of the sample's surface with a sharp tip (AFM tip), which is attached to a flexible cantilever (its operation mimics that of a spring). Specifically, the AFM tip can

approach the sample's surface to few nanometers, and scan over it in order to probe the surface characteristics. Because of the interaction between surface's atoms or molecules and the tip, the cantilever is deflected towards or away from the surface, due to the attractive or repulsive forces that are developed. These forces can be electrostatic, magnetic, or Van der Waals.

As demonstrated in **Figure 3.9**, the deflection of the cantilever is detected through an incident laser beam, which is reflected off the back of the cantilever onto a position-sensitive photo diode detector, tracking the changes of the reflected beam direction (position and angle). Specifically, as the cantilever bends due to the interactions of the tip with the sample, the laser beam deviates from its original path. This deviation is captured from the photodiode, activating a feedback process, where the cantilever returns to its original position, adjusting the distance between the tip and the sample accordingly, either by approaching it or by drifting apart. Consequently, as the tip scans across the surface, an accurate topographic map of the surface feature is constructed.

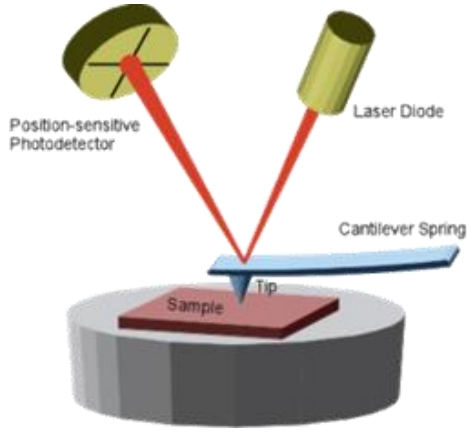


Figure 3.9: Representation of the working principle of AFM [224].

Depending both on the material properties of the sample (i.e. conductive, non-conductive) and the desirable application, AFM can operate in various environments (air, vacuum, liquid), in two modes: Static or Contact Mode and Dynamic Mode (see **Figure 3.10**.

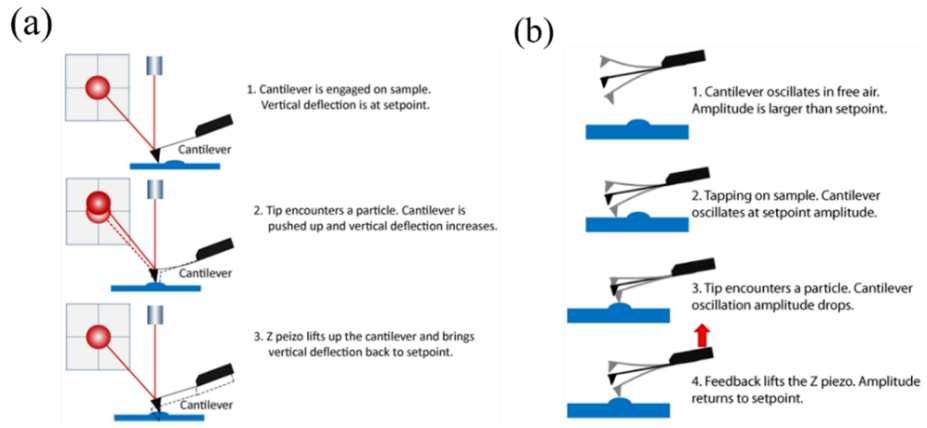


Figure 3.10: AFM cantilever motion in (a) Contact Mode, and (b) Tapping Mode.

In Contact mode, the tip remains perpetually in contact with the surface, operating in the repulsive regime of the curve, depicted in **Figure 3.11**. When the tip is approaching the sample's surface within a distance of less than 1 nm, a repulsive force is developed due to the electron cloud overlap. Due to this force, the tip is not penetrating the sample surface, but it preserves the constant contact between the tip and the sample. This mode is suitable for the high-resolution imaging of flat and soft samples, with precise topographical details. It is important to note that the cantilever is quite flexible in order not to damage the specimens. Dynamic Mode can be further divided into tapping and non-contact mode. In tapping mode (intermittent mode), both attractive and repulsive forces dominate. In specific, during the non-contact segment of the oscillation, due to van der Waals forces, which act as attractive forces between the tip and the sample surface, the tip is attracted towards the surface, whilst during their brief contact, repulsive forces are developed when the tip oscillates downwards, preventing in this way the penetration and damaging of the sample (see **Figure 3.11**). The cantilever, in this case, is forced to oscillate at or near its resonance frequency, reducing the lateral forces and the potential damage of the sample. In non-contact mode, while the tip has no direct contact with the sample, imaging is achieved through its interaction with the sample through Van der Waals forces (attractive forces). This mode allows the surface imaging of very delicate samples and usually the tip-sample distance is maintained at several nanometers, in order to avoid physical contact.

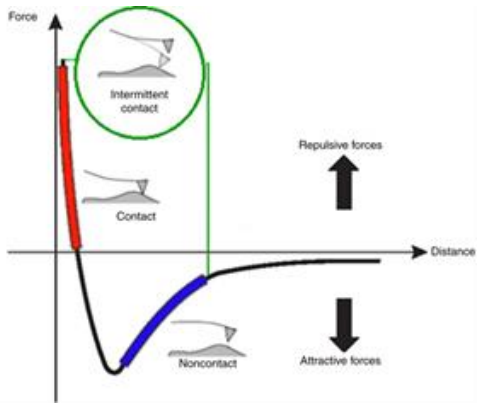


Figure 3.11: Force as function of the tip/sample distance [225].

PeakForce Quantitative Nanomechanical Mapping (**PeakForce QNM**) is an advanced imaging mode in Atomic Force Microscopy (AFM) utilized for the study of heterogenous samples, such as nanocomposites and polymers, where variations in mechanical properties play important role on the material performance. This technique furnishes high-resolution nanoscale mappings of the samples, while simultaneously providing quantitative information over their mechanical properties. **PeakForce QNM** is utilized for the high-resolution imaging of the samples with piconewton (pN) sensitivity, rendering feasible the visualization of the daintiest details, such as atomic defects in molecular structures [226]. The AFM tip approaches the sample's surface and encounters it, following a controlled, intermittent tapping motion. As the tip comes in contact with the surface, a small peak force is exerted onto it and the deflection of the cantilever is measured consistently, as the tip scans an area of interest. The applied force is constantly being adjusting in order to maintain the steady tip-sample interaction, assuring the high-resolution visualization and integrity of the sample's surface. In **Figure 3.12**, the interaction between the tip and the surface is illustrated in a diagram that is known as "the heartbeat", which is in essence a force vs time plot. At point A, the tip is far from the sample and therefore there is minimal force (or no force at all) applied to it. As the tip gradually approaches the surface, attractive forces, such as van der Waals, electrostatic or capillary forces, begin to pull the cantilever downward towards the surface, resulting in a negative force, as the graph is below the horizontal axis. At point B, the cantilever is bending even more towards the surface, as attractive forces surpass its stiffness, causing the tip to contact the surface. As can be seen in the graph, between point B and C, the force increases until the modulation's Z position reaches its lowest point (point C), where the force takes and maintains its maximum

value during the interaction period through the system feedback. As the probe is retracted, the force is diminishing until it reaches its minimum point D, which is referred to as the pull-off point, and adhesion can be measured. When the tip finally disengages, it is only affected by long-range forces, resulting in minimal or zero force when the tip is fully withdrawn from the sample (point E).

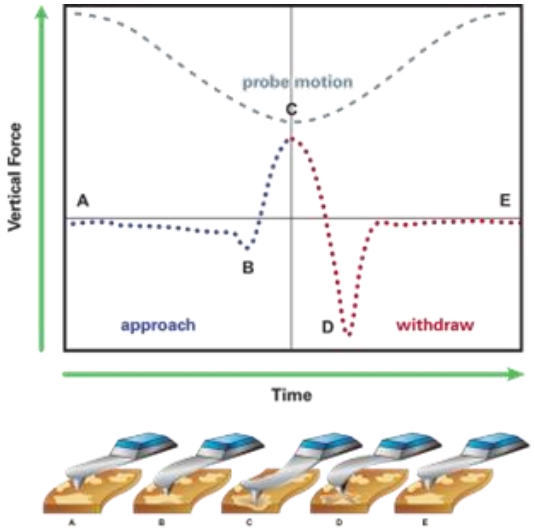


Figure 3.12: Force as a function of time in a PeakForce QNM cycle and the corresponding movement of the tip.

In **PeakForce QNM** mode, high-resolution maps of mechanical properties across the sample surface can be made, providing valuable insights into the material's nanomechanical behavior. As the AFM tip scans across the sample surface, it renders feasible the collection of important quantitative information focusing on the nanomechanical properties of a material. Apart from the surface topographical information obtained through high-resolution imaging, mechanical properties such as stiffness, elasticity, adhesion, and deformation can be measured at the nanoscale [227]. The generation of detailed maps of these mechanical properties of the sample surface is conducted through the application of controlled forces and by measuring cantilever's response. Specifically, information over the adhesion properties of the sample can be extracted through the analysis of force-distance curves obtained during scanning [228]. The modulus of elasticity can be obtained through the measurement of indentation depth of the AFM tip into the sample surface, while applying contact mechanics models, therefore calculating the local Young's modulus of the material [229]. Measurements over the energy dissipation mechanisms and the dynamical mechanical behavior of the material can be extracted through the analysis of cantilever's response

to the applied force, therefore giving information for the viscoelasticity of the sample [229].

In this dissertation, AFM was utilized for the surface characterization of mechanically exfoliated graphene, as well as the monitoring of its morphological alterations upon the imposition of external strain, by employing PeakForce QNM.

3.4 In-situ mechanical testing

In-situ tensile testing of 2D materials and nanocomposites is a critical method for understanding their mechanical properties and their behavior at the nano- and micro-scale. This testing method involves subjecting the material to tensile forces while observing in real-time its structure and deformation characteristics, typically using advanced microscopy techniques. Specifically, in-situ tensile tests of both 2D materials and nanocomposites combined with real time imaging techniques is beneficial for the understanding of the mechanical response of nanomaterials like nanoparticles, nanotubes, and nanosheets, facilitating the establishment of morphology-mechanics correlations [230], while revealing intrinsic mechanisms like fiber strengthening and CNT pullout in nanocomposites [231]. Advanced imaging techniques, such as Scanning Electron Microscopy (SEM), Transmission Electron Microscopy (TEM) and Atomic Force Microscopy (AFM) combined with in-situ tensile tests play a crucial role in providing comprehensive information on the structure, morphology, and composition of low-dimensional materials [232][233][234]. The combination of Raman technique with tensile testing is also a very beneficial approach, providing insight over the microstructure and the mechanical properties of both 2D materials and graphene-based nanocomposites [235][236]. Additionally, in-situ tensile tests using microelectromechanical systems (MEMS) devices for graphene and graphene oxide nanosheets, enable direct thickness mapping, high-resolution electron beam linking, and mechanical testing [237][238]. Moreover, combining tensile test with atomistic simulations, such as Molecular Dynamic Simulations (MDs), sheds light over the filler's contribution on graphene's based nanocomposites concerning their mechanical properties, such as their elastic modulus [175], and elucidates the mechanical properties and the failure mechanisms of 2D materials [239].

In this dissertation, the tensile testing of the samples was conducted with a micro-tensile tester (MT-200, Deben UK Ltd, Woolpit, UK) equipped with 5, 50 and 210 N loadcells (see **Figure 3.13**), accommodating samples with maximum thickness of 1 mm. The maximum displacement of the grips reaches 30 mm, with a step accuracy of 10 μm. This machine is fully controlled by a computer and has a sensitivity of 0.005 N.

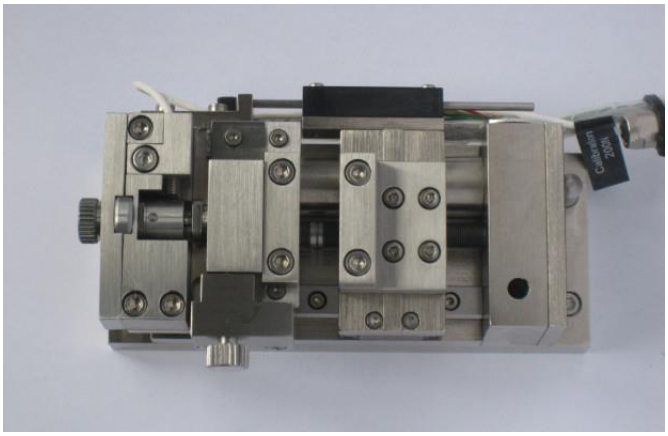


Figure 3.13: Illustration of the micro-tensile tester.

Depending on the desirable experimental procedure, the micro-tensile tester was adapted under or inside the instrument of interest, in order to study the samples' response to the application of incremental strain. Precisely, the micro-tensile tester was mounted onto a Raman microscope stage (**Figure 3.14a**) to assure the simultaneous acquisition of samples' Raman spectra in combination with the application of load on the sample. The tester was also adapted under a custom-built digital optical microscope camera (composed of the objective lens, the tube lens, a C-MOS camera and the microscope holder) in order to observe the crack propagation of a sample with an inflicted defect (**Figure 3.14b**), as well as inside the AFM chamber for the simultaneous monitoring of the samples' morphology (**Figure 3.14c**). The samples studied were graphene flakes of various number of layers, representative and distinguished among the 2D material for their exceptional mechanical properties, as well as graphene-based nanolaminates, presenting outstanding strength and Young's modulus, ideal for high performance applications.

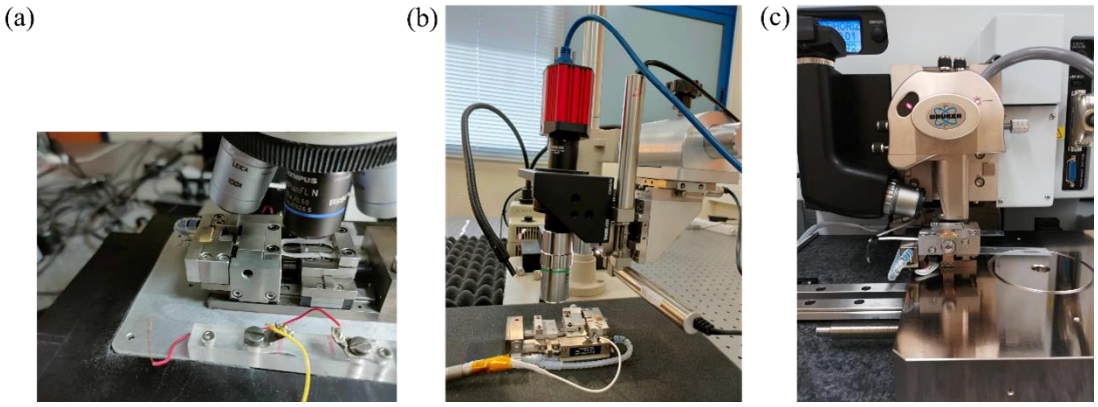


Figure 3.14: Deben micro-tester under (a) Raman, (b) High resolution camera, and (c) AFM, for the in-situ tensile testing experiments.

3.5 Scanning Electron Microscopy (SEM)

Scanning Electron Microscopy is an advanced imaging technique with high resolution imaging capabilities, rendering feasible the examination of topography and composition of a sample at micro- and nano- scale [240]. Its principle relies on the acceleration of focused electrons due to the implementation of high voltage onto a sample. This interaction between the focused electron beam and the material atoms generates signals collected by detectors and converted into digital images on a computer screen [240]. Within the framework of this study, the SEM instrument employed was a Field Emission SEM (FE-SEM) (Zeiss SUPRA 35VP), and a voltage of 10-15 kV (**Figure 3.15**).

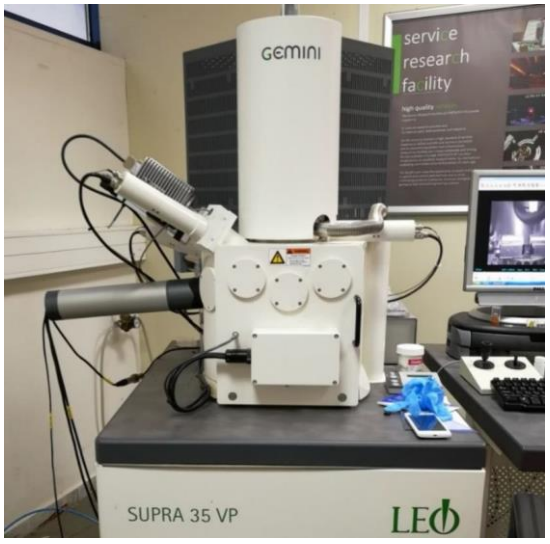


Figure 3.15: Scanning Electron Microscope.

4. Using large-size graphene sensor for the assessment of stress concentration in the vicinity of a notch

In the present chapter, the use of monolayer CVD graphene is proposed to monitor the stress concentration near a defect in polymer of high interest such as, poly (methyl methacrylate) (PMMA). Combining in-situ Raman spectroscopy, which is a powerful diagnostic technique, with uniaxial tensile testing, the stress/strain distribution around the defect can be probed via monitoring the wavenumber shift of the spectroscopic features of graphene, with high spatial resolution. Experimental findings are supported by Finite Elements Analysis.

4.1 Experimental methods for measuring the stress concentration factor

Understanding the mechanical performance of materials and predicting potential failure points is crucial in various engineering applications. As depicted in Chapter 2, the presence of defects – flaws, scratches and notches - can significantly alter the stress distribution leading to localized stress concentrations and premature failure [241][242]. The investigation of stress concentration in materials is of great importance in various fields, such as astronautics and aeronautics, where localized stress can jeopardize the safety of launched vehicles [243]. Therefore, several techniques are employed for the assessment of the stress field depending on the material type, with most of the studies focusing on isotropic, orthotropic, and composite materials [242][244] [245]. Polymers are also widely utilized in industrial applications due to their exceptional mechanical performance, attributed to the high strength-to-weight ratio, flexibility, and resistance to corrosion and chemicals [246][247][248][249]. Polymers are classified into those maintaining their mechanical properties despite the existence of notches, and those, such as thermoplastics, which below the glass transition temperature (T_g) exhibit brittle fracture when subjected to an external force[250][251]. Notch-sensitive polymers include amorphous (polymethyl methacrylate – PMMA, polycarbonate - PC [252]) and some semi-crystalline thermoplastic polymers (polyethylene-PE, polypropylene-PP)

[253], which can be affected by either irregularities at the molecular level [254] or macroscopic imperfections [255]. Therefore, a comprehensive understanding of how polymers respond to notches, also including the investigation of the stress concentration in the areas close to defects, is essential for designing reliable and durable polymer-based systems. Similarly, this is extremely important in the design of engineered components based on advanced materials, such as composites. In this regard, investigating the stress concentration to the areas close to defects facilitates the understanding of the fracture behaviour of polymers, aiming to the development of techniques that renders them more resilient to fracture [256][257].

In general, the experimental measurement of stress concentration in polymers is possible by utilizing various approaches, such as Digital Image Correlation (DIC) [258], caustics [259], photoelasticity measurements [260], laser scanning thermography [261], ultrasonic testing [262], and acoustic emission testing [263]. However, each of the aforementioned techniques present several drawbacks; for instance, DIC requires specific surface preparation, caustics necessitate the sample surface to be reflective, whereas photoelasticity can be applied only to transparent samples. Moreover, advanced imaging techniques like scanning electron microscopy (SEM) and atomic force microscopy (AFM) [264] are used for the detection and visualization of the morphological strain-induced deformations, at micro or nanoscale, however they do not provide quantitative information of the stress concentration close to an irregularity. Strain gauges are also widely used to provide direct measurements of strain, nevertheless not close to the discontinuity, as they measure strain over a larger area, capturing average strain across the gauge length. On the contrary, minute strain gauges are much smaller and can achieve higher resolution. However, their small size is accompanied by installation issues, as they require more careful handling and precise placement, as well as by higher cost and complexity, as they may need specialized equipment for accurate measurement and data acquisition [265]. Capacitive [266], [267] or resistive [268], [269] strain sensors transform the external applied strain into changes in the capacitance or the resistance of these components, respectively [270]. Unlike capacitive strain sensors, which suffer from very low sensitivity (Gauge Factor ≤ 1), resistive strain sensors are highly sensitive (Gauge Factor typically higher than 10), but they are difficult to calibrate due to their nonlinearity, and their sensing performance is less reversible upon dynamic loadings [271]. In addition, there are also optical strain sensors which rely on the measured light power difference as a result of

the change in transmission, caused by deformation [272], [273]. Fiber-optic strain gauges can achieve resolution (that may even be in the order of nanostrain [274]), and exhibit high sensitivity (in the order of pm/με)[275], being suitable for real-time monitoring applications of small strains [276]. It is important to consider that the attachment of the above-mentioned devices near a stress concentration site is an intrusive methodology, and the results obtained represent averages measured over the active area of the strain gauge (on the scale of millimetres). Therefore, in order to investigate the stress concentration around a defect, numerical techniques such as Finite Element Analysis (FEA) are employed to simulate the response of the defected material to mechanical stimulus [277].

A way to monitor stress distribution with high spatial resolution involves the use of Raman active materials, either as coatings or as additives. This technique relies on the sensitivity of the Raman peaks to the bond strain; in fact, due to the anharmonic nature of the chemical bonds and the consequent change of their force constant with interatomic separation, the Raman spectra of crystalline materials shift under the imposition of stress or strain [278]. Tension causes frequency downshift (phonon softening), while compression causes frequency upshift (phonon hardening). Galiotis et al. utilized in-situ Raman spectroscopy to measure strain distribution at the edge of a circular notch in a Kevlar 49 epoxy unidirectional composite laminate [279] by monitoring the wavenumber shift of the 1615 cm^{-1} peak attributed to the aromatic ring C-C stretching vibrational mode. Raman spectroscopy is a powerful technique for the estimation of stress and strain in graphene [280] and carbonaceous materials [281], and other high performance fibres [282]. In particular, due to its high intrinsic sensitivity upon external stimulation offered by its low dimension [283], [284], [278], graphene has been proposed as an effective strain sensor; for instance, strain sensing on large areas was performed by following the shift of 2D peak upon various cyclic deformation sequences [284]. Raman metrology on graphene also enabled to assess stress transfer characteristics in graphene/ polymer systems [285][286][287], to derive stress-strain curves for graphene flakes in tension and compression [288], to shed light on the relation between flake morphology and its properties [289][290].

4.2 Specimen fabrication

The synthesis of large-sized monolayer graphene sheets was conducted using the chemical vapor deposition (CVD) method, on a solid copper catalyst of 35 μm thickness and 99.95% purity from JX Nippon Mining & Metals®, in an AIXTRON® BlackMagic Pro CVD semi-industrial chamber (see **Figure 4.1(a)**). Before inserting the Cu foils into the chamber, they were cleaned with isopropanol, in order to remove any organic contaminants.

During the CVD process, the pressure inside the chamber was reduced to 0.1 mbar, while a mixture of Argon and Hydrogen gases was inserted in ratios of 250 sccm and 1000 sccm, respectively. The Cu foil was then annealed at 1070°C for 5 minutes. Followingly, the hydrogen flow was decreased to 960 sccm, while 10 sccm of methane was introduced as the carbon source for the growth of graphene on the copper surface. After 5 minutes at 1070°C, the hydrogen flow was stopped, while methane flow continued, and the chamber was slowly cooled to 650°C at a rate of 60°C/min, after which the methane flow was terminated. The Cu foil remained in an argon atmosphere until it cooled to 150°C, with a flow rate of 1000 sccm. The profile of temperature of the CVD process as a function of time is illustrated in **Figure 4.1b**.

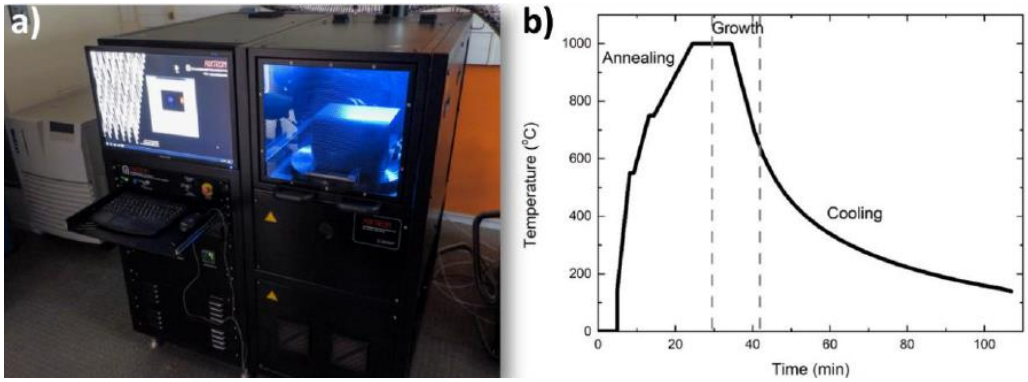


Figure 4.1: (a) AIXTRON BM Pro CVD reactor for graphene production on solid Cu, (b) Temperature evolution during the CVD method.

After the CVD growth, the graphene/Cu foils were cut into orthogonal (1 cm × 2 cm) shapes, and the wet transfer stage was followed. In specific, for the creation of the polymeric film to facilitate the graphene transfer onto the desirable transfer, a commercial solution of PMMA in anisole (Microchem 495K) was diluted at 3 wt%. A thin PMMA film was spin coated at 2500 rpm for 120 s onto CVD graphene grown on Cu foil, in order to form a homogenous protecting polymer layer, which was then

annealed at 120 ºC for 10 min so as to remove the solvent. Followingly, oxygen plasma was used to remove graphene from the backside of the Cu foil. Cu was then etched away by using a 0.15M ammonium persulfate solution and the floating PMMA – graphene stack was first rinsed with 3D water and then deposited onto a PMMA target substrate (Plexiglass, Rohm, slab with thickness ca. 1 mm), which had been formerly coated with a formvar (SP1-CHEM) ultra-thin film in order to improve graphene's adhesion [291]. Afterwards, the system was dried and heated at 40 ºC under vacuum for 30 min to remove possible trapped water molecules at the interface between graphene membrane and bulk polymer. In order to create a defect, a circular hole with a diameter of ~400 μm was induced by using a microdrill in the middle of each rectangular specimen with an overall length of 35 mm, a gauge length of 25 mm, and a width of 10 mm. The width to diameter ratio was equal to approximately 22, in order to avoid the contribution of the effects from the side edges [292]. A final annealing process at 120 ºC for an hour, under the application of a slight pressure, was performed to heal possible zones of weak adhesion at the interface created upon microdrilling. The procedure is depicted in **Figure 4.2**.

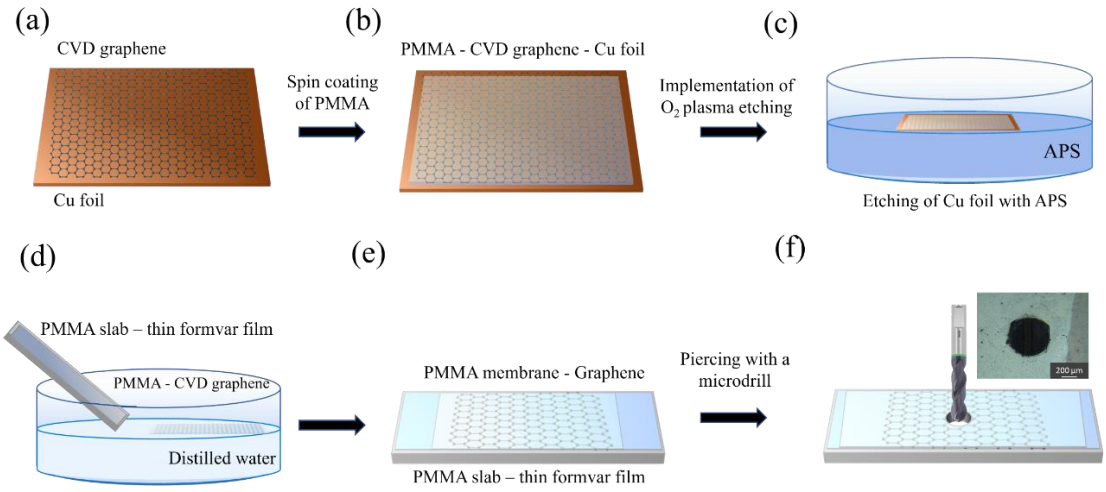


Figure 4.2: (a) CVD graphene on Cu substrate, (b) PMMA is spin-coated upon the CVD-Cu foil, (c) O2 plasma is employed for the removal of graphene at the back of the foil, and then Cu is etched via APS, (d) A PMMA sheet coated with a ultrathin film of formvar resin is inserted in the transfer device, (e) PMMA-coated graphene is finally deposited on the PMMA sheet, (f) Creation of the sub-mm defect (inset: top-view of the defect at the optical microscope).

4.2 Quality control of the CVD graphene membrane

The quality of graphene after deposition and micro-drilling was investigated by Raman spectroscopic mapping. Representative Raman spectra of the CVD graphene encapsulated in PMMA (black line) and of neat PMMA (red line) are shown in **Figure 4.3(a)**, where both spectra include the characteristic peaks of PMMA at ∼1450 cm^{-1} , ∼1730 cm^{-1} and ∼2952 cm^{-1} [293][294]. The successful deposition of the graphene monolayer on the PMMA slab is demonstrated by inspection of its Raman spectrum, i.e. the G and 2D peaks, and their homogeneous distributions (**Figure 4.3 (b-e)**) [208]. Specifically, from the statistical analysis of the Raman mappings (**Figure 4.4**), it is found that the average values of 2D peak position and FWHM are, respectively, 2613 cm^{-1} (see **Figure 4.3 (b)**) and 40 cm^{-1} (see **Figure 4.3(d)**), while the I_{2D}/I_G ratio is in average ~1.3 (**Figure 4.3(e)**), confirming the monolayer nature of the deposited graphene [295]. The position of the G peak at around 1591 cm^{-1} (**Figure 4.3(c)**) indicates that graphene experiences residual compression which can be attributed both to the transfer and to the annealing process that was performed to improve adhesion with the polymer. The presence of the D peak indicates the existence of defects in the edge region. The G and 2D peaks of graphene were fitted using single Lorentzian curves after background correction.

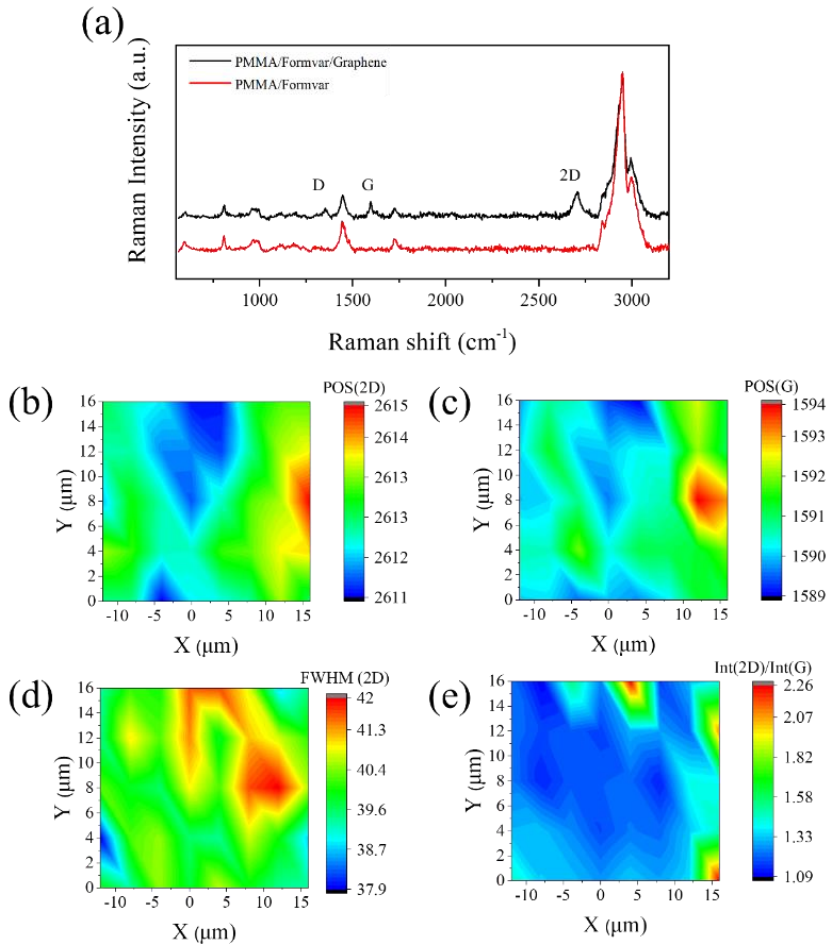


Figure 4.3: (a) Representative Raman spectra of PMMA coated with formvar resin and of CVD graphene-PMMA film deposited on the PMMA specimen, (b) Spatial contour mapping of the position of 2D, (c) G peaks, (d) 2D width, and (e) I(2D)/I(G) ratio.

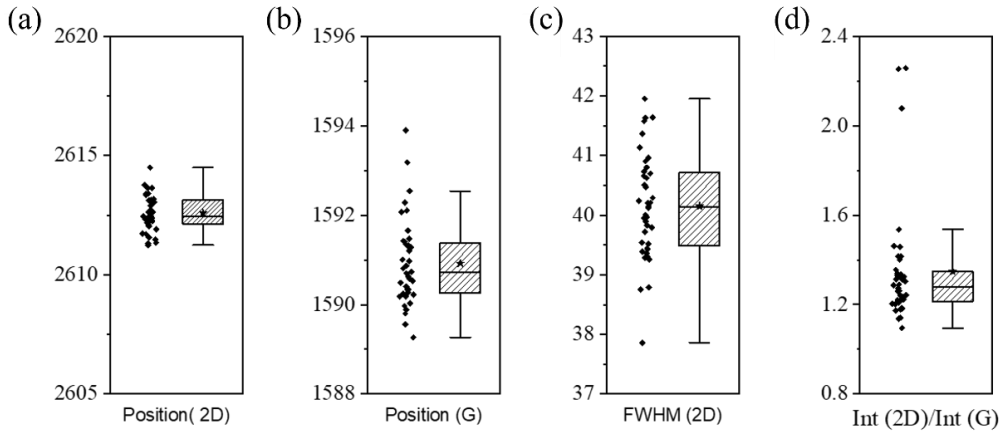


Figure 4.4: Box plots of (a) 2D peak position, (b) G peak position, (c) FWHM of 2D peak, and (d) ratio of the intensities of 2D and G peaks.

4.4 *In-situ* Raman spectroscopy combined with micro-tensile testing

The tensile tests were conducted with a micro-tensile tester (MT-200, Deben UK Ltd, Woolpit, UK), equipped with a 200 N loadcell, which was mounted onto Raman microscope stage (**Figure 4.5**). The rectangular specimens were loaded in tension in a quasistatic way, with a crosshead displacement speed of 0.2 mm min^{-1}. Tensile deformation was applied in steps of 0.5%, up to 2%. At each deformation, in-situ Raman line-mapping was conducted, starting from the edge of the hole and terminating 2 mm afar from it, perpendicular to the loading direction, in order to monitor the 2D peak's position shift. The spectra were acquired using a Raman microscope (InVia Renishaw) with a 1200 grooves/mm grating and a laser of 785 nm excitation wavelength, while the laser power was relatively low, equal to 1.1 mW, to avoid overheating of the specimen. The spot size of laser was ≈1 μm with 100× objective lens.

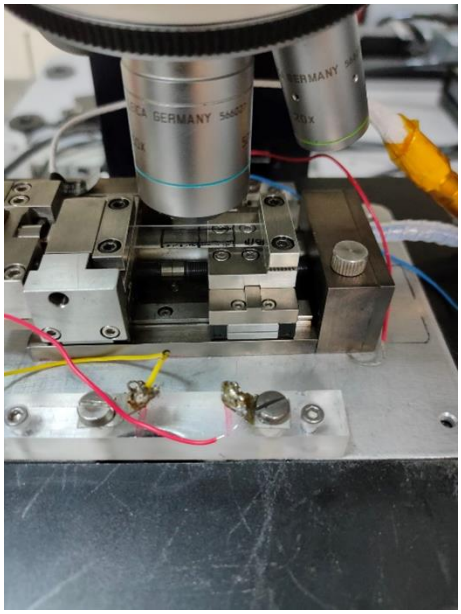


Figure 4.5: Deben micro-tester under Raman spectrometer for the in-situ tensile testing experiments.

A calibration curve has been preliminarily built to correlate the Raman wavenumber shift of graphene characteristic peak to the applied strain. To achieve this, the specimen was subjected to incremental uniaxial tensile strains up to 2.0%, in steps of 0.5%, and, simultaneously, Raman spectra were acquired several mm far from the notch. Specifically, by correlating the fitted position of the 2D peak (ω_{2D}) in the far field to the applied strain, a unique calibration curve was produced for the system at hand as it is presented in **Figure 4.6(b)**. In fact, it is well established that when graphene is subjected

to tension, phonon softening occurs and the 2D peak undergoes a redshift [210]. The linear shift of the 2D peak indicates that the interface is intact in the far field even at 2% of applied strain and this is attributed to the use of formvar as buffer layer to improve the adhesion between graphene sensor and the underlying PMMA specimen. The strain sensitivity is expressed by the slope of the linear fitting equation ($\partial\omega_{2D}/\partial\varepsilon$) and was calculated to be ≈ -15.9 cm^{-1}/%. This value is in line with reported strain sensitivities for similar CVD graphene/polymer systems [296]. As expected, it is smaller compared to the strain sensitivity determined experimentally for pristine graphene obtained via mechanical exfoliation (60 cm^{-1}/% [210]) and this has been attributed in previous studies to the wrinkled morphology of the CVD grown graphene [284][289].

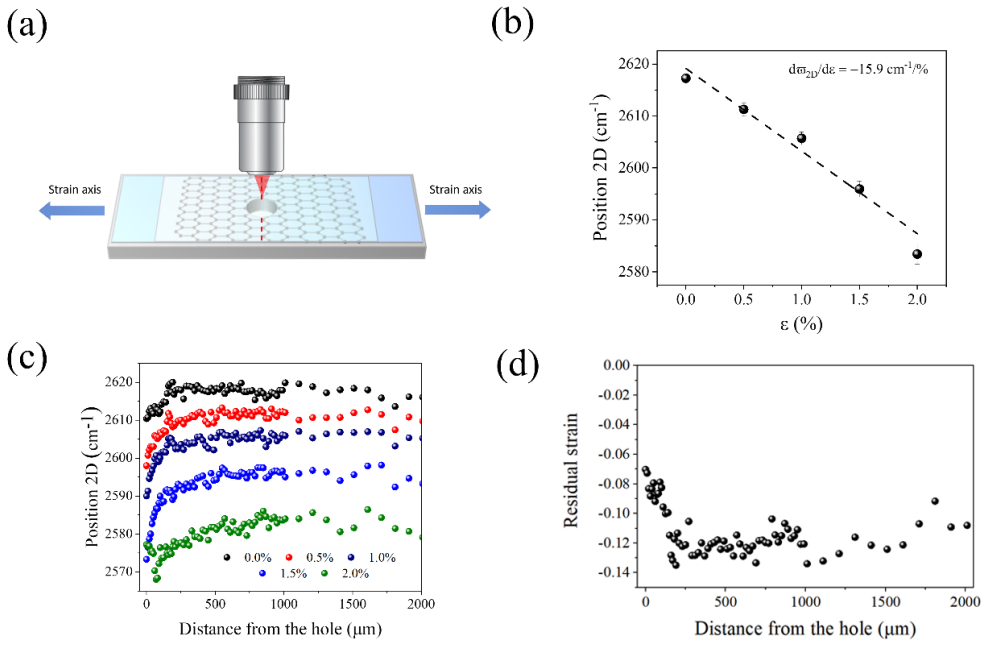


Figure 4.6: (a) Illustration of Raman mapping path and the load axis, (b) Shift of the 2D peak as a function of the applied strain far from the hole, (c) Position of 2D peak as a function of the distance from the hole, for several strain levels, and d) Profile of residual biaxial compression of graphene in unstrained configuration..

The strain distribution in the vicinity of the hole was investigated by performing, at each applied strain, a detailed 2 mm-long Raman line mapping, starting from the edge of the hole and perpendicular to the loading direction (as illustrated in **Figure 4.6(a)**). The position of the 2D peak as a function of the distance from the hole is plotted in **Figure 4.6(c)**, in the unstrained configuration and for each applied strain, and it evident

that ω_{2D} it is not constant over the mapping line. Specifically, the 2D peak in the vicinity of the hole is shifted at lower wavenumbers compared to the far-field zone, suggesting a higher strain field around the defect. In the unstrained configuration, the residual biaxial compression of graphene derived from transfer and annealing process can be estimated on the basis of the shift rate of the 2D peak for graphene flakes under biaxial deformations [287][297], being ~0.12% in the far field and gradually reducing to 0.07% at the notch root (**Figure 4.6(d)**). This trend can be ascribed to the gradual release of graphene residual compression derived from the drilling operation. Upon the application of the tensile deformation, the position of the 2D peak progressively red-shifts, while still dependent on the distance from hole. However, at 2.0% strain, a non-monotonic trend of ω_{2D} is observed; in fact, at the notch root, ω_{2D} is slightly blue-shifted compared to the position at 1.5% of applied strain, and then decreases linearly until a minimum is reached at ~70 μm far from it, thus suggesting a partial local adhesive failure between graphene sensor and PMMA. Afterwards, ω_{2D} increases until a plateau is reached as already observed in the previous steps.

The experimentally determined 2D peak position has been then converted into strain $\boldsymbol{\varepsilon(y)}$ using the calibration curve depicted in **Figure 4.8(b)**, according to the following equation:

$$\varepsilon(y) = \frac{\omega_{2D}|_{\varepsilon,y} - \omega_{2D}|_{\varepsilon=0\%,y}}{k_{2D}} \tag{4.1}$$

where $\omega_{2D}|_{\varepsilon,y}$ and $\omega_{2D}|_{\varepsilon=0\%,y}$ are the positions of the 2D peak at the same measured point y at applied strain ε and at $\varepsilon = 0\%$, respectively; $k_{2D}$is the strain sensitivity obtained from the calibration curve shown in **Figure 4.6(b)**.

In **Figure 4.9(a)**, the strain distributions around the hole are presented for each applied strain. As expected, the strain is maximum in the vicinity of the hole, with the maximum values recorded at 0.85%, 1.27%, and 2.14% for 0.5%, 1.0% and 1.5%, respectively, and then decays in a non-linear manner, until a plateau value is reached at more than 500 μm far from the defect. In the case of 2.0% external applied strain, close to the edge of the defect, the strain of the graphene is 1.94%, whilst 70 μm further from the edge rises at 2.48%, and then follows the same behaviour as in the previous cases. Optical inspection of the specimen stretched at 2%, in the neighborhood of the hole, reveals the

presence of microcracks and local delamination at the edge of the notch (see **Figure 4.7**Σφάλμα! Το αρχείο προέλευσης της αναφοράς δεν βρέθηκε.). Potential solutions for the improvement of the polymer/graphene interface could involve functionalization routes [298] and surface treatments to enhance adhesion [299].

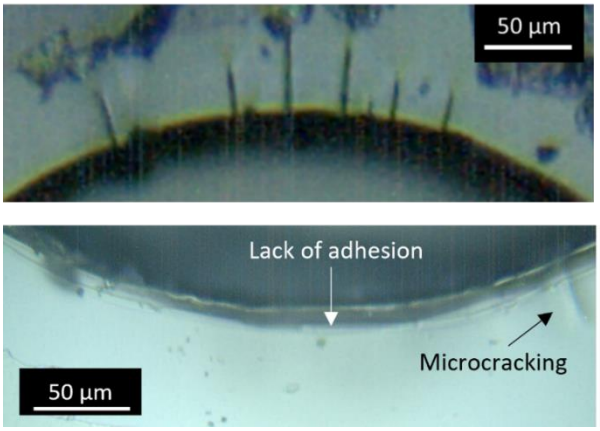


Figure 4.7: Optical images of the area at the vicinity of the hole, after the sample has been subjected to 2.0% applied strain.

It is important to note here that the proposed graphene-based sensor enables strain measurements with high resolution. Actually, the spatial resolution of such measurements is only limited by the wavelength of the incident laser beam and the optical arrangement used to focus the beam onto the specimen. Therefore, the spatial resolution of the proposed sensor is considered to be approximately of the order of the diffraction limit, which is ~500 nm for the Raman system adopted in this study and previous attempts from some of the authors [286]. Another important parameter is the strain resolution of the proposed graphene-based sensor, defined as the smallest difference in relative strain that it can measure, which can be calculated as [284]:

$$Resolution\ (\mu\varepsilon) = \frac{Resolution\ of\ the\ Raman\ spectrometer\ (cm^{-1})}{Raman\ strain\ sensitivity\ \left(\frac{cm^{-1}}{\%strain}\right)} \times 10000 \qquad (4.2)$$

By considering that the resolution of the measured wavenumber shift can be estimated at 0.1 cm^{-1} and that the Raman strain sensitivity of the system under investigation is 15.9 $cm^{-1}/\%$, the resolution of the proposed graphene-based sensor is of ~ ±62 με.

The stress distribution was then derived using Hooke's law, assuming that the PMMA adopted in this study has a linear elastic behaviour with a Young's modulus *E* of 1.75 GPa (see **Figure 4.8**).

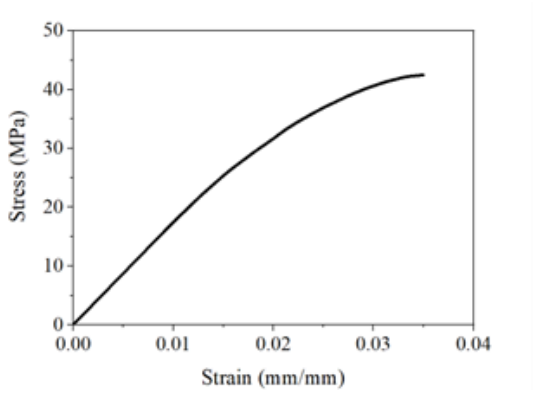


Figure 4.8: Stress-strain curve for the PMMA.

The stress profiles are depicted in **Figure 4.9(b)**, showing obviously the same behaviour as strain does, with the maximum stress recorded at 15 MPa, 22.4 MPa and 37.6 MPa for 0.5%, 1.0% and 1.5%, respectively, suggesting that the area close to the hole is more favorable for the creation of a possible crack. The case of 2.0% external applied strain was not considered, as Hooke's law is not valid in the non-elastic region.

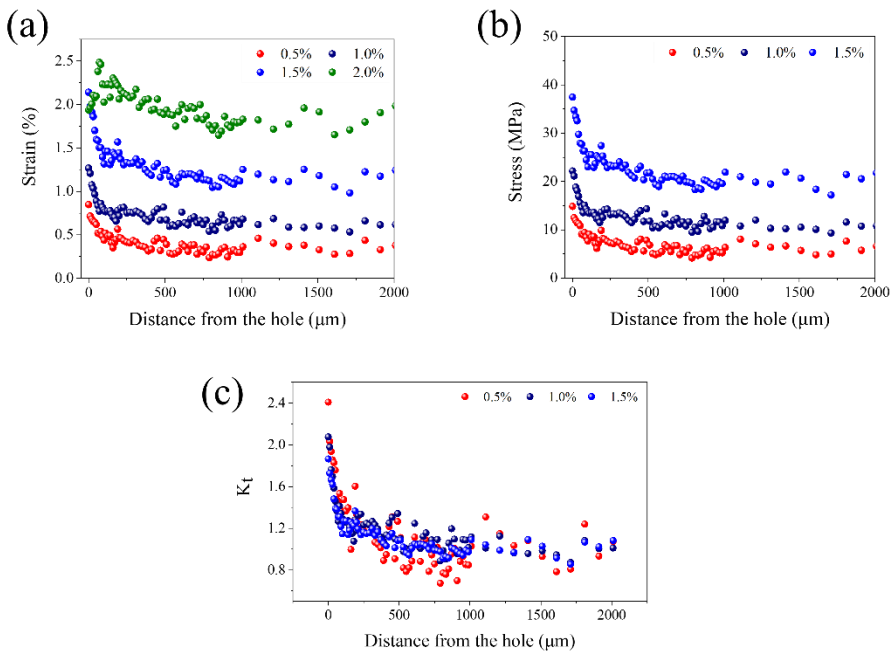


Figure 4.9: (a) Distribution of the actual strain and (b) Distribution of the stress at various levels of applied strain as a function of the distance from the hole perpendicular to the load direction. (c) Stress concentration factor for various external applied strains as a function of the distance from the hole perpendicular to the load direction.

The stress concentration observed around a defect is quantified by the factor K_T , which is defined as the ratio of the highest stress (σ_{max}) to the far-field stress (σ_∞) on the axis

normal to the applied load for a finite plate: $K_t = \sigma_{max}/\sigma_\infty$ [279]. As can be seen in **Figure 4.9(c)**, the maximum K_T value is calculated at 2.41, 2.08, and 1.86 for 0.5%, 1% and 1.5% applied strain, respectively. As the distance from the hole increases, K_t drops abruptly in all cases. As the stress concentration factor records its maximum value close to the hole and then diminishes gradually, it is certain that this will be the initiating point of a future crack. K_t drops as the applied strain increases; this can be ascribed to possible minor damage propagation (e.g. crazing [300] and microcracking) resulting from the very high values of stress concentration to which the material is subjected near the notch, as already demonstrated by Aryjal et al. [279], or lack of the interface (see **Figure 4.7**).

The strain distribution around a circular hole in an infinite plate subjected to tensile loading can be described analytically, using equations derived from the classical elasticity theory. Specifically, the typical equilibrium equations of an isotropic material are given by generalized Hooke's law equations (absence of body forces):

$$\frac{\partial \sigma_{xx}}{\partial x} + \frac{\partial \sigma_{xy}}{\partial x} = 0 \quad (4.3a)$$

$$\frac{\partial \sigma_{xy}}{\partial x} + \frac{\partial \sigma_{yy}}{\partial y} = 0 \quad (4.3b)$$

Under generalized plane stress state, the above equations can be satisfied by using the Airy' s stress function $\varphi(x, y)$. The stress components can be expressed as:

$$\sigma_{xx} = \frac{\partial^2 \varphi}{\partial y^2} \quad (4.4a)$$

$$\sigma_{yy} = \frac{\partial^2 \varphi}{\partial x^2} \quad (4.4b)$$

$$\sigma_{xy} = -\frac{\partial^2 \varphi}{\partial x \partial y} \quad (4.4c)$$

The compatibility conditions for strains, assuming there are no body forces, must be satisfied as follows:

$$\nabla^2(\sigma_{xx} + \sigma_{yy}) = \left(\frac{\partial^2}{\partial x^2} + \frac{\partial^2}{\partial y^2}\right)(\sigma_{xx} + \sigma_{yy}) = 0 \quad (4.5)$$

Where ∇^2 is the Laplace operator.

The symmetry of our system allows the use of polar coordinates, therefore from now on, polar coordinates will be considered.

$$\sigma_{rr} = \sigma_{xx}|_{\theta=0} = \left.\frac{\partial^2\varphi}{\partial y^2}\right|_{\theta=0} = \frac{1}{r}\frac{\partial\varphi}{\partial r} + \frac{1}{\mathrm{r}^2}\frac{\partial^2\varphi}{\partial\theta^2} \quad (4.6a)$$

$$\sigma_{\theta\theta} = \sigma_{yy}\big|_{\theta=0} = \left.\frac{\partial^2\varphi}{\partial x^2}\right|_{\theta=0} = \frac{\partial^2\varphi}{\partial r^2} \quad (4.6b)$$

$$\sigma_{r\theta} = \sigma_{xy}\big|_{\theta=0} = -\left.\frac{\partial^2\varphi}{\partial x\partial y}\right|_{\theta=0} = -\frac{\partial}{\partial x}\left(\frac{\partial\varphi}{\partial y}\right)$$

$$= -\left[\frac{\partial}{\partial r}\cos\theta - \frac{\sin\theta}{r}\frac{\partial}{\partial\theta}\right]\left[\frac{\partial\varphi}{\partial r}\sin\theta + \frac{\cos\theta}{r}\frac{\partial\varphi}{\partial\theta}\right]$$

$$= -\left[\frac{\partial^2\varphi}{\partial r^2}\sin\theta\cos\theta + \frac{\cos^2\theta}{r}\left(\frac{\partial^2\varphi}{\partial r\partial\theta} - \frac{1}{r}\frac{\partial\varphi}{\partial\theta}\right)\right.$$

$$\left. - \frac{\sin\theta}{r}\left(\frac{\partial^2\varphi}{\partial r\partial\theta}\sin\theta + \frac{\partial\varphi}{\partial r}\cos\theta\right) - \frac{\sin\theta}{\mathrm{r}^2}\left(\frac{\partial^2\varphi}{\partial\theta^2}\cos\theta - \frac{\partial\varphi}{\partial\theta}\sin\theta\right)\right] \Longrightarrow$$

$$\sigma_{r\theta} = \frac{1}{\mathrm{r}^2}\frac{\partial\varphi}{\partial\theta} - \frac{1}{r}\frac{\partial^2\varphi}{\partial r\partial\theta} \quad (4.6c)$$

Considering the uniaxial stress, the boundary conditions far from the hole can be written in cartesian coordinates as:

$$\sigma_{xx}(x\to\infty, y) = \sigma_\infty \quad (4.7a)$$

$$\sigma_{yy}(x\to\infty, y) = 0 \quad (4.7b)$$

$$\sigma_{xy}(x\to\infty, y) = 0 \quad (4.7c)$$

So, far from the hole $(r\to\infty, \theta)$ after transformation to polar coordinates, we have:

$$\sigma_{rr}(r\to\infty, \theta) = \frac{\sigma_{xx}+\sigma_{yy}}{2} + \left(\frac{\sigma_{xx}-\sigma_{yy}}{2}\right)\cos 2\theta + \sigma_{xy}\sin 2\theta \Longrightarrow$$

$$\sigma_{rr}(r\to\infty, \theta) = \frac{\sigma_\infty}{2} + \frac{\sigma_\infty}{2}\cos 2\theta \quad (4.8a)$$

$$\sigma_{\theta\theta}(r\to\infty, \theta) = \frac{\sigma_{xx}+\sigma_{yy}}{2} - \left(\frac{\sigma_{xx}-\sigma_{yy}}{2}\right)\cos 2\theta - \sigma_{xy}\sin 2\theta \Longrightarrow$$

$$\sigma_{\theta\theta}(r \to \infty, \theta) = \frac{\sigma_\infty}{2} - \frac{\sigma_\infty}{2}\cos 2\theta \quad (4.8b)$$

$$\sigma_{r\theta}(r \to \infty, \theta) = -\left(\frac{\sigma_{xx} - \sigma_{yy}}{2}\right)\sin 2\theta + \sigma_{xy}\cos 2\theta \Longrightarrow$$

$$\sigma_{r\theta}(r \to \infty, \theta) = -\frac{\sigma_\infty}{2}\sin 2\theta \quad (4.8c)$$

Nevertheless, the system is subjected to a remote bi-axial loading state at $r \to \infty$, so the boundary conditions can be expressed as:

$$\sigma_{rr}(r \to \infty, \theta) = \frac{\sigma_\infty}{2} \quad (4.9a)$$

$$\sigma_{\theta\theta}(r \to \infty, \theta) = \frac{\sigma_\infty}{2} \quad (4.9b)$$

At the hole $(r = a, \theta)$, the radial and the shear stresses are equal to 0, while there is no condition required for the tangential stress. So the boundary conditions for this case are:

$$\sigma_{rr}(r = \alpha, \theta) = 0 \quad (4.10c)$$

$$\sigma_{r\theta}(r = \alpha, \theta) = 0 \quad (4.10d)$$

In the case of an axisymmetric stress distribution, all derivatives of θ vanish, as there is no dependance of the field variables upon it. So, the equation for $\varphi(r)$, in polar coordinates can be written as:

$$\varphi(r) = C_1 + C_2 \log r + C_3 \mathrm{r}^2 + C_4 \mathrm{r}^2 \log r \quad (4.11)$$

The stress components can be expressed as follows:

$$\sigma_{rr} = \frac{1}{r}\frac{\partial \varphi}{\partial r} = \frac{C_2}{\mathrm{r}^2} + 2C_3 + C_4(2\log r + 1) \quad (4.12a)$$

$$\sigma_{\theta\theta} = \frac{\partial^2 \varphi}{\partial r^2} = -\frac{C_2}{\mathrm{r}^2} + 2C_3 + C_4(2\log r + 3) \quad (4.12b)$$

$$\sigma_{r\theta} = 0\,, due\ to\ symmetry \quad (4.12c)$$

The boundary conditions in this case are $(4.9a,\ 4.9c)$. The general solution must support finite stresses at $r \to \infty$, so $C_4 = 0$, while $C_2, C_3 \neq 0$. So, by applying the boundary conditions we can estimate the coefficients:

$$\sigma_{rr}(r \to \infty) = 2C_3 = \frac{\sigma_\infty}{2} \Longrightarrow C_3 = \frac{\sigma_\infty}{4} \qquad (4.13a)$$

$$\sigma_{rr}(r = a) = \frac{C_2}{a^2} + \frac{\sigma_\infty}{2} = 0 \Longrightarrow C_2 = -a^2\frac{\sigma_\infty}{2} \quad (4.13b)$$

So, the solutions for the stress equations are:

$$\sigma_{rr,axisymmetrix} = \frac{\sigma_\infty}{2}\left[1 - \left(\frac{a}{r}\right)^2\right] \quad (4.14a)$$

$$\sigma_{\theta\theta,axisymmetric} = \frac{\sigma_\infty}{2}\left[1 + \left(\frac{a}{r}\right)^2\right] \quad (4.14b)$$

$$\sigma_{r\theta,axisymmetric} = 0 \qquad (4.14c)$$

In the case where there is θ dependency, the homogeneous biharmonic operation in polar coordinates is:

$$\nabla^4\varphi = \frac{\partial^4\varphi}{\partial\theta^4} + \frac{2}{\mathrm{r}^2}\frac{\partial^4\varphi}{\partial r^2\partial\theta^2} + \frac{1}{\mathrm{r}^4}\frac{\partial^4\varphi}{\partial\theta^4} + \frac{2}{r}\frac{\partial^3\varphi}{\partial r^3}$$

$$-\frac{2}{\mathrm{r}^3}\frac{\partial^3\varphi}{\partial r\partial\theta^2} - \frac{1}{\mathrm{r}^2}\frac{\partial^2\varphi}{\partial r^2} + \frac{4}{\mathrm{r}^4}\frac{\partial^4\varphi}{\partial\theta^4} + \frac{1}{r}\frac{\partial^3\varphi}{\partial r^3} \quad (4.15)$$

Due to the θ periodicity, the solution of the above equation can be assumed to be:

$$\varphi(r,\theta) = g(r)\cos 2\theta \quad (4.16)$$

So, the biharmonic equation becomes:

$$\nabla^4\varphi = \left(\frac{d^4g}{dr^4} + \frac{2}{r}\frac{d^3g}{dr^3} - \frac{9}{\mathrm{r}^2}\frac{d^2g}{dr^2} + \frac{9}{\mathrm{r}^3}\frac{dg}{dr}\right)\cos 2\theta = 0 \quad (4.17)$$

This expression can be valid if

$$\frac{d^4g}{dr^4} + \frac{2}{r}\frac{d^3g}{dr^3} - \frac{9}{\mathrm{r}^2}\frac{d^2g}{dr^2} + \frac{9}{\mathrm{r}^3}\frac{dg}{dr} = 0 \quad (4.18)$$

The solution given for the above differential equation is:

$$g(r) = C_1 + C_2\mathrm{r}^2 + C_3\mathrm{r}^4 + \frac{C_4}{\mathrm{r}^2} \quad (4.19)$$

By replacing $g(r)$ into the expression for $\varphi(r,\theta)$,

$$\varphi(r,\theta) = \left(C_1 + C_2 \mathrm{r}^2 + C_3 \mathrm{r}^4 + \frac{C_4}{\mathrm{r}^2}\right)\cos 2\theta \quad (4.20)$$

Introducing (17) into equations $(4.a-c)$, the stress components are:

$$\sigma_{rr,non\ axisymmetric}(r,\theta) = -\left(2C_2 + 4\frac{C_1}{\mathrm{r}^2} + 6\frac{C_4}{\mathrm{r}^4}\right)\cos 2\theta \quad (4.21a)$$

$$\sigma_{\theta\theta,non\ axisymmetric}(r,\theta) = \left(2C_2 + 12C_3\mathrm{r}^2 + 6\frac{C_4}{\mathrm{r}^4}\right)\cos 2\theta \quad (4.21b)$$

$$\sigma_{r\theta,non\ axisymmetric}(r,\theta) = \left(2C_2 + 6C_3\mathrm{r}^2 - 2\frac{C_1}{\mathrm{r}^2} - 6\frac{C_4}{\mathrm{r}^4}\right)\sin 2\theta \quad (4.21c)$$

The values for the constants can occur by employing the boundary condition far from the hole $(r \to \infty, \theta)$,

$$C_1 = \sigma_\infty \frac{a^2}{2} \quad (4.22a)$$

$$C_2 = -\frac{\sigma_\infty}{4} \quad (4.22b)$$

$$C_3 = 0 \quad (4.22c)$$

$$C_4 = -\sigma_\infty \frac{a^4}{4} \quad (4.22d)$$

Whereas, at the hole $(r = a, \theta)$:

$$2C_2 + 4\frac{C_1}{\mathrm{a}^2} + 6\frac{C_4}{\mathrm{a}^4} = 0 \quad (4.23a)$$

$$2C_2 - 2\frac{C_1}{\mathrm{a}^2} - 6\frac{C_4}{\mathrm{a}^4} = 0 \quad (4.23b)$$

By replacing the constants,

$$\sigma_{rr,non\ axisymmetric} = \frac{\sigma_\infty}{2}\left(1 - 4\left(\frac{a}{r}\right)^2 + 3\left(\frac{a}{r}\right)^4\right)\cos 2\theta \quad (4.24a)$$

$$\sigma_{\theta\theta,non\ axisymmetric} = -\frac{\sigma_\infty}{2}\left(1 + 3\left(\frac{a}{r}\right)^4\right)\cos 2\theta \quad (4.24b)$$

$$\sigma_{r\theta,non\ axisymmetric} = -\frac{\sigma_\infty}{2}\left(1 + 2\left(\frac{a}{r}\right)^2 - 3\left(\frac{a}{r}\right)^4\right)\sin 2\theta \quad (4.24c)$$

So, the complete stress field is given by the equations:

$$\sigma_{rr} = \sigma_{rr,axisymmetrix} + \sigma_{rr,non\ axisymmetric}$$
$$= \frac{\sigma_\infty}{2}\left(1 - \left(\frac{a}{r}\right)^2\right) + \frac{\sigma_\infty}{2}\left(1 - 4\left(\frac{a}{r}\right)^2 + 3\left(\frac{a}{r}\right)^4\right)\cos 2\theta \quad (4.25a)$$

$$\sigma_{\theta\theta} = \sigma_{\theta\theta,axisymmetric} + \sigma_{\theta\theta,non\ axisymmetric}$$
$$= \frac{\sigma_\infty}{2}\left(1 + \left(\frac{a}{r}\right)^2\right) - \frac{\sigma_\infty}{2}\left(1 + 3\left(\frac{a}{r}\right)^4\right)\cos 2\theta \quad (4.25b)$$

$$\sigma_{r\theta} = \sigma_{r\theta,axisymmetric} + \sigma_{r\theta,non\ axisymmetric}$$
$$= -\frac{\sigma_\infty}{2}\left(1 + 2\left(\frac{a}{r}\right)^2 - 3\left(\frac{a}{r}\right)^4\right)\sin 2\theta \quad (4.25c)$$

Where σ_{rr} is the radial stress, $\sigma_{\theta\theta}$ is the tangential stress, $\sigma_{r\theta}$ is the shear stress, σ_∞ is the remote stress, a is the hole radius, r is the radial coordinate and θ is the polar angle.

Figure 4.10(a) illustrates the theoretically obtained stress distribution profile around a circular hole in the specimen under external strains of 0.5%, 1.0%, and 1.5%. The highest stress occurs at the edge of the notch, measuring 18.7 MPa, 32.8 MPa, and 60.8 MPafor the respective strain levels. The stress values obtained are higher than those derived experimentally, which can be attributed to the deficiencies of the theoretical approach which assumes perfect adhesion between the two constituents. In all cases, the stress decreases with distance from the hole, reaching a plateau approximately 500 μm away. Similarly, the stress concentration factor in the case of 0.5%, in which K_t value presents its higher value experimentally, exhibits the same trend as the stress, displaying a maximum value of 2.96 at the hole's edge and then decreases until it reaches a plateau (**Figure 4.10 (b)**). Comparing the stress concentration factor, obtained both experimentally and analytically, it appears that both follow the same profile behaviour, exhibiting a minor deviation in the maximum K_t value (**Figure 4.10 (c)**). This can be attributed to the fact that even though PMMA is a material considered linear elastic at low strains, it may exhibit some degree of plasticity due to the high stress close to the hole, leading to a lower K_t value compared to the one derived from the analytical model.

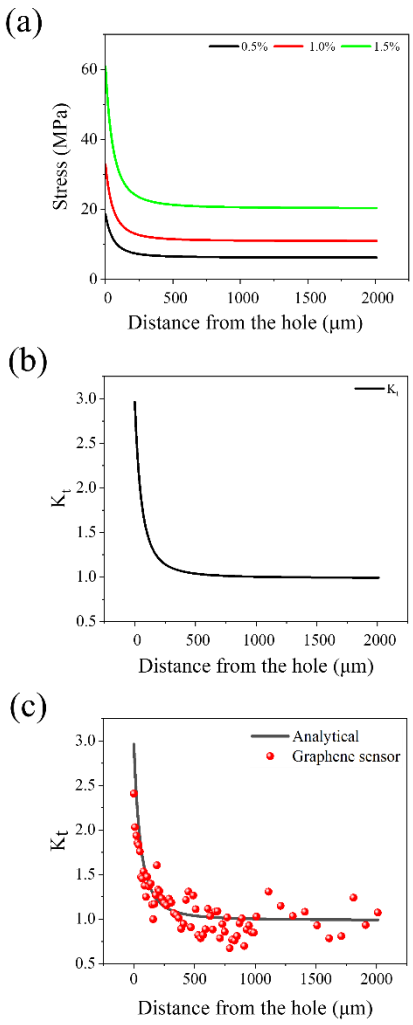


Figure 4.10: (a) Analytically extracted distribution of stress on the tensile axis, at various levels of applied strain as a function of the distance from the hole, (b) Stress concentration factor as a function of the distance from the hole perpendicular to the load direction, and, (c) Comparison between stress concentration factor obtained from the analytically derived expressions of stress $\sigma_{\theta\theta}$ and experimental Raman data, as a function of the distance from the hole perpendicular to the load direction.

A Finite Element Analysis (FEA) based on Abaqus computational package was conducted, in order to precisely quantify the stress distribution around the circular hole with less time-consuming and equally precise means. Considering FEA, both the substrate and the graphene were considered isotropic materials with elastic properties, with Young's moduli of 1.75 GPa [301] and 1 TPa [127] respectively, whereas their corresponding Poisson ratios were 0.3 [302] and 0.165 [301]. Given the small thickness of the specimen compared to its other dimensions, plane stress conditions were assumed for the analysis. In such a configuration, the stresses in the plane, particularly the longitudinal stresses, are dominant, while the stress through the thickness can be

considered negligible. As a result, the specimen was modelled in 2D to focus on the in-plane stresses, simplifying the analysis while still capturing the critical mechanical behaviour relevant to uniaxial stress loading [303]. Each part was meshed with 4-node, 2-dimensional, nonlinear, quadrilateral shell elements with reduced integration. A dense mesh around the vicinity of the whole was implemented, resulting in a total of 10548 elements (4284 elements for graphene part and 6264 elements for the substrate part) (see **Figure 4.11**).

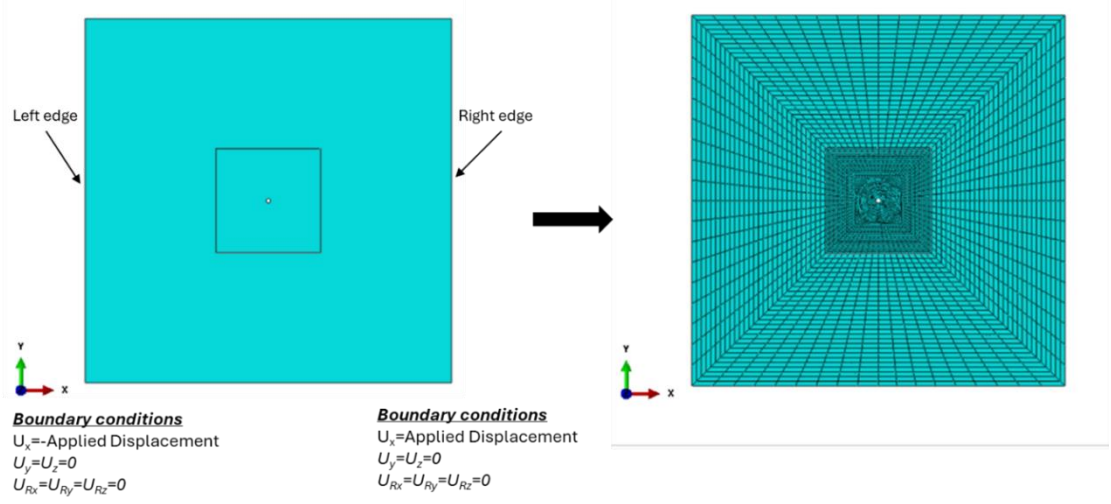


Figure 4.11: FEA geometry, mesh definition and boundary conditions.

The specimen was subjected to uniaxial displacement, conducting a two-dimensional analysis. A 4-node, 2-dimensional, nonlinear shell element type was used and Python scripting through Abaqus was implemented to generate the structures with 400 μm hole diameter and the external applied displacements, in accordance with the experiments.

The contour plots of the axial stress present the same behaviour for each external applied strain, thus in **Figure 4.12(a)** an indicative stress contour plot is presented for the case of 0.5% external applied strain. It can be noticed that the same values of axial stress are developed on each side of the hole, with the maximum stress occurring at the edge of the notch. Finally, it is quite evident that the stress decays dramatically as we move far from the notch, in the perpendicular direction of the applied strain. **Figure 4.12(b)** shows the stress distribution profile around the circular hole of the specimen for 0.5%, 1.0%, and 1.5% external strain. It is observed that the maximum value of stress is located at the edge of the notch and equals to 20.3, 40.7, and 61.0 MPa for 0.5%, 1.0%, and 1.5% applied strain, respectively. The higher stress values compared to the experimentally derived ones can be attributed to the assumption of perfect

interface between bulk PMMA and PMMA/graphene membrane. Furthermore, a stress decay is observed in all cases, reaching a plateau, at a distance of 500 μm far from the hole. The stress concentration factor follows the same behaviour as stress, with the maximum value being 2.52 at the edge of the hole and then decay dramatically until reaching a plateau (**Figure 4.12(c)**).

It is clear that the profile of the stress concentration factor, obtained experimentally through the elaboration of the Raman data, and numerically via FEA (see **Figure 4.12(d)**), exhibit not only the same profile behaviour but also the same values, as almost the same K_t value is recorded at the edge of the defect. This result is particularly significant, as the experimental monitoring of the stress distribution across a defect is quite difficult and challenging, and therefore, the approach to this problem, until now is mainly numerical [277]. The herein obtained stress concentration factor of 2.41 (for the case of 0.5% applied strain) agrees to previous studies in literature on PMMA, i.e. the implementation of DIC combined with FEA, where a stress concentration factor of 2.38 was reported [258]. Generally, the stress concentration at areas close to defects is not measured directly via an experimental method, but rely on the combination of an experimental method with FEA, or the study is conducted solely through FEA, as no experimental method can approach the point of increased stress concentration. The difference between these studies and the present study lies on the fact that there no need of combination of the experimental and the numerical technique, but FEA are used only for the validation of experimental results. Furthermore, it is worth noting that in the case of FEA implementation, the adhesion between PMMA and graphene is perfect, and there are not any interface issues, in comparison with the experimental one, which indicates that despite the practical difficulties, graphene can be perfectly used as a strain sensor for polymers. However, it is worth mentioning that this case is valid for low external applied strains, as at higher ones the interface issues start playing a significant role at the response of the system, up to an external strain of 2.0% where there is a lack of adhesion between the sensor and the polymer at the vicinity of the defect. This further proves the reliability of the proposed method and encourages the use of graphene sensors in the investigation of stress concentration in other polymers and composites.

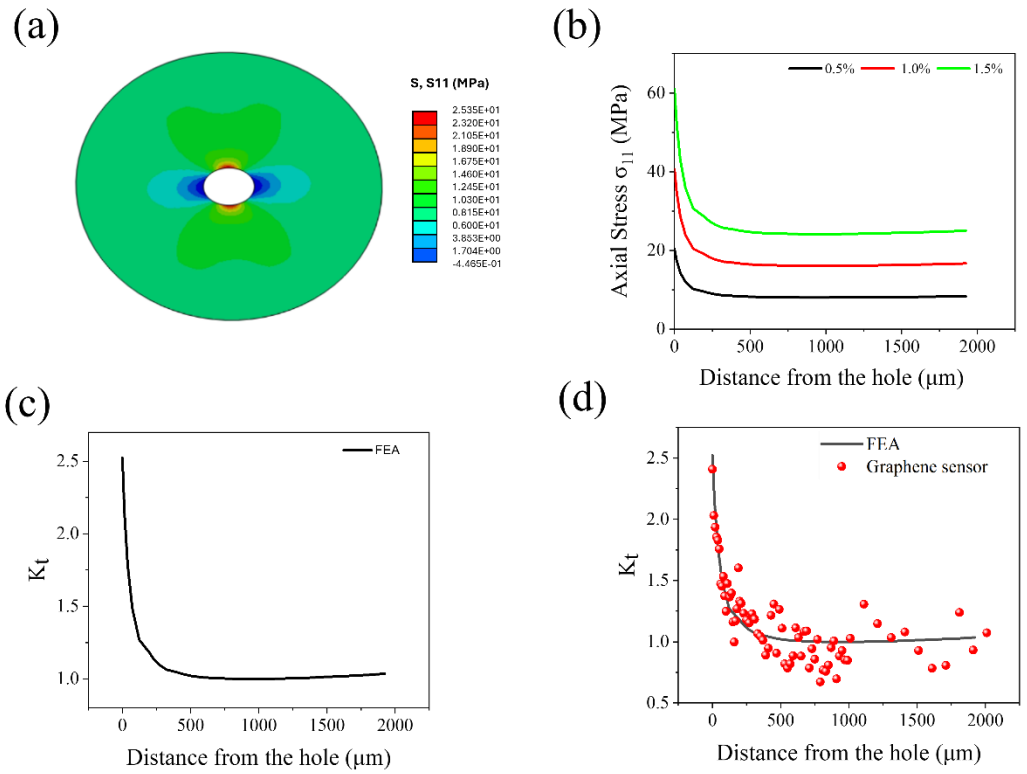


Figure 4.12: (a) Stress contour plot for 0.5% external applied strain, (b) Theoretically predicted distribution of stress on the tensile axis, at various levels of applied strain as a function of the distance from the hole, (c) Stress concentration factor as a function of the distance from the hole perpendicular to the load direction and (d) Comparison between stress concentration factor obtained from FEA and experimental Raman data (for an applied strain of 0.5%), as a function of the distance from the hole perpendicular to the load direction.

Comparing the K_t extracted experimentally, analytically and numerically, for the case of 0.5% applied strain, it is evident that it presents the same profile trend, with minor deviations in its maximum value **(Figure 4.13)**. This can be attributed to the fact that in general, theoretical models provide a more simplified view and do not consider the complexities of real-world materials.

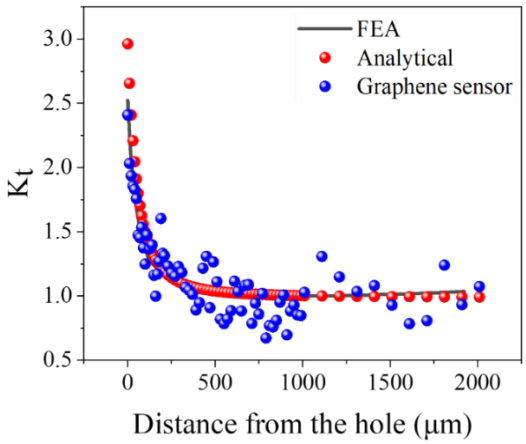


Figure 4.13: Comparison between stress concentration factor obtained from FEA, analytical expressions and experimental Raman data, as a function of the distance from the hole perpendicular to the load direction.

4.5 Conclusion

The use of CVD graphene as sensor for monitoring the strain/stress distributions around a defect in a polymer subjected to uniaxial tensile loading has been showcased. Owing to the strain sensitivity of the 2D Raman peak of graphene, it is possible to gain quantitative insight on the stress distribution around a defect with sub-micron spatial resolution. Herein, the stress concentration factor for PMMA at the lowest applied strain was calculated to be 2.41, which lies remarkable close to the values of 2.52 and 2.96 derived from Finite Element Analysis and analytical expressions, respectively, and other studies in the literature for similar systems.

Considering the above, the use of cm-size graphene grown by Chemical Vapour Deposition (CVD) to assess the stress concentration around a sub-mm scale circular defect in a polymeric material, by exploiting in-situ micro-Raman spectroscopy combined with tensile testing has proven to be a successful approach experimentally, verified by numerical simulations. Thus, this technique combination can be reliable in the assessment of stress concentration in polymers, or other materials such as graphene-based nanocomposites, in which graphene can act both as a sensor and as a reinforcing filler.

5. Fracture toughness of graphene-PMMA nanolaminates

This chapter deals with the study of fracture mechanisms in a novel class of graphene nanocomposites, the CVD graphene/polymer nanolaminates, when subjected to tension. The incorporation of continuous CVD graphene monolayer into nanolaminates has been demonstrated to be effective towards the increase of Young's modulus and tensile strength of polymer matrix [192]. Their exceptional mechanical properties alongside with their multifunctionality render them highly valuable for a wide range of demanding high-performance applications [52] (i.e. as gas barriers [192], for sensing applications [304], for EMI shielding [32], in electronic applications [305], as strain sensors [306], etc.). Therefore, understanding the fracture behaviour of this class of materials is necessary for their integration into advanced engineering applications. Herein, CVD graphene-based nanolaminates of different graphene content were produced via the iterative lift-off/float-on procedure [32]. In order to study their fracture behaviour, a hole-shaped defect was induced at the centre of the specimens as described in the following section. Next, a thorough investigation of the nanocomposites' fracture behaviour was conducted by in-situ monitoring the mechanical loading of the nanolaminate with a high-resolution camera. As will be shown, this method revealed useful information over the microcrack formation and eventually the fracture toughness of the nanocomposite. SEM was also used in order to garner insight over crack path initiation from the induced defect. Moreover, in-situ Raman spectroscopy was combined with the micromechanical testing of graphene-based nanolaminates in order to provide information over the fracture procedure and to derive fracture parameters, such as the Stress Concentration Factor (SCF – described in Chapter 2), or the maximum stress that these nanocomposites can withstand near the defect.

5.1 Fabrication of PMMA/CVD graphene nanolaminates

For the production of ultrathin PMMA films, commercially available solutions of PMMA in anisole (Microchem 495K A6, Microchem Corp., Erlenbach, Switzerland) of various concentrations were employed. The fabrication of the polymeric layers on top of the substrates of interest was conducted via a spin-coating technique. Spin

coating is a widely used, straightforward method which enables the production of uniform polymeric films on top of flat surfaces, with thickness spanning from a few nanometers to microns. The process involves the deposition of a small amount of the polymer solution at the centre of a flat surface, and then its rotation at high speed (static dispense), in order to spread the polymeric liquid across the surface by the generated centrifugal force (see **Figure 5.1**).

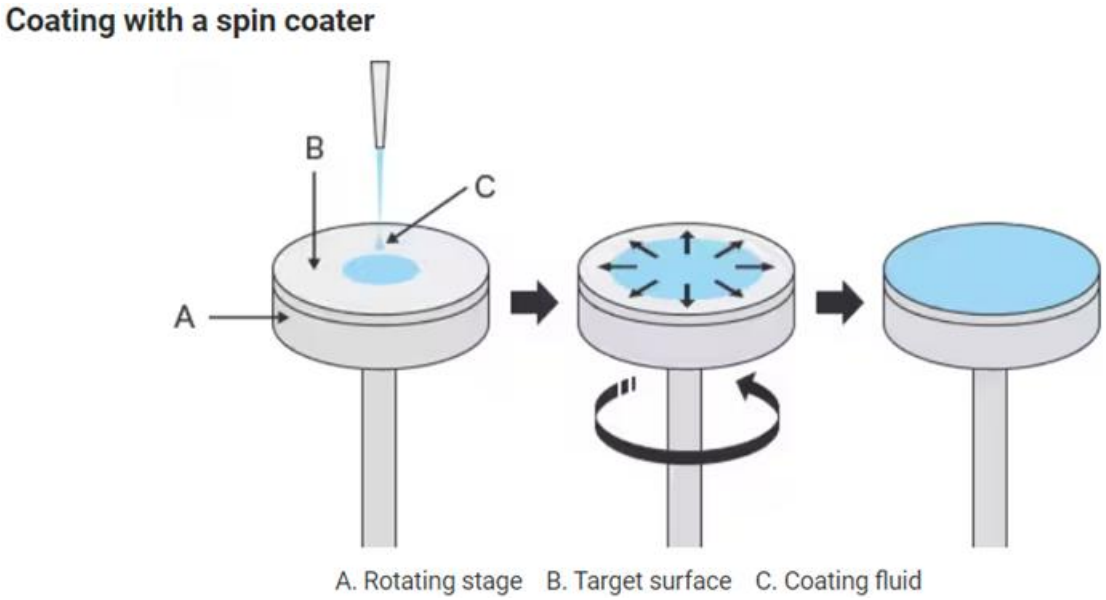


Figure 5.1: Illustration of the spin-coating process [307].

As the substrate spins, the solvent of the solution is evaporating, leaving a continuous thin film of the desired material, whose thickness depends on the angular speed of spinning, the viscosity, the environmental conditions and concentration of the solution, and the solvent used [308]. One way to accurately determine the final thickness of the film is the construction of an empirical "spin curve" (**Figure 5.2**), for a given spinning time, based on the combination of the experimental data of measured polymeric layers with the equation which connects their thickness (t) with the angular speed (ω) used in spin coating:

$$t \propto \frac{1}{\sqrt{\omega}} \tag{5.1}$$

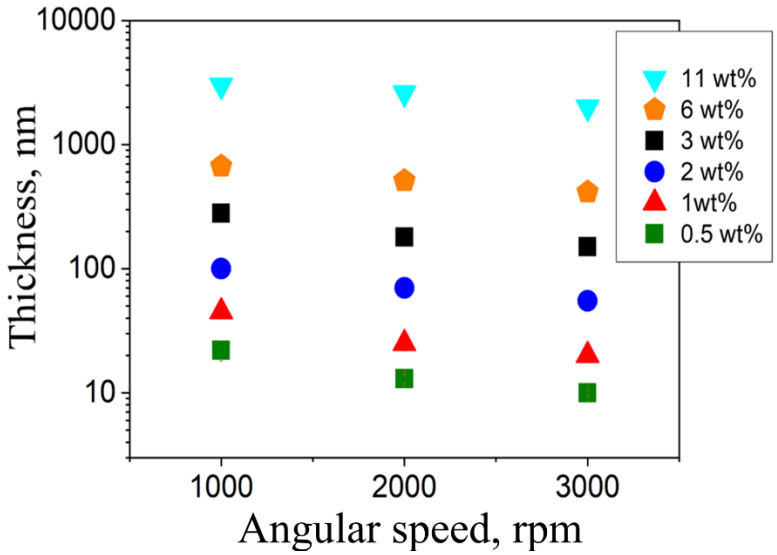


Figure 5.2: Thickness of PMMA films produced by various anisole concentrations, as a function of the angular speed.

Therefore, the angular speed is adjusted accordingly in order to obtain the polymeric layer of desirable thickness. The thickness of the polymeric layer is crucial in determining the final content of graphene, as described in equation (5.2):

$$V_{gr} = \frac{t_{gr}}{t_{gr}+t_{polymer}} = \frac{N*t_{gr}}{t_{nanolaminate}} \quad (5.2)$$

where N is the total number of monolayer CVD graphene sheets used, $t_{gr} = 0.334\ nm$ is the thickness of each graphene layer and $t_{nanolaminate}$ is the total thickness of the nanolaminate.

The CVD graphene/PMMA nanolaminates were fabricated through a Lift-Off/Float-On process, characterized by a semi-automatic, sequential transfer of graphene layers which are coated with an ultrathin PMMA film, onto a substrate, using consecutive wet depositions [85][82] combined with an all-fluidic manipulation system [309]. Specifically, the deposition process was carried out into specially designed devices comprised of conical polytetrafluoroethylene (PTFE) tanks equipped with manual control flow valves, adapted from intravenous infusion devices, for regulating the inlet and outlet fluids (see **Figure 5.3**). The geometry of the inner section of the transfer tank is important, as the inclined walls allow the stable attachment of the substrate and a reduction of the height of the concave meniscus.

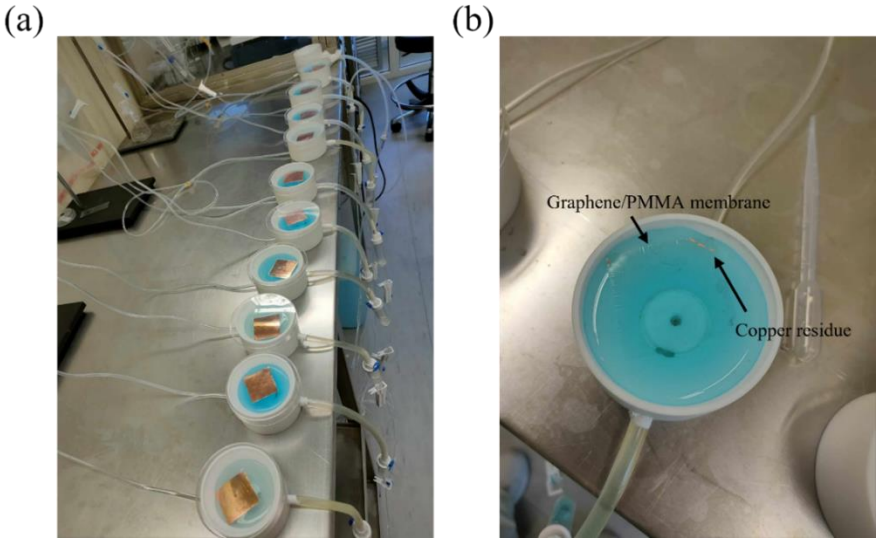


Figure 5.3: (a) Array of cone-shaped PTFE tanks for the wet transfer process, (b) Graphene/PMMA membrane during the etching of copper.

Initially, a PMMA supportive layer is deposited via spin-coating onto a graphene/Cu foil of 35 mm x 35 mm, and then placed in a transfer tank filled with APS solution to remove the Cu (**Figure 5.3**). When the etching of Cu is completed, distilled water is inserted into the tank, in order to rinse the nanofilm, thus removing any metallic residues that may act as defects. The first deposition of graphene/PMMA nanofilm performed onto a thick Cu foil, and then it is dried at 40 ^{o}C under vacuum for 30 min, and then post-baked at 150 ^{o}C for 5 min, in order to improve adhesion. Then the next graphene/PMMA nanofilm is deposited onto the previous one and the same process is followed. This etching/lift-off procedure is performed simultaneously in several transfer tanks, in order to accelerate the production process, and the cycle is repeated until the desired number of PMMA/graphene layers is achieved. Therefore, at the end of the iterative procedure, the desired number of graphene/PMMA layers are transferred onto the same Cu substrate, which is then etched away at the final step of the process, leaving a freestanding nanolaminate which is rinsed and dried.

The thickness of each nanolaminate membrane was measured by taking the average value of 10 via a digital micro-meter with a resolution of 0.1 μm (Mitutoyo, Japan) (see Σφάλμα! Το αρχείο προέλευσης της αναφοράς δεν βρέθηκε.). The thickness of neat PMMA was 6.1μm (0.00% volume fraction). Two volume fractions of graphene were considered, namely 0.035% and 0.12%. The former nanolaminate was 5.8 μm thick and included 6 CVD graphene monolayers, while the latter was 5.7 μm thick and included

20 CVD graphene monolayers. In Σφάλμα! Το αρχείο προέλευσης της αναφοράς δεν βρέθηκε. the conditions used for the production of nanolaminates of different volume fractions are summarized.

Table 5.1: Information over the produced graphene/PMMA nanolaminates.

Graphene Volume fraction (%)	**Nominal Polymer Thickness (nm)**	**Angular speed (RPM)**	**Solution in Anisole (wt%)**	**Number of layers**	**Final thickness (μm)**
0.00	250	1500	3	20	6.1
0.035	750	1000	6	6	5.8
0.12	250	1500	3	20	5.7

The nanolaminates were cut into stripes of 42 mm and a width of 2 mm (measured via optical microscopy with a 5x lens) and were secured onto paper testing cards using a two-part cold curing epoxy resin (Araldite 2011, Huntsman Advanced Materials, UK) in order to avoid any possible damage at the gripping area by the clamps (see **Figure 5.4**). The gauge length (L_0), was also measured by an optical microscope, using a 5x lens, approximately at 25 mm. It is evident that the neat PMMA film is "colourless" (**Figure 5.4(a)**), whilst as the number of graphene layers that are added as fillers is increasing, the darker the nanolaminates become, respectively (**Figure 5.4(b,c)**).

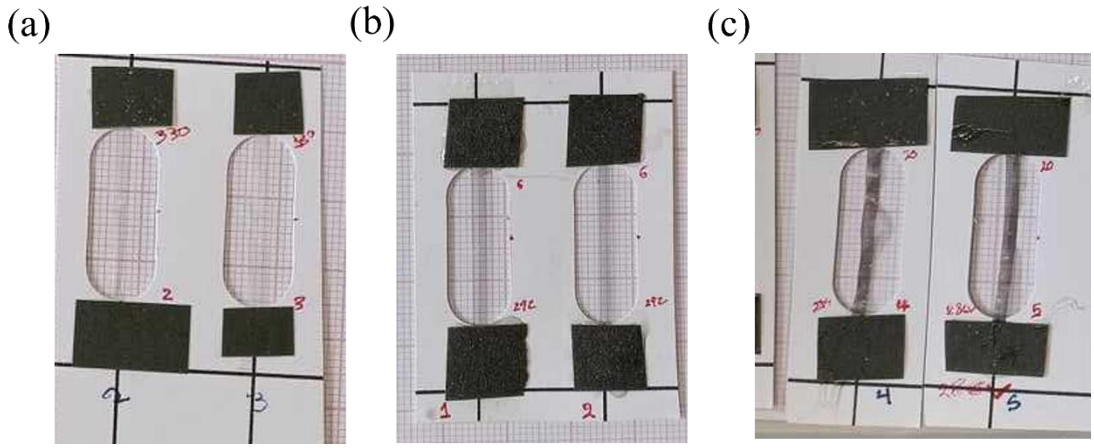


Figure 5.4: (a) Neat PMMA film, Graphene/PMMA nanolaminates of (b) 0.035% and (c) 0.12% volume fraction, respectively.

5.2 Fracture processes in defected graphene-PMMA nanolaminates

The micro-tensile tester (MT-200, Deben UK Ltd, Woolpit, UK), equipped with a 5 N loadcell was used for the tensile test of the samples, which were loaded in tension with a crosshead displacement speed of 0.2 mm min^{-1}, corresponding to a strain rate of 0.008 min^{-1}. The strain is calculated considering the elongation of the sample (displacement) ΔL and the gauge length (L_0), while the stress can be derived by considering the recorded force, the thickness, and the width of the nanolaminate.

To assess the effect of a defect in the mechanical behaviour of the nanolaminates, both as-prepared defect-free and defected samples were compared. The defect of each nanolaminate was introduced at its centre using a tabletop 1064 nm Nd:YAG laser (Rofin) was used (see **Figure 5.5**). Specifically, the centre of the specimens was irradiated, forming a see-through hole of ~ 300 μm radius, which is approximately 6 times smaller than the overall width, securing this way that there will not be edge effects leading to the premature failure of the nanocomposite. Irradiation involved a single laser pulse, and the following conditions: laser voltage of 300 V, pulse width of 1.0 ms, and a laser spot size of 200 μm.

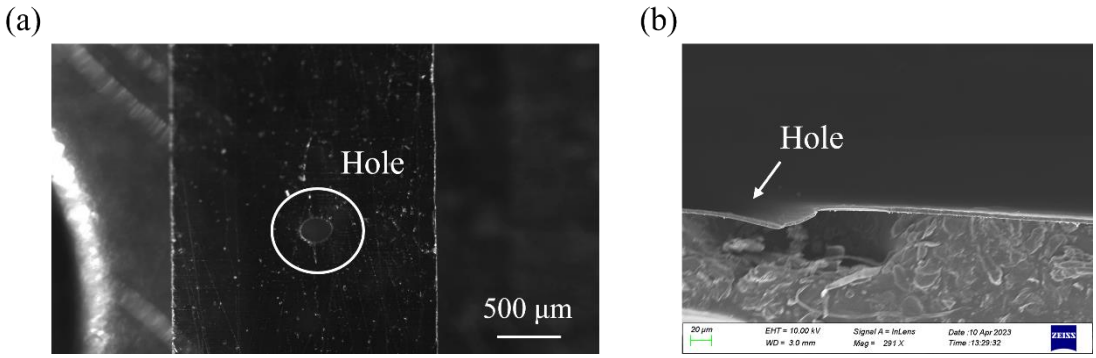


Figure 5.5: (a) Top-view (via optical microscope using a 5x lens) and (b) Cross sectional view (via SEM) of nanolaminates with a defect-hole at the centre of a nanolaminate specimen.

Representative stress-strain curves of graphene-based nanolaminates and neat PMMA film are shown in **Figure 5.6**, for both pristine and defected configurations.

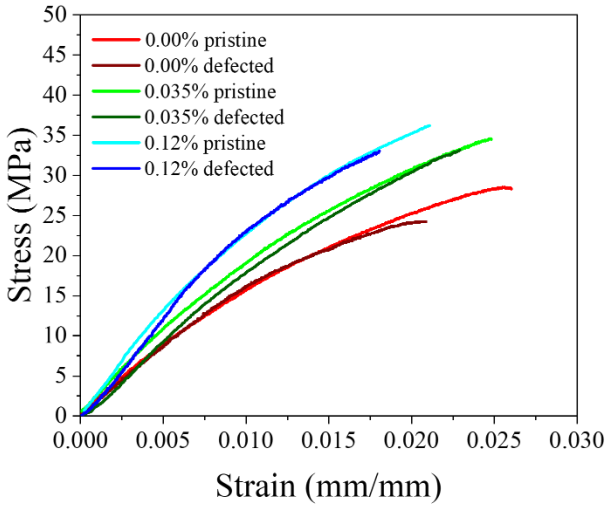


Figure 5.6: Representative stress-strain curves of neat PMMA (0.00%) and graphene-based nanolaminates (0.035% and 0.12%), in the as-prepared and defected states.

The stress-strain curves indicate that the incorporation of graphene content into nanolaminates enhances significantly their stiffness. The Young's modulus which is indicative of a material's stiffness, is derived from the slope at low strain (up to 0.4%) of an average of 10 samples, corresponding to $E_m = 1.75\ GPa$ for the neat PMMA, $E_c = 2.10\ GPa$ for the nanolaminates with $V_G = 0.035\%$, and $E_c = 2.70\ GPa$ for the nanolaminates with $V_G = 0.12\%$.

Table 5.2: Information over the mechanical properties of graphene/PMMA nanolaminates.

Graphene Volume fraction (%)		**0.00**	**0.035**	**0.118**
Young's Modulus (GPa)		1.75 ± 0.14	2.10 ± 0.15	2.70 ± 0.13
Strength (MPa)	As – prepared	28.3 ± 0.5	34.6 ± 0.7	36.2 ± 0.8
	Defected	24.2 ± 0.8	33.7 ± 0.9	32.4 ± 0.6
Elongation at break (%)	As – prepared	2.60 ± 0.20	2.40 ± 0.12	2.10 ± 0.15
	Defected	2.10 ± 0.10	2.20 ± 0.20	1.97 ± 0.10

A framework over the estimation of the overall properties of graphene-based nanocomposites based on the properties of their individual constituents and their complex interactions in microscale can be provided via the construction of micromechanical models [310]. These models enable the comprehensive analysis of factors like volume fraction, interface characteristics, nanofiller dimension, and orientation, which significantly influence the overall mechanical behaviour of the nanocomposites [311][312][313]. In specific, the prediction of properties such as Young's modulus, yield strength, and thermal conductivity, contributes to the design of materials with enhanced mechanical and thermal behaviour, resulting to the optimization of the nanocomposite [314]. Furthermore, these models provide the theoretical basis for the prediction and understanding of the mechanical behaviour of graphene-based composites, reducing the need for numerous experimental trials, thus offering a cost-effective and efficient approach to material design and development [315]. The primary methods proposed for the prediction of the effective properties of heterogeneous materials from the constituent properties include analytical methods, such as Rule of Mixtures (RoM), a simple linear approximation according to which the overall properties of the composite can be calculated based on the volume fractions and properties of its constituents, or Mori-Tanaka model, which provides information over the composite's elastic properties based on the interaction between the inclusions (e.g., graphene) and the matrix [316] [317], and semi-empirical methods, such as Halpin-Tsai model, which takes into account the shape, orientation, and distribution of the reinforcing phase within the matrix [318][319] in order to estimate the Young's modulus of the composite.

The Rule of Mixtures (RoM) is the most prevalent common method for the estimation of mechanical properties, such as Young's modulus E_c, based on some idealized assumptions, such as the infinite length of the filler, its alignment to one direction and the perfect bonding with the matrix, in composite materials including Carbon Fibre Reinforced Polymers (CFRPs) [320], Fibre Metal Laminates (FMLS) [321], and nanostructure-hybrid fibre composites [322]. Assuming that the strain is uniform across the composite, the effective modulus of the composite can be calculated via the Voigt model:

$$E_c = E_f V_f + E_m V_m \tag{5.3}$$

Where E_f, E_m are the moduli of the filler and the matrix, and V_f, V_m are the volume fraction of the filler and the matrix, respectively.

Figure 5.7 illustrates the linear relationship between the Young's modulus of the nanolaminates as a function of their graphene content. It is evident that the addition of only 0.12% CVD graphene leads to an increase of the Young's modulus by ~50%. The effective Young's modulus obtained is $E_{eff.} = 804\ GPa$, which is considerably close to the one obtained effective modulus in similar system ($E_{eff.} = 846\ GPa$)[323] and the Young's modulus of the pristine monolayer graphene [324]. It is worth noting that these values are significantly higher than the values estimated for similar laminate systems produced using methods such as stacking and folding [83].

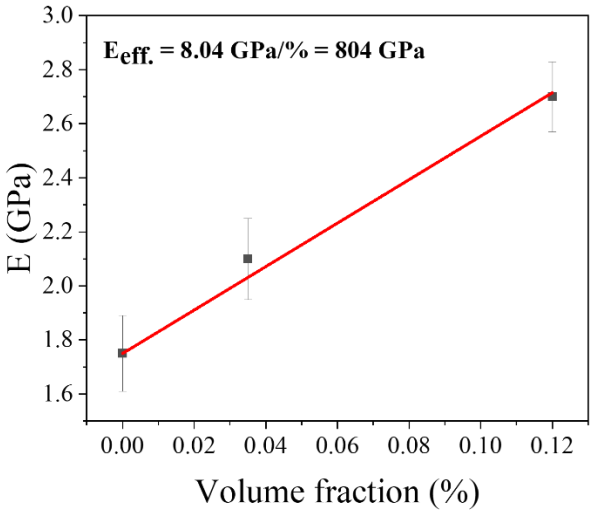


Figure 5.7: Young's modulus of the graphene-based nanolaminates as a function of graphene volume fraction.

The addition of CVD graphene layers into the nanolaminates leads to a significant improvement of the ultimate tensile strength of the pristine samples compared to the neat PMMA of approximately 28% (see **Figure 5.8(a)**). The strain at break is almost the same for the neat PMMA and the low volume fraction nanolaminates, whereas the high volume fraction nanolaminates present embrittlement (see **Figure 5.8(a)**). This embrittlement can be attributed to the thickness and the morphology of the Cu foils used as a substrate during the CVD growth, which typical exhibit a roughness value of R_a~40 nm [325]. From the thickness values of PMMA layers of each volume fraction, it is evident that the lower the volume fraction, the thicker the PMMA layer becomes

in comparison with the higher volume fractions. This entails that the roughness of the Cu foil does not affect the thicker polymeric layers, in contrast with the thinner ones, thus inserting inherent defects to the system, whose role is significant and potentially can contribute to the premature failure of the system. Furthermore, the high volume fraction nanolaminates are produced via numerous itinerary depositions, rendering possible the formation of ruptures or tear of the graphene/polymeric layer due to their low thickness, potentially resulting to the reduced strength of graphene, and slightly to the stiffness, as indicated in Σφάλμα! Το αρχείο προέλευσης της αναφοράς δεν βρέθηκε..

When the defect is introduced, both the strain at break and the strength of all samples drop. In the case of the neat PMMA, the strain at break drops by ~19% and the strength by ~17%. These percentages are reduced significantly in graphene-based nanolaminates for which the strain at break falls by ~8% and ~6%, whereas the strength declines by ~6% and ~7%, for the low and high volume fraction nanolaminates, respectively. The lower percentage drops derived for graphene nanolaminates, testify for the "activation" of impeding mechanisms for crack progression (such as these detailed in **Chapter 2**) after the reinforcement with CVD graphene fillers. Comparison of the ultimate tensile strength between the defected nanolaminates and the defected neat PMMA, unveils an improvement of ~40%. Therefore, the incorporation of a small number of large graphene layers can significantly reinforce PMMA nanolaminates.

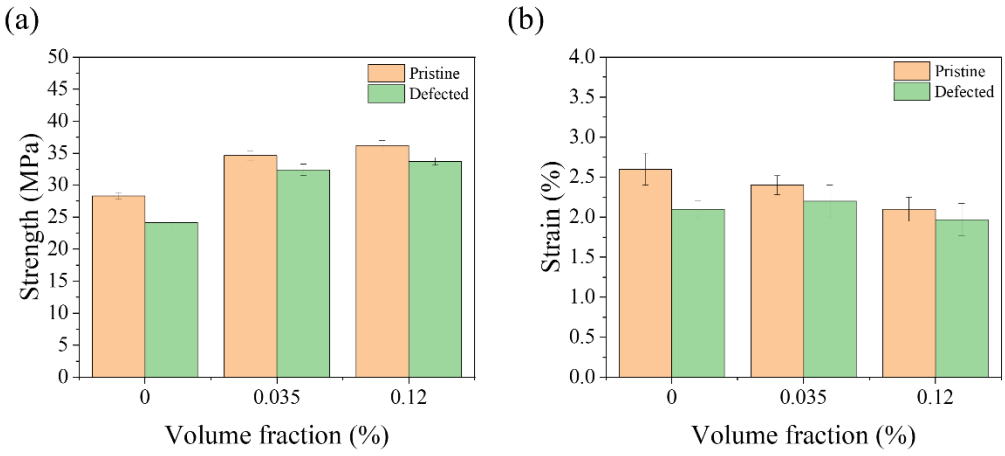


Figure 5.8: (a) Ultimate tensile stress and, (b) Strain at break of the neat PMMA (0.00%) and graphene-based nanolaminates (0.035% and 0.12%), in the as-prepared and defected state.

To gain further insight into the fracture of the defected graphene-based nanolaminates, the Griffith's criterion (*Equation 2.11*) was considered, using the radius of the hole as a_C, and the ultimate tensile strength as σ_C. The fracture toughness of the neat PMMA is $0.55 \pm 0.07\ MPa\ m^{1/2}$, whereas in the low and high volume fraction nanolaminates it increases to $0.81 \pm 0.05\ MPa\ m^{1/2}$ and $0.72 \pm 0.05\ MPa\ m^{1/2}$, respectively (see **Figure 5.9**). The slight decrease of fracture toughness in the case of the nanolaminate with V_G = 0.12% compared to the nanolaminate with V_G = 0.035% may be attributed to possible defects introduced in the laminate structure upon multiple deposition process. It is interesting to note that the fracture toughness of the graphene-based nanolaminates is significantly higher than the neat PMMA, with the low and high volume fraction nanolaminates presenting an increase of ~48% and ~31%, respectively, which is associated with the developed mechanisms resisting crack propagation as described in **Chapter 2**. This showcases that CVD graphene is an excellent candidate for the efficient reinforcement of a nanocomposite, even at low contents. Nevertheless, there are other systems in the literature, such as epoxy resins including rubber beads, presenting even higher increase of fracture toughness, which comes at a cost of reducing the nanocomposite's strength [161]. In these approaches, graphene derivatives, such as GNPs, are also incorporated in the nanocomposites to improve their mechanical properties [161].

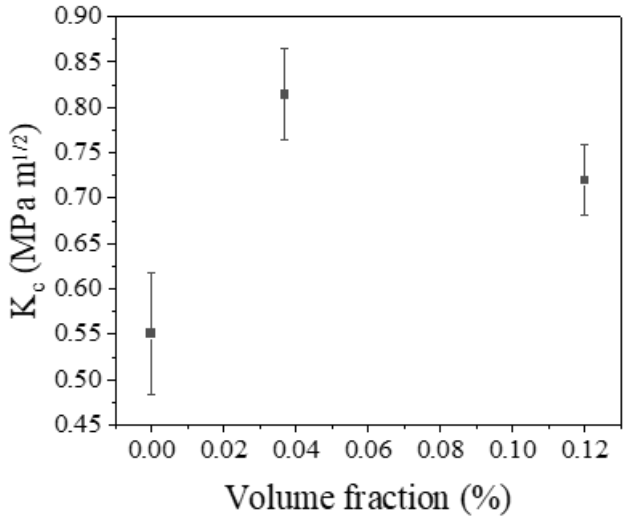


Figure 5.9: Fracture toughness of the neat PMMA (0.00%) and graphene-based nanolaminates (0.035% and 0.12%).

During the tensile procedure, the top-view of the examined nanolaminates was monitored by a high-resolution camera, and recorded in real-time with a frame rate of 5 frames per second (**Chapter 3** – **Section 4**), providing information over crack initiation and propagation. For all the specimens, during the tensile test, the shape of the hole is altered compared to the initial circular configuration, and becomes more elliptical. Most importantly, two crack tips form at each side of the hole at a critical strain. The points of the crack initiation are those which experience the highest deformation and stress levels. During the stage of the stable crack propagation, a plastic zone ahead of the crack tip is formed, due to the complex interplay of mechanical forces. Precisely, these mechanical forces lead to a complex stress distribution near the crack tip, including the tensile stress ahead of the crack, the compressive stress behind it, and shear stress along the crack surfaces, resulting to a plastic deformation which contributes to the blunting of the crack tip, affecting the stress distribution and the overall fracture process [326]. Specifically, the tensile stress is the primary driving force for the crack propagation, as the stress that material undergoes ahead of the crack tip, causes further opening and extension of the crack within the material, leaving the material behind experiencing a compressive strain, which contributes to the overall deformation and failure of the material. Shear stress acts along the crack surfaces, causing a sliding motion of each side of the crack, which further contributes to the opening of the crack and the propagation of the fracture.

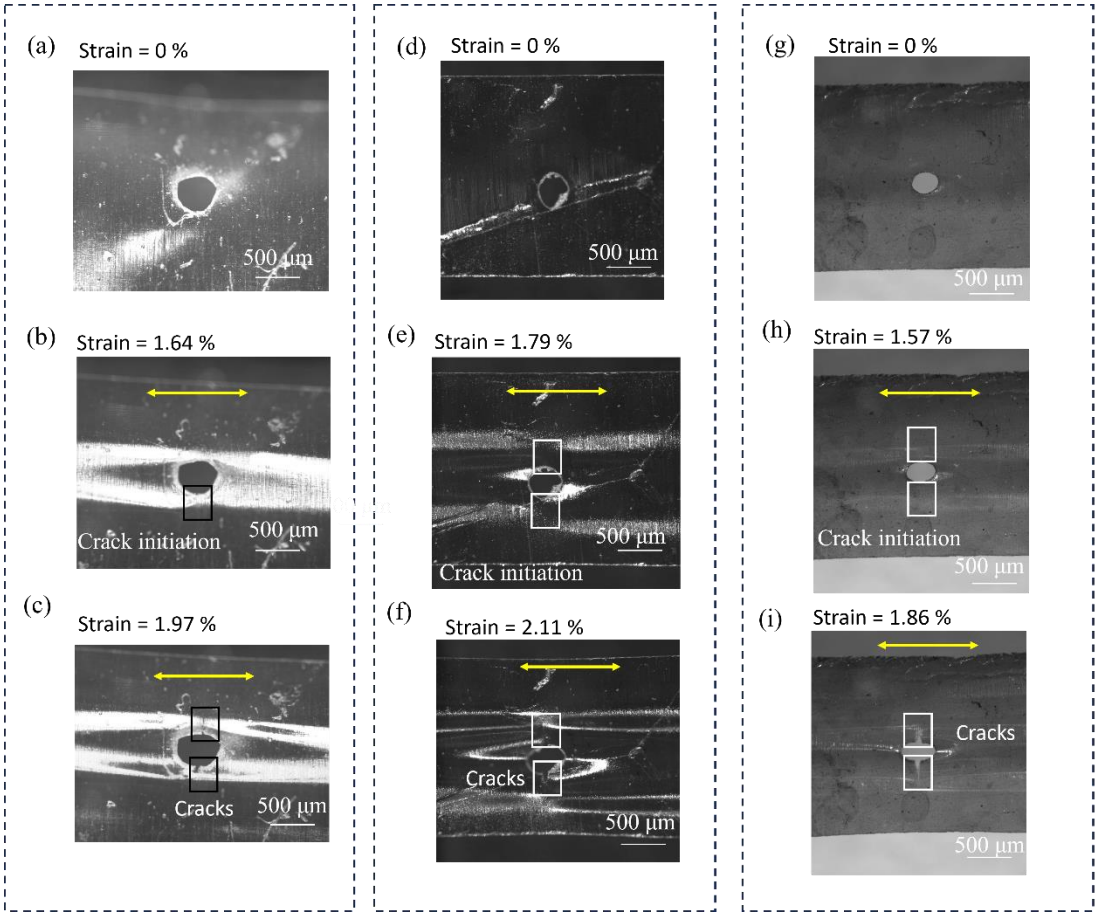


Figure 5.10: Real-time optical examination of the neat PMMA and graphene based nanolaminates subjected to tensile loading. Neat PMMA at rest (a), when crack initiates (b), and before final failure (c). Low/high volume fraction graphene nanolaminates at rest (e/i), when crack initiates (f/j), and before final failure (g/k). The yellow arrows indicate the load axis.

Figure 5.10(a,d,g) depicts the unstrained configuration of 0.00%, 0.035%, and 0.12% nanolaminates, while frames of the nanolaminates when crack initiation occurs, are depicted in **Figure 5.10(b,e,h)**. **Figure 5.10(c,f,i)** corresponds to the last frame before fracture. The images in **Figure 5.10(b/c, e/f, h/i)** are also presented at higher magnification in **Figure 5.11.** The strain at which the crack initiation occurs at each case corresponds to the left red dashed line of the **Figure 5.11(c,f,i)**, whereas the strain at which the final failure occurs corresponds to the right red dashed line.

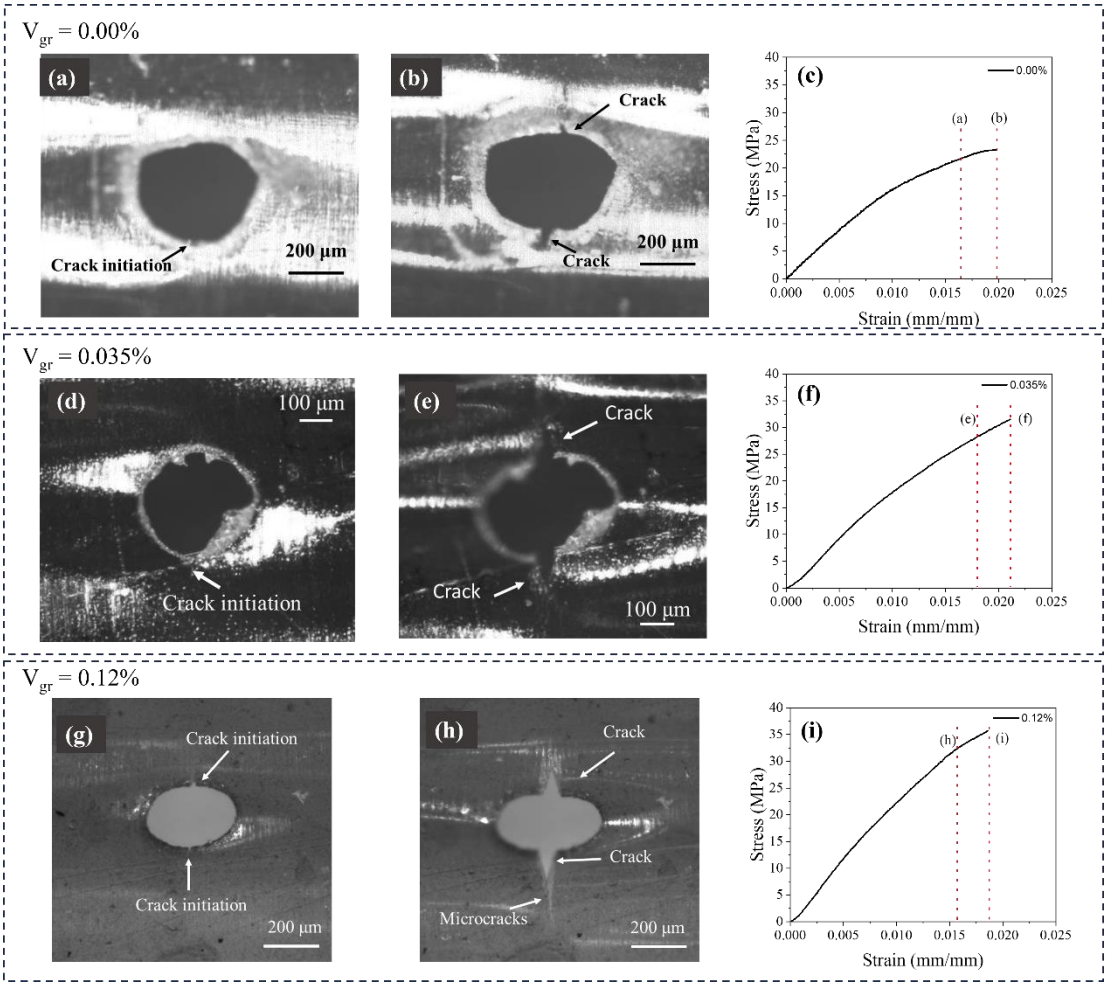


Figure 5.11: Images of higher magnification for the case of 0.00%, 0.035%, and 0.12% nanolaminates, when crack initiates(a,d,g) and before the final fracture (b,e,h). (c,f,i)The stress-strain curves for neat PMMA, low, and high volume fraction graphene nanolaminates, respectively. In each stress-strain curve the crack initiation and the final fracture are depicted with the letters of the corresponding image.

The crack formation in the case of the PMMA film does not appear simultaneously in both the sides of the hole (see **Figure 5.10(b), Figure 5.11(a)**), most likely due to the different defect curvature in the respective regions (due to the low absorption of pure PMMA at 1064 nm, there is no complete ablation throughout the entire irradiated zone), whilst the crack formation in the case of 0.035% and 0.12%, appears almost simultaneously in the upper and lower area of the hole's edge (see **Figure 5.10(e,h), Figure 5.11(d,g)**). Calculating the integrated area after the crack onset in the stress-strain curves of **Figure 5.11(c,f,i)**, the energy dissipation is $0.075 \pm 0.006\, J/cm^3$, $0.093 \pm 0.008\, J/cm^3$, and $0.100 \pm 0.010\, J/cm^3$, for 0.00%, 0.035%, and 0.12% nanolaminates, respectively. The energy dissipation in the case of the PMMA film is lower than the graphene-based nanolaminates, which can be attributed to the absence

of crack impeding mechanisms, unlike the graphene-based nanolaminates, in which mechanisms that procrastinate the fracture procedure are developed. Typical cross-sectional SEM images were also taken from the fractured specimens in order to observe the morphology of the crack path and to gain further information on fracture (see **Figure 5.12**). In the case of the neat PMMA (**Figure 5.12(a)**), the texture of the crack surface appears smooth and no evidence of any impeding mechanism for crack progression appears. On the contrary, in the graphene-based nanolaminates that possess a clear multi-layer architecture, a rough crack surface texture is observed, with the individual polymeric layers being distinguishable from each other, highlighting their severe delamination (especially the case of V_{Gr} = 0.12%). The individual layers show failure at different points (**Figure 5.12(b,c)**), thus suggesting that crack has not propagated uniformly in all layers, probably due to the deflection occurring at the different graphene/PMMA interfaces [327]. This is likely associated with the increased fracture toughness, compared to the neat PMMA.

Concluding, neat PMMA is the first to fail, due to the absence of crack impeding mechanisms, whilst between the two graphene/PMMA nanolaminates examined, the 0.035% exhibits superior mechanical properties. In fact, crack impeding mechanisms (i.e. deflection) exist in both 0.035% and 0.12% nanolaminates, however, the existence of many graphene/PMMA interfaces in the latter case leads to embrittlement, resulting to premature failure in comparison to the former nanolaminate.

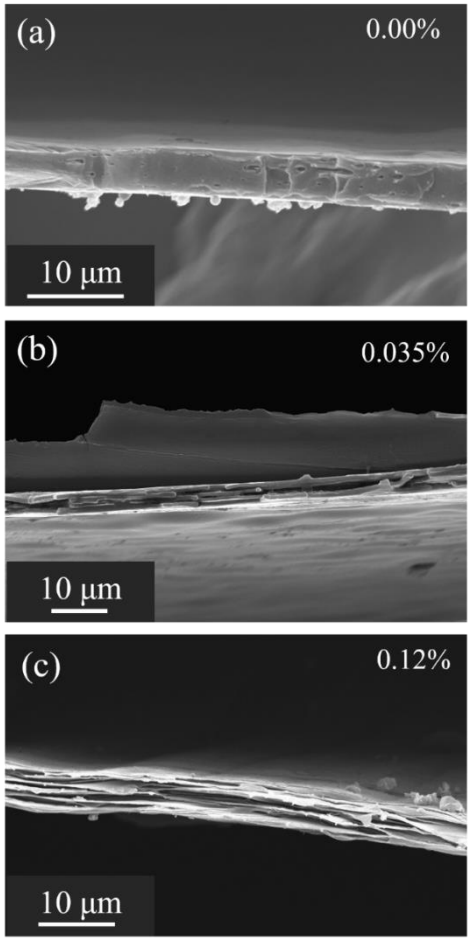


Figure 5.12: *Cross-sectional SEM images of the crack path in the case of (a) neat PMMA, (b) 0.035% and (c) 0.12% volume fraction.*

5.3 Monitoring the stress distribution across the area of a defect using Raman spectroscopy

As seen in **Figure 5.6**, the nanolaminates in which a defect has been introduced, break at significantly lower strain than those without defects. Hence, a need over the quantification of stress distribution at the vicinity of the defect is arising. As mentioned in **Chapter 3**, Raman spectroscopy is a powerful technique adopted to assess stress transfer characteristics in graphene/ polymer systems [285][328][287]. In **Chapter 4**, CVD graphene has been demonstrated to be effective as a sensor for the assessment of stress concentration around circular defects in polymeric materials, by exploiting in-situ micro-Raman spectroscopy combined with tensile testing. This approach has been proven to be successful experimentally, owing to the strain sensitivity of the 2D Raman

peak of graphene, providing quantitative insight on the stress distribution around a defect with sub-micron spatial resolution. In the previous paragraph, graphene's role as a reinforcing filler was highlighted. In this paragraph, the role of graphene, both as sensor and reinforcing filler will be showcased.

Firstly, Raman spectroscopy was employed for the quality control of graphene during the lamination process (see **Figure 5.14**). A representative Raman spectrum of the graphene/PMMA nanolaminate is illustrated in **Figure 5.13**. The presence of graphene is evident by the typical features in the Raman spectrum [208], as the 2D peak is present at ~2706 cm^{-1} revealing that graphene experiences a slight residual compression, and the G peak is present at ~1590 cm^{-1}. The weak D peak located at ~1350 cm^{-1} manifests a low defect density. In the spectrum, also the Raman peaks of PMMA are visible at ~1450 cm^{-1} [293], ~1730 cm^{-1} [293] and ~2952 cm^{-1} [294].

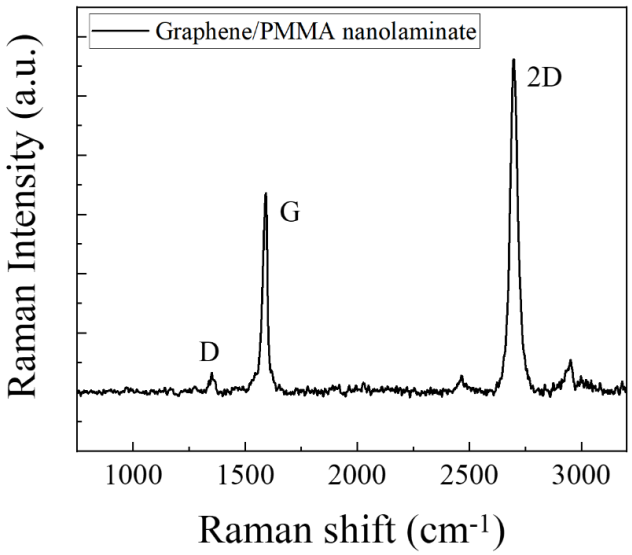


Figure 5.13: Raman spectrum of a graphene/PMMA nanolaminate.

The high quality of graphene in the produced nanolaminates is preserved throughout the samples, as indicated by the Int(2D)/Int(G) and the Int(D)/Int(G) Raman peak peak intensity ratio. Specifically, Raman mappings obtained from the samples at rest (see **Figure 5.14**), where ***Y (μm)*** represents the distance from the hole and ***X (μm)*** the offset from the in-plane axis of symmetry that is perpendicular to the load axis. The Raman mappings were conducted with a Y-axis step of 10 μm close to the edge of the hole (Y values < 300 μm) and with a step of 20 μm at distances exceeding Y = 300 μm. The average values of Int(2D)/Int(G) are ~2.1 (for 0.035%, see **Figure 5.15(a)**) and ~1.75 (for 0.12%, see **Figure 5.15(b)**). while the Int(D)/Int(G) average values are quite small

(~0.05 for 0.035%, see **Figure 5.15(a)**) and ~0.06 for 0.12%, see **Figure 5.15(b)**). The low values of Int(D)/Int(G) can be attributed to the minor structural defects that may be induced during the stacking process of the alternating Gr/PMMA layers and to the polycrystalline nature of our CVD graphene [329]. It is important to note that even close to the defect, the quality of the specimens does not deteriorate, as indicated from the Int(2D)/Int(G) and the Int(D)/Int(G) ratios (see **Figure 5.14**).

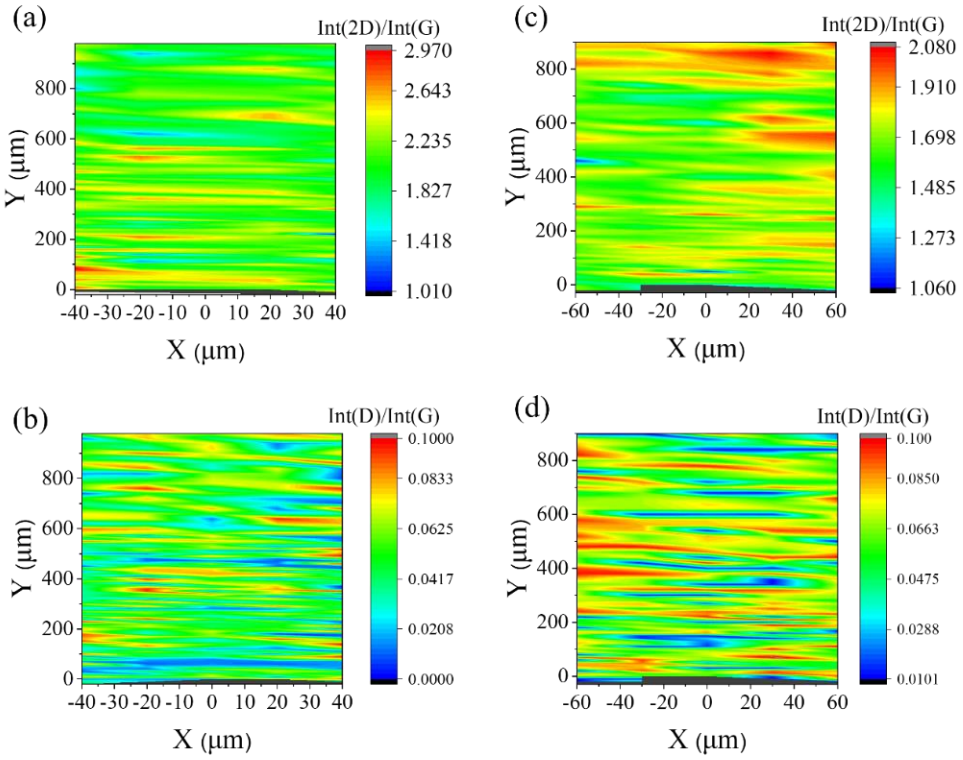


Figure 5.14: (a, b) Spatial contour mapping of Int(2D)/Int(G) and Int(D)/Int(G) for graphene volume fractions 0.035%, and (c, d) for 0.12% at rest, respectively (no application of strain).

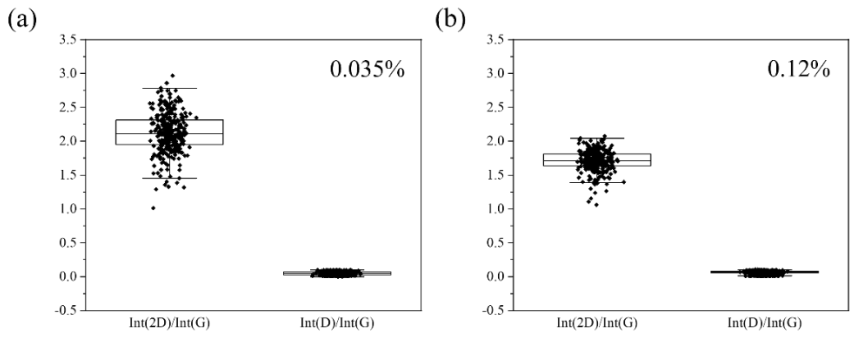


Figure 5.15: Box plots of the average values of *Int(2D)/Int(G) and Int(D)/Int(G) for nanolaminates of graphene volume fractions (a) 0.035%, and (b) 0.12 at rest, respectively (no application of strain).*

The performance of the material was tested combining mechanical testing with in-situ Raman spectroscopy. During the experiment, the tensile testing of the samples was conducted in a step-wise manner (in steps of 0.1%, up to 0.5%). At each step, *in-situ* Raman linear mappings have been conducted on the nanolaminates with a Renishaw Invia Raman Spectrometer, starting from the edge of the hole and terminating 1 mm afar from it, perpendicular to the loading direction, by acquiring spectra at steps of 10 μm, using a 514 nm laser excitation and a 50x objective. The laser power was kept below 1 mW in order to avoid laser-induced heating of the specimens. The mappings considered in each step were the following: (i) two perpendicular to the load axis mappings, at the upper and the lower edge of the hole and (ii) one mapping at the far-field (**Figure 5.16**). The duration of the Raman mappings was approximately 1.5 – 2 hours for each strain. All the Raman spectra were baseline-corrected, and the characteristic peaks of graphene were fitted with Lorentzian functions, to record the spectroscopic parameters (peak position and full width at half maximum, FWHM) at each position of the mapping.

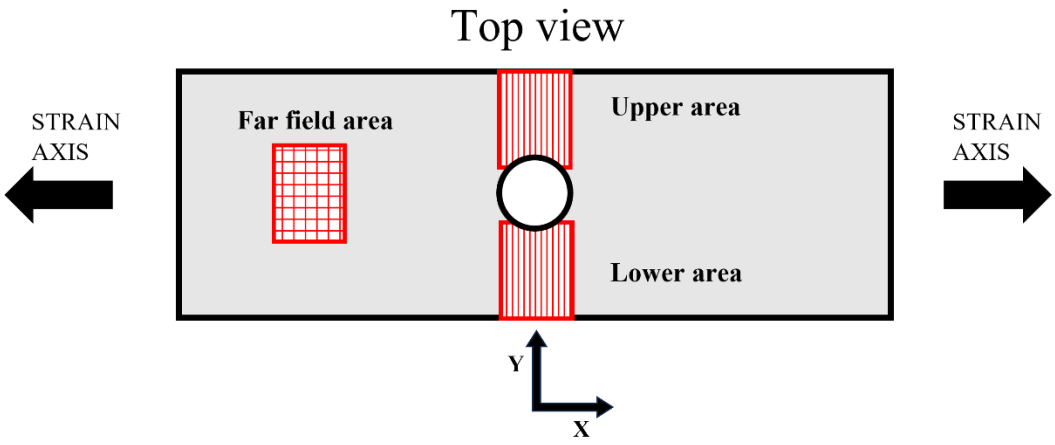


Figure 5.16: Schematic illustration of the top view of graphene/PMMA nanolaminates.

Figure 5.18 and **Figure 5.19** present the evolution of the position of the graphene 2D peak for nanolaminates of 0.035% and 0.12% volume fractions, respectively, before and after the imposition of quasi-static tensile strain. As mentioned previously, the position of pristine graphene's 2D Raman peak is highly sensitive to tensile strain, with a redshift rate of $\approx -60 cm^{-1}/\%$ [280][210], whereas this shift rate has been reported

to be substantially lower in the case of CVD graphene, or graphene-polymer coatings due to its polycrystalline nature [284]. **Figure 5.18(a,b)** and **Figure 5.19(a,b)** show a detailed position mapping of the 2D peak corresponding to regions A and B of the samples at rest. When no strain is applied, the 2D peak's position is approximately 2705 cm^{-1} for the case of 0.035% Gr/PMMA and 2701 cm^{-1} for the case of 0.12% Gr/PMMA. The deviation from 2682 cm^{-1}, which is the expected value for stress-free graphene [280], manifests that graphene undergoes residual compression arising from the nanolaminate production procedure [192]. Specifically, in the unstrained configuration, the residual biaxial compression of graphene derived from transfer and annealing process can be estimated ~0.15% and ~0.13% in the far field and gradually reducing to ~0.13% and ~0.11% at the notch root, for graphene content of, respectively, 0.035% and 0.12%, respectively (see **Figure 5.17(a,b)**).

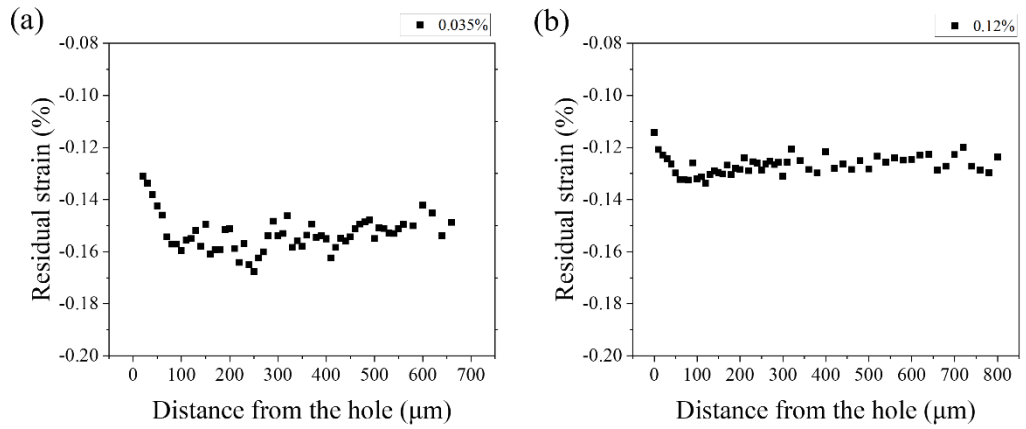


Figure 5.17: Profile of residual biaxial compression of (a)0.035% and (b) 0.12% graphene-based nanolaminates in the unstrained configuration.

For successively increased external applied strain deformations up to ~0.5% (see **Figure 5.18(c-f)** and **Figure 5.19(c-f)**), the 2D peak position progressively shifts towards lower wavenumbers, while the wavenumber location is found to be dependent on both the perpendicular to the load axis distance from hole (Y) and the offset from the in-plane axis of symmetry that is perpendicular to the load axis (X). The highest red-shifting of the 2D peak is observed near (X,Y) = (0,0), indicating that the stress concentration is maximized near this point.

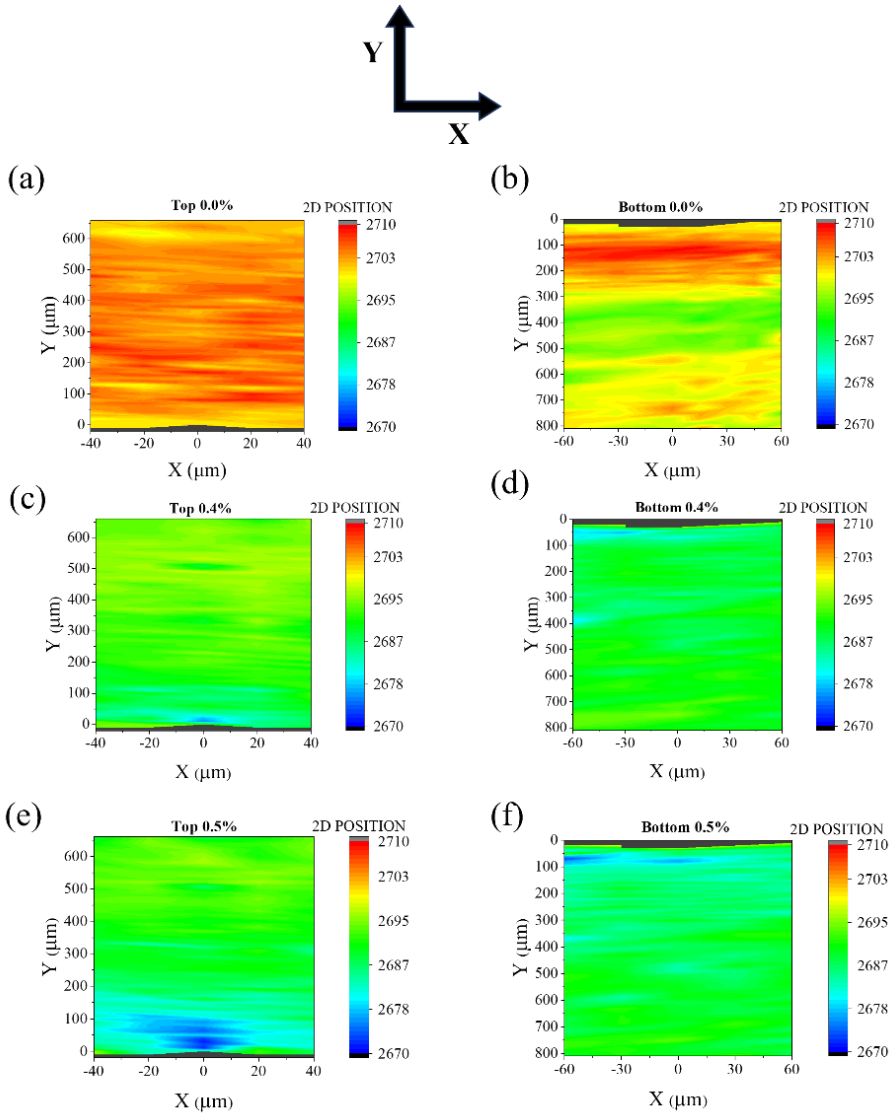


Figure 5.18: Spatial contour mappings for the case of 0.035% volume fraction (a) at the top, and (b) at the bottom area when no strain is applied, (c) at the top, and (d) at the bottom area when 0.4% deformation is applied and, (e) at the top, and (f) at the bottom area when 0.5% deformation is applied.

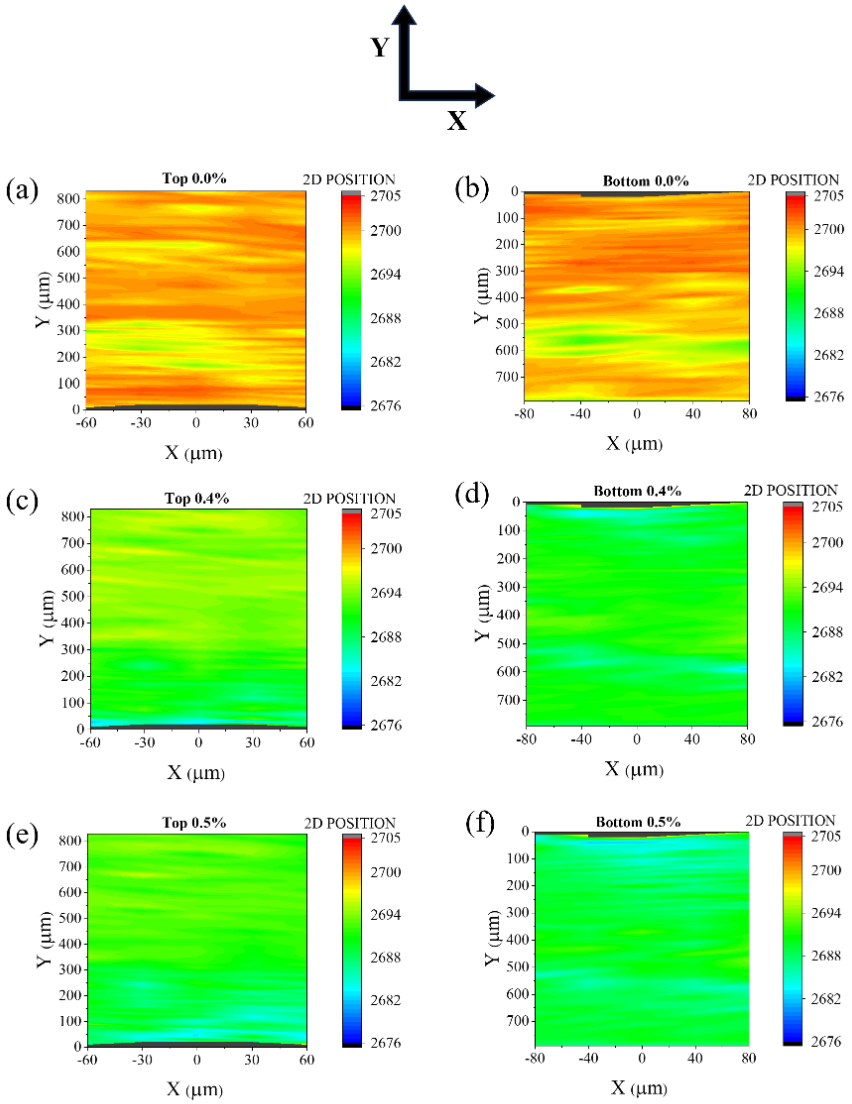


Figure 5.19: Spatial contour mappings for the case of 0.12% volume fraction (a) at the top, and (b) at the bottom area when no strain is applied, (c) at the top, and (d) at the bottom area when 0.4% deformation is applied and , (e) at the top, and (f) at the bottom area when 0.5% deformation is applied.

Detailed Raman mappings of the 2D peak position as a function of distance from the hole, for the low and high volume fraction nanolaminates, extracted from the one side of **Figure 5.18** (top) and **Figure 5.19** (top), for simplicity reasons, respectively, are depicted in **Figure 5.20** and **Figure 5.21**.

Figure 5.20 presents the detailed linear mappings of the 2D Raman peak position for each x- coordinate (as illustrated in the schematic picture; *X =-40 μm, X =-20 μm, X =0 μm, X =20 μm, X =40 μm*), for the nanolaminates with low volume fraction. Each graph depicts the spatial profile of the position of the 2D peak (along the mapping line) for applied strains from 0.0% to 0.5%. Due to the application of strain, the position of the

2D peak shifts in a non-linear manner at the vicinity of the defect, reaching a plateau at Y values exceeding 300 μm. Even though this redshift of the 2D peak close to the defect occurs in the same way for all cases, the highest redshift at 0.5% applied strain corresponds to X =0 μm coordinate. At X =0 μm, the position of the 2D peak is roughly 2691 cm^{-1} far from the defect, whereas at the nearest point it drops down to 2671 cm^{-1}, presenting a redshift of ~ 34 cm^{-1} compared to the unstrained state (which is 2705 cm^{-1}).

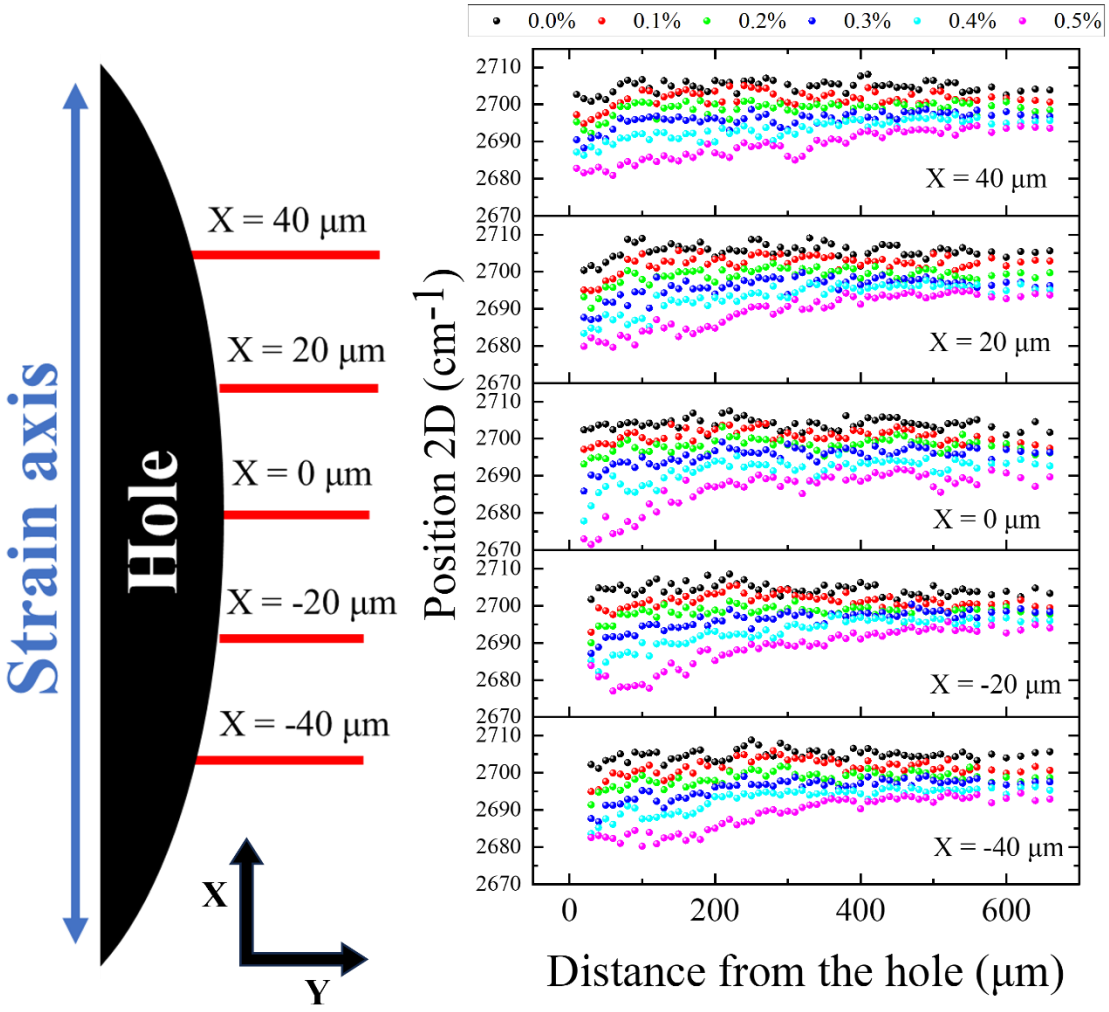


Figure 5.20: Line mappings of 2D peak position as a function of the distance from the hole for each x-coordinate for the case of 0.035% volume fraction, at different applied strain levels (0.0% - 0.5%)

Similarly, **Figure 5.21** depicts the detailed linear mappings of the 2D Raman peak position for each x- coordinate (as illustrated in the schematic picture; *X =-60 μm, X =-30 μm, X =0 μm, X =30 μm, X =60 μm*), for the nanolaminates of high volume fraction, with each graph including linear Raman mapping for applied strains from 0.0% to 0.5%.

Likewise, due to the strain application, the position of the 2D peak shifts in a non-linear manner at the vicinity of the defect, reaching a plateau at Y values exceeding 300 μm, in all cases. At 0.5% strain, the 2D peak at $X = 0\ \mu m$ is nearly 2693 cm^{-1} far from the defect, and 2683 cm^{-1} at the point of nearest proximity to this defect. Considering that at 0% strain, the 2D peak is ~2701 cm^{-1}, the maximum redshift achieved close to the defect is ~18 cm^{-1}, which is ~40 % lower compared to the maximum redshift achieved in the case of 0.035% nanolaminates.

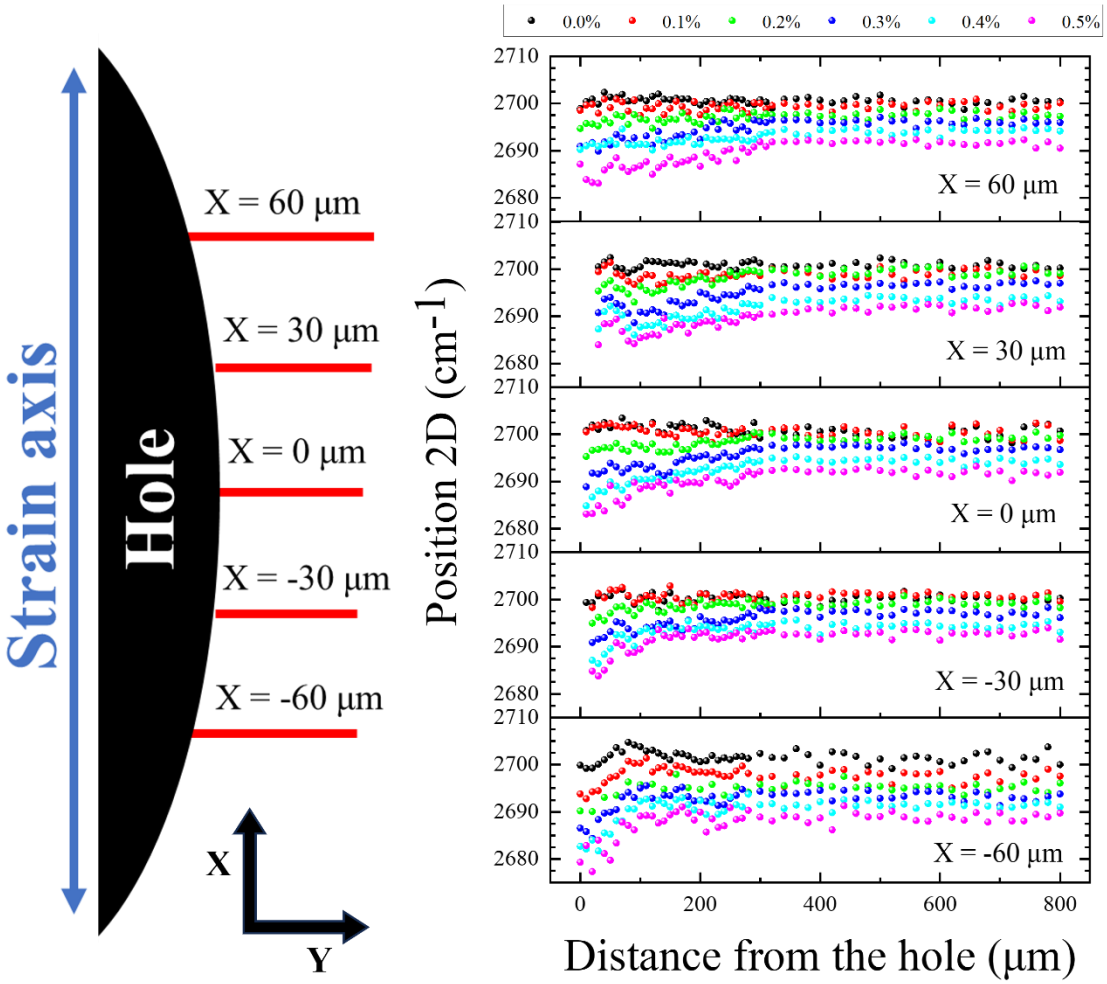


Figure 5.21: *Line mappings of 2D peak position as a function of the distance from the hole for each x-coordinate for the case of 0.12% volume fraction, at different applied strain levels (0.0% - 0.5%).*

In order to determine the stress sensitivity of graphene in the nanolaminate configuration, $\Delta\omega_{far\ field}$ (the shift of 2D peak's position value at far field at each applied strain compared to the initial configuration) shall be expressed as a function of the stress that graphene experiences at each applied strain ($\sigma_{graphene}$). To determine

$\sigma_{graphene}$, a new methodology was implemented. Exploiting the capability of direct force measurements (using DEBEN micro-mechanical) during the in-situ Raman experiment, the stress that the nanolaminate experiences can be derived directly from the force data. Previously, indirect methods for assessing the mechanical properties were employed, correlating Raman shifts of graphene peaks, due to strain application, with theoretical models to extract information over stress [210][330]. In the approach presented herein, the observed shift of graphene Raman peaks was directly correlated with the stress derived from the analysis of experimentally-derived stress-strain curves of the nanolaminates **Figure 5.22(a,b)**. It is important to note here that, as the duration of each strain step during the Raman mapping was quite long (~2 hours) the nanolaminates experienced relaxation, which is manifested by the stress drop at long time after the application of a constant deformation (depicted with red points in **Figure 5.22**). This can be attributed to the inherent viscoelastic behaviour of the polymer matrix, which is dominant in nanolaminates (V_m>99%) and leads to a stress decrease when the specimens are subjected to a constant strain over time [331][332]. Consequently, the stress transfer from the polymeric matrix to the graphene inclusion is time dependent.

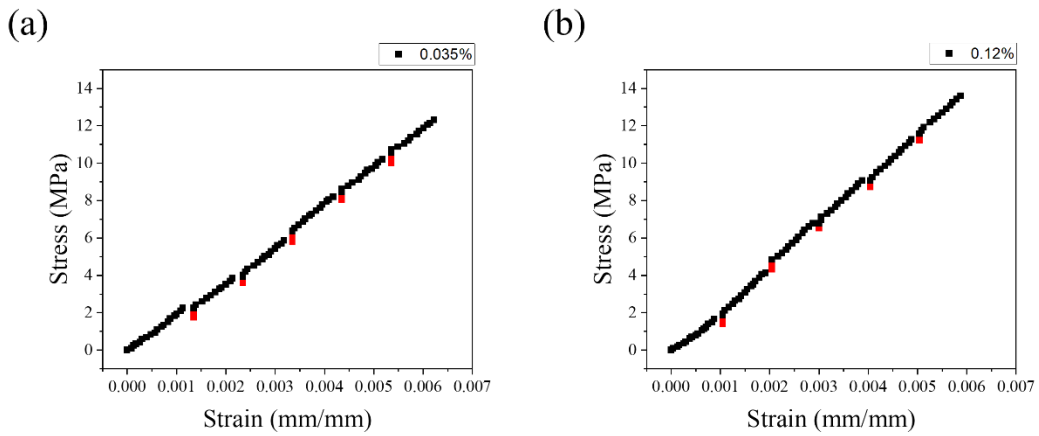


Figure 5.22: Stress-strain curve with a quasi-static step for nanolaminates of (a) 0.035% and, (b) 0.12% volume fraction.

In light of that, the modulus of the nanolaminates under investigation has been derived from the slope of relaxed the stress-strain curves depicted in **Figure 5.22,** yielding 1.78 GPa, and 2.27 GPa, for the 0.035% and 0.12% nanolaminates respectively.

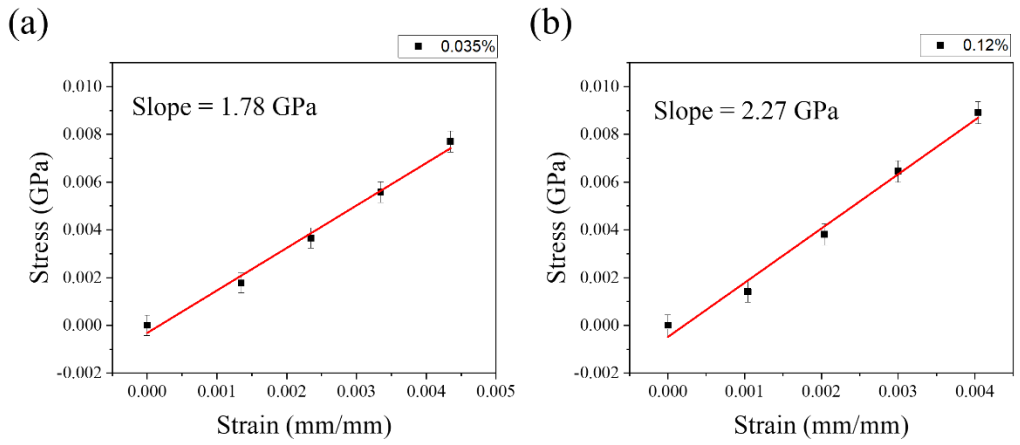


Figure 5.23: Modulus of the nanolaminates as derived from the stress-strain curves for the case of (a) 0.035% and, (b) 0.12% volume fraction nanolaminates.

By fitting the moduli of the nanolaminates in the relaxed state to the rule of mixture, an effective modulus of graphene of 560 GPa has been derived. (see **Figure 5.24**). In this analysis, the stress relaxation of PMMA matrix has been taken into account, as well. This value is ~25% lower than the effective Young's modulus obtained from the continuous mechanical test (see **Figure 5.7**; $E_{eff.} = 804\ GPa$). As explained previously, this drop is attributed to the relaxation phenomenon associated with the high duration of each interval of the incrementally applied strain.

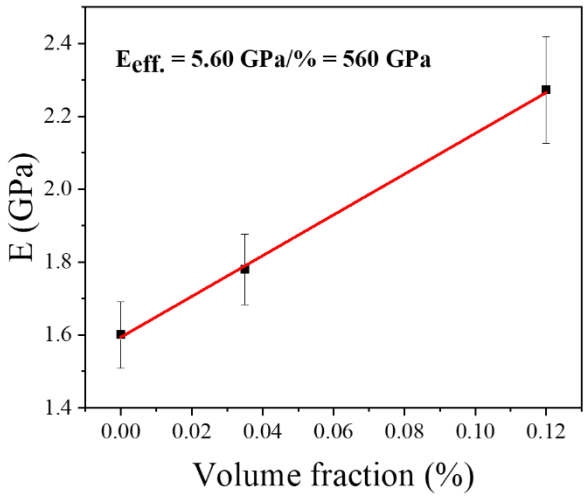


Figure 5.24: Young's modulus of the neat PMMA and graphene-based nanolaminates as a function of graphene volume fraction. Effective modulus of graphene derived from the slope.

Knowing the value of the effective modulus of graphene in the nanolaminate configuration, $\sigma_{graphene}$ can be calculated for each applied strain, using Hooke's law

($\sigma_{graphene} = \varepsilon E_{graphene}$). Therefore, for both the Raman experiments performed on the two nanolaminates, the far-field shift of the 2D peak position has been plotted as a function of the graphene stress. The slope of $\Delta\omega_{far\ filed} = f(\sigma_{graphene})$ have been found to be $3.71\ {}^{\mathrm{cm}^{-1}}/_{GPa}$ and $3.64\ {}^{\mathrm{cm}^{-1}}/_{GPa}$, for the 0.035% and 0.12% nanolaminates, respectively (see Σφάλμα! Το αρχείο προέλευσης της αναφοράς δεν βρέθηκε.). Therefore, the stress sensitivity of the system will be set as the average value of the individual stress sensitivities, $3.68\ {}^{\mathrm{cm}^{-1}}/_{GPa}$.

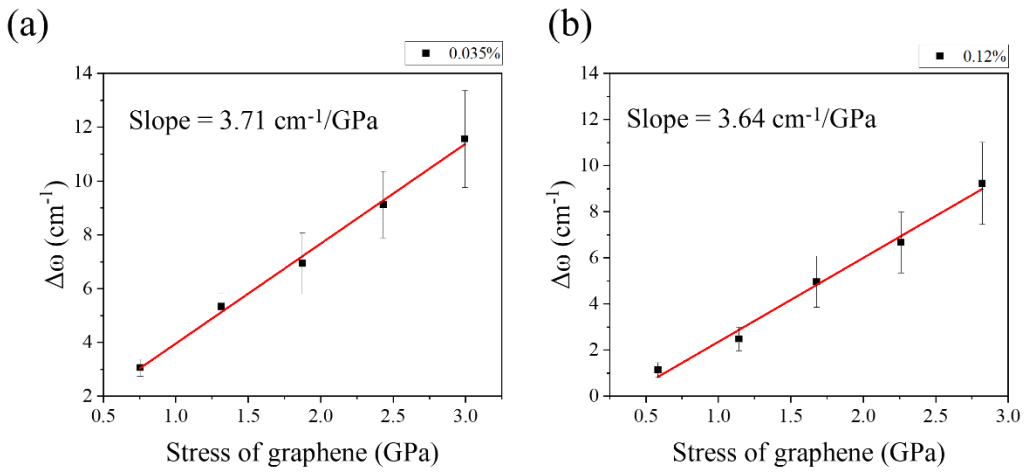


Figure 5.25: Stress sensitivity for (a)0.035% and (b)0.12% volume fraction nanolaminates.

Next, the local stress that graphene experiences in each point furthering away from the defect can be derived by dividing $\Delta\omega$ with the derived stress sensitivity ($3.68\ {}^{\mathrm{cm}^{-1}}/_{GPa}$).

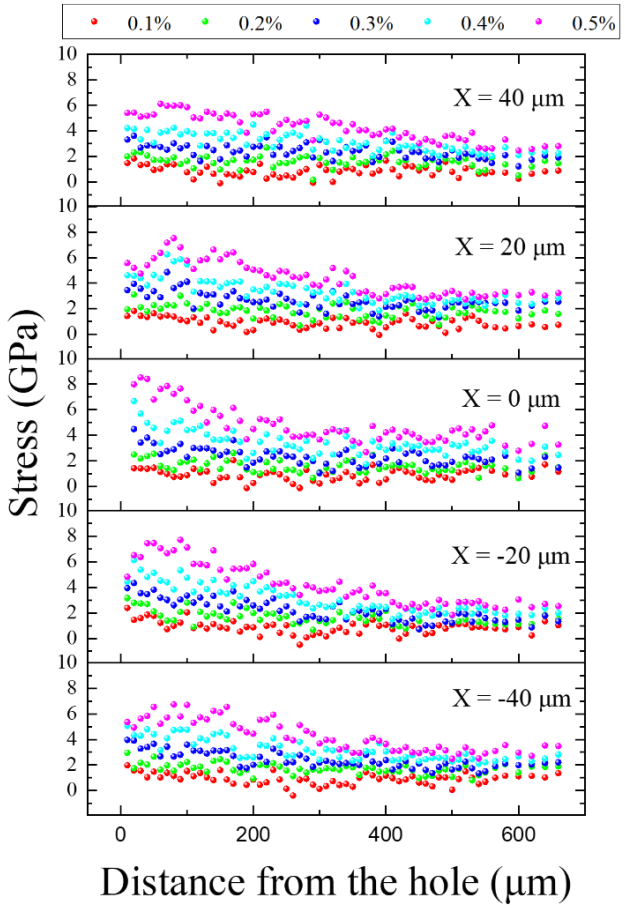


Figure 5.26: Line mappings of stress of graphene as a function of the x- coordinate and the distance from the hole for the case of 0.035%.

Figure 5.26 illustrates the spatial distribution of graphene stress as a function of the distance from the edge of the hole, for each X coordinate, in the case of 0.035% volume fraction nanolaminates. The stress graphene endures at applied strain 0.5%, as a reinforcement filler at low volume fraction nanolaminates at (X,Y)=(0,0) is ~8.5 GPa, which is the highest tensile strength ever observed for an embedded material, either in a form of sheets or as a filament close to a defect. Normally, the maximum stress that graphene can endure is ~5 GPa [134]. This again verifies that graphene is the strongest material that can be used for the reinforcement of composites. From the topographical study conducted, it is evident that at the areas close to the central point (as the offset from X=0 µm increases), the stress is a little lower than that of X=0, nevertheless, is quite high for a reinforcing material exceeding the reported values of pristine graphene even at areas X= 20 µm from the central point.

On the contrary, in the case of the high volume fraction nanolaminates (**Figure 5.27**), the maximum stress close to the defect is approximately half compared to that presented in the case of 0.035% volume fraction, as at Y=0 μm the stress is approximately 5 GPa when subjected to 0.5% external applied, a value which is also recorded at pristine graphene, which exhibits a fracture strength below 5 GPa when subjected to 0.4% external applied deformation [134].

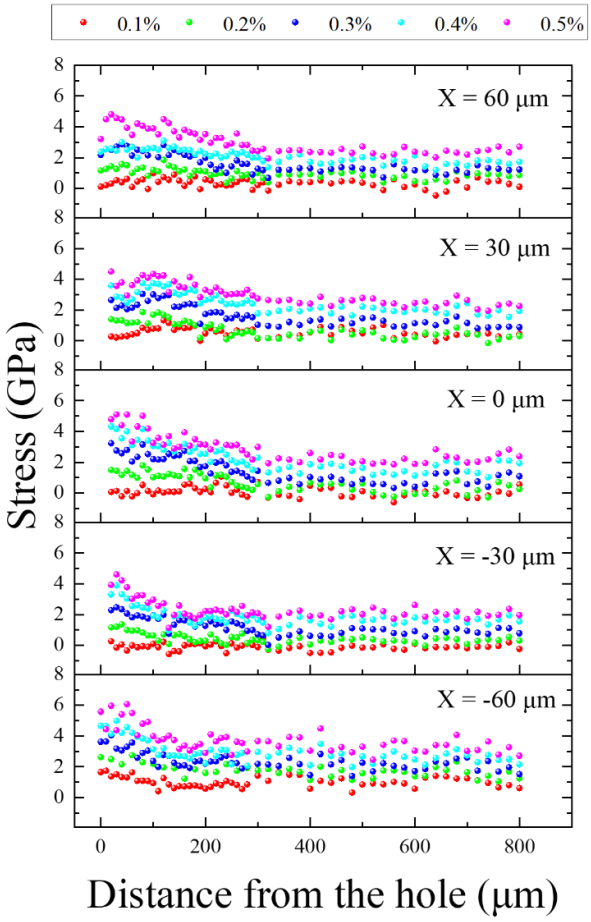


Figure 5.27: Line mappings of stress of graphene as a function of the x- coordinate and the distance from the hole for the case of 0.12% volume fraction.

Followingly, the stress concentration factor K_t, given by the Equation 5.4, where $\boldsymbol{\sigma_{max}}$ is the stress perpendicular to the load axis, at Y=0, and $\boldsymbol{\sigma}$ is the stress at the far field, was determined for the nanolaminates of each volume fraction.

$$\boldsymbol{K_t = \frac{\sigma_{max}}{\sigma}} \tag{5.4}$$

The stress concentration factor (SCF) was derived for each applied strain up to 0.5%, as it has been observed that at higher external applied levels, K_t remains constant or

diminishes [279]; as for higher strains, the material starts to fail close to the defect, by delaminating or due to cracks induced in the individual graphene sheets [333]. The determination of SCF is crucial for the comprehension of stress distribution close to defects existing in a material and especially in nanocomposites, as it can provide valuable information, over the prediction of their mechanical response and the failure mechanisms [49].

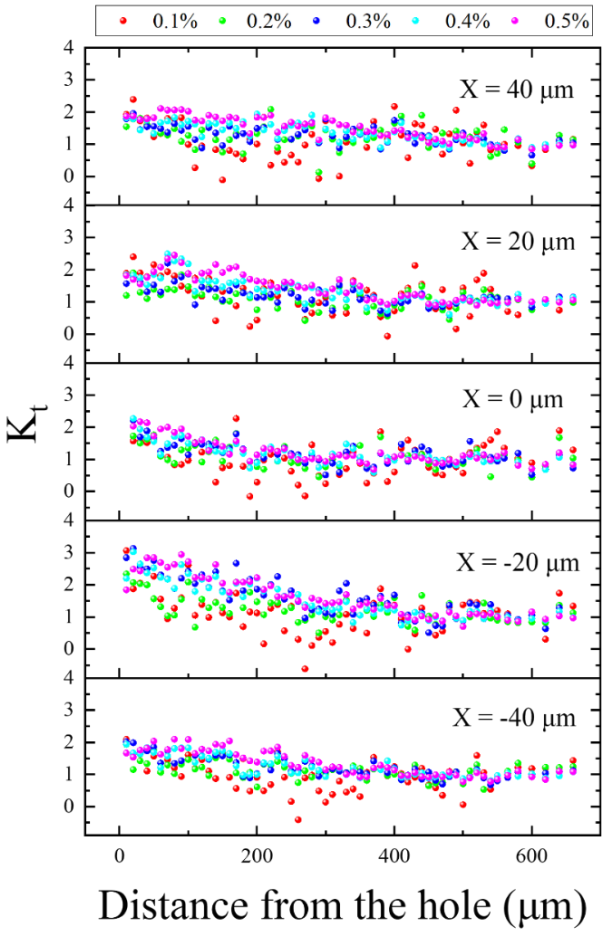


Figure 5.28: Line mappings of Stress Concentration Factor Kt as a function of the distance from the hole, for each x- coordinate, for the case of 0.035%.

In **Figure 5.28**, the topographical study of SCF for the case of low volume fraction nanolaminates is presented. In all X-coordinates the SCF ranges within 2.2 – 3, with the highest value observes at (X,Y) = (-20,0). The load that graphene experiences at the edge of the hole at X=-20 µm is approximately 3 times higher than that of the far field, whilst at the other X coordinates is 2-2.5 times higher. This implies that it is more probable for a crack to form near (-20,0), which could eventually lead to the failure of the specimens. Fracture occurring at coordinate X≠0 µm can be attributed either to

microdefects introduced during the laser irradiation procedure for the hole creation, or to errors in accurately determining the x-coordinate position.

Respectively, K_t for the case of 0.12% volume fraction nanolaminates, for each X coordinate, is presented in **Figure 5.29**. Herein, K_t is approximately 5.5 times higher at the edge of the hole at X=0, 30 μm, whilst in the neighboring areas reduces to 4 and 2 times (for more distant x-coordinates), compared to the far-field. This indicates that it is almost twice as probable (compared to the 0.035% nanolaminates) that a crack will arise from the edge of hole, implying that they are more brittle. This comes in agreement with the findings in **Figure 5.6**, in which nanolaminates of 0.12% volume fraction, fail earlier than those of 0.035% volume fraction (the ones containing a defect) and exhibit lower fracture toughness, with their corresponding K_c values being $0.72\ MPa\ m^{1/2}$ for the 0.12% and $0.81\ MPa\ m^{1/2}$ for the 0.035%. Moreover, for low external strains of up to 0.2%, it is highly probable that the Raman spectroscopy data exhibit considerable variation, conceivably due to the inadequate stretching of the sample. It is important to note that according to theory [102], the maximum stress concentration is expected at the minimum cross section of the specimen, perpendicular to the load axis. Possible deviations from this behaviour (i.e. fracture at coordinate X≠0 μm) can be ascribed either to further microdefects developed during laser irradiation for the hole creation, or the determination of the right positioning of the x coordinates.

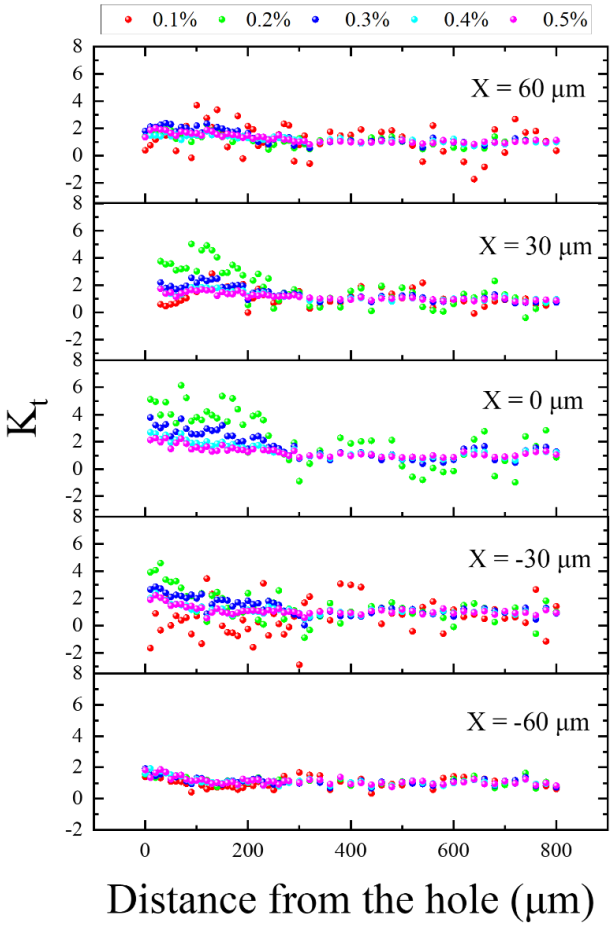


Figure 5.29: Line mappings of Stress Concentration Factor K_t as a function of the distance from the hole, for each *x- coordinate, for the case of 0.12%.*

The stress concentration factor is high in low strains of up to 0.2%, in both 0.035% and 0.12% nanolaminates, and then diminishes, remaining constant for higher applied strains. The increased stress concentration at low strains leads to the formation of phenomena like local microcracking, which results to the decrease of K_t.

5.4 Conclusions

In this thesis we have demonstrated that the graphene-based nanolaminates present significantly higher resilience to fracture than the neat PMMA, with the fracture toughness of the low and high volume fraction samples being ~48% and ~31% higher than that of the PMMA. Specifically, the fracture toughness of the neat PMMA is $0.55 \pm 0.07\ MPa\ m^{1/2}$, whereas in the low and high volume fraction nanolaminates it increases to $0.81 \pm 0.05\ MPa\ m^{1/2}$ and $0.72 \pm 0.05\ MPa\ m^{1/2}$, respectively. This

indicates that due to the addition of CVD graphene, mechanisms that impede the ultimate failure of the material in the form of microcracking deflection etc, are developed. Although the high volume fraction nanolaminates contain higher graphene content (and thus are stiffer than both the low fraction ones and the neat PMMA) they tend to fail prematurely, displaying a more brittle fracture, as they exhibit a two times higher stress concentration factor compared with the low volume fraction ones.

Furthermore, the knowledge over the stress distribution at the vicinity of the defect (hole in our case) is pivotal in understanding and predicting the final fracture of the material, as the stress concentration and thus the SCF vary significantly in nanocomposites, including graphene-based nanocomposites, depending on the type and the dispersion of nanofillers [334], the interfacial interactions [335] and the loading conditions [336]. Therefore, the comparison between the SCF occurring in a wide range of materials and experimental conditions is quite difficult, and that is the reason why there is no universal definition. Furthermore, the measurement of the stress concentration close to a defect, is also a quite challenging procedure, and therefore, the experimental calculation of the SCF is difficult. In fact, in most of the cases, computational modeling methods, such as Finite Element Analysis (FEA) or Molecular Dynamic simulations (MDs) is involved for the prediction of SCF [337].

Herein, Raman spectroscopy in combination with micromechanical testing was employed for the conduction of spectral mappings across a defect, in order to identify the areas presenting the higher stress concentration, which are more prone to failure. According to the analysis of stress distribution, the maximum stress that the material experiences is ~8.5 GPa and ~5 GPa, for the low and high volume fraction nanolaminates, respectively. This is a groundbreaking result proving that a small number of CVD graphene sheets used as nanofiller can provide both superior strength and resilience to a nanocomposite, exhibiting remarkable resistance to crack propagation. Comparing the SCF of high and low volume fraction nanolaminates, the former is significantly higher, indicating that fracture will occur faster in this material; this is validated from the more brittle behaviour of the 0.12% nanolaminates.

Concluding, these results prove that graphene, except from being a material with unique properties, it can be exceptional as a nanofiller. Graphene-based nanolaminates of low volume fraction present significantly higher ultimate tensile strength and fracture

toughness, indicating their remarkable resistance to crack propagation. Therefore, potentially, graphene-based nanolaminates can be used in various high performance applications.

6. Crack propagation and related morphological changes of exfoliated graphene monitored via Atomic Force Microscopy

This Chapter deals with the investigation of fracture mechanics (theoretically described in detail in Chapter 2) and other strain-induced morphological alterations of notched single and few layered graphene produced via mechanical exfoliation. Exfoliated graphene represents the ideal material for the investigation at the nanoscale of the morphological alterations that refer to changes in size, shape of the structure of the graphene sheets, when they are subjected to external deformation. The presence of a defect, such as a notch, in combination with the application of strain can lead to the stress concentration at the tip of the notch, resulting to a localized deformation or premature failure of the material. This, as well described in the previous Chapters of this Thesis, is of foremost importance in practical applications of graphene-based devices, as graphene sheets serve as reinforcing or conductive elements for applications such as nanomechanical devices or sensors [338][339]. As described in the Chapter, a novel technique based on the use of AFM nanoindentation tool has been implemented to inflict nanometric scale defect with controlled geometry and size into the graphene flakes. In-situ monitoring of flake morphology and crack propagation has been performed by adjusting a micro-tensile tester under the Atomic Force Microscope, allowing the accurate inspection of graphene features with high-resolution, as well as the extraction of fracture toughness. Therefore, a comprehensive examination of strain-induced morphological patterns in notched graphene sheets has been conducted, aiming to unveil novel insights and contribute to the advancement of nanotechnology field, through the design and optimization of nanomaterials with tailored properties and functionalities for future applications.

6.1 Production and selection of exfoliated graphene samples

Graphene flakes were produced via the mechanical cleavage method from HOPG (High Order Pyrolitic Graphite) using a commercially available scotch tape and were followingly deposited onto a SU8/PMMA substrate. SU8/PMMA-supported graphene

flakes were at first examined under the optical microscope, and both monolayer (see **Figure 6.1(a)**) and few-layered (see **Figure 6.1(b)**) flakes having adequately large size (higher than 10 × 10 μm^2) were selected for this investigation, in order to avoid edge effects and to ensure efficient load transfer [286].

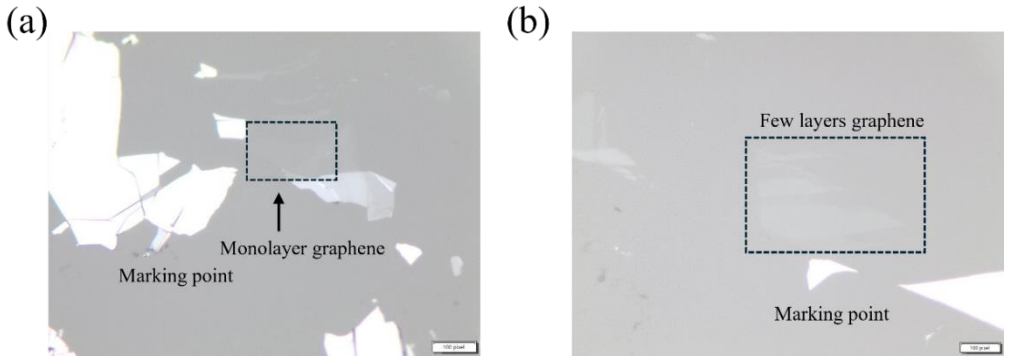


Figure 6.1: Optical micrographs of typical (a) monolayer and (b) few layers graphene flakes obtained through mechanical exfoliation of HOPG.

6.2 Quality control of the specimens via Raman spectroscopy and Atomic Force Microscopy

Raman spectroscopy was employed for the characterization and quality control of the selected samples (see Chapter 3). In **Figure 6.2(a,c)**, a monolayer (see inset) and a few-layered graphene are depicted, respectively. Indicative Raman spectra of mono- and few-layered graphene are illustrated in **Figure 6.2(b,d)**, respectively. Important information, such as the existence of residual strain, doping or the number of layers of the samples can be extracted from the typical features of the 2D and G peaks, which are prominent in Raman spectra.

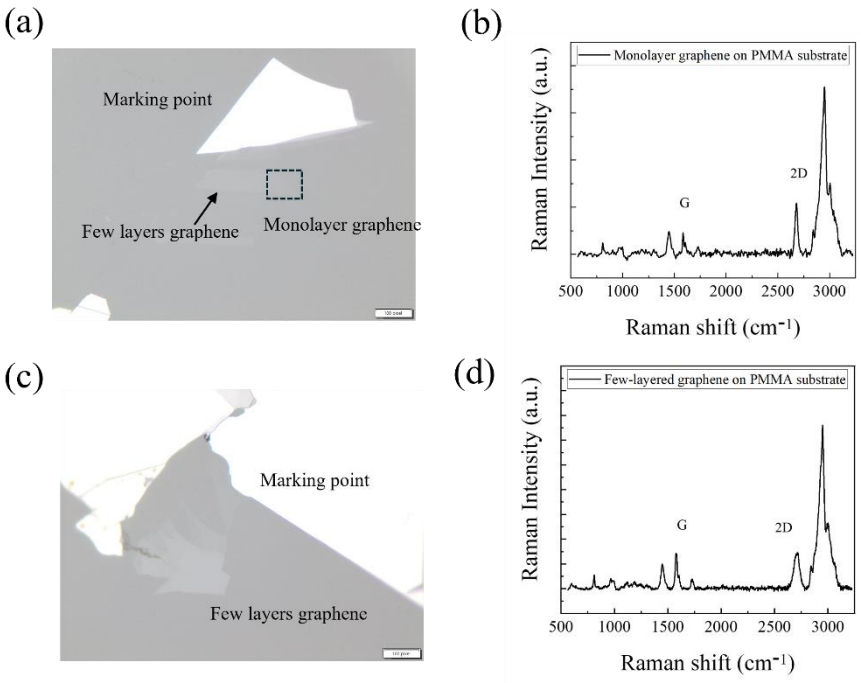


Figure 6.2: Illustration of (a) monolayer, (c) few layers graphene flakes under the optical microscope, and their corresponding Raman spectra at (b,d).

The 2D peak for the monolayer graphene is centered at ~2682 cm^{-1} (see **Figure 6.2(b)**) indicating that it is stress-free [340], and the FWHM of the peak fitted by a single Lorentzian is 28 cm^{-1}, while the G peak position is located at around 1582 cm^{-1} and has a FWHM of 14 cm^{-1}. The relatively narrow FWHM of the 2D peak and the ratio of intensities I_{2D}/I_G ~2 confirm the monolayer nature of the graphene flake under investigation. For the flake shown in **Figure 6.2(c)**, the 2D peak is centered at 2708 cm^{-1}, with a larger FWHM of 63 cm^{-1}, suggesting that this is a few-layered flake[341]. The G peak position is observed at around ~1580 cm^{-1} and has a FWHM of 14 cm^{-1} (**Figure 6.2(d)**). In both the flakes, the D peak located at 1350 cm^{-1} is negligible, indicating that graphene is defect-free. The I_{2D}/I_G ratio for the few layered graphene is ~1.3, verifying the high quality of the flakes. Apart from the graphene features, the spectra include the characteristic peaks of PMMA at ~1450 cm^{-1} [293] ~1730 cm^{-1} [293] and ~2952 cm^{-1}[294].

The morphology of graphene flakes was visualized by using Atomic Force Microscopy (AFM). The AFM images of the graphene flakes were acquired by an AFM microscope (Dimension Icon Bruker) using a Scanasyst-air probe of stiffness ~0.40 N/m and the topographical images of the flakes were obtained by the operating Peak Force QNM mode. **Figure 6.3** shows topographical images of a monolayer and a few-layered flake.

By using the cross-section function of the NanoScope® software, the height of the mono and few-layered flake under investigation was found to be ~0.5 nm and ~3.0 nm, respectively, thus confirming the monolayer and few-layered nature of the flakes. Moreover, some patterns can be detected by AFM, which could be ascribed to adhesive residue upon exfoliation process. The detection of these patterns was not possible neither through the optical microscope, nor through the Raman spectroscope.

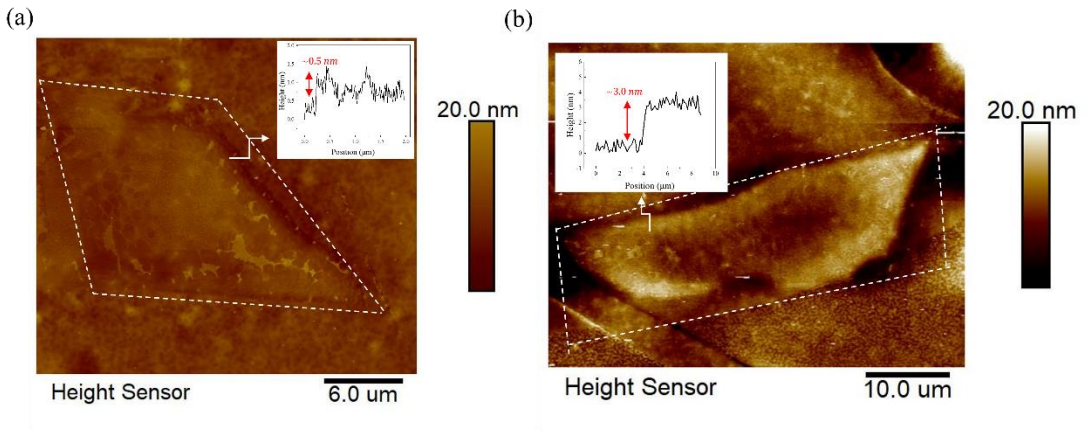


Figure 6.3: AFM topographical image of (a) a monolayer, and (b) a few-layered flake. Dashed lines are a guide to eye-emphasizing flake boundaries.

6.3 Optimization of AFM tip-induced defect

In order to create a defect with controlled nanometric size and shape and in a precise position of the micrometric graphene flakes, an ad-hoc methodology was implemented, which is based on the use of the nanoindenting and nanoscratching tool of the AFM. The application of small forces (μN) and the nanometric lateral size resolution give the possibility to create defects in the two-dimensional material without traumatizing its surrounding areas or damaging its interface with the substrate. Specifically, a dedicated probe for nanoindenting and scratching applications (DNISP, Bruker) consisting of a natural diamond tip (nominal apex radius of 40 nm) mounted on a stainless steel rectangular cantilever (stiffness 286.52 N/m and frequency of 65 kHz) was adopted for the defect creation (see **Figure 6.4**). The location, size and the applied indenting force were set in Tapping mode, using the function “Point and Shoot” of the NanoScope® software. It is important to note that the DNISP probe is not for use in general AF M imaging; therefore, the topography of the graphene flakes after the creation of the

defects has been observed in PeakForce QNM mode, as already mentioned in par. 6.2, using a Scanasyst-air probe (spring constant ~0.40 N/m, frequency ~70 kHz, tip radius ~2 nm).

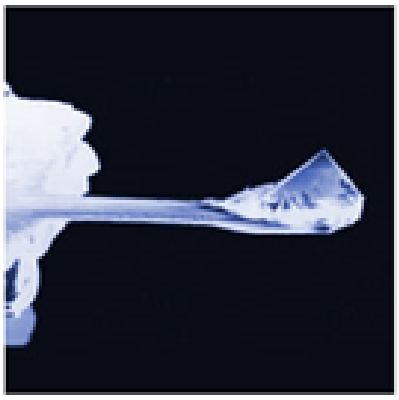


Figure 6.4: SEM of the DNISP AFM probe.

A preliminary investigation to set the adequate force required for the local tearing of graphene, without causing further deformation or damage to the sample, was conducted. Specifically, a region of interest was selected, and a defect was created onto the graphene surface , applying forces from 1 to 20 μN . The AFM image depicted in **Figure 6.5** shows the creation of defects (indicated by capital letters A-K) in monolayer graphene supported on PMMA, using different indenting forces listed in **Table 6.1**. In the case of forces smaller than 10 μN, no damage could be successfully inflicted to the specimen. From 10 μN to 14 μN, the DNISP tip cuts graphene, with the diameter of the hole-shaped defect being relatively steady (~ 0.1 μm), while from 15 μN to 20 μN the diameter of the defect has clearly increased (~ 0.2 μm) and areas close to it, have been slightly lifted. The shape of the defects conforms with the shape of the tip in all cases; however, the lateral size of the produced hole increases with the applied force, as higher force induces higher indentation depth into the sample.

Next, a line-shaped defect was induced by using force of 10 μN. The nanoscratching process consists of repetitive nanoindentation at adjacent locations along a specific pattern (in this case a 1.5 μm-long line). From the AFM image shown in **Figure 6.5(b)**, it is evident that employing forces up to 5 μN does not result in the formation of a clear line cut. On the contrary, increasing the force above 10 μN causes the damage of the substrate, reducing the adhesion of the flake with it, resulting to its further lifting of the edges of the cut. In light of that, the indenting force was not further increased.

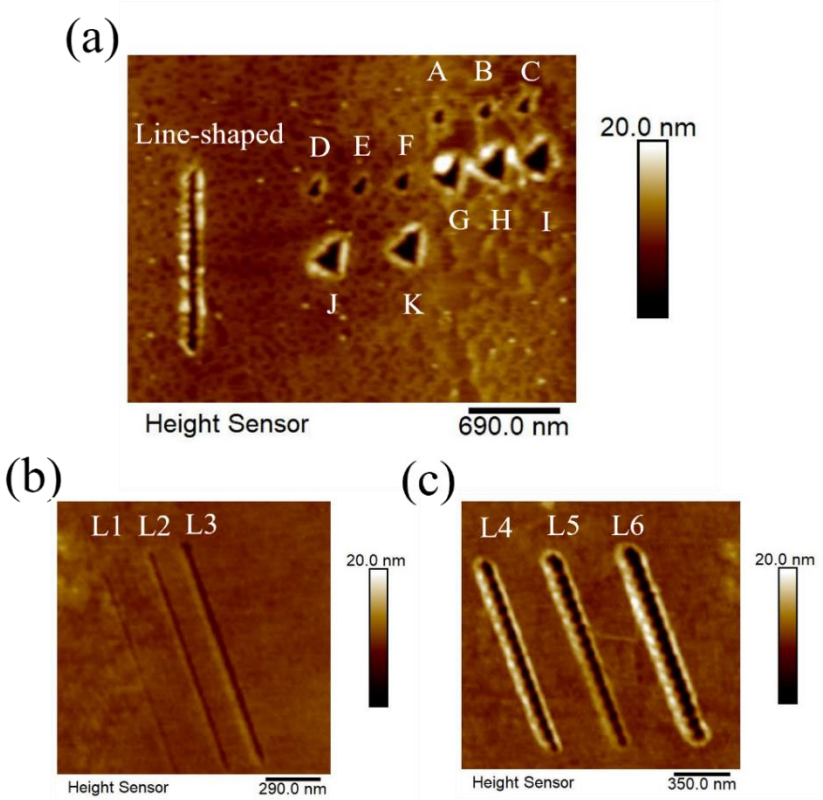


Figure 6.5: Preliminary investigation of nanoindentation/ nanoscratching process for the creation of a defect, (a) spots (denoted as A – K (see Table 6.1)) and, (b,c) line-cuts (denoted as L1 – L6 (see Table 6.2)): AFM images of a graphene monolayer supported on PMMA after application of different indenting forces.

Table 6.1: Correspondence of nanoindentation force with the defect shown in the AFM image shown in Figure 6.5*(a).*

	A	B	C	D	E	F	G	H	I	J	K	Line
Force (µN)	10	11	12	13	14	15	16	17	18	19	20	10

Table 6.2: Correspondence of nanoindentation force with the line-cut defect shown in the AFM image shown in Figure 6.5*(b,c)* .

	L1	L2	L3	L4	L5	L6
Force (µN)	3	4	5	10	15	17

A high-resolution AFM image of the line scratch created in the monolayer graphene shows that the notch tip has a triangular geometry that replicates the shape of the diamond tip; no further corrugations or damage has occurred in the graphene flake in

the proximity of the notch, (**Figure 6.6**), thus suggesting the feasibility of the proposed technique for the investigation of fracture mechanics in notched graphene flakes.

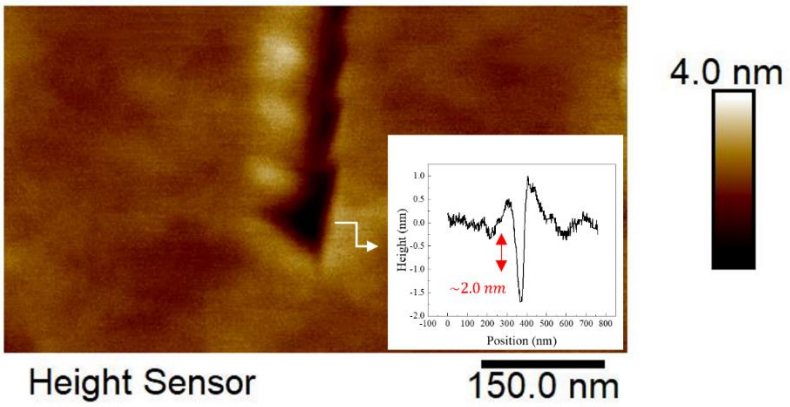


Figure 6.6: High-resolution image of a typical notch induced at the edge of the graphene flake.

6.4 Cracking of exfoliated graphene: formation and propagation

Comprehensive insight into strain-induced changes of graphene's surface morphology can be achieved via the combination of AFM with micro-tensile testing of the simply supported graphene flakes. Particularly, the real-time observation of the material's behaviour under load can unravel deformation mechanisms providing direct evidence of phenomena such as crack initiation and propagation.

The examination of graphene's morphology close to the defect is extremely important and very few studies in the literature have been reported so far [10-14]. AFM images can reveal the formation of structural defects, such as vacancies, adatoms, or grain boundaries, near the defect site [342]. When the sample is subjected to tension, a defect acts as a point of high stress concentration causing morphological alterations at the region around it. This induced localized deformation can cause non-uniform surface features or height variations, while strain-induced wrinkles or ripples can also be present [343][344]. When the applied strain reaches a critical value, causing the crack initiation at the vicinity of the defect, AFM images can capture this propagation and provide indicative images of discontinuities or step-like features in graphene's surface. Therefore, AFM provides valuable insights into how defects influence the morphology and mechanical behaviour of graphene under tension, offering a nanoscale perspective on the material's response to applied stress [345][112].

6.4.1 The case of monolayer graphene

The morphological alterations in notched graphene under the application of a tensile deformation were monitored via AFM in PeakForce QNM mode using a Scanasyst-air probe (spring constant ~0.40 N/m, frequency ~70 kHz, tip radius ~2 nm). The micro-tensile tester (Deben MT200) was adjusted under the microscope, as shown in **Figure 6.7**. Next, a defect was inflicted on each graphene flake examined, following the methodology described in **par. 6.3**, and reference images (before the imposition of strain) were acquired for comparison purposes.

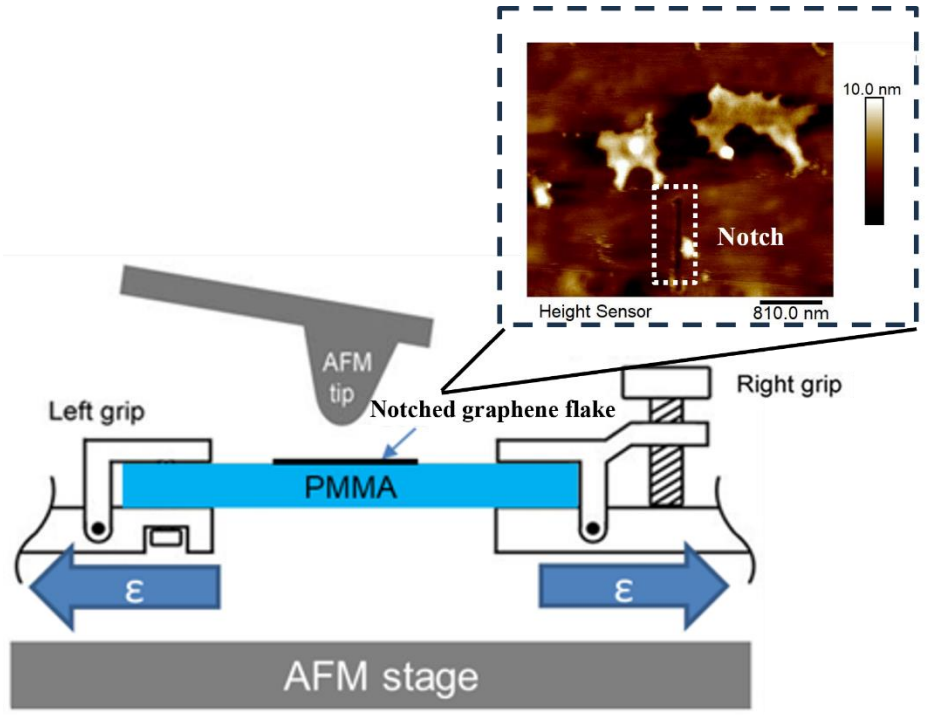


Figure 6.7: Schematic illustration of the specimen configuration to impart measurable strain to notched graphene. The load axis is the horizontal axis.

Figure 6.8 shows the AFM images that were acquired from the notched monolayer graphene (with the dimension of the line-cut defect being ~ 1.0 μm length and ~ 0.1 μm width) under the application of a uniaxial tensile loading. The images depicted, refer to actual graphene strain of 0.00%, 0.39%, 0.45%, 0.51%, 0.57% and 1.1%, as derived from the phonon secular equations [210] (prior to in-situ AFM investigation, preliminary experiments were conducted on the same specimen to measure the phonon

shift upon the imposition of an applied strain via Raman spectroscopy, as described also in Chapter 4). The loading increases quasi-statically by small increments (~ 0.06%). For simplicity, images taken when no change occurs during the tensile procedure (e.g. during actual graphene strain 0.00% - 0.39%, when no fracture is observed), are omitted.

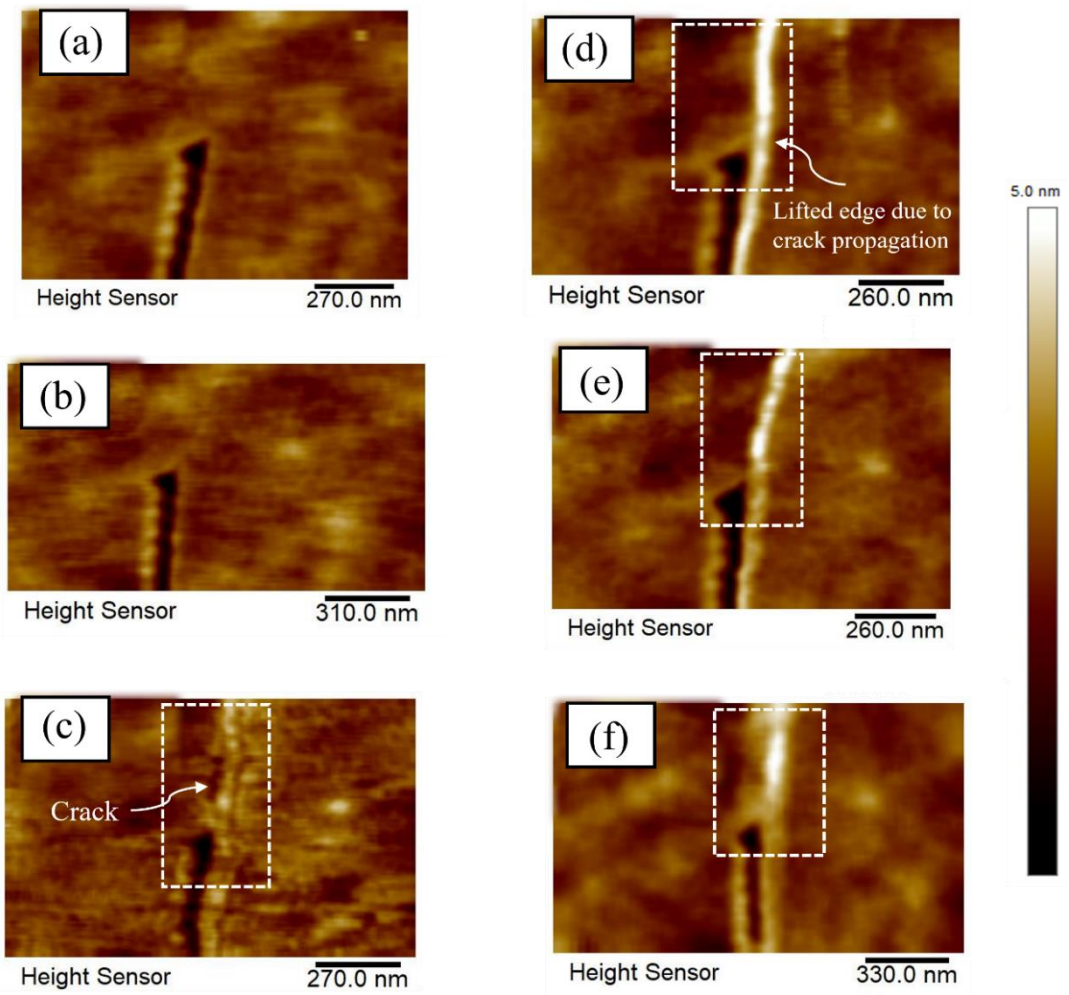


Figure 6.8: AFM visualization close to the line-cut defect at the edge of the graphene sheet at various actual graphene strains (a) 0.00%, (b) 0.39%, (c) 0.45%, (d) 0.51%, (e) 0.57%, and (f) 1.1%. The load axis is the horizontal axis.

Graphene remains intact, despite the existence of the line-cut defect at actual strain up to 0.39% (**Figure 6.8(a,b)**). It is interesting noting that at 0.45% strain, a crack arises and propagates from the tip of the line-cut defect (see **Figure 6.8(c)**), and this is in agreement with previous studies on crack propagation in graphene as indirectly monitored via Raman spectroscopic mapping [134]. In most cases, the crack propagation is almost instantaneous across the sample, and that is due to the brittle nature of graphene when it presents a defect [129]; after crack initiation, propagation

rapidly enters its unstable phase, and develops perpendicularly to the load direction, leaving lifted edges, alongside the crack (**Figure 6.8(d-f)**). It is evident from the adhesion image that the crack arising from the defect, has teared the graphene sheet from the lower to the upper edge (**Figure 6.9)**.

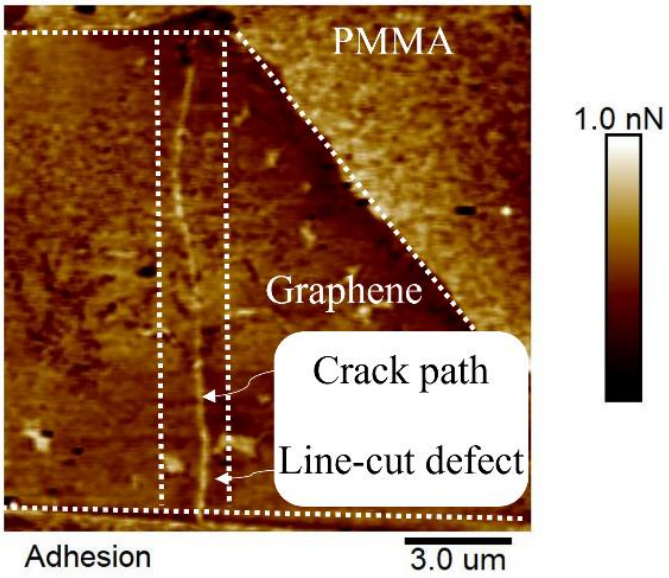


Figure 6.9: Adhesion mapping of the graphene flake after the application of incremental strain. The load axis is the horizontal axis.

Figure 6.10 compares the morphology of the monolayer graphene flake, before and after the tensile test. In **Figure 6.10(a)**, the height image of graphene's surface before the application of strain is given, where no corrugations or any other damage occurs, close to the induced defect. However, after the application of the incremental strain and the unloading of the sample, the crack has initiated from the defect and has propagated throughout the sample, perpendicularly to the applied load (**Figure 6.10(b)**). The crack path can be interpreted as the most favorable path that is followed for the relief of the stress concentration. It is evident that the presence of the crack in combination with the applied load has inflicted the splitting of the material, leaving two edges of the graphene layer slightly lifted (**Figure 6.9)**.

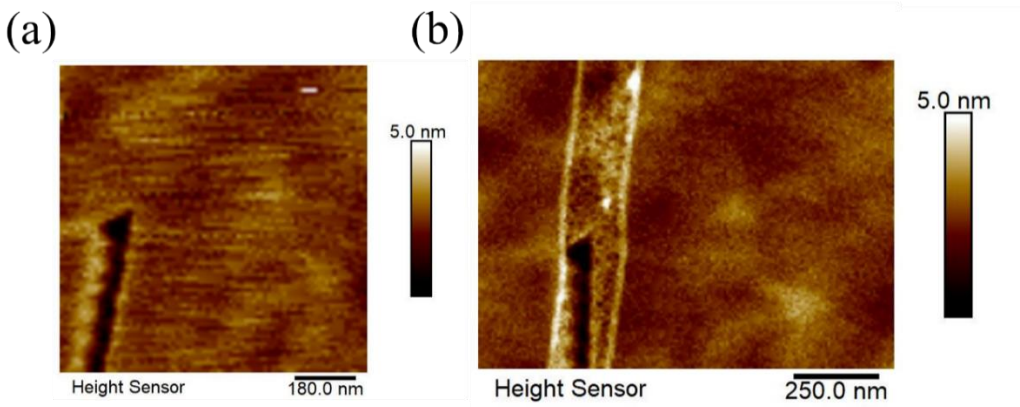


Figure 6.10: Topographic mapping of the graphene flake (a) before, and (b) after the application of incremental strain. The load axis is the horizontal axis.

Figure 6.11(a,b) shows a high-resolution topographic image of the fracture and the corresponding adhesion mapping. In between the free edges of graphene created due to the crack propagation, the surface of SU8/PMMA is displayed, where the adhesion has higher value, and an increased surface roughness compared to the graphene sheet is observed. Very interestingly, at the edges of the fracture line graphene appears slightly lifted, and this can be ascribed to local lack of adhesion (as revealed by the lower adhesion forces in the corresponding mapping). In order to measure the distances between the two edges of the crack and the zone where graphene is lifted, a cross section of the white-dashed line depicted in **Figure 6.11(a),** is given in **Figure 6.11(c)**. The distance between the two free graphene edges is approximately 122 nm (blue dashed lines), while the difference in the height of the lifted edges compared to the rest of the graphene sheet is approximately 1.5 nm (green dashed lines). The PMMA with the lifted graphene edges has a height difference of approximately 2 nm (red dashed lines), and the inner part of the crack has a vertical distance of approximately 0.4 - 1 nm compared to regions outside the crack (magenta dashed lines). This range of values, which exceeds the thickness of monolayer graphene (0.334 nm), is due to the roughness of the PMMA/SU8 substrate.

The observation of a crack arising close to the defect and its propagation perpendicular to the load axis can be attributed to several factors related to the nature of the defect and the material's mechanical response. In general, stress distribution within the material is greatly affected by the existence of a defect, as it may act as point of stress concentration. In turn, this increased local stress results to a higher localized deformation of the material [346]. If the localized stress surpasses the material's fracture

strength, it will lead to crack initiation. Therefore, graphene's inherent material properties, such as fracture toughness and interlayer bond strength are important parameters in the study of crack propagation. It is important to note that perfect graphene presents very high strength and resistance to fracture ($\approx 100\ GPa$ [347]); nevertheless, if a defect is present, due to stress concentration close to it, the actual strength is can be much lower (≈ 10 GPa or less [348]), and therefore crack formation becomes easier. The direction of crack propagation is mainly affected by stress distribution, which is determined by the geometry and the location of the defect, as well as the applied stress. The defect created before the load application, is located at the edge of the graphene sheet and the direction of crack propagation is perpendicular to the strain axis, minimizing the overall stress on the material. In general, the stress distribution near the edges of graphene varies from that in the center, and this strain gradient occurs due to several factors, such as boundary defects (i.e. edge vacancies, edge atoms, etc.), the presence of free edges, material geometry, and its mechanical properties. Precisely, the edge atoms, have higher potential energy compared to inner atoms, as they participate in fewer covalent bonds and bond-bending angles compared to atoms located in the interior regions of the sheets, and therefore contributing less to the flexural rigidity (its ability to resist bending or deformation under stress) of the material and rendering them prone to buckling under compressive loads [349]. Thus, edges exhibit higher strain levels under the same stress conditions and crack initiation is more likely at the edge of a graphene sheet (which is independent from the existence of a notch).

Considering that the Young' modulus of monolayer graphene is 1 TPa, when the actual strain of graphene is $\sim 0.45\%$, the tensile strength can be estimated to be ~ 4.5 GPa, a value that is much lower than $100\ GPa$. This significant drop of the tensile strength, as already observed in similar systems where tensile strength values below 5 GPa are recorded [134][348], is attributed to the presence of the defect.

Delving into the stress field at the vicinity of the crack, where fracture mode I predominates, the stress components are given by the equations described in Chapter 2 [108]. When the crack is formed perpendicularly to the load axis ($\theta = 0$), and the stress field is described by the equation:

$$\sigma_{yy} = \frac{K_I}{\sqrt{2\pi r}} \tag{6.1}$$

Where $\sigma_{yy} = \sigma$ is the applied strain. Thus, the SIF can be expressed as follows:

$$K_I = \sigma\sqrt{2\pi r} \tag{6.2}$$

Fracture will occur when the crack formed will transcend from the stable phase to the unstable. At this point, stress σ exceeds a critical value σ_c, and K_I reaches the value of K_{IC}, which is the fracture toughness of the material, and for a crack of a length is given by the equation:

$$K_{IC} = \sigma_c\sqrt{\pi a} \tag{6.3}$$

Considering that the crack length is 1 μm, the K_{IC} of graphene can be estimated to be $7.97 \pm 2.10\ MPa\sqrt{m}$, which is higher than values quoted in literature for graphene [129][134]. According to the study of Zhao et al. [134], when the crack is sharp, the estimated value of K_{IC} is approximately 4.0 $MPa\sqrt{m}$, whilst in the case of a blunt crack, K_{IC} is approximately 9.2 $MPa\sqrt{m}$. Therefore, it can be safely concluded that the crack is blunt.

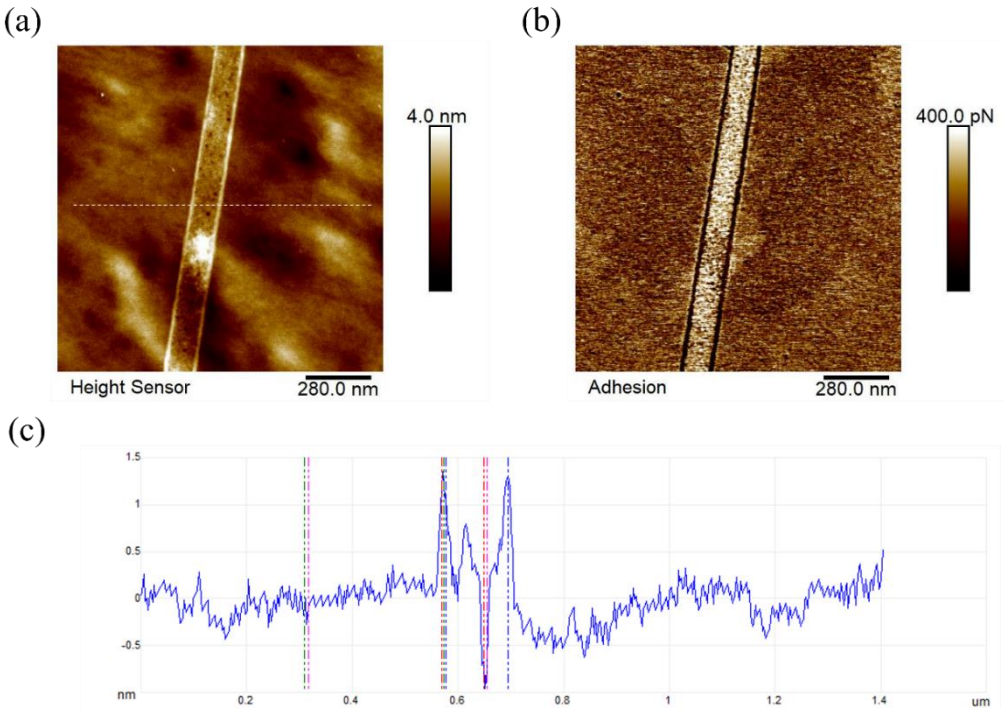


Figure 6.11: High-resolution (a) topographic and (b) adhesion mapping of the fracture in supported monolayer graphene. (c) Cross-section at the white-dashed line in (a) displaying the horizontal distance between the teared graphene edges (blue dashed lines), the height of the lifted edges compared to the rest graphene sheet (green dashed lines) and the PMMA (red dashed lines), the height difference between the PMMA and the regions outside the crack (magenta dashed lines). The load axis is the horizontal axis.

6.4.2 The case of few-layered graphene

The morphology of a notched few-layer graphene (lower than 10 layers) flake under uniaxial tension was also investigated. In the case of the flake in **Figure 6.12**, we can observe the existence of some wrinkles before the application of the load, without forming any motif, which can be attributed either to the intrinsic stress during the exfoliation procedure [350], either to the interaction between the graphene layers and the SU8/PMMA substrate. The creation of the defect did not cause any damage to the neighbouring area, as no corrugation or wrinkle formation is observed.

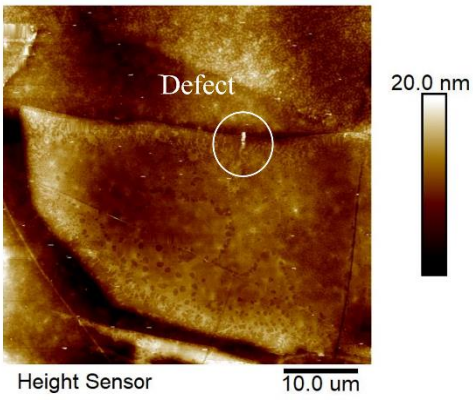


Figure 6.12: Topographic mapping of a few-layered graphene flake when no strain is applied. The defect induced is marked inside the white circle.

Next, the specimen was subjected to step-wise incremental loading, and after each step AFM images were taken for the examination of the area close to the defect, in order to monitor the crack formation. From **Figure 6.13(a)** we can observe that at 0.32% actual strain, a small crack seems to be formed at the edge of the defect, which propagates at 0.62% strain, even though it is not clear in the height image of **Figure 6.13(b)**, but it is apparent in the adhesion image. The fracture toughness K_{IC} of the multilayer graphene is approximately $11.0 \pm 2.3\ MPa\sqrt{m}$, which is higher than the value of monolayer graphene. The fracture is evident at 0.95% actual strain, in both the height and the adhesion images (see **Figure 6.13(c)**).

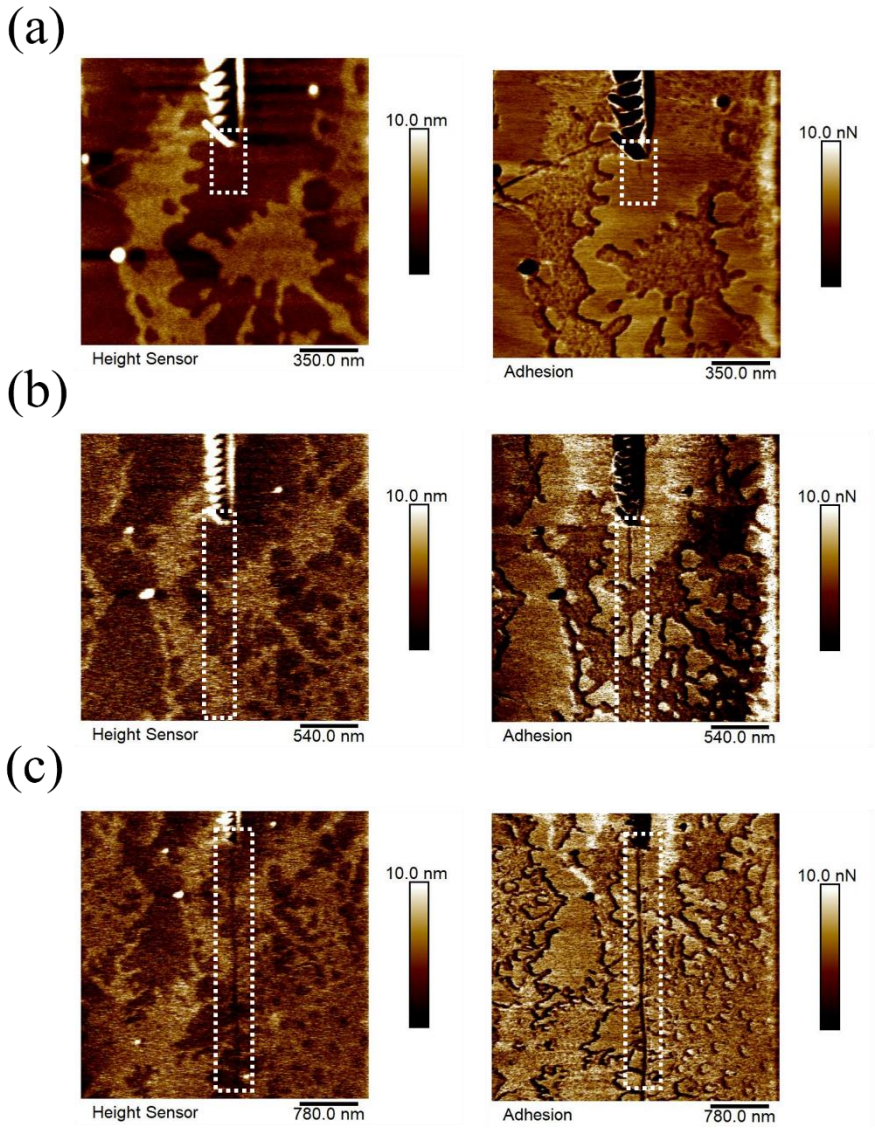


Figure 6.13: Topographic and adhesion mapping of the graphene flake when (a) 0.32%, (b) 0.62%, and (c) 0.95% actual strain. The load axis is the horizontal axis.

In **Figure 6.14** the topographical mappings in areas where the crack has propagated are given. As in the case of the monolayer flake that was studied earlier, the crack has propagated perpendicularly to the applied load, nevertheless, deflects when it encounters an "anomaly" (**Figure 6.14(f)**), and returns to the perpendicular direction, reaching the lower boundary of the flake. The tearing of the graphene sheets is evident also in **Figure 6.14(d),** where two wrinkles (see into the white frame) parallel to the load axis stop their propagation at the free edge of the teared graphene sheets. The crack path can be interpreted as the path that is the most favorable for the stress concentration relief.

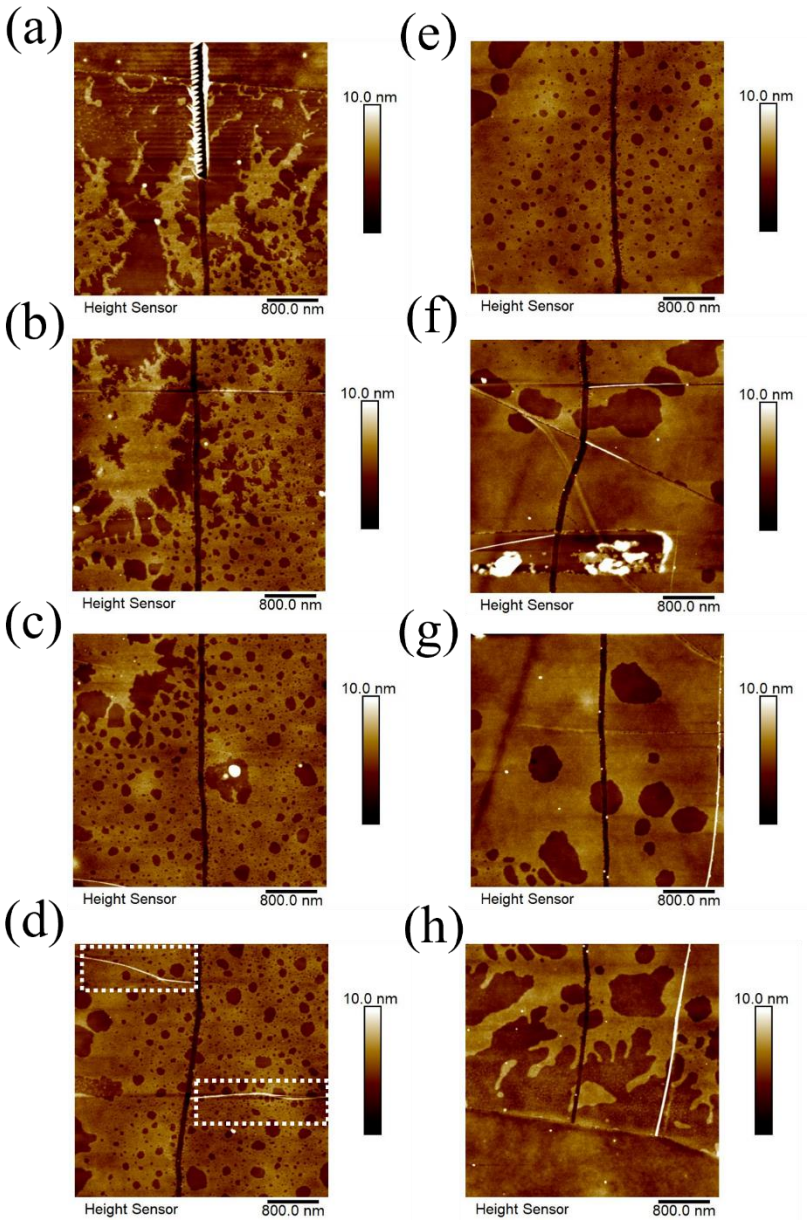


Figure 6.14: Topographic mapping of the few-layers graphene flake upon unloading. The load axis is the horizontal axis.

Comparing the crack propagation process in the monolayer and the few-layer graphene flakes studied in this dissertation, it is observed that the crack initiation occurs in most of the cases at approximately 0.45% and 0.62% actual strain, respectively. These findings agree with similar systems in literature (as was previously mentioned in **par. 6.4.1**), where crack propagation in monolayer graphene occurs at strain levels between 0.40 % - 0.44 %, with K_{IC} being approximately 4.0 $MPa\sqrt{m}$ and 9.2 $MPa\sqrt{m}$ for sharp and blunt crack respectively [134]. In the case of few layered graphene, the extra sheets contribute to the mechanical stability of the system, providing some level of mechanical

reinforcement and stress distribution between the sheets, therefore, they tend to exhibit enhanced resistance to the crack initiation [132], or the propagation will be slower, in case that some (and not all the) sheets tear apart [351]. Nevertheless, it is also possible that few-layered graphene contains more structural defects which may facilitate the crack propagation process. This ability of distributing and dissipating the stress to the adjacent layers, cannot be found in monolayer graphene, which is more susceptible to fracture as there are no other supporting layers.

6.4.3 Other strain-induced morphological features observed in monolayer and few-layered graphene

One interesting phenomenon during crack propagation is crack deflection [134]. As seen in **Figure 6.15(a)** no crack is formed when the sample is at rest. However, at actual graphene strain 0.45%, a crack initially is formed in an oblique angle relative to the primary loading axis, but then deflects and realigns perpendicular to the loading axis (see **Figure 6.15(b)**). In general, the fracture path occurs primarily along the zigzag direction, which exhibits slightly lower fracture energy compared to the armchair direction [352]. Nonetheless, it has been demonstrated in literature that regardless of the flake's crystallographic orientation, the crack path becomes approximately perpendicular to the tensile axis, as a result of the asymmetric stress field at the crack tip [353][134].

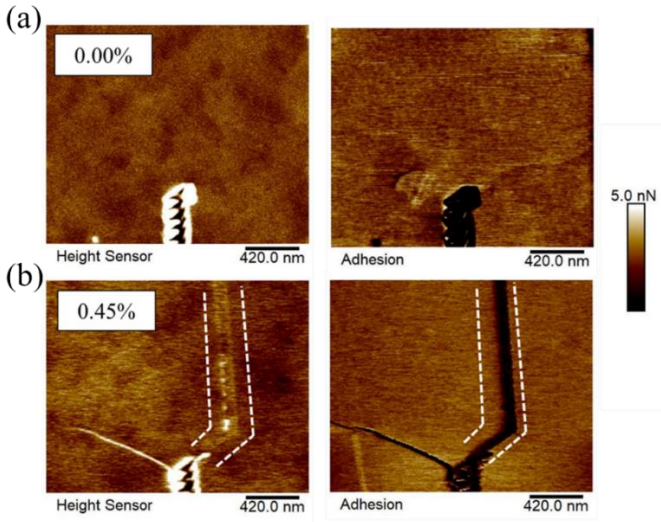


Figure 6.15:Topographic and adhesion mapping of a monolayer graphene (a) at rest, and (b) at 0.45% actual strain.

Crack deflection is not a phenomenon limited to monolayer graphene, but is also observed in few layered graphene, however the morphology observed is more complex. **Figure 6.16(a)** illustrates the morphology of few-layers graphene at rest, while **Figure 6.16(b)** shows the area close to the induced defect. It is evident that the creation of the defect has not created any damage to the area close to it.

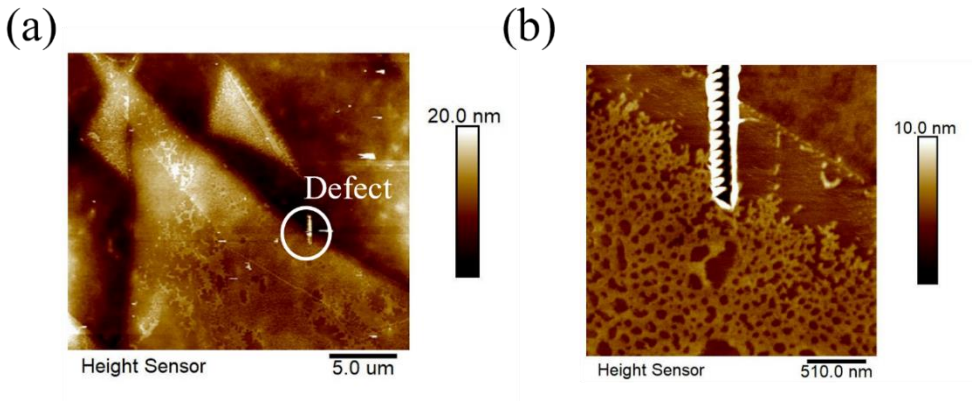


Figure 6.16: Topographic mapping (a) of a few layers flake, and (b) the area close to an induced defect, when sample is at rest.

At 0.62% actual strain, the surface's morphology has been clearly altered. The morphological mappings of the areas close to the defect existing in the graphene edge is depicted in **Figure 6.17**. Herein, both crack (noted as "A") and wrinkle (noted as "B") formation arise from the edge of the defect, at actual graphene strain 0.62% and 0.32% (**Figure 6.17(a)**). The crack arises from the tip of the defect (**Figure 6.17(a)**) and propagates at an angle to the load axis (**Figure 6.17(a, b, c_i)**). Then, the crack deflects and orients perpendicularly to the load axis (**Figure 6.17c_i**), and stops when it crosses paths with another crack (**Figure 6.17(d_i)**). Furthermore, the increased stress concentration has given rise to a wrinkle system, which is expressed through the existence of undulations or folds on the graphene surface (**Figure 6.17(a,b)**). These wrinkles come across with other folds or generate new ones (**Figure 6.17(b,c_{ii})**) due to the increased strain gradient of the area, and their termination occurs when they meet a free edge of the graphene sheet, which has been created due to the propagation of a crack (**Figure 6.17(d_{ii}, e_{iii})**).

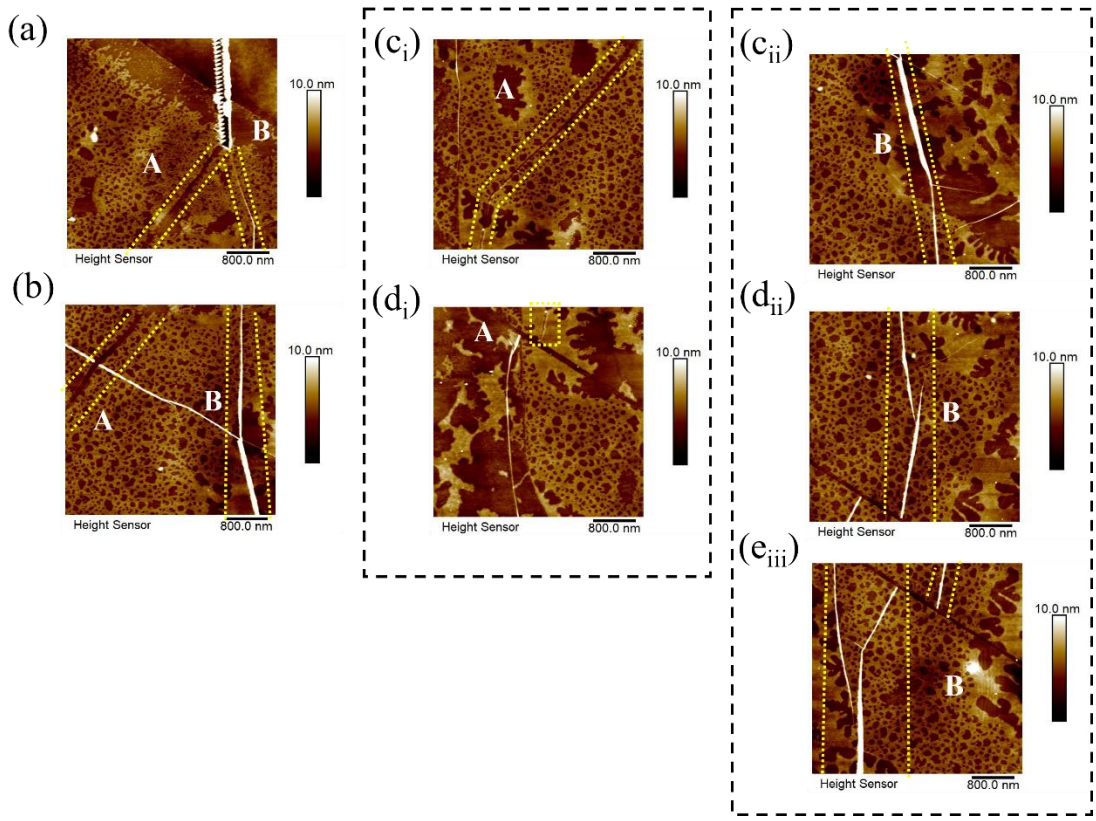


Figure 6.17: Topographic mappings of the corrugations initiated from induced defect at the upper edge of the graphene sheet (a- eii). The load axis is the horizontal axis.

Lastly, except from the wrinkles, cracks, and other corrugations, in a monolayer graphene flake, a unique morphology has appeared (**Figure 6.18)**. The corrugations observed cannot be classified as regular wrinkles or ripples as they appear to have a radial pattern possibly due to the complex strain gradient at the tip of the defect. Specifically, the corrugations that lie in proximity to the defect align almost radially to its tip, whereas the farther their distance, the more parallel they become (perpendicular to the load axis).

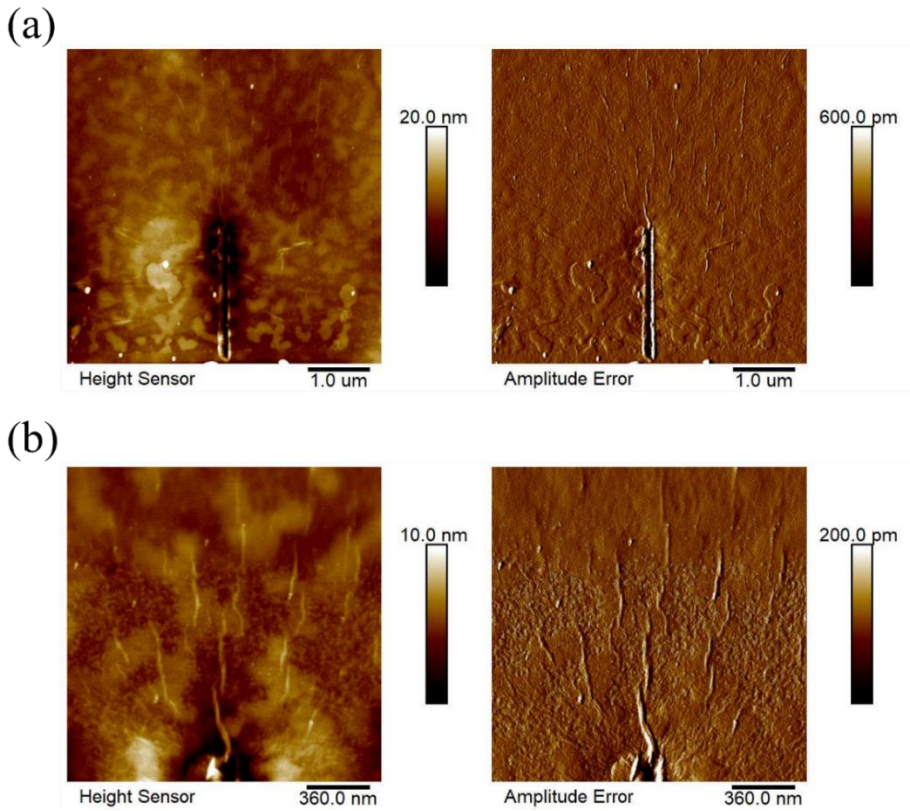


Figure 6.18: (a) Unique morphology induced on graphene's surface due to the presence of a defect, (b) zoom at the area near the tip of the defect. The load axis is the horizontal axis.

6.5 Fatigue of exfoliated graphene

Fatigue study of materials has always been of high interest, as fatigue failure can occur at stress levels much lower than the static fracture strength [354]. As graphene stands out among 2D materials due to its unique characteristics, the exploration of its mechanical fatigue is important in applications such as stretchable electronics and artificial skins [354][355][356]. Cui et al. examined the fatigue of suspended monolayer and few-layer graphene (via AFM), demonstrating a fatigue life of more than 10^9 cycles at a mean stress of 71 GPa [354]. According to the authors, fatigue failure in monolayer occurs without progressive damage, while Molecular Dynamic simulations (MDs) reveal that fracture is preceded by stress mediated by stress-mediated bond reconfigurations near defective sites [354]. The same group showed that, in the case substrate-supported graphene, the van der Waals interactions at the graphene-polymer interface can induce substantial fatigue fracture of graphene through a combination of in-plane shear and out-of-plane tear mechanisms [356]. Wang et al. studied the strain

transfer at the graphene-polymethyl methacrylate (PMMA) interface under repetitive loading with 0.7% strain, by combining in-situ Raman spectroscopy and AFM measurements, reporting a stress transfer efficiency loss of ~ 40% after 10 cycles, due to graphene buckling [355].

Herein, mechanically exfoliated graphene flakes deposited onto SU8/PMMA are subjected to cyclic mechanical loading. After graphene's deposition onto the substrate, the specimen was subjected to uniaxial tension, until the actual graphene strain is approximately 0.45% and then the strain was released slowly, in order for the sample to return to its initial state. In that way, the 1st cycle of the cyclic mechanical loading was completed, and this procedure was followed for 1000 cycles. This small external strain was chosen in order for the substrate to be in the elastic area, and not be plastically deformed, allowing the stress transfer from PMMA to graphene [357][296]. In **Figure 6.19(a)**, the morphology of a monolayer graphene flake which does not have any prior induced defect is depicted, while in **Figure 6.19(b_i, c_i, d_i)** graphene's morphology at 200th, 500th, and 1000th cycles, respectively is presented. During previous cycles, some minor alterations occurred at the area, but there were no wrinkles or folds formed. High resolution topographic images of the craze formed are depicted in **Figure 6.19(b_{ii}, c_{ii}, d_{ii})**. Specifically, at 200th cycle, it seems like a crack has occurred, with the sheet being locally lifted after its creation (**Figure 6.19(b_{ii})**). However, its morphology is slightly altered on the 500th and 1000th cycle (**Figure 6.19 (b,c)**) likely due to the strain redistribution at the area.

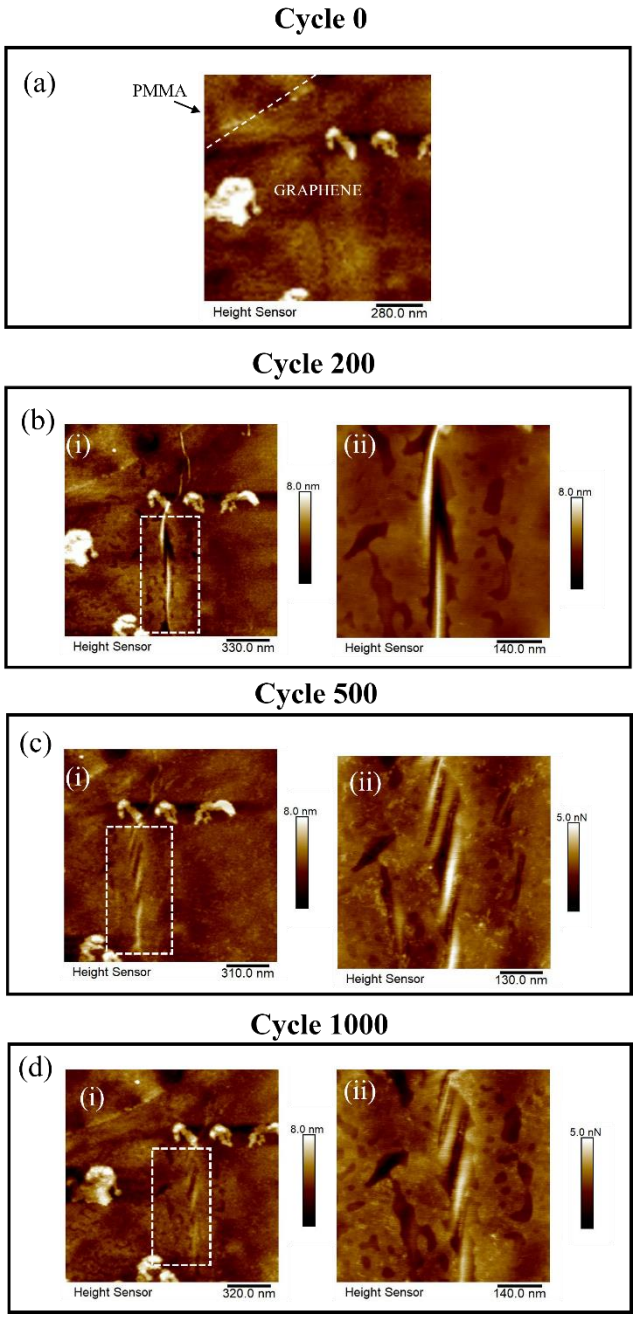


Figure 6.19: Topographic mappings of the graphene flake at (a) rest, (b) 200th, (c) 500th, (d) 1000th cycle. The images indicated by (ii) illustrate the area with the corrugation of the corresponding (i). The load axis is the horizontal axis.

In general, in monolayer exfoliated graphene, corrugations occur locally, and they are not dispersed throughout the sample. For instance, in **Figure 6.20(a,b)**, a craze has been created in the 200th cycle onto the graphene's surface, initiating from the upper edge of the sheet, uplifting the area within which it propagates. As seen in **Figure 6.20**, in the case of 1000th cycles, the wrinkle only acquired greater length, while no signs of other wrinkle patterns were observed (**Figure 6.20(a-d)**).

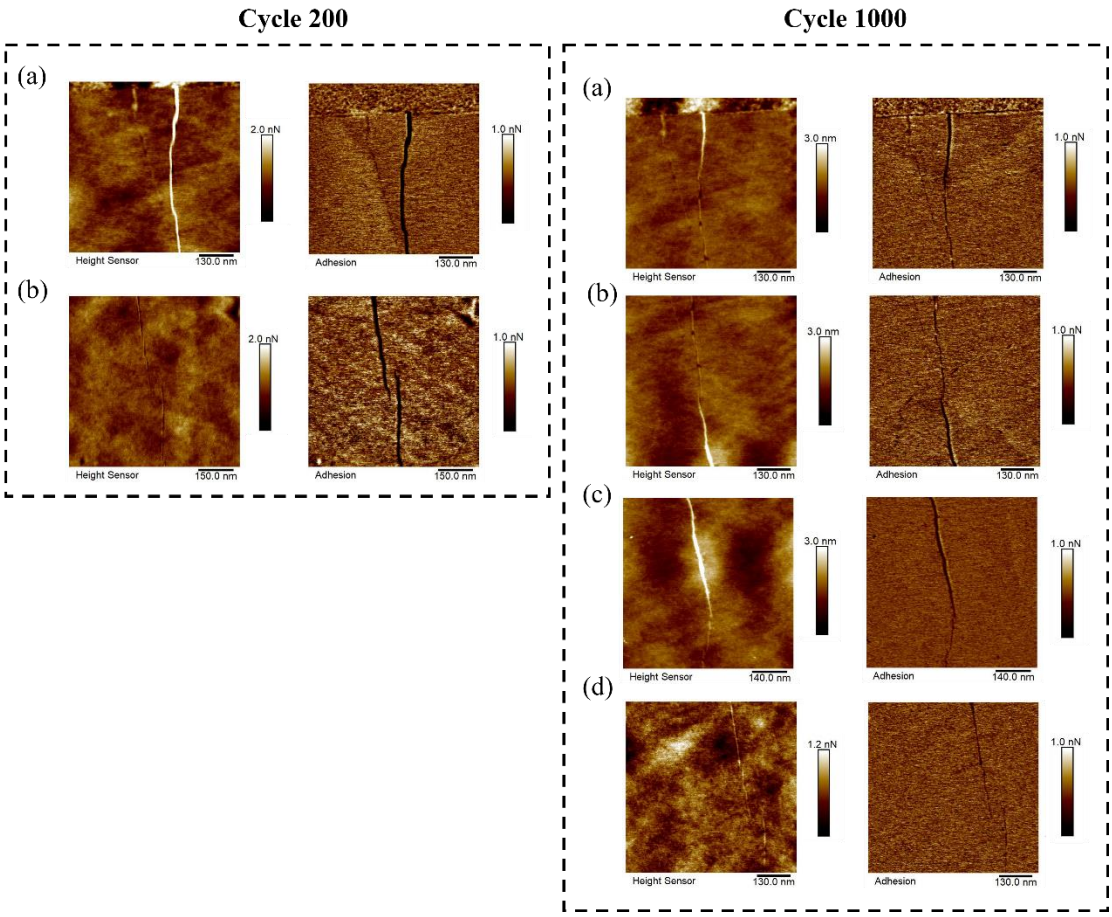


Figure 6.20: High-resolution topographic and adhesion mapping of graphene surface close to a craze at 200th cycles and 1000th cycles. The load axis is the horizontal axis.

The morphology of few-layered graphene sheets is slightly different. For instance, apart from the wrinkle formation and propagation throughout the sample, due to the strain gradient induced, from both tension and compression, also other features (i.e. ripples) appear on the surface of the sheets (**Figure 6.21**). Particularly, as seen in **Figure 6.21(a)** during the 1st cycle no significant change is observed at the morphology of the graphene flake. However, at 200th cycles apparent morphological changes are perceived **Figure 6.21(b)** and are marked in the black (Left area) and red (Right area) circle. Specifically, intense ripples (**Figure 6.21(b$_i$)**), as well as bifurcation signs (**Figure 6.21(b$_{ii}$)**) appear on graphene surface caused by the stress field induced due to the cyclic loading/unloading procedure.

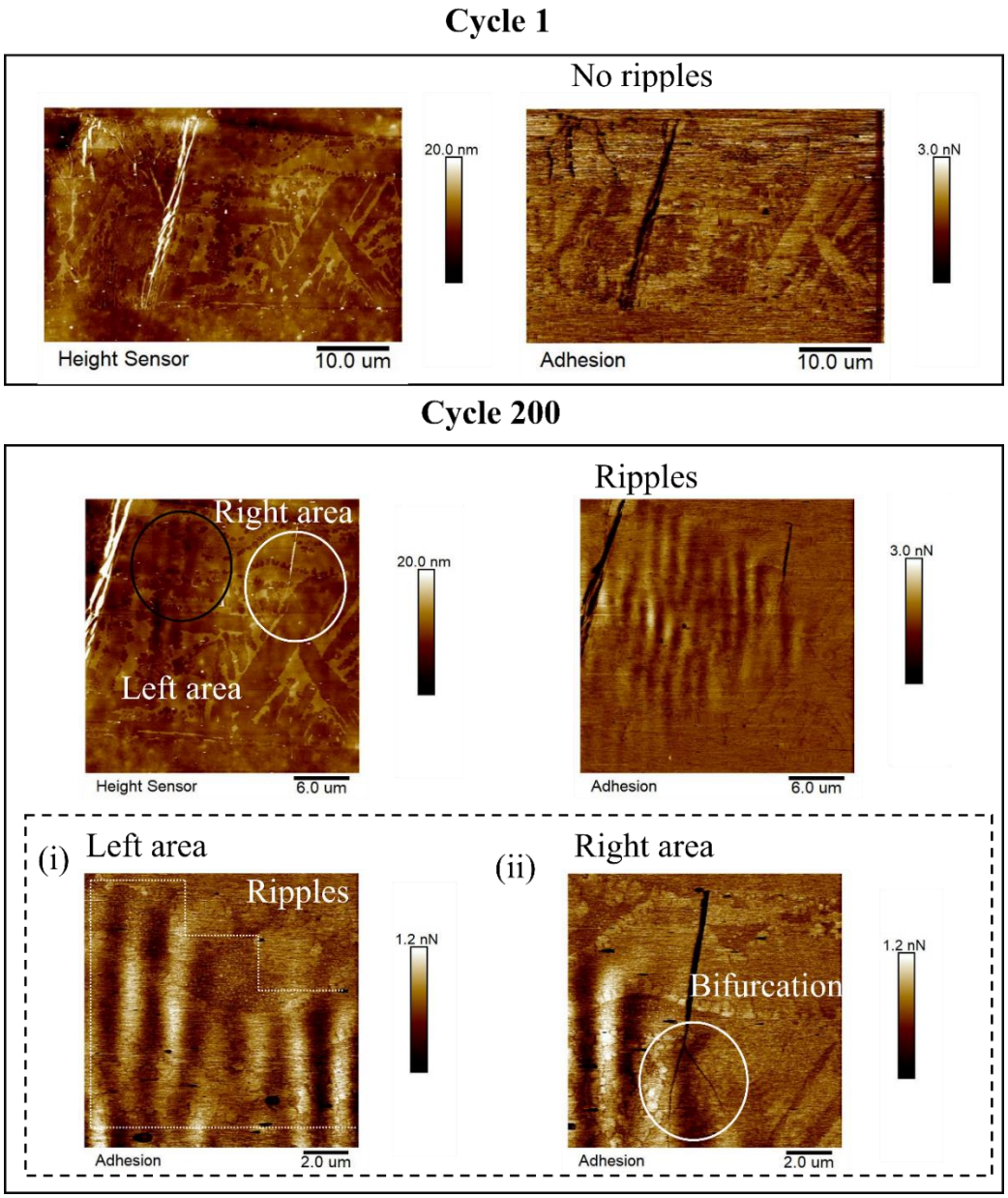


Figure 6.21: Topographic and adhesion mappings of few-layer graphene surface at (a) 1st, and (b) 200th cycles. During the 200th cycles there are obvious morphological changes, such as (b_i) ripples and (b_{ii}) bifurcation signs. The load axis is the horizontal axis.

The morphology of few-layered graphene flake is depicted at 200th (**Figure 6.22(a)**), 500th (**Figure 6.22((b)**) and 1000th cycles (**Figure 6.22((c)**). Apart from the few isolated wrinkles appearing at 200th (**Figure 6.22(a)**), a wrinkling system appears due to the compression-tension loading at the 500th cycles (**Figure 6.22((b)**). However, in the 1000th cycle, this wrinkling system seems to subside (**Figure 6.22((c)**), perhaps due to the repetitive stretching procedure and the surface tension existing in thin films [358].

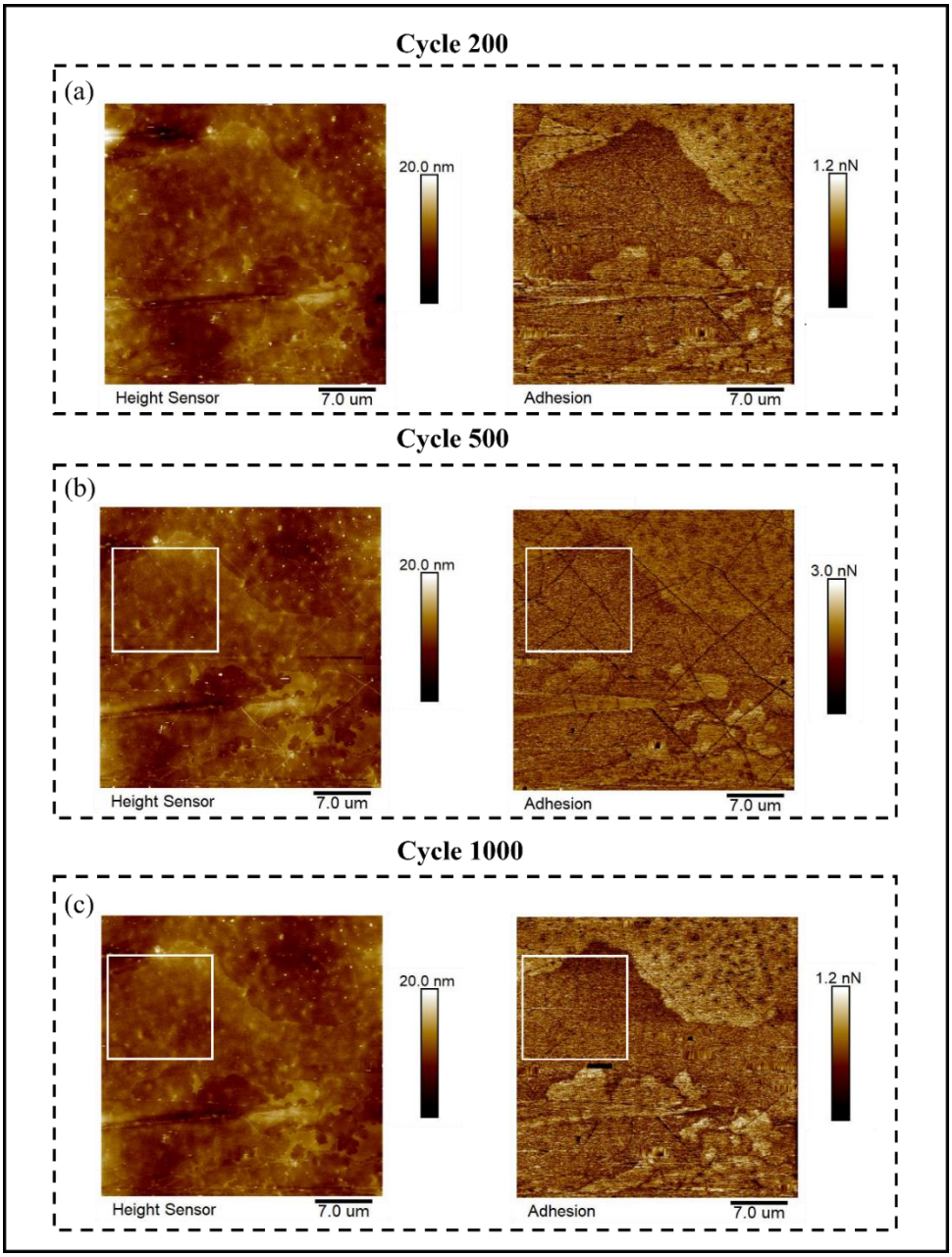


Figure 6.22: Topographic and adhesion mappings of few-layer graphene surface at (a) 200th cycles and (b) 500th cycles with the formation of a wrinkle system, and (c) 1000th cycles. The load axis is the horizontal axis.

The alteration in the morphology of wrinkling pattern displayed at 500th and 1000th cycles (white boxes – **Figure 6.22(b,c)**) are depicted in **Figure 6.23**. Comparison between the morphology at these cycles indicates that although at 500th cycles a system of intersecting wrinkles has formed, at 1000th cycles most of these wrinkles have disappeared and ripples have emerged, due to the alterations in strain gradient.

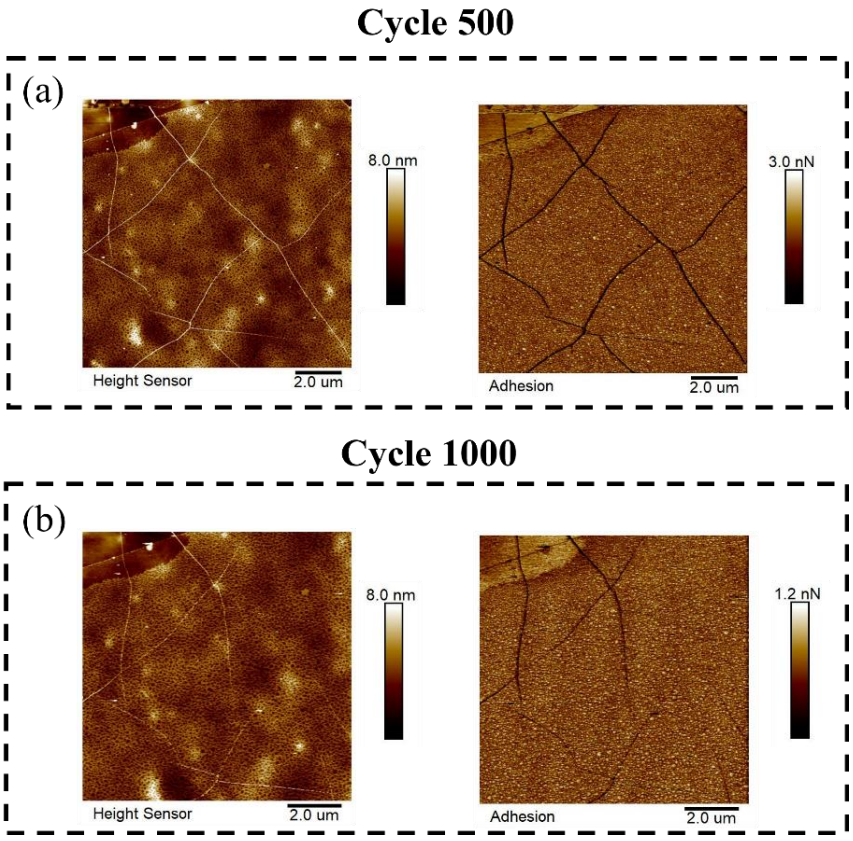


Figure 6.23: Topographic and adhesion mappings of few-layer graphene surface at (a) 500th cycle and (b) 1000th cycles. The load axis is the horizontal axis.

In **Figure 6.24**, the upper edge of the few-layered graphene sheet is depicted. It is clear that wrinkles are formed from the edge of the sheets at the 200th cycle, however in the 500th cycle the wrinkle formation is way more pronounced due to the repetitive changes in the stress field, resulting in a more intense pattern creation.

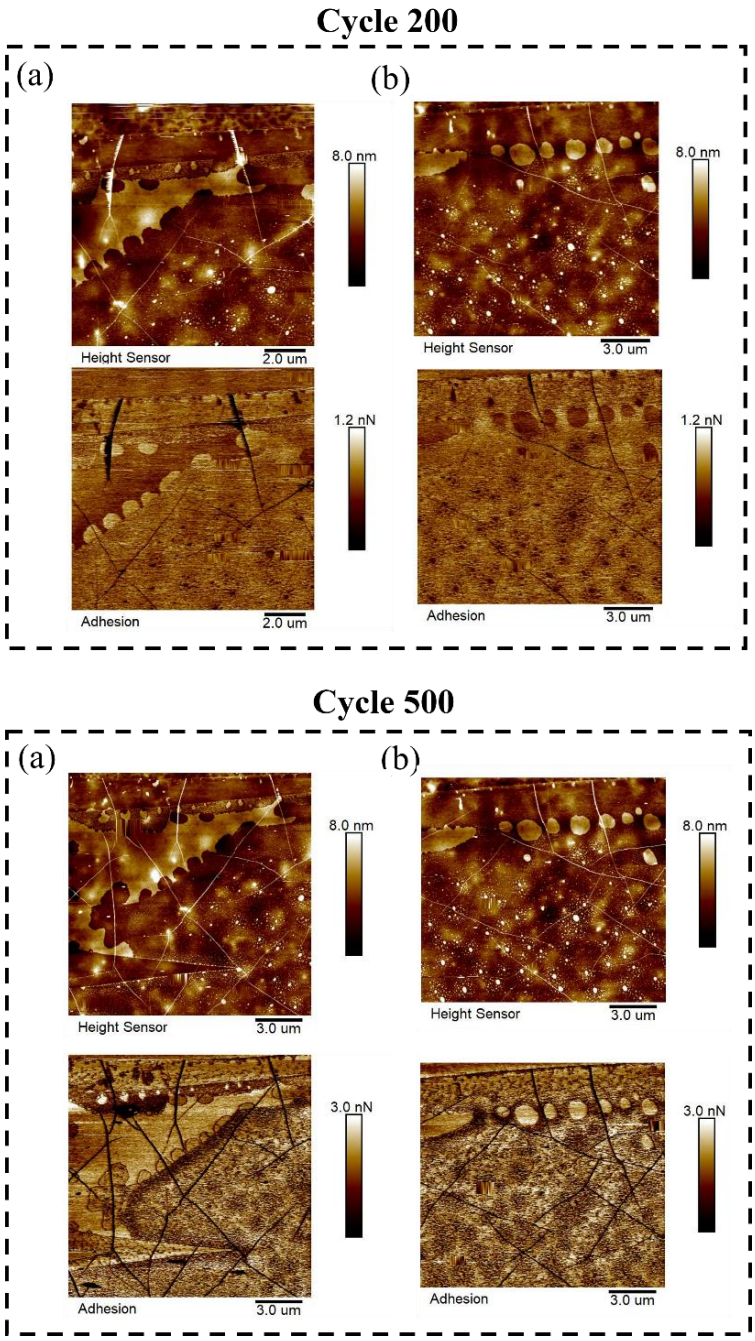


Figure 6.24: Topographic and adhesion mappings of few-layer graphene surface at (a) 200th cycles and (b) 500th cycles with the formation of a wrinkle system. The load axis is the horizontal axis.

6.6 Conclusions

Concluding, the presence of a defect on exfoliated graphene sheets plays a crucial role on its mechanical behaviour as it introduces localized stress concentration on its tip, rendering certain regions more susceptible to mechanical failure than others. Moreover,

the presence of a substrate is known to affect the mechanical response of graphene, due to their Young's modulus mismatch, leading to the appearance of patterns such as wrinkles. In fact, the application of external strain causes morphological alterations which seem to be different depending on the number of layers comprising the graphene flakes. Cracks and wrinkles are more localized on monolayer than in few-layer graphene. Herein, a new nanoscratching methodology was adopted to pre-crack graphene samples, by using an AFM diamond tip, in order to study the mechanical response of graphene. Crack initiation occurs in monolayer graphene at actual strain 0.45%, whereas for the case of few-layered graphene, it occurs at slightly higher applied strain, 0.62%, due to the additional support provided by the adjacent graphene layers, and the fracture toughness K_{IC} of the few-layered graphene ($11.0 \pm 2.3\ MPa\sqrt{m}$) is higher than the value of monolayer graphene ($7.97 \pm 2.10\ MPa\sqrt{m}$). Crack deflection, which is a crack delaying mechanism, was also observed in the case of monolayer graphene. Moreover, wrinkles form at 0.51% strain in the case of monolayer graphene, which is higher that the strain required to initiate cracking, due to the strain gradient close to the crack. On the contrary, in the case of few-layered graphene, wrinkles are formed in an early stage of 0.32% applied strain, possibly because in the case of a graphene stack, the presence of neighboring graphene layers can aid in the stress redistribution through the formation of wrinkles. Fatigue testing of the graphene samples up to 1000 cycles revealed that in the case of monolayer graphene, the wrinkles and folds appearing are localized, while in the case of few and multilayer stacks these features (along with ripples) are more spread throughout the flakes, forming patterns that are not observed in the former case.

7. Conclusions and Future work

In this dissertation, a thorough examination over the fracture behavior of graphene and graphene-based nanolaminates was conducted.

Firstly, a combination of Raman spectroscopy with micromechanical testing was employed for the promotion of CVD graphene as a strain sensor in a defected polymer, like PMMA, which is utilized in numerous industrial and research applications. Initially, CVD graphene was successfully transferred onto a PMMA slab. Then a defect was introduced at the center of the specimen, maintaining the structural integrity of both graphene and polymer at the nearby areas. Subsequently, when the polymer was subjected to incremental uniaxial deformation up to 2.0% (in steps of 0.5%), the 2D Raman peak position shifted towards lower wavenumber, confirming its high sensitivity. The ω_{2D} of graphene in the far field was utilized in order to construct a unique calibration curve for the system at hand, from which its strain sensitivity was extracted (≈ -15.9 cm^{-1}/%). The experimentally determined 2D peak position was then converted into strain using the calibration curve, revealing the strain distribution across the hole, which was maximum at the vicinity of the defect followed by a non-linear reduction, reaching a plateau at $\sim 500\ \mu m$. The resolution of the proposed graphene-based sensor is of ~ ±62 με. Furthermore, the stress profiles were extracted by using Hooke's law, following the same trend as the strain, while the stress concentration factor K_T was quantified for the PMMA at 2.41, being in line with the literature. K_T follows the same behavior as stress, nevertheless, as the applied strain increases, it drops due to minor damage propagation, resulting from the high stress concentration values exhibited near the notch. The validation of the experiment was conducted both numerically (using FEA), where the stress concentration factor was found to be 2.52, and analytically, where the stress concentration factor was found to be 2.96. Therefore, the use of CVD graphene as a strain sensor close to defects existing in PMMA is validated. Leveraging the sensitivity of graphene's 2D Raman peak to the imposition of external strain, it is feasible to obtain quantitative insight on the stress distribution around a defect with sub-micron spatial resolution. Further research can be conducted to enhance the practical application and commercial viability of CVD graphene-based strain sensors. Alongside these promising results, future work may include the further optimization of large-scale transfer of CVD graphene onto diverse polymer substrates and composite materials in order to ensure the consistency and the scalability of this

kind of strain sensors. Meanwhile, investigation over the adaptability and the multifunctionality can be studied, for instance exploring integration strategies for connecting graphene strain sensors with electronic data acquisition systems, including wireless communication for real-time monitoring applications or assess the biocompatibility and functionality of graphene strain sensors for potential applications in medical devices, such as monitoring physiological strains in biomedical implants or wearable health monitors.

Furthermore, the role of CVD graphene as an enhancing filler in graphene-based nanolaminates was investigated, focusing on the material's fracture toughness, crack initiation, and energy dissipation. Specifically, introducing monolayer graphene nanofillers into PMMA can elevate the ultimate tensile stress by 28%, and achieve an increased Young's modulus ($2.10 \pm 0.15\ GPa$ and $2.70 \pm 0.13\ GPa$, for nanolaminates with 0.035% and 0.12% volume fraction of graphene) in comparison to the neat PMMA ($1.75 \pm 0.14\ GPa$). This improvement in both strength and stiffness of the materials reveals the potential of these materials for high performance applications. Nevertheless, their fracture toughness was yet to be explored. In this thesis it is shown that the incorporation of CVD graphene sheets in graphene-based nanolaminates significantly improves the fracture toughness of the nanocomposites by 55% (at 0.035%) and 31% (at 0.12%). This indicates that the layered structure of the nanolaminates combined with the exceptional mechanical properties of CVD graphene contributes to higher resistance to crack propagation, owing to the emergence of crack delaying mechanisms, like microcracks and crack deflection. At this point it should be mentioned that the 0.12% volume fraction nanolaminates present more brittle behaviour, despite that they include a higher number of graphene sheets, due to the thin nature of the polymeric layers and the inherent defects caused by the itinerary depositions during the preparation procedure. Furthermore, crack initiation in the neat PMMA occurs earlier than in the graphene-based nanocomposites, due to the lack of the reinforcing filler and the mechanisms that procrastinate the final fracture. CVD graphene sheets increase the energy dissipation during the fracture procedure, due to the existence of mechanisms such as crack deflection, which impede the initiation and propagation of the crack.

Valuable insight over the fracture procedure was gained via the study of stress distribution across specimens containing a defect. Precisely, following the previously

mentioned methodology (combining Raman spectroscopy with the micromechanical testing), spectral Raman mappings are acquired close to the defect, identifying areas that display higher stress concentration, potentially leading to failure of the material. The analysis of stress distribution reveals that the nanolaminates of 0.035% and 0.12% volume fraction experience maximum stresses of ~8.5 GPa and ~5 GPa close to the defect, respectively. This result demonstrates that even a small number of CVD graphene sheets used as nanofillers can significantly enhance the strength and resilience of a nanocomposite, showing exceptional resistance to crack propagation. Also, the Stress Concentration Factor (SCF) for the low volume fraction nanolaminates is ~3.0 and ~5.5, for 0.035% and 0.12%, suggesting that fracture will occur earlier in the case of high volume fraction nanolaminates, which is verified by the brittle behaviour displayed through their dynamic tensile testing. Both SCFs are higher than the case of the neat PMMA, nevertheless, the toughness of PMMA is much lower, due to the absence of fracture impeding mechanisms.

Future research can be directed towards the involvement of advanced imaging and characterization techniques, such as Scanning Electron Microscopy (SEM), and computational modelling techniques, such as Molecular Dynamics simulations (MDs) and Finite Element Analysis (FEA), to gain valuable insight over the crack initiation and propagation in nanoscale and provide deeper insights into the fracture delaying mechanisms, such as crack bridging and crack deflection. Moreover, an investigation over the fatigue of the graphene-based nanolaminates can be conducted, studying the fracture toughness of graphene under repeated stress cycles and identifying any potential degradation mechanisms. Future research may also include the development of hybrid nanocomposites, where other 2D materials can act synergistically as a filler in the nanolaminates, potentially leading to a further enhancement of their fracture resistance. Thus, the study of the fracture behavior of graphene-based nanolaminates offers a broad area considering future research, and leads to the development of high-performance materials with superior mechanical properties and wide-ranging industrial applications.

Another approach of investigating the fracture toughness of graphene included the study of mono- and multi- layered mechanically exfoliated graphene, through the combination of AFM with micromechanical tensile testing. This approach provided valuable insight into the mechanical behavior of the material and revealed that the

presence of nano/micro-defects can play a critical role not only in initiating cracks and influencing fracture toughness, but also at the creation of various wrinkling patterns. Considering this, the actual graphene strain could be extracted at each applied strain during the tensile procedure. A new methodology was developed for the controlled cutting of the samples, without damaging the areas close to it, in order to assure that any change in the surface morphology will be attributed to the existence of this defect. By combining *in-situ* AFM with micromechanical testing, the fracture behavior of graphene flakes was assessed. Monolayer graphene, exhibiting exceptional mechanical properties is proven to be highly susceptible to fracture due to the presence of the induced defect, as it acts as a point of stress concentration. Few-layered and multilayered graphene, are also prone to a more rapid failure due to the defect's presence, nevertheless, the interlayer interactions enhance the resistance to crack propagation, due to the support provided from each layer to the other, exhibiting higher fracture toughness ($11.0 \pm 2.3\ MPa\sqrt{m}$) than in the case of the monolayer graphene ($7.97 \pm 2.10\ MPa\sqrt{m}$). Fatigue testing of the graphene flakes was also conducted (up to 1000 cycles) resulting to various wrinkle patterns. These patterns are observed both in mono- and multi- layered graphene, indicative of the deformation caused by the presence of the defect, however with one main difference: in the case of monolayer graphene, the wrinkles are more localized, whereas in the case of few layered graphene, wrinkles are distributed throughout the sample, forming various patterns, due to the interaction between the graphene layers. These findings not only deepen our understanding of the fracture mechanics of exfoliated graphene but also provide valuable guidelines for optimizing its use in various high-performance applications. By addressing the interplay between defects, crack initiation, and wrinkle formation, we can better harness the unique properties of graphene to develop more robust and reliable materials and devices. Future work can involve the study of both fracture toughness and fatigue of various 2D materials using a SEM instrument, in order to observe any existing fracture impeding mechanisms in real-time.

References

[1] H. He, T. Sekine, T. Kobayashi, Direct transformation of cubic diamond to hexagonal diamond, Appl. Phys. Lett. 81 (2002) 610–612. https://doi.org/10.1063/1.1495078.

[2] H.W. Kroto, J.R. Heath, S.C. O'Brien, R.F. Curl, R.E. Smalley, C60: Buckminsterfullerene, Nature 318 (1985) 162–163. https://doi.org/10.1038/318162a0.

[3] S. Iijima, T. Ichihashi, Single-shell carbon nanotubes of 1-nm diameter, Nature 363 (1993) 603–605. https://doi.org/10.1038/363603a0.

[4] K.S. Novoselov, A.K. Geim, S. V. Morozov, D. Jiang, Y. Zhang, S. V. Dubonos, I. V. Grigorieva, A.A. Firsov, Electric Field Effect in Atomically Thin Carbon Films, Science (80-.). 306 (2004) 666–669. https://doi.org/10.1126/science.1102896.

[5] V. Georgakilas, J.A. Perman, J. Tucek, R. Zboril, Broad Family of Carbon Nanoallotropes: Classification, Chemistry, and Applications of Fullerenes, Carbon Dots, Nanotubes, Graphene, Nanodiamonds, and Combined Superstructures, Chem. Rev. 115 (2015) 4744–4822. https://doi.org/10.1021/cr500304f.

[6] A.K. Geim, K.S. Novoselov, The rise of graphene, Nat. Mater. 6 (2007) 183–191. https://doi.org/10.1038/nmat1849.

[7] G. Yang, L. Li, W.B. Lee, M.C. Ng, Structure of graphene and its disorders: a review, Sci. Technol. Adv. Mater. 19 (2018) 613–648. https://doi.org/10.1080/14686996.2018.1494493.

[8] P.R. Wallace, The Peak Theory of Graphite, Phys. Rev. 71 (1947) 622–634. https://doi.org/10.1103/PhysRev.71.622.

[9] M. Orlita, M. Potemski, Dirac electronic states in graphene systems: optical spectroscopy studies, Semicond. Sci. Technol. 25 (2010) 063001. https://doi.org/10.1088/0268-1242/25/6/063001.

[10] K.I. Bolotin, K.J. Sikes, Z. Jiang, M. Klima, G. Fudenberg, J. Hone, P. Kim, H.L. Stormer, Ultrahigh electron mobility in suspended graphene, Solid State Commun. 146 (2008) 351–355. https://doi.org/10.1016/j.ssc.2008.02.024.

[11] A.H. Castro Neto, F. Guinea, N.M.R. Peres, K.S. Novoselov, A.K. Geim, The electronic properties of graphene, Rev. Mod. Phys. 81 (2009) 109–162. https://doi.org/10.1103/RevModPhys.81.109.

[12] M. Yoon, J. Howe, G. Tibbetts, G. Eres, Z. Zhang, Polygonization and anomalous graphene interlayer spacing of multi-walled carbon nanofibers, Phys. Rev. B 75 (2007) 165402. https://doi.org/10.1103/PhysRevB.75.165402.

[13] Y. Zhang, T.-T. Tang, C. Girit, Z. Hao, M.C. Martin, A. Zettl, M.F. Crommie, Y.R. Shen, F. Wang, Direct observation of a widely tunable peakgap in bilayer graphene, Nature 459 (2009) 820–823. https://doi.org/10.1038/nature08105.

[14] Y.X. Pang, M. Yew, Y. Yan, P. Khine, A. Filbert, S. Manickam, D.C.Y. Foo,

N. Sharmin, E. Lester, T. Wu, C.H. Pang, Application of supercritical fluid in the synthesis of graphene materials: a review, J. Nanoparticle Res. 23 (2021) 204. https://doi.org/10.1007/s11051-021-05254-w.

[15] A.P. Kauling, A.T. Seefeldt, D.P. Pisoni, R.C. Pradeep, R. Bentini, R.V.B. Oliveira, K.S. Novoselov, A.H. Castro Neto, The Worldwide Graphene Flake Production, Adv. Mater. 30 (2018). https://doi.org/10.1002/adma.201803784.

[16] M. Yi, Z. Shen, A review on mechanical exfoliation for the scalable production of graphene, J. Mater. Chem. A 3 (2015) 11700–11715. https://doi.org/10.1039/C5TA00252D.

[17] X. Gu, Y. Zhao, K. Sun, C.L.Z. Vieira, Z. Jia, C. Cui, Z. Wang, A. Walsh, S. Huang, Method of ultrasound-assisted liquid-phase exfoliation to prepare graphene, Ultrason. Sonochem. 58 (2019) 104630. https://doi.org/10.1016/j.ultsonch.2019.104630.

[18] X. Huang, Y. Li, X. Yin, J. Tian, W. Wu, Liquid-Phase Exfoliation of Kaolinite by High-Shear Mixer with Graphite Oxide as an Amphiphilic Dispersant, Langmuir 35 (2019) 13833–13843. https://doi.org/10.1021/acs.langmuir.9b02236.

[19] C. Backes, D. Campi, B.M. Szydlowska, K. Synnatschke, E. Ojala, F. Rashvand, A. Harvey, A. Griffin, Z. Sofer, N. Marzari, J.N. Coleman, D.D. O'Regan, Equipartition of Energy Defines the Size–Thickness Relationship in Liquid-Exfoliated Nanosheets, ACS Nano 13 (2019) 7050–7061. https://doi.org/10.1021/acsnano.9b02234.

[20] W.S. Hummers, R.E. Offeman, Preparation of Graphitic Oxide, J. Am. Chem. Soc. 80 (1958) 1339–1339. https://doi.org/10.1021/ja01539a017.

[21] D.R. Dreyer, S. Park, C.W. Bielawski, R.S. Ruoff, The chemistry of graphene oxide, Chem. Soc. Rev. 39 (2010) 228–240. https://doi.org/10.1039/B917103G.

[22] H.C. Schniepp, J.-L. Li, M.J. McAllister, H. Sai, M. Herrera-Alonso, D.H. Adamson, R.K. Prud'homme, R. Car, D.A. Saville, I.A. Aksay, Functionalized Single Graphene Sheets Derived from Splitting Graphite Oxide, J. Phys. Chem. B 110 (2006) 8535–8539. https://doi.org/10.1021/jp060936f.

[23] N.I. Zaaba, K.L. Foo, U. Hashim, S.J. Tan, W.-W. Liu, C.H. Voon, Synthesis of Graphene Oxide using Modified Hummers Method: Solvent Influence, Procedia Eng. 184 (2017) 469–477. https://doi.org/10.1016/j.proeng.2017.04.118.

[24] M. Zhou, Y. Wang, Y. Zhai, J. Zhai, W. Ren, F. Wang, S. Dong, Controlled Synthesis of Large-Area and Patterned Electrochemically Reduced Graphene Oxide Films, Chem. – A Eur. J. 15 (2009) 6116–6120. https://doi.org/10.1002/chem.200900596.

[25] K. Parvez, S. Yang, X. Feng, K. Müllen, Exfoliation of graphene via wet chemical routes, Synth. Met. 210 (2015) 123–132. https://doi.org/10.1016/j.synthmet.2015.07.014.

[26] C. Tsakonas, M. Dimitropoulos, A.C. Manikas, C. Galiotis, Growth and in situ

characterization of 2D materials by chemical vapour deposition on liquid metal catalysts: a review, Nanoscale 13 (2021) 3346–3373. https://doi.org/10.1039/D0NR07330J.

[27] P.Y. Huang, C.S. Ruiz-Vargas, A.M. van der Zande, W.S. Whitney, M.P. Levendorf, J.W. Kevek, S. Garg, J.S. Alden, C.J. Hustedt, Y. Zhu, J. Park, P.L. McEuen, D.A. Muller, Grains and grain boundaries in single-layer graphene atomic patchwork quilts, Nature 469 (2011) 389–392. https://doi.org/10.1038/nature09718.

[28] J. Lin, Z. Peng, Y. Liu, F. Ruiz-Zepeda, R. Ye, E.L.G. Samuel, M.J. Yacaman, B.I. Yakobson, J.M. Tour, Laser-induced porous graphene films from commercial polymers, Nat. Commun. 5 (2014) 5714. https://doi.org/10.1038/ncomms6714.

[29] M.F. El-Kady, V. Strong, S. Dubin, R.B. Kaner, Laser Scribing of High-Performance and Flexible Graphene-Based Electrochemical Capacitors, Science (80-.). 335 (2012) 1326–1330. https://doi.org/10.1126/science.1216744.

[30] X. Langston, K.E. Whitener, Graphene Transfer: A Physical Perspective, Nanomaterials 11 (2021) 2837. https://doi.org/10.3390/nano11112837.

[31] Y.-H. Deng, Transfer of graphene onto arbitrary substrates via sublimable carrier, (2020). https://doi.org/10.48550/arXiv.2010.11534.

[32] C. Pavlou, M.G. Pastore Carbone, A.C. Manikas, G. Trakakis, C. Koral, G. Papari, A. Andreone, C. Galiotis, Effective EMI shielding behaviour of thin graphene/PMMA nanolaminates in the THz range, Nat. Commun. 12 (2021) 1–9. https://doi.org/10.1038/s41467-021-24970-4.

[33] F. Kessler, P.A.R. Muñoz, C. Phelan, E.C. Romani, D.R.G. Larrudé, F.L. Freire, E.A. Thoroh de Souza, C.J.S. de Matos, G.J.M. Fechine, Direct dry transfer of CVD graphene to an optical substrate by in situ photo-polymerization, Appl. Surf. Sci. 440 (2018) 55–60. https://doi.org/10.1016/j.apsusc.2018.01.142.

[34] S. Ullah, X. Yang, H.Q. Ta, M. Hasan, A. Bachmatiuk, K. Tokarska, B. Trzebicka, L. Fu, M.H. Rummeli, Graphene transfer methods: A review, Nano Res. 14 (2021) 3756–3772. https://doi.org/10.1007/s12274-021-3345-8.

[35] T. Kobayashi, M. Peako, N. Kimura, K. Shimizu, K. Kadono, N. Umezu, K. Miyahara, S. Hayazaki, S. Nagai, Y. Mizuguchi, Y. Murakami, D. Hobara, Production of a 100-m-long high-quality graphene transparent conductive film by roll-to-roll chemical vapor deposition and transfer process, Appl. Phys. Lett. 102 (2013). https://doi.org/10.1063/1.4776707.

[36] F. Bonaccorso, A. Lombardo, T. Hasan, Z. Sun, L. Colombo, A.C. Ferrari, Production and processing of graphene and 2d crystals, Mater. Today 15 (2012) 564–589. https://doi.org/10.1016/S1369-7021(13)70014-2.

[37] X.-D. Chen, Z.-B. Liu, C.-Y. Zheng, F. Xing, X.-Q. Yan, Y. Chen, J.-G. Tian, High-quality and efficient transfer of large-area graphene films onto different substrates, Carbon N. Y. 56 (2013) 271–278. https://doi.org/10.1016/j.carbon.2013.01.011.

[38] B. Zhuang, S. Li, S. Li, J. Yin, Ways to eliminate PMMA residues on graphene —— superclean graphene, Carbon N. Y. 173 (2021) 609–636. https://doi.org/10.1016/j.carbon.2020.11.047.

[39] K. Kumar, Y.-S. Kim, E.-H. Yang, The influence of thermal annealing to remove polymeric residue on the electronic doping and morphological characteristics of graphene, Carbon N. Y. 65 (2013) 35–45. https://doi.org/10.1016/j.carbon.2013.07.088.

[40] M.K. Egbo, A fundamental review on composite materials and some of their applications in biomedical engineering, J. King Saud Univ. - Eng. Sci. 33 (2021) 557–568. https://doi.org/10.1016/j.jksues.2020.07.007.

[41] K.K. Chawla, Composite Materials, Springer New York, New York, NY, 2012. https://doi.org/10.1007/978-0-387-74365-3.

[42] D.D.L. Chung, Composite Materials, Springer London, London, 2010. https://doi.org/10.1007/978-1-84882-831-5.

[43] D. Hull, T.W. Clyne, An Introduction to Composite Materials, Cambridge University Press, 1996. https://doi.org/10.1017/CBO9781139170130.

[44] S.Z. Al Sheheri, Z.M. Al-Amshany, Q.A. Al Sulami, N.Y. Tashkandi, M.A. Hussein, R.M. El-Shishtawy, The preparation of carbon nanofillers and their role on the performance of variable polymer nanocomposites, Des. Monomers Polym. 22 (2019) 8–53. https://doi.org/10.1080/15685551.2019.1565664.

[45] V.B. Mohan, K. Lau, D. Hui, D. Bhattacharyya, Graphene-based materials and their composites: A review on production, applications and product limitations, Compos. Part B Eng. 142 (2018) 200–220. https://doi.org/10.1016/j.compositesb.2018.01.013.

[46] E. Manias, Stiffer by design, Nat. Mater. 6 (2007) 9–11. https://doi.org/10.1038/nmat1812.

[47] M.L. Studebaker, The Chemistry of Carbon Black and Reinforcement, Rubber Chem. Technol. 30 (1957) 1400–1483. https://doi.org/10.5254/1.3542764.

[48] T. Kuilla, S. Bhadra, D. Yao, N.H. Kim, S. Bose, J.H. Lee, Recent advances in graphene based polymer composites, Prog. Polym. Sci. 35 (2010) 1350–1375. https://doi.org/10.1016/j.progpolymsci.2010.07.005.

[49] R. Atif, I. Shyha, F. Inam, Mechanical, Thermal, and Electrical Properties of Graphene-Epoxy Nanocomposites—A Review, Polymers (Basel). 8 (2016) 281. https://doi.org/10.3390/polym8080281.

[50] S. Imani Yengejeh, S.A. Kazemi, A. Öchsner, Carbon nanotubes as reinforcement in composites: A review of the analytical, numerical and experimental approaches, Comput. Mater. Sci. 136 (2017) 85–101. https://doi.org/10.1016/j.commatsci.2017.04.023.

[51] Z. Li, L. Wang, Y. Li, Y. Feng, W. Feng, Carbon-based functional nanomaterials: Preparation, properties and applications, Compos. Sci. Technol. 179 (2019) 10–40. https://doi.org/10.1016/j.compscitech.2019.04.028.

[52] K. Hu, D.D. Kulkarni, I. Choi, V. V. Tsukruk, Graphene-polymer

nanocomposites for structural and functional applications, Prog. Polym. Sci. 39 (2014) 1934–1972. https://doi.org/10.1016/j.progpolymsci.2014.03.001.

[53] K.M.F. Shahil, A.A. Balandin, Thermal properties of graphene and multilayer graphene: Applications in thermal interface materials, Solid State Commun. 152 (2012) 1331–1340. https://doi.org/10.1016/j.ssc.2012.04.034.

[54] W. Guo, C. Cheng, Y. Wu, Y. Jiang, J. Gao, D. Li, L. Jiang, Bio-Inspired Two-Dimensional Nanofluidic Generators Based on a Layered Graphene Hydrogel Membrane, Adv. Mater. 25 (2013) 6064–6068. https://doi.org/10.1002/adma.201302441.

[55] M.S. Mannoor, H. Tao, J.D. Clayton, A. Sengupta, D.L. Kaplan, R.R. Naik, N. Verma, F.G. Omenetto, M.C. McAlpine, Graphene-based wireless bacteria detection on tooth enamel, Nat. Commun. 3 (2012) 763. https://doi.org/10.1038/ncomms1767.

[56] H. Tetsuka, R. Asahi, A. Nagoya, K. Okamoto, I. Tajima, R. Ohta, A. Okamoto, Optically Tunable Amino-Functionalized Graphene Quantum Dots, Adv. Mater. 24 (2012) 5333–5338. https://doi.org/10.1002/adma.201201930.

[57] L. Britnell, R.M. Ribeiro, A. Eckmann, R. Jalil, B.D. Belle, A. Mishchenko, Y.-J. Kim, R. V. Gorbachev, T. Georgiou, S. V. Morozov, A.N. Grigorenko, A.K. Geim, C. Casiraghi, A.H.C. Neto, K.S. Novoselov, Strong Light-Matter Interactions in Heterostructures of Atomically Thin Films, Science (80-.). 340 (2013) 1311–1314. https://doi.org/10.1126/science.1235547.

[58] A.A. Balandin, S. Ghosh, W. Bao, I. Calizo, D. Teweldebrhan, F. Miao, C.N. Lau, Superior Thermal Conductivity of Single-Layer Graphene, Nano Lett. 8 (2008) 902–907. https://doi.org/10.1021/nl0731872.

[59] K.S. Novoselov, A.K. Geim, S. V. Morozov, D. Jiang, M.I. Katsnelson, I. V. Grigorieva, S. V. Dubonos, A.A. Firsov, Two-dimensional gas of massless Dirac fermions in graphene, Nature 438 (2005) 197–200. https://doi.org/10.1038/nature04233.

[60] W. Cai, A.L. Moore, Y. Zhu, X. Li, S. Chen, L. Shi, R.S. Ruoff, Thermal Transport in Suspended and Supported Monolayer Graphene Grown by Chemical Vapor Deposition, Nano Lett. 10 (2010) 1645–1651. https://doi.org/10.1021/nl9041966.

[61] Z. Li, R.J. Young, R. Wang, F. Yang, L. Hao, W. Jiao, W. Liu, The role of functional groups on graphene oxide in epoxy nanocomposites, Polymer (Guildf). 54 (2013) 5821–5829. https://doi.org/10.1016/j.polymer.2013.08.026.

[62] C.E. Corcione, F. Freuli, A. Maffezzoli, The aspect ratio of epoxy matrix nanocomposites reinforced with graphene stacks, Polym. Eng. Sci. 53 (2013) 531–539. https://doi.org/10.1002/pen.23292.

[63] L. Ramos-Galicia, L.N. Mendez, A.L. Martínez-Hernández, A. Espindola-Gonzalez, I.R. Galindo-Esquivel, R. Fuentes-Ramirez, C. Velasco-Santos, Improved Performance of an Epoxy Matrix as a Result of Combining Graphene Oxide and Reduced Graphene, Int. J. Polym. Sci. 2013 (2013) 1–7. https://doi.org/10.1155/2013/493147.

[64] Y.-J. Wan, L.-C. Tang, D. Yan, L. Zhao, Y.-B. Li, L.-B. Wu, J.-X. Jiang, G.-Q. Lai, Improved dispersion and interface in the graphene/epoxy composites via a facile surfactant-assisted process, Compos. Sci. Technol. 82 (2013) 60–68. https://doi.org/10.1016/j.compscitech.2013.04.009.

[65] L. Cao, X. Liu, H. Na, Y. Wu, W. Zheng, J. Zhu, How a bio-based epoxy monomer enhanced the properties of diglycidyl ether of bisphenol A (DGEBA)/graphene composites, J. Mater. Chem. A 1 (2013) 5081. https://doi.org/10.1039/c3ta01700a.

[66] C. Hsu, M. Hsu, K. Chang, M. Lai, P. Liu, T. Chuang, J. Yeh, W. Liu, Physical study of room-temperature-cured epoxy/thermally reduced graphene oxides with various contents of oxygen-containing groups, Polym. Int. 63 (2014) 1765–1770. https://doi.org/10.1002/pi.4763.

[67] X. Wang, L. Song, W. Pornwannchai, Y. Hu, B. Kandola, The effect of graphene presence in flame retarded epoxy resin matrix on the mechanical and flammability properties of glass fiber-reinforced composites, Compos. Part A Appl. Sci. Manuf. 53 (2013) 88–96. https://doi.org/10.1016/j.compositesa.2013.05.017.

[68] J. Wang, Z. Shi, Y. Ge, Y. Wang, J. Fan, J. Yin, Solvent exfoliated graphene for reinforcement of PMMA composites prepared by in situ polymerization, Mater. Chem. Phys. 136 (2012) 43–50. https://doi.org/10.1016/j.matchemphys.2012.06.017.

[69] Z. Chen, H. Lu, Constructing sacrificial bonds and hidden lengths for ductile graphene/polyurethane elastomers with improved strength and toughness, J. Mater. Chem. 22 (2012) 12479. https://doi.org/10.1039/c2jm30517h.

[70] I.A. Kinloch, J. Suhr, J. Lou, R.J. Young, P.M. Ajayan, Composites with carbon nanotubes and graphene: An outlook, Science (80-.). 362 (2018) 547–553. https://doi.org/10.1126/science.aat7439.

[71] F. da Luz, F. Garcia Filho, M. Del-Río, L. Nascimento, W. Pinheiro, S. Monteiro, Graphene-Incorporated Natural Fiber Polymer Composites: A First Overview, Polymers (Basel). 12 (2020) 1601. https://doi.org/10.3390/polym12071601.

[72] J. Kang, V.K. Sangwan, J.D. Wood, M.C. Hersam, Solution-Based Processing of Monodisperse Two-Dimensional Nanomaterials, Acc. Chem. Res. 50 (2017) 943–951. https://doi.org/10.1021/acs.accounts.6b00643.

[73] M. Engel, D.B. Farmer, J.T. Azpiroz, J.-W.T. Seo, J. Kang, P. Avouris, M.C. Hersam, R. Krupke, M. Steiner, Graphene-enabled and directed nanomaterial placement from solution for large-scale device integration, Nat. Commun. 9 (2018) 4095. https://doi.org/10.1038/s41467-018-06604-4.

[74] W. Xu, Y. He, H. Xie, S. Qin, L. Tan, T. Wu, J. Qu, Ultrafast Fabrication of Graphene-Reinforced Nanocomposites via Synergy of Steam Explosion and Alternating Convergent-Divergent Flow, Small 17 (2021). https://doi.org/10.1002/smll.202100017.

[75] H. Mao, X. Wang, Use of in-situ polymerization in the preparation of graphene / polymer nanocomposites, New Carbon Mater. 35 (2020) 336–343.

https://doi.org/10.1016/S1872-5805(20)60493-0.

[76] D. Zhu, Z. Yang, J. Zhao, H. Guo, L. Gao, Ultrahigh energy density of polymer nanocomposites containing electrostatically self-assembled graphene oxide and hydrotalcite nanosheets, Ceram. Int. 47 (2021) 33766–33774. https://doi.org/10.1016/j.ceramint.2021.08.288.

[77] M. Yang, Y. Hou, N.A. Kotov, Graphene-based multilayers: Critical evaluation of materials assembly techniques, Nano Today 7 (2012) 430–447. https://doi.org/10.1016/j.nantod.2012.08.006.

[78] D.D. Kulkarni, I. Choi, S.S. Singamaneni, V. V. Tsukruk, Graphene Oxide−Polyelectrolyte Nanomembranes, ACS Nano 4 (2010) 4667–4676. https://doi.org/10.1021/nn101204d.

[79] K. Hu, M.K. Gupta, D.D. Kulkarni, V. V. Tsukruk, Ultra-Robust Graphene Oxide-Silk Fibroin Nanocomposite Membranes, Adv. Mater. 25 (2013) 2301–2307. https://doi.org/10.1002/adma.201300179.

[80] G. Decher, Fuzzy Nanoassemblies: Toward Layered Polymeric Multicomposites, Science (80-.). 277 (1997) 1232–1237. https://doi.org/10.1126/science.277.5330.1232.

[81] C. Jiang, S. Markutsya, Y. Pikus, V. V. Tsukruk, Freely suspended nanocomposite membranes as highly sensitive sensors, Nat. Mater. 3 (2004) 721–728. https://doi.org/10.1038/nmat1212.

[82] P. Liu, Z. Jin, G. Katsukis, L.W. Drahushuk, S. Shimizu, C.-J. Shih, E.D. Wetzel, J.K. Taggart-Scarff, B. Qing, K.J. Van Vliet, R. Li, B.L. Wardle, M.S. Strano, Layered and scrolled nanocomposites with aligned semi-infinite graphene inclusions at the platelet limit, Science (80-.). 353 (2016) 364–367. https://doi.org/10.1126/science.aaf4362.

[83] B. Wang, Z. Li, C. Wang, S. Signetti, B. V. Cunning, X. Wu, Y. Huang, Y. Jiang, H. Shi, S. Ryu, N.M. Pugno, R.S. Ruoff, Folding Large Graphene-on-Polymer Films Yields Laminated Composites with Enhanced Mechanical Performance, Adv. Mater. 30 (2018). https://doi.org/10.1002/adma.201707449.

[84] X. Li, J. Warzywoda, G.B. McKenna, Mechanical responses of a polymer graphene-sheet nano-sandwich, Polymer (Guildf). 55 (2014) 4976–4982. https://doi.org/10.1016/j.polymer.2014.08.008.

[85] I. Vlassiouk, G. Polizos, R. Cooper, I. Ivanov, J.K. Keum, F. Paulauskas, P. Datskos, S. Smirnov, Strong and Electrically Conductive Graphene-Based Composite Fibers and Laminates, ACS Appl. Mater. Interfaces 7 (2015) 10702–10709. https://doi.org/10.1021/acsami.5b01367.

[86] S.W.J. Kuan, C.W. Frank, C.C. Fu, D.R. Allee, P. Maccagno, R.F.W. Pease, Ultrathin polymer films for microlithography, J. Vac. Sci. Technol. B Microelectron. Process. Phenom. 6 (1988) 2274–2279. https://doi.org/10.1116/1.584069.

[87] S.W.J. Kuan, C.W. Frank, Y.H. Yen Lee, T. Eimori, D.R. Allee, R.F.W. Pease, R. Browning, Ultrathin poly(methylmethacrylate) resist films for microlithography, J. Vac. Sci. Technol. B Microelectron. Process. Phenom. 7

(1989) 1745–1750. https://doi.org/10.1116/1.584450.

[88] D. Pierleoni, M. Minelli, S. Ligi, M. Christian, S. Funke, N. Reineking, V. Morandi, F. Doghieri, V. Palermo, Selective Gas Permeation in Graphene Oxide–Polymer Self-Assembled Multilayers, ACS Appl. Mater. Interfaces 10 (2018) 11242–11250. https://doi.org/10.1021/acsami.8b01103.

[89] H. Watanabe, T. Ohzono, T. Kunitake, Fabrication of Large, Robust Nanomembranes from Diverse, Cross-Linked Polymeric Materials, Macromolecules 40 (2007) 1369–1371. https://doi.org/10.1021/ma062850q.

[90] V. Krishnan, K. Sakakibara, T. Mori, J.P. Hill, K. Ariga, Manipulation of thin film assemblies: Recent progress and novel concepts, Curr. Opin. Colloid Interface Sci. 16 (2011) 459–469. https://doi.org/10.1016/j.cocis.2011.08.005.

[91] A.K. Pathak, M. Borah, A. Gupta, T. Yokozeki, S.R. Dhakate, Improved mechanical properties of carbon fiber/graphene oxide-epoxy hybrid composites, Compos. Sci. Technol. 135 (2016) 28–38. https://doi.org/10.1016/j.compscitech.2016.09.007.

[92] H. Li, M.W. Fu, J. Lu, H. Yang, Ductile fracture: Experiments and computations, Int. J. Plast. 27 (2011) 147–180. https://doi.org/10.1016/j.ijplas.2010.04.001.

[93] B.R. Lawn, D.B. Marshall, Brittle Solids: From Physics and Chemistry to Materials Applications, Annu. Rev. Mater. Res. 52 (2022) 441–471. https://doi.org/10.1146/annurev-matsci-070121-042249.

[94] F. Dammaß, D. Schab, H. Rohm, M. Kästner, Rate- and temperature-dependent ductile-to-brittle fracture transition: Experimental investigation and phase-field analysis for toffee, Eng. Fract. Mech. 297 (2024) 109878. https://doi.org/10.1016/j.engfracmech.2024.109878.

[95] Ductility, (n.d.). www.nuclear-power.com/nuclear-engineering/materials-science/material-properties/ductility/.

[96] A.A. Alsayed, Physics of Open Fractures: Reconsidering Tissue Viability, Contamination Risk and Importance of Wound Debridement, J. Appl. Math. Phys. 09 (2021) 176–182. https://doi.org/10.4236/jamp.2021.91012.

[97] Y. Kurotani, H. Tanaka, Fatigue fracture mechanism of amorphous materials from a density-based coarse-grained model, Commun. Mater. 3 (2022) 67. https://doi.org/10.1038/s43246-022-00293-9.

[98] W. Li, X. Li, B. Liu, Q. Fang, C. Jiang, Transgranular highly localized deformation and fracture mechanism in ductile CrFeNi medium-entropy alloys, Mater. Sci. Eng. A 859 (2022) 144175. https://doi.org/10.1016/j.msea.2022.144175.

[99] S. Lynch, Failures of metallic components involving environmental degradation and material- selection issues, Corros. Rev. 35 (2017) 191–204. https://doi.org/10.1515/corrrev-2017-0023.

[100] VI. The phenomena of rupture and flow in solids, Philos. Trans. R. Soc. London. Ser. A, Contain. Pap. a Math. or Phys. Character 221 (1921) 163–198. https://doi.org/10.1098/rsta.1921.0006.

[101] G.R. Irwin, Analysis of Stresses and Strains Near the End of a Crack Traversing a Plate, J. Appl. Mech. 24 (1957) 361–364. https://doi.org/10.1115/1.4011547.

[102] T.L. Anderson, Fracture Mechanics: Fundamentals and Applications, Third Edit, n.d.

[103] S. Yamini, R.J. Young, Stability of crack propagation in epoxy resins, Polymer (Guildf). 18 (1977) 1075–1080. https://doi.org/10.1016/0032-3861(77)90016-7.

[104] M. Denny, K. Mach, S. Tepler, P. Martone, Indefatigable: an erect coralline alga is highly resistant to fatigue, J. Exp. Biol. 216 (2013) 3772–3780. https://doi.org/10.1242/jeb.091264.

[105] V. Sukumara Pillai, A. Kolios, S.T. Lie, Failure assessment of cracked uni-planar square hollow section T-, Y- and K-joints using the new BS 7910:2013+A1:2015, Arch. Appl. Mech. 89 (2019) 835–845. https://doi.org/10.1007/s00419-018-1423-5.

[106] Ductile vs. Brittle Fracture, (n.d.). mechanicalc.com/reference/fracture-mechanics#LEFM.

[107] D.G.R. WILLIAM D. CALLISTER, JR., Materials Science and Engineering AN INTRODUCTION, n.d.

[108] Mechanical Behaviour of Engineering Materials, Springer Berlin Heidelberg, Berlin, Heidelberg, 2007. https://doi.org/10.1007/978-3-540-73448-2.

[109] F. Sun, B.R.K. Blackman, A DIC method to determine the Mode I energy release rate G, the J-integral and the traction-separation law simultaneously for adhesive joints, Eng. Fract. Mech. 234 (2020) 107097. https://doi.org/10.1016/j.engfracmech.2020.107097.

[110] C.R.C. and D.P.G. W. L. Bradley, Studies of Mode I and Mode II Delamination Using a J-Integral Analysis and In-Situ Observations of Fracture in the SEM, (1989). https://doi.org/[W. L. Bradley, C. R. Corleto and D. P. Goetz, “Studies of Mode I and Mode II Delamination Using a J-Integral Analysis and In-Situ Observations of Fracture in the SEM,” 1989.

[111] Definition of J-integral, (n.d.). https://www.efunda.com/formulae/solid_mechanics/fracture_mechanics/fm_epfm_J.cfm.

[112] M.D. Bhatt, H. Kim, G. Kim, Various defects in graphene: a review, RSC Adv. 12 (2022) 21520–21547. https://doi.org/10.1039/D2RA01436J.

[113] W. Tian, W. Li, W. Yu, X. Liu, A Review on Lattice Defects in Graphene: Types, Generation, Effects and Regulation, Micromachines 8 (2017) 163. https://doi.org/10.3390/mi8050163.

[114] L. Liu, M. Qing, Y. Wang, S. Chen, Defects in Graphene: Generation, Healing, and Their Effects on the Properties of Graphene: A Review, J. Mater. Sci. Technol. 31 (2015) 599–606. https://doi.org/10.1016/j.jmst.2014.11.019.

[115] L. Wei, Z. Gao, Recent research advances on corrosion mechanism and

protection, and novel coating materials of magnesium alloys: a review, RSC Adv. 13 (2023) 8427–8463. https://doi.org/10.1039/D2RA07829E.

[116] T.A. Aljohani, M.I. Albeladi, B.A. Alshammari, Improving pitting corrosion resistance of the commercial titanium through graphene oxide-titanium oxide composite, Heliyon 7 (2021) e07289. https://doi.org/10.1016/j.heliyon.2021.e07289.

[117] A. Zandiatashbar, G.-H. Lee, S.J. An, S. Lee, N. Mathew, M. Terrones, T. Hayashi, C.R. Picu, J. Hone, N. Koratkar, Effect of defects on the intrinsic strength and stiffness of graphene, Nat. Commun. 5 (2014) 3186. https://doi.org/10.1038/ncomms4186.

[118] D. Zhang, H. Zhu, C. Zhang, J. Wang, H. Guo, Crack initiation and propagation of defects adjacent to the X65 pipeline spiral weld under axial tensile force, Int. J. Press. Vessel. Pip. 200 (2022) 104814. https://doi.org/10.1016/j.ijpvp.2022.104814.

[119] L. Lan, C. Qiu, L. Du, Effective grain size dependence of crack propagation resistance in low carbon steel, Theor. Appl. Fract. Mech. 124 (2023) 103762. https://doi.org/10.1016/j.tafmec.2023.103762.

[120] Y. Chang, X. Pan, L. Zheng, Y. Hong, Microstructure refinement and grain size distribution in crack initiation region of very-high-cycle fatigue regime for high-strength alloys, Int. J. Fatigue 134 (2020) 105473. https://doi.org/10.1016/j.ijfatigue.2020.105473.

[121] H.T. Wang, Y. Tian, Q.B. Ye, R.D.K. Misra, Z.D. Wang, G.D. Wang, Determining role of microstructure on crack arrest and propagation phenomenon in low-carbon microalloyed steel, Mater. Sci. Eng. A 761 (2019) 138009. https://doi.org/10.1016/j.msea.2019.06.019.

[122] A. Khalifeh, Stress Corrosion Cracking Behavior of Materials, in: Eng. Fail. Anal., IntechOpen, 2020. https://doi.org/10.5772/intechopen.90893.

[123] J. Zhou, F. Xian, J. Shen, Mechanisms during Strain Rate-Dependent Crack Propagation of Copper Nanowires Containing Edge Cracks, Nanomaterials 13 (2023) 1231. https://doi.org/10.3390/nano13071231.

[124] P. Rossi, Influence of the Loading Rate on the Cracking Process of Concrete in Quasi-Static Loading Domain, CivilEng 4 (2022) 1–11. https://doi.org/10.3390/civileng4010001.

[125] D.M. Neto, M.F. Borges, E.R. Sérgio, F. V. Antunes, Effect of Residual Stresses on Fatigue Crack Growth: A Numerical Study Based on Cumulative Plastic Strain at the Crack Tip, Materials (Basel). 15 (2022) 2156. https://doi.org/10.3390/ma15062156.

[126] T. Zhang, X. Li, H. Gao, Fracture of graphene: a review, Int. J. Fract. 196 (2015) 1–31. https://doi.org/10.1007/s10704-015-0039-9.

[127] C. Lee, X. Wei, J.W. Kysar, J. Hone, Measurement of the Elastic Properties and Intrinsic Strength of Monolayer Graphene, Science (80-.). 321 (2008) 385–388. https://doi.org/10.1126/science.1157996.

[128] A. Castellanos-Gomez, V. Singh, H.S.J. van der Zant, G.A. Steele, Mechanics

of freely-suspended ultrathin layered materials, Ann. Phys. 527 (2015) 27–44. https://doi.org/10.1002/andp.201400153.

[129] P. Zhang, L. Ma, F. Fan, Z. Zeng, C. Peng, P.E. Loya, Z. Liu, Y. Gong, J. Zhang, X. Zhang, P.M. Ajayan, T. Zhu, J. Lou, Fracture toughness of graphene, Nat. Commun. 5 (2014) 3782. https://doi.org/10.1038/ncomms4782.

[130] B. Jang, A.E. Mag-isa, J.-H. Kim, B. Kim, H.-J. Lee, C.-S. Oh, T. Sumigawa, T. Kitamura, Uniaxial fracture test of freestanding pristine graphene using in situ tensile tester under scanning electron microscope, Extrem. Mech. Lett. 14 (2017) 10–15. https://doi.org/10.1016/j.eml.2016.11.001.

[131] E. Cadelano, P.L. Palla, S. Giordano, L. Colombo, Nonlinear Elasticity of Monolayer Graphene, Phys. Rev. Lett. 102 (2009) 235502. https://doi.org/10.1103/PhysRevLett.102.235502.

[132] M.U. Arshad, Y. Gan, C. Wei, J. Li, C. Wu, M. Naraghi, Fracture Toughness Characteristics of Stacked Bilayer Graphene via Far-Field Displacement Measurements, Small 19 (2023). https://doi.org/10.1002/smll.202302499.

[133] Z. Zhang, X. Zhang, Y. Wang, Y. Wang, Y. Zhang, C. Xu, Z. Zou, Z. Wu, Y. Xia, P. Zhao, H.T. Wang, Crack Propagation and Fracture Toughness of Graphene Probed by Raman Spectroscopy, ACS Nano 13 (2019) 10327–10332. https://doi.org/10.1021/acsnano.9b03999.

[134] X. Zhao, B. Mao, M. Liu, J. Cao, S.J. Haigh, D.G. Papageorgiou, Z. Li, R.J. Young, Controlling and Monitoring Crack Propagation in Monolayer Graphene Single Crystals, Adv. Funct. Mater. 32 (2022). https://doi.org/10.1002/adfm.202202373.

[135] A. Sheraz, N. Mehmood, M.M. Çiçek, İ. Ergün, H.R. Rasouli, E. Durgun, T.S. Kasırga, High elasticity and strength of ultra-thin metallic transition metal dichalcogenides, Nanoscale Adv. 3 (2021) 3894–3899. https://doi.org/10.1039/D1NA00225B.

[136] S. Wang, Z. Qin, G.S. Jung, F.J. Martin-Martinez, K. Zhang, M.J. Buehler, J.H. Warner, Atomically Sharp Crack Tips in Monolayer MoS 2 and Their Enhanced Toughness by Vacancy Defects, ACS Nano 10 (2016) 9831–9839. https://doi.org/10.1021/acsnano.6b05435.

[137] X. Zhang, H. Nguyen, X. Zhang, P.M. Ajayan, J. Wen, H.D. Espinosa, Atomistic measurement and modeling of intrinsic fracture toughness of two-dimensional materials, Proc. Natl. Acad. Sci. 119 (2022). https://doi.org/10.1073/pnas.2206756119.

[138] G. Wang, Y. Wang, S. Li, Q. Yang, D. Li, S.T. Pantelides, J. Lin, Engineering the Crack Structure and Fracture Behavior in Monolayer MoS 2 By Selective Creation of Point Defects, Adv. Sci. 9 (2022). https://doi.org/10.1002/advs.202200700.

[139] H. Nguyen, X. Zhang, J. Wen, X. Zhang, P.M. Ajayan, H.D. Espinosa, Engineering the fracture resistance of 2H-transition metal dichalcogenides using vacancies: An in-silico investigation based on HRTEM images, Mater. Today 70 (2023) 17–32. https://doi.org/10.1016/j.mattod.2023.10.002.

[140] Y. Yang, Z. Song, G. Lu, Q. Zhang, B. Zhang, B. Ni, C. Wang, X. Li, L. Gu, X. Xie, H. Gao, J. Lou, Intrinsic toughening and stable crack propagation in hexagonal boron nitride, Nature 594 (2021) 57–61. https://doi.org/10.1038/s41586-021-03488-1.

[141] S.-C. Her, K.-C. Zhang, Mode I Fracture Toughness of Graphene Reinforced Nanocomposite Film on Al Substrate, Nanomaterials 11 (2021) 1743. https://doi.org/10.3390/nano11071743.

[142] C.E. Athanasiou, M.Y. Jin, C. Ramirez, N.P. Padture, B.W. Sheldon, High-Toughness Inorganic Solid Electrolytes via the Use of Reduced Graphene Oxide, Matter 3 (2020) 212–229. https://doi.org/10.1016/j.matt.2020.05.003.

[143] A. Nieto, A. Bisht, D. Lahiri, C. Zhang, A. Agarwal, Graphene reinforced metal and ceramic matrix composites: a review, Int. Mater. Rev. 62 (2017) 241–302. https://doi.org/10.1080/09506608.2016.1219481.

[144] M. Pakhomov, A. Dmitrievskiy, V. Stolyarov, Mechanical properties of nanocomposition ceramics with graphene, in: 2023: p. 040004. https://doi.org/10.1063/5.0117559.

[145] Y.R. Zhou, J. Jiao, Z.Y. Jiang, H. Liu, Y. Gao, X.X. Lv, Y.J. Ai, Toughening mechanisms of Ti3SiC2- and TiB2- toughened SiC matrix prepared via reactive melt infiltration, J. Mater. Res. 36 (2021) 4963–4973. https://doi.org/10.1557/s43578-021-00402-3.

[146] C. Ramírez, 10 years of research on toughness enhancement of structural ceramics by graphene, Philos. Trans. R. Soc. A Math. Phys. Eng. Sci. 380 (2022). https://doi.org/10.1098/rsta.2022.0006.

[147] A.G. Sheinerman, Modeling of fracture toughness enhancement and reduction in fully dense ceramic/graphene composites, Eur. J. Mech. - A/Solids 98 (2023) 104891. https://doi.org/10.1016/j.euromechsol.2022.104891.

[148] A. Agrawal, J. Charleston, R. Mirzaeifar, Experimental investigation of mechanical behavior at the microstructure of copper-graphene thin films, Mater. Sci. Eng. A 862 (2023) 144492. https://doi.org/10.1016/j.msea.2022.144492.

[149] B. Pu, X. Zhang, X. Chen, X. Lin, D. Zhao, C. Shi, E. Liu, J. Sha, C. He, N. Zhao, Exceptional mechanical properties of aluminum matrix composites with heterogeneous structure induced by in-situ graphene nanosheet-Cu hybrids, Compos. Part B Eng. 234 (2022) 109731. https://doi.org/10.1016/j.compositesb.2022.109731.

[150] B. Hwang, W. Kim, J. Kim, S. Lee, S. Lim, S. Kim, S.H. Oh, S. Ryu, S.M. Han, Role of Graphene in Reducing Fatigue Damage in Cu/Gr Nanolayered Composite, Nano Lett. 17 (2017) 4740–4745. https://doi.org/10.1021/acs.nanolett.7b01431.

[151] Z. Lin, S. Zhang, L. Ren, Z. Shen, G. Tang, P. Shi, T. Zheng, B. Ding, Y. Guo, Y. Chen, Q. Li, J. Peng, Y. Zhong, Enhanced strength and toughness of Ni/graphene composite via three-dimensional graphene-like nanosheets network, Compos. Part B Eng. 253 (2023) 110499. https://doi.org/10.1016/j.compositesb.2023.110499.

[152] S. Ali, F. Ahmad, P.S.M.M. Yusoff, N. Muhamad, E. Oñate, M.R. Raza, K. Malik, A review of graphene reinforced Cu matrix composites for thermal management of smart electronics, Compos. Part A Appl. Sci. Manuf. 144 (2021) 106357. https://doi.org/10.1016/j.compositesa.2021.106357.

[153] G. Chang, L. Wang, Y. Zhang, X. Li, K. Chen, D. Kan, W. Zhang, S. Zhang, L. Dong, L. Li, X. Bai, H. Zhang, W. Huo, Superior Thermal Conductivity of Graphene Film/Cu-Zr Alloy Composites for Thermal Management Applications, ACS Appl. Mater. Interfaces 14 (2022) 56156–56168. https://doi.org/10.1021/acsami.2c18101.

[154] H. Zhang, J. Xu, J. Zhang, J. An, Study on Interlaminar Fracture Toughness of the CNTs-CF/epoxy Resin Composites, J. Phys. Conf. Ser. 2468 (2023) 012067. https://doi.org/10.1088/1742-6596/2468/1/012067.

[155] Y. He, K. Duan, L. Yao, J. Tang, J. Zhang, D. Jiang, Q. Liu, Y. Lu, Synergistic toughening on CFRP via in-depth stitched CNTs, Compos. Part B Eng. 254 (2023) 110605. https://doi.org/10.1016/j.compositesb.2023.110605.

[156] D.A. Hawkins, A. Haque, Fracture Toughness of Carbon-Graphene/Epoxy Hybrid Nanocomposites, Procedia Eng. 90 (2014) 176–181. https://doi.org/10.1016/j.proeng.2014.11.833.

[157] P. Lamichhane, D. Dhakal, I.N. Jayalath, L. Baxter, S. Chaudhari, R. Vaidyanathan, Polyaniline and graphene nanocomposites for enhancing the interlaminar fracture toughness and thermo-mechanical properties of carbon fiber/epoxy composites, (2022). https://doi.org/10.48550/arXiv.2207.09500.

[158] P.-C. Chuang, C.- Yu Chao, M. Yang, J.-L. Tsai, Investigating fracture toughness of graphene epoxy nanocomposites using single edge notched bending specimens, J. Mech. 39 (2023) 105–112. https://doi.org/10.1093/jom/ufad007.

[159] S.J. Lee, S.J. Yoon, I.-Y. Jeon, Graphene/Polymer Nanocomposites: Preparation, Mechanical Properties, and Application, Polymers (Basel). 14 (2022) 4733. https://doi.org/10.3390/polym14214733.

[160] X. Lu, N. Hiremath, K. Hong, M.C. Evora, V.H. Ranson, A.K. Naskar, G.S. Bhat, N.-G. Kang, J.W. Mays, Improving mechanical properties of carbon nanotube fibers through simultaneous solid-state cycloaddition and crosslinking, Nanotechnology 28 (2017) 145603. https://doi.org/10.1088/1361-6528/aa6223.

[161] F. Wang, L.T. Drzal, Y. Qin, Z. Huang, Enhancement of fracture toughness, mechanical and thermal properties of rubber/epoxy composites by incorporation of graphene nanoplatelets, Compos. Part A Appl. Sci. Manuf. 87 (2016) 10–22. https://doi.org/10.1016/j.compositesa.2016.04.009.

[162] A.B. Irez, E. Bayraktar, I. Miskioglu, Fracture Toughness Analysis of Epoxy-Recycled Rubber-Based Composite Reinforced with Graphene Nanoplatelets for Structural Applications in Automotive and Aeronautics, Polymers (Basel). 12 (2020) 448. https://doi.org/10.3390/polym12020448.

[163] Y. Zheng, H. Xu, H. Jing, Q. Ren, Z. Liu, Z. Gao, Q. Ban, Graphene dispersed by pyrene-terminated polyethylene glycol for reinforced epoxy composites, J.

Appl. Polym. Sci. 139 (2022). https://doi.org/10.1002/app.52110.

[164] S. Jiang, Y. Chen, G. Duan, C. Mei, A. Greiner, S. Agarwal, Electrospun nanofiber reinforced composites: a review, Polym. Chem. 9 (2018) 2685–2720. https://doi.org/10.1039/C8PY00378E.

[165] M.A. Rafiee, J. Rafiee, I. Srivastava, Z. Wang, H. Song, Z. Yu, N. Koratkar, Fracture and Fatigue in Graphene Nanocomposites, Small 6 (2010) 179–183. https://doi.org/10.1002/smll.200901480.

[166] J. Jin, R. Rafiq, Y.Q. Gill, M. Song, Preparation and characterization of high performance of graphene/nylon nanocomposites, Eur. Polym. J. 49 (2013) 2617–2626. https://doi.org/10.1016/j.eurpolymj.2013.06.004.

[167] X. Wang, M. Song, Toughening of polymers by graphene, Nanomater. Energy 2 (2013) 265–278. https://doi.org/10.1680/nme.13.00024.

[168] P. Xu, J. Loomis, R.D. Bradshaw, B. Panchapakesan, Load transfer and mechanical properties of chemically reduced graphene reinforcements in polymer composites, Nanotechnology 23 (2012) 505713. https://doi.org/10.1088/0957-4484/23/50/505713.

[169] J.L. Suter, M. Vassaux, P. V. Coveney, Large-Scale Molecular Dynamics Elucidates the Mechanics of Reinforcement in Graphene-Based Composites, Adv. Mater. 35 (2023). https://doi.org/10.1002/adma.202302237.

[170] X. Wang, J. Jin, M. Song, An investigation of the mechanism of graphene toughening epoxy, Carbon N. Y. 65 (2013) 324–333. https://doi.org/10.1016/j.carbon.2013.08.032.

[171] S. Chatterjee, F. Nafezarefi, N.H. Tai, L. Schlagenhauf, F.A. Nüesch, B.T.T. Chu, Size and synergy effects of nanofiller hybrids including graphene nanoplatelets and carbon nanotubes in mechanical properties of epoxy composites, Carbon N. Y. 50 (2012) 5380–5386. https://doi.org/10.1016/j.carbon.2012.07.021.

[172] J. Wang, X. Jin, C. Li, W. Wang, H. Wu, S. Guo, Graphene and graphene derivatives toughening polymers: Toward high toughness and strength, Chem. Eng. J. 370 (2019) 831–854. https://doi.org/10.1016/j.cej.2019.03.229.

[173] L. Tam, D.-J. Lee, V. Kumar, Editorial: Polymer composites based on nanofillers: design, properties, and applications, Front. Mater. 10 (2023). https://doi.org/10.3389/fmats.2023.1216973.

[174] M. Zhou, J. Liu, H. Yang, L. Zhang, A multi-scale analysis on reinforcement origin of static and dynamic mechanics in graphene-elastomer nanocomposites, Compos. Sci. Technol. 228 (2022) 109617. https://doi.org/10.1016/j.compscitech.2022.109617.

[175] M. Batyrow, K. Dericiler, B.A. Palabiyik, B.S. Okan, H. Öztürk, I. Erucar, Combining tensile test results with atomistic predictions of elastic modulus of graphene/polyamide-6,6 nanocomposites, Mater. Today Commun. 35 (2023) 105636. https://doi.org/10.1016/j.mtcomm.2023.105636.

[176] M.A. Al-Saleh, A.A. Yussuf, S. Al-Enezi, R. Kazemi, M.U. Wahit, T. Al-Shammari, A. Al-Banna, Polypropylene/Graphene Nanocomposites: Effects of

GNP Loading and Compatibilizers on the Mechanical and Thermal Properties, Materials (Basel). 12 (2019) 3924. https://doi.org/10.3390/ma12233924.

[177] P. Govindaraj, A. Sokolova, N. Salim, S. Juodkazis, F.K. Fuss, B. Fox, N. Hameed, Distribution states of graphene in polymer nanocomposites: A review, Compos. Part B Eng. 226 (2021) 109353. https://doi.org/10.1016/j.compositesb.2021.109353.

[178] R. Aitbelale, A. Timesli, Effect of functionalized graphene addition on mechanical and thermal properties of high density polyethylene, J. Polym. Eng. 43 (2023) 343–353. https://doi.org/10.1515/polyeng-2022-0200.

[179] Y.T. Park, Y. Qian, C. Chan, T. Suh, M.G. Nejhad, C.W. Macosko, A. Stein, Epoxy Toughening with Low Graphene Loading, Adv. Funct. Mater. 25 (2015) 575–585. https://doi.org/10.1002/adfm.201402553.

[180] J. Wang, C. Li, X. Zhang, L. Xia, X. Zhang, H. Wu, S. Guo, Polycarbonate toughening with reduced graphene oxide: Toward high toughness, strength and notch resistance, Chem. Eng. J. 325 (2017) 474–484. https://doi.org/10.1016/j.cej.2017.05.090.

[181] Y.-H. Yu, Y.-Y. Lin, C.-H. Lin, C.-C. Chan, Y.-C. Huang, High-performance polystyrene/graphene-based nanocomposites with excellent anti-corrosion properties, Polym. Chem. 5 (2014) 535–550. https://doi.org/10.1039/C3PY00825H.

[182] C. Vallés, D.G. Papageorgiou, F. Lin, Z. Li, B.F. Spencer, R.J. Young, I.A. Kinloch, PMMA-grafted graphene nanoplatelets to reinforce the mechanical and thermal properties of PMMA composites, Carbon N. Y. 157 (2020) 750–760. https://doi.org/10.1016/j.carbon.2019.10.075.

[183] S. Chandrasekaran, N. Sato, F. Tölle, R. Mülhaupt, B. Fiedler, K. Schulte, Fracture toughness and failure mechanism of graphene based epoxy composites, Compos. Sci. Technol. 97 (2014) 90–99. https://doi.org/10.1016/j.compscitech.2014.03.014.

[184] U. Dubey, S. Kesarwani, R.K. Verma, Incorporation of graphene nanoplatelets/hydroxyapatite in PMMA bone cement for characterization and enhanced mechanical properties of biopolymer composites, J. Thermoplast. Compos. Mater. 36 (2023) 1978–2008. https://doi.org/10.1177/08927057221086833.

[185] S. Guanhong, Effect of Graphene Content on the Mechanical Properties of PMMA Composites, in: 2023: pp. 954–967. https://doi.org/10.1007/978-981-19-3842-9_74.

[186] S.S. Rahman, M.B. Mahmud, A.R. Monfared, P.C. Lee, C.B. Park, Achieving outstanding toughness of PMMA while retaining its strength, stiffness, and transparency using in situ developed TPEE nanofibrils, Compos. Sci. Technol. 236 (2023) 109994. https://doi.org/10.1016/j.compscitech.2023.109994.

[187] C. Bacali, M. Badea, M. Moldovan, C. Sarosi, V. Nastase, I. Baldea, R.S. Chiorean, M. Constantiniuc, The Influence of Graphene in Improvement of Physico-Mechanical Properties in PMMA Denture Base Resins, Materials (Basel). 12 (2019) 2335. https://doi.org/10.3390/ma12142335.

[188] HARDNESS AND TRIBOLOGICAL PROPERTIES OF PMMA COMPOSITE REINFORCED BY HYBRID GRAPHENE AND TiO2 NANOPARTICLES USED IN DENTAL APPLICATIONS, J. Egypt. Soc. Tribol. 19 (2022) 36–47. https://doi.org/10.21608/jest.2022.231178.

[189] E. Paz, F. Forriol, J.C. del Real, N. Dunne, Graphene oxide versus graphene for optimisation of PMMA bone cement for orthopaedic applications, Mater. Sci. Eng. C 77 (2017) 1003–1011. https://doi.org/10.1016/j.msec.2017.03.269.

[190] S.S. Abdullah, M.A. Kadhim, E. Al-Bermany, Graphene-Reinforced the Structure and Mechanical Properties of New PMMA-PVA Hybrid Nanocomposites, IOP Conf. Ser. Mater. Sci. Eng. 1094 (2021) 012138. https://doi.org/10.1088/1757-899X/1094/1/012138.

[191] S. Peng, M. He, Z. Yang, K. Zhang, B. Xue, S. Qin, J. Yu, G. Xu, Fabrication of reinforced and toughened PC/PMMA composites by tuning the migration and selective location of graphenes during melt blending, RSC Adv. 10 (2020) 28527–28535. https://doi.org/10.1039/D0RA04790B.

[192] A. Baldanza, M.G. Pastore Carbone, C. Brondi, A.C. Manikas, G. Mensitieri, C. Pavlou, G. Scherillo, C. Galiotis, Chemical Vapour Deposition Graphene–PMMA Nanolaminates for Flexible Gas Barrier, Membranes (Basel). 12 (2022) 611. https://doi.org/10.3390/membranes12060611.

[193] B.A. Alshammari, M.S. Alsuhybani, A.M. Almushaikeh, B.M. Alotaibi, A.M. Alenad, N.B. Alqahtani, A.G. Alharbi, Comprehensive Review of the Properties and Modifications of Carbon Fiber-Reinforced Thermoplastic Composites, Polymers (Basel). 13 (2021) 2474. https://doi.org/10.3390/polym13152474.

[194] N. Maqsood, M. Rimašauskas, Characterization of carbon fiber reinforced PLA composites manufactured by fused deposition modeling, Compos. Part C Open Access 4 (2021) 100112. https://doi.org/10.1016/j.jcomc.2021.100112.

[195] A. Sayam, A.N.M.M. Rahman, M.S. Rahman, S.A. Smriti, F. Ahmed, M.F. Rabbi, M. Hossain, M.O. Faruque, A review on carbon fiber-reinforced hierarchical composites: mechanical performance, manufacturing process, structural applications and allied challenges, Carbon Lett. 32 (2022) 1173–1205. https://doi.org/10.1007/s42823-022-00358-2.

[196] H. Varela-Rizo, M. Weisenberger, D.R. Bortz, I. Martin-Gullon, Fracture toughness and creep performance of PMMA composites containing micro and nanosized carbon filaments, Compos. Sci. Technol. 70 (2010) 1189–1195. https://doi.org/10.1016/j.compscitech.2010.03.005.

[197] J. Li, Toughness Enhancement of Poly(methyl methacrylate) (PMMA)/Poly(3-hydroxybutyrate-co-3-hydroxyvalerate) (PHBV) Nanocomposites by Multiwall Carbon Nanotubes (MWNT), J. Nanomater. 2022 (2022) 1–5. https://doi.org/10.1155/2022/9791775.

[198] N. Swaroop, P. Katiyar, K.K. Pandey, F. Tarannum, M. Umar, S. Paul, N. V. Dayama, A. Ahmed, R. Singh, A Comparative Evaluation of Flexural and Impact Strength of Polymethyl Methacrylate (PMMA) Reinforced With Graphene and Multi-Walled Carbon Nanotubes: An In Vitro Study, Cureus

(2023). https://doi.org/10.7759/cureus.40024.

[199] J.-F. Lemineur, H. Wang, W. Wang, F. Kanoufi, Emerging Optical Microscopy Techniques for Electrochemistry, Annu. Rev. Anal. Chem. 15 (2022) 57–82. https://doi.org/10.1146/annurev-anchem-061020-015943.

[200] T. Umakoshi, Near-field optical microscopy toward its applications for biological studies, Biophys. Physicobiology 20 (2023) e200011. https://doi.org/10.2142/biophysico.bppb-v20.0011.

[201] M. Xu, J. Liu, J. Sun, X. Xu, Y. Hu, B. Liu, Optical Microscopy and Electron Microscopy for the Morphological Evaluation of Tendons: A Mini Review, Orthop. Surg. 12 (2020) 366–371. https://doi.org/10.1111/os.12637.

[202] T. Terasawa, K. Saiki, Graphene: Synthesis and Functionalization, in: 2017: pp. 101–132. https://doi.org/10.1007/978-4-431-56496-6_4.

[203] R.R. Nair, P. Blake, A.N. Grigorenko, K.S. Novoselov, T.J. Booth, T. Stauber, N.M.R. Peres, A.K. Geim, Fine Structure Constant Defines Visual Transparency of Graphene, Science (80-.). 320 (2008) 1308–1308. https://doi.org/10.1126/science.1156965.

[204] Jablonski diagram, (n.d.). https://www.edinst.com/blog/what-is-raman-spectroscopy/.

[205] A. Milani, M. Tommasini, V. Russo, A. Li Bassi, A. Lucotti, F. Cataldo, C.S. Casari, Raman spectroscopy as a tool to investigate the structure and electronic properties of carbon-atom wires, Beilstein J. Nanotechnol. 6 (2015) 480–491. https://doi.org/10.3762/bjnano.6.49.

[206] M. Lazzeri, C. Attaccalite, L. Wirtz, F. Mauri, Impact of the electron-electron correlation on phonon dispersion: Failure of LDA and GGA DFT functionals in graphene and graphite, Phys. Rev. B 78 (2008) 081406. https://doi.org/10.1103/PhysRevB.78.081406.

[207] R. Yang, S. Yue, Y. Quan, B. Liao, Crystal symmetry based selection rules for anharmonic phonon-phonon scattering from a group theory formalism, Phys. Rev. B 103 (2021) 184302. https://doi.org/10.1103/PhysRevB.103.184302.

[208] L.M. Malard, M.A. Pimenta, G. Dresselhaus, M.S. Dresselhaus, Raman spectroscopy in graphene, Phys. Rep. 473 (2009) 51–87. https://doi.org/10.1016/j.physrep.2009.02.003.

[209] Y. Park, K.P.S.S. Hembram, R. Yoo, B. Jang, W. Lee, S.-G. Lee, J.-G. Kim, Y.-I. Kim, D.J. Moon, J.-K. Lee, J.-K. Lee, Reinterpretation of Single-Wall Carbon Nanotubes by Raman Spectroscopy, J. Phys. Chem. C 123 (2019) 14003–14009. https://doi.org/10.1021/acs.jpcc.9b02174.

[210] T.M.G. Mohiuddin, A. Lombardo, R.R. Nair, A. Bonetti, G. Savini, R. Jalil, N. Bonini, D.M. Basko, C. Galiotis, N. Marzari, K.S. Novoselov, A.K. Geim, A.C. Ferrari, Uniaxial strain in graphene by Raman spectroscopy: <math display="inline"> <mi>G</mi> </math> peak splitting, Grüneisen parameters, and sample orientation, Phys. Rev. B 79 (2009) 205433. https://doi.org/10.1103/PhysRevB.79.205433.

[211] J.R. A. C. Ferrari, Interpretation of Raman spectra of disordered and

amorphous carbon, Phys. Rev. B 61 (2000). https://doi.org/10.1103/PhysRevB.61.14095.

[212] A.C. Ferrari, J. Robertson, Interpretation of Raman spectra of disordered and amorphous carbon, Phys. Rev. B 61 (2000) 14095–14107. https://doi.org/10.1103/PhysRevB.61.14095.

[213] J.E. Lee, G. Ahn, J. Shim, Y.S. Lee, S. Ryu, Optical separation of mechanical strain from charge doping in graphene, Nat. Commun. 3 (2012) 1024. https://doi.org/10.1038/ncomms2022.

[214] B. Bekdüz, U. Kaya, M. Langer, W. Mertin, G. Bacher, Direct growth of graphene on Ge(100) and Ge(110) via thermal and plasma enhanced CVD, Sci. Rep. 10 (2020) 12938. https://doi.org/10.1038/s41598-020-69846-7.

[215] M.M. Haidari, H. Kim, J.H. Kim, M. Park, H. Lee, J.S. Choi, Doping effect in graphene-graphene oxide interlayer, Sci. Rep. 10 (2020) 8258. https://doi.org/10.1038/s41598-020-65263-y.

[216] O. Frank, G. Tsoukleri, J. Parthenios, K. Papagelis, I. Riaz, R. Jalil, K.S. Novoselov, C. Galiotis, Compression Behavior of Single-Layer Graphenes, ACS Nano 4 (2010) 3131–3138. https://doi.org/10.1021/nn100454w.

[217] L.M. Malard, J. Nilsson, D.C. Elias, J.C. Brant, F. Plentz, E.S. Alves, A.H. Castro Neto, M.A. Pimenta, Probing the electronic structure of bilayer graphene by Raman scattering, Phys. Rev. B 76 (2007) 201401. https://doi.org/10.1103/PhysRevB.76.201401.

[218] L.M. Malard, M.H.D. Guimarães, D.L. Mafra, M.S.C. Mazzoni, A. Jorio, Group-theory analysis of electrons and phonons in N -layer graphene systems, Phys. Rev. B 79 (2009) 125426. https://doi.org/10.1103/PhysRevB.79.125426.

[219] A.C. Ferrari, J.C. Meyer, V. Scardaci, C. Casiraghi, M. Lazzeri, F. Mauri, S. Piscanec, D. Jiang, K.S. Novoselov, S. Roth, A.K. Geim, Raman Spectrum of Graphene and Graphene Layers, Phys. Rev. Lett. 97 (2006) 187401. https://doi.org/10.1103/PhysRevLett.97.187401.

[220] X. Wang, J.W. Christopher, A.K. Swan, 2D Raman peak splitting in graphene: Charge screening and lifting of the K-point Kohn anomaly, Sci. Rep. 7 (2017) 13539. https://doi.org/10.1038/s41598-017-13769-3.

[221] J. Sonntag, K. Watanabe, T. Taniguchi, B. Beschoten, C. Stampfer, Charge carrier density dependent Raman spectra of graphene encapsulated in hexagonal boron nitride, Phys. Rev. B 107 (2023) 075420. https://doi.org/10.1103/PhysRevB.107.075420.

[222] Z. Komínková, M. Kalbáč, Raman spectroscopy of strongly doped CVD-graphene, Phys. Status Solidi 250 (2013) 2659–2661. https://doi.org/10.1002/pssb.201300070.

[223] D.G. Yablon, Overview of Atomic Force Microscopy, in: Scanning Probe Microsc. Ind. Appl., Wiley, 2013: pp. 1–14. https://doi.org/10.1002/9781118723111.ch1.

[224] AFM (Atomic Force Microscope), (n.d.). https://physik.uni-greifswald.de/en/research-groups/soft-matter-and-biophysics-prof-christiane-

helm/methods/afm-atomic-force-microscope/.

[225] R. Tararam, P.S. Garcia, D.K. Deda, J.A. Varela, F. de Lima Leite, Atomic Force Microscopy: A Powerful Tool for Electrical Characterization, in: Nanocharacterization Tech., Elsevier, 2017: pp. 37–64. https://doi.org/10.1016/B978-0-323-49778-7.00002-3.

[226] S.S. Nair, C. Wang, K.J. Wynne, AFM Peakforce QNM mode for measurement of nanosurface mechanical properties of Pt-cured silicones, Prog. Org. Coatings 126 (2019) 119–128. https://doi.org/10.1016/j.porgcoat.2018.10.008.

[227] D.R. Streltsov, K.M. Borisov, A.A. Kalinina, A.M. Muzafarov, Quantitative Elasticity Mapping of Submicron Silica Hollow Particles by PeakForce QNM AFM Mode, Nanomaterials 13 (2023) 1916. https://doi.org/10.3390/nano13131916.

[228] G. Stan, P. Namboodiri, Open-loop amplitude-modulation Kelvin probe force microscopy operated in single-pass PeakForce tapping mode, Beilstein J. Nanotechnol. 12 (2021) 1115–1126. https://doi.org/10.3762/bjnano.12.83.

[229] X. Chang, S. Hallais, K. Danas, S. Roux, PeakForce AFM Analysis Enhanced with Model Reduction Techniques, Sensors 23 (2023) 4730. https://doi.org/10.3390/s23104730.

[230] P. Nautiyal, B. Boesl, A. Agarwal, Application of In-Situ Mechanics Approach in Materials Science Problems, in: In-Situ Mech. Mater., Springer International Publishing, Cham, 2020: pp. 141–203. https://doi.org/10.1007/978-3-030-43320-8_5.

[231] C. Rudolf, B. Boesl, A. Agarwal, In Situ Mechanical Testing Techniques for Real-Time Materials Deformation Characterization, JOM 68 (2016) 136–142. https://doi.org/10.1007/s11837-015-1629-8.

[232] A. Patra, C.S. Rout, Electron Diffraction-Based Techniques for 2D Layered Materials, in: Adv. Anal. Tech. Charact. 2D Mater., AIP Publishing LLCMelville, New York, 2022: pp. 6-1-6–16. https://doi.org/10.1063/9780735425422_006.

[233] J. Zhong, D. He, Combination of Universal Mechanical Testing Machine with Atomic Force Microscope for Materials Research, Sci. Rep. 5 (2015) 12998. https://doi.org/10.1038/srep12998.

[234] K.K. Al-Quraishi, Q. He, W. Kauppila, M. Wang, Y. Yang, Mechanical testing of two-dimensional materials: a brief review, Int. J. Smart Nano Mater. 11 (2020) 207–246. https://doi.org/10.1080/19475411.2020.1791276.

[235] S. Feng, W. Wang, S. Wang, X. Cui, Y. Yang, F. Xu, L. Liu, Z. Xu, Controlling and visualizing fracture of 2D crystals by wrinkling, J. Mech. Phys. Solids 174 (2023) 105253. https://doi.org/10.1016/j.jmps.2023.105253.

[236] I. Royaud, M. Ponçot, D. Chapron, P. Bourson, In-situ microstructural measurements, in: Des. Fabr. Charact. Multifunct. Nanomater., Elsevier, 2022: pp. 73–121. https://doi.org/10.1016/B978-0-12-820558-7.00017-0.

[237] K. Kim, J.C. Yoon, J. Kim, J.H. Kim, S.W. Lee, A. Yoon, Z. Lee, Dedicated preparation for in situ transmission electron microscope tensile testing of

exfoliated graphene, Appl. Microsc. 49 (2019) 3. https://doi.org/10.1007/s42649-019-0005-5.

[238] C. Cao, J.Y. Howe, D. Perovic, T. Filleter, Y. Sun, In situ TEM tensile testing of carbon-linked graphene oxide nanosheets using a MEMS device, Nanotechnology 27 (2016) 28LT01. https://doi.org/10.1088/0957-4484/27/28/28LT01.

[239] A. Xu, M. Saleh, D. Bhattacharyya, Experimental and computational analysis of the in situ tensile deformation of 2D honeycomb lattice structures in Ni single crystals, Compos. Part B Eng. 186 (2020) 107823. https://doi.org/10.1016/j.compositesb.2020.107823.

[240] C. Temiz, Scanning Electron Microscopy, in: Electron Microsc., IntechOpen, 2022. https://doi.org/10.5772/intechopen.103956.

[241] A.J. Kinloch, R.J. Young, Fracture Behaviour of Polymers, Springer Netherlands, Dordrecht, 1995. https://doi.org/10.1007/978-94-017-1594-2.

[242] R.H. Patel, B.P. Patel, Effect of various discontinuities present in a plate on stress concentration: a review, Eng. Res. Express 4 (2022) 032001. https://doi.org/10.1088/2631-8695/ac8c1b.

[243] Y. Zhou, Z.J. Bai, L.F. Zeng, X. Gong, Study on Finite Element Method for Solving Stress Concentration Problem, Appl. Mech. Mater. 914 (2023) 175–180. https://doi.org/10.4028/p-o061r2.

[244] M.M. Makki, B. Chokri, Determination of Stress Concentration for Orthotropic and Isotropic Materials Using Digital Image Correlation (DIC), in: 2015: pp. 517–530. https://doi.org/10.1007/978-3-319-14532-7_53.

[245] M. Mohamed Makki, B. Chokri, Experimental, analytical, and finite element study of stress concentration factors for composite materials, J. Compos. Mater. 51 (2017) 1583–1594. https://doi.org/10.1177/0021998316659915.

[246] M.A. Karim, M.Z. Abdullah, A.F. Deifalla, M. Azab, A. Waqar, An assessment of the processing parameters and application of fibre-reinforced polymers (FRPs) in the petroleum and natural gas industries: A review, Results Eng. 18 (2023) 101091. https://doi.org/10.1016/j.rineng.2023.101091.

[247] Y. Kim, M.-S. Kim, H.-J. Jeon, J.-H. Kim, K.W. Chun, Mechanical Performance of Polymer Materials for Low-Temperature Applications, Appl. Sci. 12 (2022) 12251. https://doi.org/10.3390/app122312251.

[248] S.B. Ulaeto, R.P. Ravi, I.I. Udoh, G.M. Mathew, T.P.D. Rajan, Polymer-Based Coating for Steel Protection, Highlighting Metal–Organic Framework as Functional Actives: A Review, Corros. Mater. Degrad. 4 (2023) 284–316. https://doi.org/10.3390/cmd4020015.

[249] A.C.C. de Leon, Í.G.M. da Silva, K.D. Pangilinan, Q. Chen, E.B. Caldona, R.C. Advincula, High performance polymers for oil and gas applications, React. Funct. Polym. 162 (2021) 104878. https://doi.org/10.1016/j.reactfunctpolym.2021.104878.

[250] L. Cai, D. He, X. Peng, J. Fan, S. Ding, X. Zeng, R. Sun, L. Ren, C. Zhong, J. Lu, X. Zeng, Notch sensitivity of polymer-based thermal interface materials, J.

Appl. Phys. 132 (2022). https://doi.org/10.1063/5.0120832.

[251] M. Zappalorto, Static notch sensitivity in orthotropic materials and composites, Eur. J. Mech. - A/Solids 85 (2021) 104094. https://doi.org/10.1016/j.euromechsol.2020.104094.

[252] X.. Zheng, H. Wang, J.. Yan, Notch strength and notch sensitivity of polymethyl methacrylate glasses, Mater. Sci. Eng. A 349 (2003) 80–88. https://doi.org/10.1016/S0921-5093(02)00584-1.

[253] S. Djukic, A. Bocahut, J. Bikard, D.R. Long, Mechanical properties of amorphous and semi-crystalline semi-aromatic polyamides, Heliyon 6 (2020) e03857. https://doi.org/10.1016/j.heliyon.2020.e03857.

[254] M. Zhong, R. Wang, K. Kawamoto, B.D. Olsen, J.A. Johnson, Quantifying the impact of molecular defects on polymer network elasticity, Science (80-.). 353 (2016) 1264–1268. https://doi.org/10.1126/science.aag0184.

[255] M. Springborg, Structural defects in polymers, Phys. B Condens. Matter 172 (1991) 225–235. https://doi.org/10.1016/0921-4526(91)90435-H.

[256] D. Ahmad, K. Patra, M. Hossain, Experimental study and phenomenological modelling of flaw sensitivity of two polymers used as dielectric elastomers, Contin. Mech. Thermodyn. 32 (2020) 489–500. https://doi.org/10.1007/s00161-019-00817-8.

[257] J.R. Pothnis, D. Kalyanasundaram, S. Gururaja, Mitigation of notch sensitivity by controlled alignment of carbon nanotubes in epoxy using electric field application, Compos. Part A Appl. Sci. Manuf. 149 (2021) 106544. https://doi.org/10.1016/j.compositesa.2021.106544.

[258] C. Stochioiu, V.-M. Marinescu, D.I. Tudose, A. Hadar, Determination of Stress Concentration Effects Using Micro-Digital Image Correlation Techniques in PMMA Specimens, Mater. Plast. 59 (2022) 119–127. https://doi.org/10.37358/MP.22.2.5591.

[259] G. Gao, Z. Li, J. Xu, Optical method of caustics applied in viscoelastic fracture analysis, Opt. Lasers Eng. 49 (2011) 632–639. https://doi.org/10.1016/j.optlaseng.2011.01.012.

[260] C.W.S. Dallas G. Smith, Photoelastic determination of mixed mode stress intensity factors, Eng. Fract. Mech. 4 (1972) 357–362. https://doi.org/10.1016/0013-7944(72)90050-1.

[261] Y. Li, Y. Song, Z. Yang, X. Xie, Use of line laser scanning thermography for the defect detection and evaluation of composite material, Sci. Eng. Compos. Mater. 29 (2022) 74–83. https://doi.org/10.1515/secm-2022-0007.

[262] G.-Y. Li, A.L. Gower, M. Destrade, An ultrasonic method to measure stress without calibration: The angled shear wave method, J. Acoust. Soc. Am. 148 (2020) 3963–3970. https://doi.org/10.1121/10.0002959.

[263] S. Yoshida, T. Sasaki, M. Usui, S. Sakamoto, D. Gurney, I.-K. Park, Residual Stress Analysis Based on Acoustic and Optical Methods, Materials (Basel). 9 (2016) 112. https://doi.org/10.3390/ma9020112.

[264] Y.Z. Peifeng Li, Zhuo Kang, Zheng Zhang, Qingliang Liao, Feng Rao, Yang Lu, In situ microscopy techniques for characterizing the mechanical properties and deformation behavior of two-dimensional (2D) materials, Mater. Today 51 (2021) 247–272. https://doi.org/10.1016/j.mattod.2021.10.009.

[265] J.H.L. Grave, M.L. Håheim, A.T. Echtermeyer, Measuring changing strain fields in composites with Distributed Fiber-Optic Sensing using the optical backscatter reflectometer, Compos. Part B Eng. 74 (2015) 138–146. https://doi.org/10.1016/j.compositesb.2015.01.003.

[266] H. Liu, J. Yan, M. Kollosche, S.A. Bentil, S. Laflamme, Surface Textures for Stretchable Capacitive Strain Sensors, Smart Mater. Struct. 29 (2020) 105037. https://doi.org/10.1088/1361-665X/aba63c.

[267] R. Nur, N. Matsuhisa, Z. Jiang, M.O.G. Nayeem, T. Yokota, T. Someya, A Highly Sensitive Capacitive-type Strain Sensor Using Wrinkled Ultrathin Gold Films, Nano Lett. 18 (2018) 5610–5617. https://doi.org/10.1021/acs.nanolett.8b02088.

[268] G. Shi, Z. Zhao, J. Pai, I. Lee, L. Zhang, C. Stevenson, K. Ishara, R. Zhang, H. Zhu, J. Ma, Highly Sensitive, Wearable, Durable Strain Sensors and Stretchable Conductors Using Graphene/Silicon Rubber Composites, Adv. Funct. Mater. 26 (2016) 7614–7625. https://doi.org/10.1002/adfm.201602619.

[269] X. Liao, W. Wang, L. Wang, K. Tang, Y. Zheng, Controllably Enhancing Stretchability of Highly Sensitive Fiber-Based Strain Sensors for Intelligent Monitoring, ACS Appl. Mater. Interfaces 11 (2019) 2431–2440. https://doi.org/10.1021/acsami.8b20245.

[270] H. Souri, H. Banerjee, A. Jusufi, N. Radacsi, A.A. Stokes, I. Park, M. Sitti, M. Amjadi, Wearable and Stretchable Strain Sensors: Materials, Sensing Mechanisms, and Applications, Adv. Intell. Syst. 2 (2020). https://doi.org/10.1002/aisy.202000039.

[271] M. Amjadi, K. Kyung, I. Park, M. Sitti, Stretchable, Skin-Mountable, and Wearable Strain Sensors and Their Potential Applications: A Review, Adv. Funct. Mater. 26 (2016) 1678–1698. https://doi.org/10.1002/adfm.201504755.

[272] J. Guo, B. Zhou, R. Zong, L. Pan, X. Li, X. Yu, C. Yang, L. Kong, Q. Dai, Stretchable and Highly Sensitive Optical Strain Sensors for Human-Activity Monitoring and Healthcare, ACS Appl. Mater. Interfaces 11 (2019) 33589–33598. https://doi.org/10.1021/acsami.9b09815.

[273] H. Zhao, K. O'Brien, S. Li, R.F. Shepherd, Optoelectronically innervated soft prosthetic hand via stretchable optical waveguides, Sci. Robot. 1 (2016). https://doi.org/10.1126/scirobotics.aai7529.

[274] A. Masoudi, T.P. Newson, High spatial resolution distributed optical fiber dynamic strain sensor with enhanced frequency and strain resolution, Opt. Lett. 42 (2017) 290. https://doi.org/10.1364/OL.42.000290.

[275] Y. Zhang, Y. Wu, Y. Han, J. Wu, J. Ren, Y. Mao, B. Mao, B. Liu, High sensitivity strain sensor based on a novel offset-core single micro-tapered fiber-optic Mach-Zehnder interferometer, Opt. Fiber Technol. 73 (2022) 103012. https://doi.org/10.1016/j.yofte.2022.103012.

[276] B. Figueroa, Fernando; Mahajan, Ajay Mohan; Sayeh, Mohammad; and Regez, Fiber-Optic Strain Gauge With High Resolution And Update Rate, 2007. https://ideaexchange.uakron.edu/mechanical_ideas/477.

[277] D. HOEY, D. TAYLOR, Fatigue in porous PMMA: The effect of stress concentrations, Int. J. Fatigue 30 (2008) 989–995. https://doi.org/10.1016/j.ijfatigue.2007.08.022.

[278] O. Frank, G. Tsoukleri, I. Riaz, K. Papagelis, J. Parthenios, A.C. Ferrari, A.K. Geim, K.S. Novoselov, C. Galiotis, Development of a universal stress sensor for graphene and carbon fibres, Nat. Commun. 2 (2011) 255. https://doi.org/10.1038/ncomms1247.

[279] B.P. Arjyal, D.G. Katerelos, C. Filiou, C. Galiotis, Measurement and modeling of stress concentration around a circular notch, Exp. Mech. 40 (2000) 248–255. https://doi.org/10.1007/BF02327496.

[280] G. Tsoukleri, J. Parthenios, K. Papagelis, R. Jalil, A.C. Ferrari, A.K. Geim, K.S. Novoselov, C. Galiotis, Subjecting a Graphene Monolayer to Tension and Compression, Small 5 (2009) 2397–2402. https://doi.org/10.1002/smll.200900802.

[281] M.G. Pastore Carbone, J. Parthenios, G. Tsoukleri, S. Cotugno, G. Mensitieri, C. Galiotis, Assessing micromechanical behaviour of PET cords in rubber matrix composites by laser Raman microscopy, Compos. Sci. Technol. 85 (2013) 104–110. https://doi.org/10.1016/j.compscitech.2013.05.017.

[282] C. Galiotis, A study of mechanisms of stress transfer in continuous- and discontinuous-fibre model composites by laser Raman spectroscopy, Compos. Sci. Technol. 48 (1993) 15–28. https://doi.org/10.1016/0266-3538(93)90116-X.

[283] M. Liu, Z. Li, X. Zhao, R.J. Young, I.A. Kinloch, Fundamental Insights into Graphene Strain Sensing, Nano Lett. 21 (2021) 833–839. https://doi.org/10.1021/acs.nanolett.0c04577.

[284] A.P.A. Raju, A. Lewis, B. Derby, R.J. Young, I.A. Kinloch, R. Zan, K.S. Novoselov, Wide-Area Strain Sensors based upon Graphene-Polymer Composite Coatings Probed by Raman Spectroscopy, Adv. Funct. Mater. 24 (2014) 2865–2874. https://doi.org/10.1002/adfm.201302869.

[285] A.C. Manikas, M.G. Pastore Carbone, C.R. Woods, Y. Wang, I. Souli, G. Anagnostopoulos, M. Hadjinicolaou, K.S. Novoselov, C. Galiotis, Stress transfer at the nanoscale on graphene ribbons of regular geometry, Nanoscale 11 (2019) 14354–14361. https://doi.org/10.1039/C9NR03166A.

[286] G. Anagnostopoulos, C. Androulidakis, E.N. Koukaras, G. Tsoukleri, I. Polyzos, J. Parthenios, K. Papagelis, C. Galiotis, Stress Transfer Mechanisms at the Submicron Level for Graphene/Polymer Systems, ACS Appl. Mater. Interfaces 7 (2015) 4216–4223. https://doi.org/10.1021/am508482n.

[287] M.G. Pastore Carbone, G. Tsoukleri, A.C. Manikas, E. Makarona, C. Tsamis, C. Galiotis, Production and Mechanical Characterization of Graphene Micro-Ribbons, J. Compos. Sci. 3 (2019) 42. https://doi.org/10.3390/jcs3020042.

[288] C. Androulidakis, G. Tsoukleri, N. Koutroumanis, G. Gkikas, P. Pappas, J. Parthenios, K. Papagelis, C. Galiotis, Experimentally derived axial stress-strain relations for two-dimensional materials such as monolayer graphene, Carbon N. Y. 81 (2015) 322–328. https://doi.org/10.1016/j.carbon.2014.09.064.

[289] Z. Li, R.J. Young, D.G. Papageorgiou, I.A. Kinloch, X. Zhao, C. Yang, S. Hao, Interfacial stress transfer in strain engineered wrinkled and folded graphene, 2D Mater. 6 (2019) 045026. https://doi.org/10.1088/2053-1583/ab3167.

[290] M.G. Pastore Carbone, A.C. Manikas, I. Souli, C. Pavlou, C. Galiotis, Mosaic pattern formation in exfoliated graphene by mechanical deformation, Nat. Commun. 10 (2019) 1572. https://doi.org/10.1038/s41467-019-09489-z.

[291] Y. Zhang, Y. Jin, J. Liu, Q. Ren, Z. Chen, Y. Zhao, P. Zhao, Strain engineering of graphene on rigid substrates, Nanoscale Adv. 4 (2022) 5056–5061. https://doi.org/10.1039/D2NA00580H.

[292] P. Ghidossi, M. El Mansori, F. Pierron, Edge machining effects on the failure of polymer matrix composite coupons, Compos. Part A Appl. Sci. Manuf. 35 (2004) 989–999. https://doi.org/10.1016/j.compositesa.2004.01.015.

[293] D. Bertoldo Menezes, A. Reyer, A. Benisek, E. Dachs, C. Pruner, M. Musso, Raman spectroscopic insights into the glass transition of poly(methyl methacrylate), Phys. Chem. Chem. Phys. 23 (2021) 1649–1665. https://doi.org/10.1039/D0CP05627H.

[294] M. Xia, Z. Su, S. Zhang, Raman spectra of bilayer graphene covered with Poly(methyl methacrylate) thin film, AIP Adv. 2 (2012). https://doi.org/10.1063/1.4739785.

[295] M. Wall, Raman Spectroscopy Optimizes Graphene Characterization, AM&P Tech. Artic. 170 (2012) 35–38. https://doi.org/10.31399/asm.amp.2012-04.p035.

[296] T. Jiang, R. Huang, Y. Zhu, Interfacial Sliding and Buckling of Monolayer Graphene on a Stretchable Substrate, Adv. Funct. Mater. 24 (2014) 396–402. https://doi.org/10.1002/adfm.201301999.

[297] C. Androulidakis, E.N. Koukaras, J. Parthenios, G. Kalosakas, K. Papagelis, C. Galiotis, Graphene flakes under controlled biaxial deformation, Sci. Rep. 5 (2015) 18219. https://doi.org/10.1038/srep18219.

[298] F. Najafi, G. Wang, S. Mukherjee, T. Cui, T. Filleter, C.V. Singh, Toughening of graphene-based polymer nanocomposites via tuning chemical functionalization, Compos. Sci. Technol. 194 (2020) 108140. https://doi.org/10.1016/j.compscitech.2020.108140.

[299] G. Anagnostopoulos, L. Sygellou, G. Paterakis, I. Polyzos, C.A. Aggelopoulos, C. Galiotis, Enhancing the adhesion of graphene to polymer substrates by controlled defect formation, Nanotechnology 30 (2019) 015704. https://doi.org/10.1088/1361-6528/aae683.

[300] D. Taylor, M. Merlo, R. Pegley, M.P. Cavatorta, The effect of stress concentrations on the fracture strength of polymethylmethacrylate, Mater. Sci. Eng. A 382 (2004) 288–294. https://doi.org/10.1016/j.msea.2004.05.012.

[301] U. Ali, K.J.B.A. Karim, N.A. Buang, A Review of the Properties and Applications of Poly (Methyl Methacrylate) (PMMA), Polym. Rev. 55 (2015) 678–705. https://doi.org/10.1080/15583724.2015.1031377.

[302] G. Cao, Atomistic Studies of Mechanical Properties of Graphene, Polymers (Basel). 6 (2014) 2404–2432. https://doi.org/10.3390/polym6092404.

[303] Plane Strain and Plane Stress, in: Elasticity, Kluwer Academic Publishers, Dordrecht, n.d.: pp. 33–40. https://doi.org/10.1007/0-306-48395-5_3.

[304] N. Bakhshaee Babaroud, M. Palmar, A.I. Velea, C. Coletti, S. Weingärtner, F. Vos, W.A. Serdijn, S. Vollebregt, V. Giagka, Multilayer CVD graphene electrodes using a transfer-free process for the next generation of optically transparent and MRI-compatible neural interfaces, Microsystems Nanoeng. 8 (2022) 107. https://doi.org/10.1038/s41378-022-00430-x.

[305] X. Huang, C. Zhi, Y. Lin, H. Bao, G. Wu, P. Jiang, Y.-W. Mai, Thermal conductivity of graphene-based polymer nanocomposites, Mater. Sci. Eng. R Reports 142 (2020) 100577. https://doi.org/10.1016/j.mser.2020.100577.

[306] C.S. Boland, U. Khan, G. Ryan, S. Barwich, R. Charifou, A. Harvey, C. Backes, Z. Li, M.S. Ferreira, M.E. Möbius, R.J. Young, J.N. Coleman, Sensitive electromechanical sensors using viscoelastic graphene-polymer nanocomposites, Science (80-.). 354 (2016) 1257–1260. https://doi.org/10.1126/science.aag2879.

[307] Spin coating, (n.d.). https://www.keyence.com/ss/products/measure/sealing/coater-type/spin.jsp.

[308] D.B. Hall, P. Underhill, J.M. Torkelson, Spin coating of thin and ultrathin polymer films, Polym. Eng. Sci. 38 (1998) 2039–2045. https://doi.org/10.1002/pen.10373.

[309] A. Boscá, J. Pedrós, J. Martínez, T. Palacios, F. Calle, Automatic graphene transfer system for improved material quality and efficiency, Sci. Rep. 6 (2016) 21676. https://doi.org/10.1038/srep21676.

[310] D.G. Papageorgiou, I.A. Kinloch, R.J. Young, Mechanical properties of graphene and graphene-based nanocomposites, Prog. Mater. Sci. 90 (2017) 75–127. https://doi.org/10.1016/j.pmatsci.2017.07.004.

[311] F.O. Edoziuno, A.A. Adediran, O.S. Adesina, C.O. Osueke, S. Siengchin, T.-C. Jen, Modeling of mechanical and essential properties of nanocomposites, in: Polym. Nanocomposites with Carbonaceous Nanofillers Aerosp. Appl., Elsevier, 2023: pp. 245–262. https://doi.org/10.1016/B978-0-323-99657-0.00010-7.

[312] F. Pashmforoush, Mechanical properties prediction of various graphene reinforced nanocomposites using transfer learning-based deep neural network, Proc. Inst. Mech. Eng. Part E J. Process Mech. Eng. 237 (2023) 1214–1223. https://doi.org/10.1177/09544089221115306.

[313] W. Jin, J. Pei, P. Xie, J. Chen, H. Zhao, Machine Learning-Based Prediction of Mechanical Properties and Performance of Nickel–Graphene Nanocomposites Using Molecular Dynamics Simulation Data, ACS Appl. Nano Mater. 6 (2023)

12190–12199. https://doi.org/10.1021/acsanm.3c01919.

[314] M. Yang, W. Li, Z. Zhao, Y. He, X. Zhang, Y. Ma, P. Dong, S. Zheng, Micromechanical modeling for the temperature-dependent yield strength of polymer-matrix nanocomposites, Compos. Sci. Technol. 220 (2022) 109265. https://doi.org/10.1016/j.compscitech.2022.109265.

[315] A. Muhammad, R. Srivastava, N. Koutroumanis, D. Semitekolos, E. Chiavazzo, P.-N. Pappas, C. Galiotis, P. Asinari, C.A. Charitidis, M. Fasano, Mesoscopic Modeling and Experimental Validation of Thermal and Mechanical Properties of Polypropylene Nanocomposites Reinforced By Graphene-Based Fillers, Macromolecules 56 (2023) 9969–9982. https://doi.org/10.1021/acs.macromol.3c01529.

[316] K. Zhang, Y. Zhang, S. Wang, Enhancing thermoelectric properties of organic composites through hierarchical nanostructures, Sci. Rep. 3 (2013) 3448. https://doi.org/10.1038/srep03448.

[317] A. Wirsén, K.T. Lindberg, A.-C. Albertsson, Graft polymerization of acrylamide onto linear low-density polyethylene film by electron beam pre-irradiation in air or argon: 3. Morphology, Polymer (Guildf). 37 (1996) 761–769. https://doi.org/10.1016/0032-3861(96)87251-X.

[318] J.C.H. and J.L.K. Affdl, The Halpin-Tsai equations: A review., Polym. Eng. Sci. 16 (1976) 344–352.

[319] S.W. TSAI, ENVIRONMENTAL FACTORS IN THE DESIGN OF COMPOSITE MATERIALS, in: Mech. Compos. Mater., Elsevier, 1970: pp. 749–767. https://doi.org/10.1016/B978-0-08-006421-5.50041-1.

[320] K. Deng, H.K. Nejadkhaki, F.M. Pasquali, A.P. Amaria, J.N. Armstrong, J.F. Hall, Rule of Mixtures Model to Determine Elastic Modulus and Tensile Strength of 3D Printed Carbon Fiber Reinforced Nylon, in: Vol. 2A 45th Des. Autom. Conf., American Society of Mechanical Engineers, 2019. https://doi.org/10.1115/DETC2019-98024.

[321] C.D. Kalfountzos, G.S.E. Bikakis, E.E. Theotokoglou, The Rule of Mixtures on the Elastic Buckling Response of Rectangular GLARE FML Plates Under Shear Stresses, in: 2020: pp. 20–25. https://doi.org/10.1007/978-3-030-47883-4_4.

[322] M.L.M. Rodzi, M.F. Ismail, M. Minhat, Applicability of Rule of Mixtures to Estimate Effective Properties of Nanocomposite Materials, in: 2020: pp. 191–205. https://doi.org/10.1007/978-981-15-4756-0_17.

[323] C. Pavlou, M.G. Pastore Carbone, A.C. Manikas, G. Trakakis, C. Koral, G. Papari, A. Andreone, C. Galiotis, Effective EMI shielding behaviour of thin graphene/PMMA nanolaminates in the THz range, Nat. Commun. 12 (2021) 4655. https://doi.org/10.1038/s41467-021-24970-4.

[324] K. Cao, S. Feng, Y. Han, L. Gao, T. Hue Ly, Z. Xu, Y. Lu, Elastic straining of free-standing monolayer graphene, Nat. Commun. 11 (2020) 284. https://doi.org/10.1038/s41467-019-14130-0.

[325] C. Pavlou, PRODUCTION & CHARACTERIZATION OF GRAPHENE-

BASED POLYMER NANOLAMINATES, University of Patras, 2022.

[326] J. Li, B. Yang, S. Wang, M.N. James, S. Xiao, T. Zhu, G. Yang, Modified Model of Crack Tip Stress Field Considering Dislocation Slip Accumulation and Crack Tip Blunting, Chinese J. Mech. Eng. 36 (2023) 47. https://doi.org/10.1186/s10033-023-00875-9.

[327] Y. Liu, H.D. Liu, V. Pelenovich, Q. Wan, J.L. Guo, Y.M. Chen, J. Zhang, L.J. Xue, Z.G. Li, B. Yang, Influences of modulation period on structure and properties of AlTiSiN/AlCrSiN nanocomposite multilayer coatings, Vacuum 193 (2021) 110516. https://doi.org/10.1016/j.vacuum.2021.110516.

[328] G. Anagnostopoulos, C. Androulidakis, E.N. Koukaras, G. Tsoukleri, I. Polyzos, J. Parthenios, K. Papagelis, C. Galiotis, Stress transfer mechanisms at the submicron level for graphene/polymer systems, ACS Appl. Mater. Interfaces 7 (2015) 4216–4223. https://doi.org/10.1021/am508482n.

[329] S.-I. Kim, J.-Y. Moon, S.-K. Hyeong, S. Ghods, J.-S. Kim, J.-H. Choi, D.S. Park, S. Bae, S.H. Cho, S.-K. Lee, J.-H. Lee, Float-stacked graphene–PMMA laminate, Nat. Commun. 15 (2024) 2172. https://doi.org/10.1038/s41467-024-46502-6.

[330] O. Frank, M. Mohr, J. Maultzsch, C. Thomsen, I. Riaz, R. Jalil, K.S. Novoselov, G. Tsoukleri, J. Parthenios, K. Papagelis, L. Kavan, C. Galiotis, Raman 2D-Peak Splitting in Graphene: Theory and Experiment, ACS Nano 5 (2011) 2231–2239. https://doi.org/10.1021/nn103493g.

[331] N. Obaid, M. Kortschot, M. Sain, Understanding the Stress Relaxation Behavior of Polymers Reinforced with Short Elastic Fibers, Materials (Basel). 10 (2017) 472. https://doi.org/10.3390/ma10050472.

[332] N. Obaid, M.T. Kortschot, M. Sain, Predicting the stress relaxation behavior of glass-fiber reinforced polypropylene composites, Compos. Sci. Technol. 161 (2018) 85–91. https://doi.org/10.1016/j.compscitech.2018.04.004.

[333] N.C. Adak, S. Chhetri, S. Sabarad, H. Roy, N.C. Murmu, P. Samanta, T. Kuila, Direct observation of micro delamination in graphene oxide incorporated carbon fiber/epoxy composite via in-situ tensile test, Compos. Sci. Technol. 177 (2019) 57–65. https://doi.org/10.1016/j.compscitech.2019.04.006.

[334] J. Wang, V.B.C. Tan, Effects of Relative Positions of Defect to Inclusion on Nanocomposite Strength, Materials (Basel). 15 (2022) 4906. https://doi.org/10.3390/ma15144906.

[335] Z. Yao, Z.-M. Huang, Stress concentration factors in the matrix with different imperfect interfaces, Int. J. Damage Mech. 23 (2014) 745–771. https://doi.org/10.1177/1056789513512345.

[336] S. Ray-Chaudhuri, K. Chawla, Stress and Strain Concentration Factors in Orthotropic Composites with Hole under Uniaxial Tension, Curved Layer. Struct. 5 (2018) 213–231. https://doi.org/10.1515/cls-2018-0016.

[337] V.S. Romanov, S. V. Lomov, I. Verpoest, L. Gorbatikh, Modelling evidence of stress concentration mitigation at the micro-scale in polymer composites by the addition of carbon nanotubes, Carbon N. Y. 82 (2015) 184–194.

https://doi.org/10.1016/j.carbon.2014.10.061.

[338] Z. Peng, X. Chen, Y. Fan, D.J. Srolovitz, D. Lei, Strain engineering of 2D semiconductors and graphene: from strain fields to peak-structure tuning and photonic applications, Light Sci. Appl. 9 (2020) 190. https://doi.org/10.1038/s41377-020-00421-5.

[339] S. Yang, Y. Chen, C. Jiang, Strain engineering of <scp>two-dimensional</scp> materials: Methods, properties, and applications, InfoMat 3 (2021) 397–420. https://doi.org/10.1002/inf2.12177.

[340] C. Androulidakis, G. Tsoukleri, N. Koutroumanis, G. Gkikas, P. Pappas, J. Parthenios, K. Papagelis, C. Galiotis, Experimentally derived axial stress–strain relations for two-dimensional materials such as monolayer graphene, Carbon N. Y. 81 (2015) 322–328. https://doi.org/10.1016/j.carbon.2014.09.064.

[341] G. Tsoukleri, J. Parthenios, C. Galiotis, K. Papagelis, Embedded trilayer graphene flakes under tensile and compressive loading, 2D Mater. 2 (2015) 024009. https://doi.org/10.1088/2053-1583/2/2/024009.

[342] E.E. Mathew, B. Manoj, Disorders in graphene: types, effects and control techniques—a review, Carbon Lett. 32 (2022) 431–450. https://doi.org/10.1007/s42823-021-00289-4.

[343] H. Wu, G. Fan, An overview of tailoring strain delocalization for strength-ductility synergy, Prog. Mater. Sci. 113 (2020) 100675. https://doi.org/10.1016/j.pmatsci.2020.100675.

[344] Q. Xu, K.E. Jensen, R. Boltyanskiy, R. Sarfati, R.W. Style, E.R. Dufresne, Direct measurement of strain-dependent solid surface stress, Nat. Commun. 8 (2017) 555. https://doi.org/10.1038/s41467-017-00636-y.

[345] D. Berman, A. Erdemir, A. V. Zinovev, A. V. Sumant, Nanoscale friction properties of graphene and graphene oxide, Diam. Relat. Mater. 54 (2015) 91–96. https://doi.org/10.1016/j.diamond.2014.10.012.

[346] C. Wang, J. Wang, A.H. Barber, Stress concentrations in nanoscale defective graphene, AIP Adv. 7 (2017). https://doi.org/10.1063/1.4996387.

[347] F. Liu, P. Ming, J. Li, Ab initio calculation of ideal strength and phonon instability of graphene under tension, Phys. Rev. B 76 (2007) 064120. https://doi.org/10.1103/PhysRevB.76.064120.

[348] Z. Dai, L. Liu, Z. Zhang, Strain Engineering of 2D Materials: Issues and Opportunities at the Interface, Adv. Mater. 31 (2019). https://doi.org/10.1002/adma.201805417.

[349] A.P. Sgouros, G. Kalosakas, K. Papagelis, C. Galiotis, Compressive response and buckling of graphene nanoribbons, Sci. Rep. 8 (2018) 9593. https://doi.org/10.1038/s41598-018-27808-0.

[350] L. Meng, Y. Li, T.S. Liu, C. Zhu, Q.Y. Li, X. Chen, S. Zhang, X. Zhang, L. Bao, Y. Huang, F. Xu, R.S. Ruoff, Wrinkle networks in exfoliated multilayer graphene and other layered materials, Carbon N. Y. 156 (2020) 24–30. https://doi.org/10.1016/j.carbon.2019.09.035.

[351] S. Feng, K. Cao, Y. Gao, Y. Han, Z. Liu, Y. Lu, Z. Xu, Experimentally measuring weak fracture toughness anisotropy in graphene, Commun. Mater. 3 (2022) 28. https://doi.org/10.1038/s43246-022-00252-4.

[352] H. Yin, H.J. Qi, F. Fan, T. Zhu, B. Wang, Y. Wei, Griffith Criterion for Brittle Fracture in Graphene, Nano Lett. 15 (2015) 1918–1924. https://doi.org/10.1021/nl5047686.

[353] Z.-E. Liu, Y. Wei, An analytical solution to the stress fields of kinked cracks, J. Mech. Phys. Solids 156 (2021) 104619. https://doi.org/10.1016/j.jmps.2021.104619.

[354] T. Cui, S. Mukherjee, P.M. Sudeep, G. Colas, F. Najafi, J. Tam, P.M. Ajayan, C.V. Singh, Y. Sun, T. Filleter, Fatigue of graphene, Nat. Mater. 19 (2020) 405–411. https://doi.org/10.1038/s41563-019-0586-y.

[355] G. Wang, E. Gao, Z. Dai, L. Liu, Z. Xu, Z. Zhang, Degradation and recovery of graphene/polymer interfaces under cyclic mechanical loading, Compos. Sci. Technol. 149 (2017) 220–227. https://doi.org/10.1016/j.compscitech.2017.06.004.

[356] T. Cui, K. Yip, A. Hassan, G. Wang, X. Liu, Y. Sun, T. Filleter, Graphene fatigue through van der Waals interactions, Sci. Adv. 6 (2020). https://doi.org/10.1126/sciadv.abb1335.

[357] L. Gong, I.A. Kinloch, R.J. Young, I. Riaz, R. Jalil, K.S. Novoselov, Interfacial Stress Transfer in a Graphene Monolayer Nanocomposite, Adv. Mater. 22 (2010) 2694–2697. https://doi.org/10.1002/adma.200904264.

[358] P. Li, M. Yang, Y. Liu, H. Qin, J. Liu, Z. Xu, Y. Liu, F. Meng, J. Lin, F. Wang, C. Gao, Continuous crystalline graphene papers with gigapascal strength by intercalation modulated plasticization, Nat. Commun. 11 (2020) 2645. https://doi.org/10.1038/s41467-020-16494-0.